MAGNETOM Flash

Issue Number 75 · 4/2019
RSNA Edition

siemens.com/magnetom-world

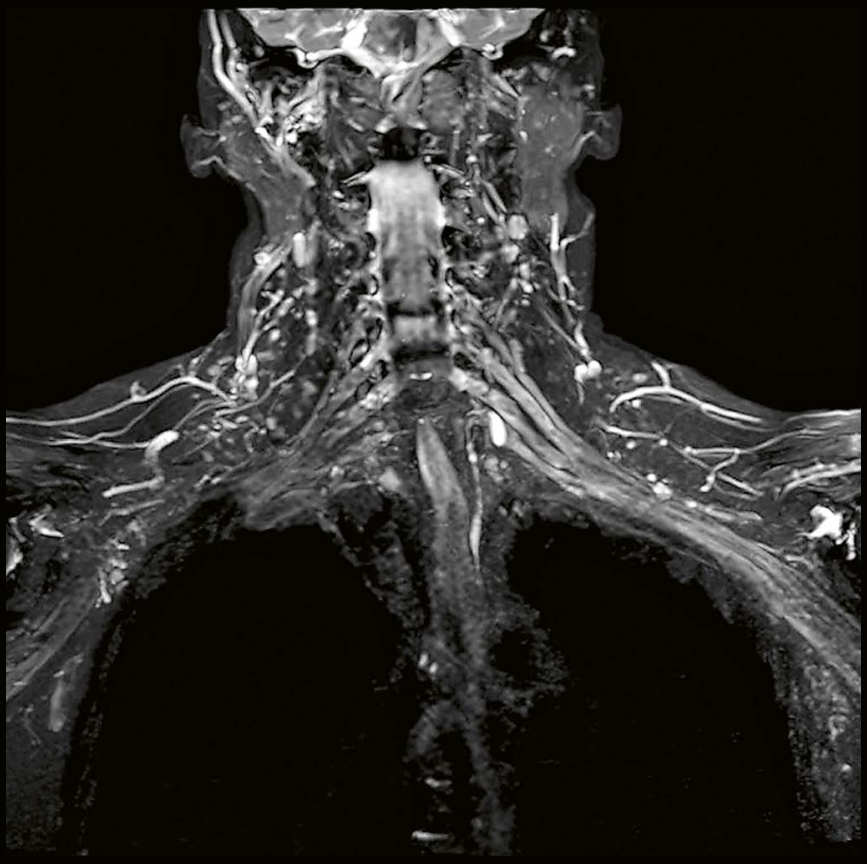

SIEMENS Healthineers

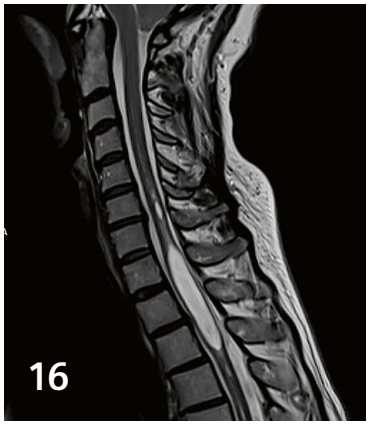

3T MRI with MAGNETOM Lumina

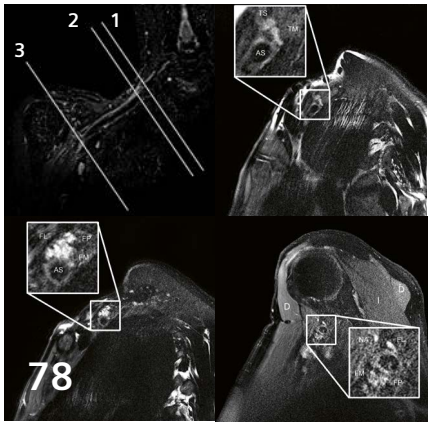

MRN in Disorders of the Peripheral Nervous System

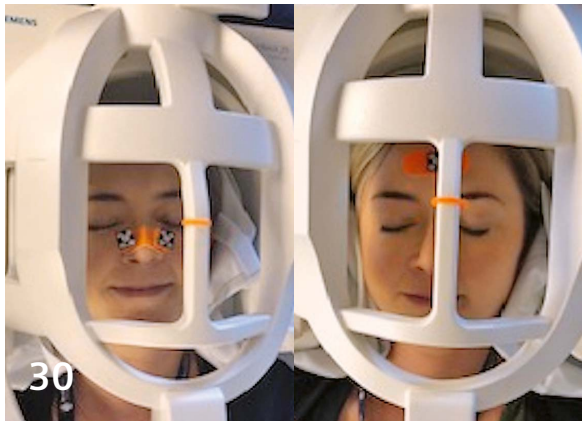

Prospective Motion Correction

Editorial Comment

AI in MR

Spotlight

Abdominal Imaging

Pediatric Imaging

Interventional MRI

Neurology

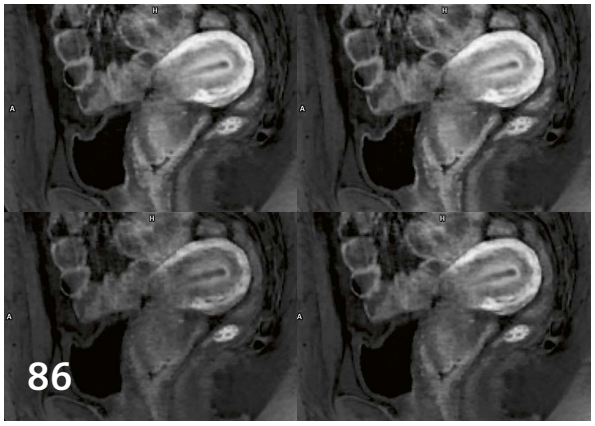

Compressed Sensing VIBE in the Female Pelvis

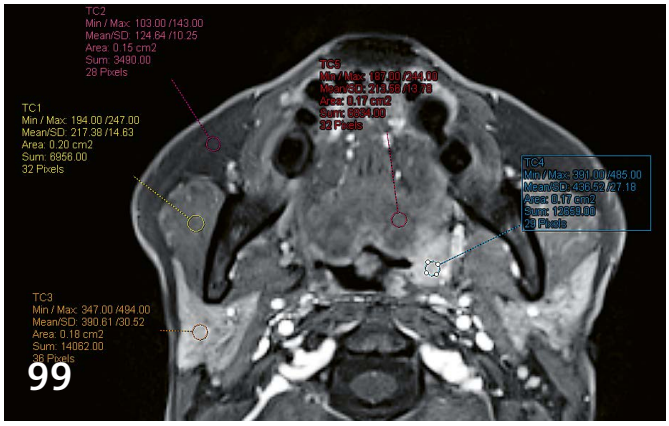

First Impressions of MAGNETOM Vida Fit

Musculoskeletal Imaging

Women's Health

Men's Health

Business

A History of Innovations

Meet Siemens Healthineers

Mark C. DeLano, MD FACR, is Director of the Division of Radiology and Biomedical Imaging at the Michigan State University (MSU) College of Human Medicine and a partner at Advanced Radiology Services, PC (ARS) in Grand Rapids, Michigan, USA. Dr. DeLano leads the MSU academic efforts of ARS, the largest clinical radiology affiliate of the MSU College of Human Medicine (CHM) with 140 subspecialized radiologists. He has served MSU in his current role since 2009 bridging the academic teaching and research missions of CHM and the subspecialized clinical radiology practice in Grand Rapids. He is also Medical Director of Adult Radiology at Spectrum Health System, overseeing radiology operations of a system of 14 hospitals and 37 outpatient imaging facilities.

The Nexus of MR with Artificial Intelligence

Dear readers and colleagues,

Artificial intelligence (AI) is maturing at a time when the need for health care transformation is enormous. We are faced with spectacular challenges in medicine and specifically in radiology by virtue of our penetrance to every patient and our impact on diagnosis, patient disposition, intervention, and costs. This nexus is manifest through AI enhancements along key vectors of innovation acquisition, diagnostics, and operations that are evident throughout this volume.

There is a natural tendency to gravitate to technological solutions to complex problems, particularly in medicine. As a medical student contemporary to the advent of magnetic resonance, the cell phone, and searchable library databases, my pocket brain was analog. Now technology brings knowledge immediately to our fingertips. Magnetic resonance sparked my interest in radiology at that time, and the amazing potential of MR continues to grow and intrigue. We are faced with expanding challenges to human cognition and complex information processing demands that exceed the capabilities of the most apt pupils. The convergence of need and technological advances engenders optimism, but it will require rethinking how we work.

AI in radiology can improve precision medicine, productivity and patient care through simplification of workflow, more efficient use of physician time, improved patient experience, and integration into the digitalized future of healthcare. AI is expanding our views of what is possible in the promotion of health, detection of disease, and optimization of treatment. The expanding interconnectedness and velocity of information flow within and between disciplines is exceeding existing routes of communication. Massive, transformative changes in infrastructure and our expectations will streamline patient care delivery in a future is being built today. Siemens Healthineers' academic-industry partnerships leverage mutual and complementary strengths in care delivery, critical thinking, rapid innovation cycles, and pragmatic deployment of new discoveries. We are proud to be part of the Siemens Healthineers strategic network helping to define and iterate the path to the future.

Much of the AI development is being driven by the demands of increasing specialization, more sophisticated algorithms, and massive data streams that need to be effectively managed in order to distill the best course of action. Humans need help. The community of like-minded collaborative scientists in the public and private sectors are engineering solutions for the health challenges facing our populations. It is in this context that I anticipate this edition of the MAGNETOM Flash. Innovation in the Siemens MR community is inspiring creative contributions to all aspects of value chain that MR provides. Computer-aided diagnosis foreshadows the promise that is AI but is only one of the many attractive facets.

After training at Duke University Radiology and Johns Hopkins Neuroradiology he returned to MSU, his alma mater to direct the MR section at MSU in East Lansing. Dr. DeLano was privileged to participate in the early development and adoption of 3T MRI in clinical practice, running a full-time, comprehensive whole body MR scanner schedule beginning in 2001. He has presented nationally and internationally on his diversified research and translational clinical experience across multiple subspecialties including cardiovascular and musculoskeletal radiology in addition to his primary specialty of neuroradiology.

His mentorship and teaching in the medical school and the MSU/Spectrum Health Diagnostic Radiology Residency spans neuroradiology, MR techniques, and cardiovascular thoracic imaging. At Spectrum Health Dr. DeLano leads cross-disciplinary initiatives in care pathway development and implementation. He facilitates AI adoption, informatics integration, and lean management in radiology throughout the system.

Patient centric MR and precision health

Technology maturation is actuating the 20+-year-old Zerhouni championed vision of precision healthcare espoused in his roadmap for clinical and translational research [2]. He described the development predictive, personalized, preemptive, and participatory future of medicine. Our ability to achieve this future state is enhanced by on our assimilation of technology into our standard work as we interpret imaging in consultation with our clinical colleagues and increasingly in partnership with our digital colleagues. AI is the piece that helps these concepts become seamlessly integrated into our common experience. Imaging of the future will capitalize on the detection of genotypic and phenotypic features and will stratify patients in terms of risk including prognosis and survival likelihood. The expansion of precision medicine toward this "4 P model" results from the confluence of technological innovation, economic imperative, and ethical necessity. This vision for the future is becoming our present reality. AI and advanced technologies are shaping how MR is conducted provides a window on a very bright future.

What is most compelling at this juncture is the increasing integration of AI technology into our workflow and the delivery of individualized health care. Technology is becoming quietly smart. Rather than a disruption, it is an integral partner in our quest to advance the care of our sick and maintenance of health. Technology is being designed to anticipate our needs and improve our performance, informed by data and personalized to the user and the patient.

Patient adaptive BioMatrix Technology

BioMatrix Technology is designed to advance toward the seamless integration goal, and the care of patients is being enhanced by these creative innovations and novel applications. These literally and figuratively touch the patient at all points of care, from patient preparation, image planning and acquisition, image reconstruction and distribution, image postprocessing and interpretation. Patients have unique, individual characteristics or biovariabilities that cause unwarranted variations in imaging results. BioMatrix helps to overcome these challenges by automatically adjusting to individual patients. By "embracing human nature" in this way, examinations are personalized and help expand precision medicine. AI powered BioMatrix and GO Technologies increase throughput, and integration into workflow is fundamental to the facilitating high quality and high-volume work while keeping patient comfort in mind.

MR driving quality and the triple aim

Avedis Donabedian's seminal work on the quality provision of health care set out necessity of attention to the structure, process, and outcome [3]. The structures and processes are evolving and the outcomes are increasingly important to drive the innovation feedback loop as we strive toward the triple aim. The structures we rely on continue to improve. This is evident in the adaptation of clinical imaging to increasing field strength, higher performance of the radio frequency architecture and gradients,

and more efficient coils. The processes that benefit the drive to value include BioMatrix empowered adaptive sensors that tailor exams to the individual's anatomy and physiology. AI and deep learning enhanced reconstruction algorithms also are value added process steps.

Ultimately, better outcomes are dependent on the integration of multiple advancements that reduce the work of the healthcare team and improve the experience of patients.

The health care system, doctors, and patients have the parallel needs. Paraphrasing Engelbert and Hagel, we need to foster environments where people engage in more fulfilling and inventive work that allows them to realize their full potential, augmented by technology to perform routine, often tedious tasks. Artificial intelligence and the digitalization of health care will empower physicians to work more efficiently, create more accurate reports, and drive more impactful care to our patients. Evidence driven accelerated scan protocols more efficiently utilize the limited and expensive MR resources. Faster scanning enhances the patient experience and allows the delivery of care to more people. Innovations in the analysis and post-processing of image data can provide quantitative data not otherwise practical or detectable by qualitative methods.

MR Fingerprinting

The objectivity of MR Fingerprinting will facilitate the detection of subtle disease and the differentiation of pathologies. MR Fingerprinting is a quantitative approach to MR that allows simultaneous measurement of multiple tissue properties in a single, time-efficient acquisition. This back-to-the-future maturation of the Damadian vision to inform diagnosis via maps of tissue relaxometry [4, 5] now enables more objective diagnoses, inter-scan comparisons facilitating longitudinal follow-up of individuals, and development of imaging biomarkers [6, 7]. The fast, highly sensitive and reproducible parametric maps hold promise to differentiate various pathologies particularly in oncology. Additionally, the capacity to differentiate the borderlands of the normal and near-pathologic tissue has frequently been the discriminator of the novice and expert. Quantitation via MRF can elevate the objectivity of diagnosis and shift observer performance ROC curves up and to the left. More accurate and timely diagnoses, preventative strategies, and interventions will shift care from the hospital to the home and reduce costs.

A state of health

Health disparities and access to health care is an ongoing challenge that requires conscious efforts from multiple approaches. The extent and magnitude of these disparities is linked to geography and availability of diagnostic equipment and the required personnel to operate advanced technology. Additionally, the capacity to understand remote communities and their specific problems requires insight to their experience. We need to be present. Borrowing from the realm of lean process improvement, we need to go to the Gemba, the real place where the action is. Digitalized interconnectivity transforms the "house call" to the "digital Gemba" and removes the limitations imposed

"The promise of today's breakthroughs is not just efficiency – it's unleashing value creation and capture in a time of mounting performance pressure. But this will require driving a fundamental shift in the nature of work."

Cathy Engelbert and John Hagel III
in *Fulfilling the Promise of AI Requires Rethinking the Nature of Work Itself*, Harvard Business Review, 2017.

by distance. We envision a "state of health" in Michigan inspired by the land grant mission of our university that created Michigan Agricultural Experiment Stations in each of our 83 counties. Founded in 1888, these stations, now named the AgBioResearch Network, have played a pivotal role in enhancing agriculture, managing natural and community resources, and enhancing the quality of life in Michigan, the nation and the world. Similarly, the remote delivery of health care across our geographically dispersed but clinically integrated network throughout the state is connected through various telehealth solutions. Virtual Cockpit is one such digitally operationalized solution which will connect subspecialized and personalized care to the remote and underserved populations of the state. These advanced technology initiatives will extend the reach of our physicians. AI and technology can also facilitate the establishment and dissemination of best practices across geographies and is scalable beyond the state boundaries. Virtual Cockpit enables the system-wide dissemination and synchronization of protocols to take advantage of the latest technology. The remote operation and management of imaging equipment ensures the same level of service at all of our sites, extending our care to all the populations we serve, without geographical barriers or limitations. The Virtual Cockpit allows the implementation of standardized work. It enables generalist technologists and physicians to achieve optimal results, and the leverage of super-users for the remote performance of subspecialty imaging. As a community-based medical school with some campuses separated by more than 400 miles but connected by fiber, this enabling technology supports our core educational mission. This will unite the primary to the quaternary to deliver the best standard of care to all.

Connections

The connection to people and purpose has reciprocal benefits to patients and providers, staving off the ravages of burn-out on our physicians. Impossibility and despair are replaced by answers, solutions, and hope. Johann Wolfgang von Goethe's aphorisms often ponder what is possible. "A man must cling to the belief that the incomprehensible is comprehensible; otherwise he would not try to fathom it." [8] We are in a transformative era where innovation is refueling our inspiration, where the real limits are less technical and more of the imagination.

Pathway companions influence behaviors to add value

Ezekiel Emanuel points out that "the most pressing problem with the US health care system is not a lack of data or analytics but changing the behavior of millions of patients and clinicians." [9] This is where the simplicity and elegance of evidence-based clinical care pathways empower changes in clinician and patient behavior. The dealer's choice, often seemingly random ordering of tests that are not acted upon or create false positives requiring expensive follow up are eliminated by adherence to pathways. Evidence-based medicine is not new and associated appropriate practices frequently do not reach the patient. Technology solutions are emerging that are making encouraging in-roads toward successful creation and adoption of care pathways informed by AI that are integrated and "assimilated" into medical practice such that resistance is futile, or at least such that appropriate care is the easier path. AI informed care pathways and distributed innovation are impacting the entire value chain of medicine. The gains we enjoy are leading to operational optimization and facilitation of patient flow through our devices and care systems, while enabling the rapid diagnosis and personalized treatment of illness and the maintenance of health. Influencing the behavior of clinicians begins in their formation. As new generations of physicians emerge to take the helm of patient care and leadership of our profession, the judicious assimilation of AI-informed care will be organically accepted.

We want it all

The proposition that MR sequences should stop when the data sufficient for diagnosis is acquired rather than when the image is subjectively pretty is difficult to sell. This determination could be based on big data analytics and outcomes, and could be quantitative. The resulting image may not necessarily satisfy the current aesthetic, but instead answer the question regarding diagnosis or indicate the next patient management steps. This has proven to be a difficult sell to the visually motivated imaging professionals. Since the arrival of 3T, acceptance of faster rather than more beautiful images have been elusive. Micron level spatial resolution may have import for select applications, but most stroke, large vessel occlusions, disc herniations, and ligament or meniscal tears do not require more resolution than obtained at lower fields. The underlying paradigm shift required is the view of imaging as data, not portraits suitable for framing. Curating this data is the goal, and success will be beautiful in a different sense. But this too will require a shift in our thinking and behavior.

Conclusions

Magnetic resonance has its foundation in the spirit of curiosity and scientific inquiry and will continue to stimulate a passion for innovation for generations. It is integrated into patient care and provides critical insights on structure

and function in health and disease. The manifest transformation of health care with and through radiology will be through earlier and preemptive diagnosis, intervention, and surveillance of patients and populations. Cost-effective health management demands health maintenance. Imaging of established, macroscopic disease must become an aberration not the norm. This will allow diversion of precious resources toward the advancing the public health needs of our communities and the vexing problems of health disparities, poverty, substance abuse, maternal mortality, and mental illness. There are underserved populations and communities that we could not serve if it was not for this technology. The scope and scale of the Siemens Healthineers imaging community, with its robust clinical and research network provides a venue for the fruitful exchange of ideas, addressing both problems and solutions. Enjoy this showcase of the latest innovation and translational science advancing the care we provide in the pages that follow.

Mark C. DeLano

References

1 Engelbert, C., Hagel, J. (2017). Fulfilling the Promise of AI Requires Rethinking the Nature of Work Itself. Harvard Business Review, 1–5. Retrieved from https://hbr.org/2017/12/fulfilling-the-promise-of-ai-requires-rethinking-the-nature-of-work-itself

2 Zerhouni E. A., et al. (2007). Transforming medicine through discovery. Major trends in biomedical research. Bulletin de L'Académie Nationale de Médecine, 191(8):1685-94.

3 Donabedian A., et al. (1985). Twenty years of research on the quality of medical care: 1964-1984. Evaluation & the Health Professions, 8(3), 243–265.

4 Damadian R. (1971). Tumor detection by nuclear magnetic resonance. Science (New York, N.Y.), 171(3976), 1151–1153. http://doi.org/10.1126/science.171.3976.1151

5 Damadian, R., Goldsmith, M., Minkoff, L. (1977). NMR in cancer: XVI. FONAR image of the live human body. Physiological Chemistry and Physics, 9(1), 97–100–108.

6 Panda, A., Mehta, B. B., Coppo, S., Jiang, Y., Ma, D., Seiberlich, N., et al. (2017). Magnetic Resonance Fingerprinting – An Overview. Current Opinion in Biomedical Engineering, 3, 56–66. http://doi.org/10.1016/j.cobme.2017.11.001

7 Ma, D., Gulani, V., Seiberlich, N., Liu, K., Sunshine, J. L., Duerk, J. L., Griswold, M. A. (2013). Magnetic resonance fingerprinting. Nature, 495(7440), 187–192. http://doi.org/10.1038/nature11971

8 Johann Wolfgang von Goethe. Maxims and Reflections (Penguin Classics), Penguin Books, 1998.

9 Emanuel, E. J., Wachter, R. M. (2019). Artificial Intelligence in Health Care: Will the Value Match the Hype? JAMA: the Journal of the American Medical Association, 321(23), 2281–2282. http://doi.org/10.1001/jama.2019.4914

We appreciate your comments.
Please contact us at magnetomworld.team@siemens-healthineers.com

Editorial Board

Review Board

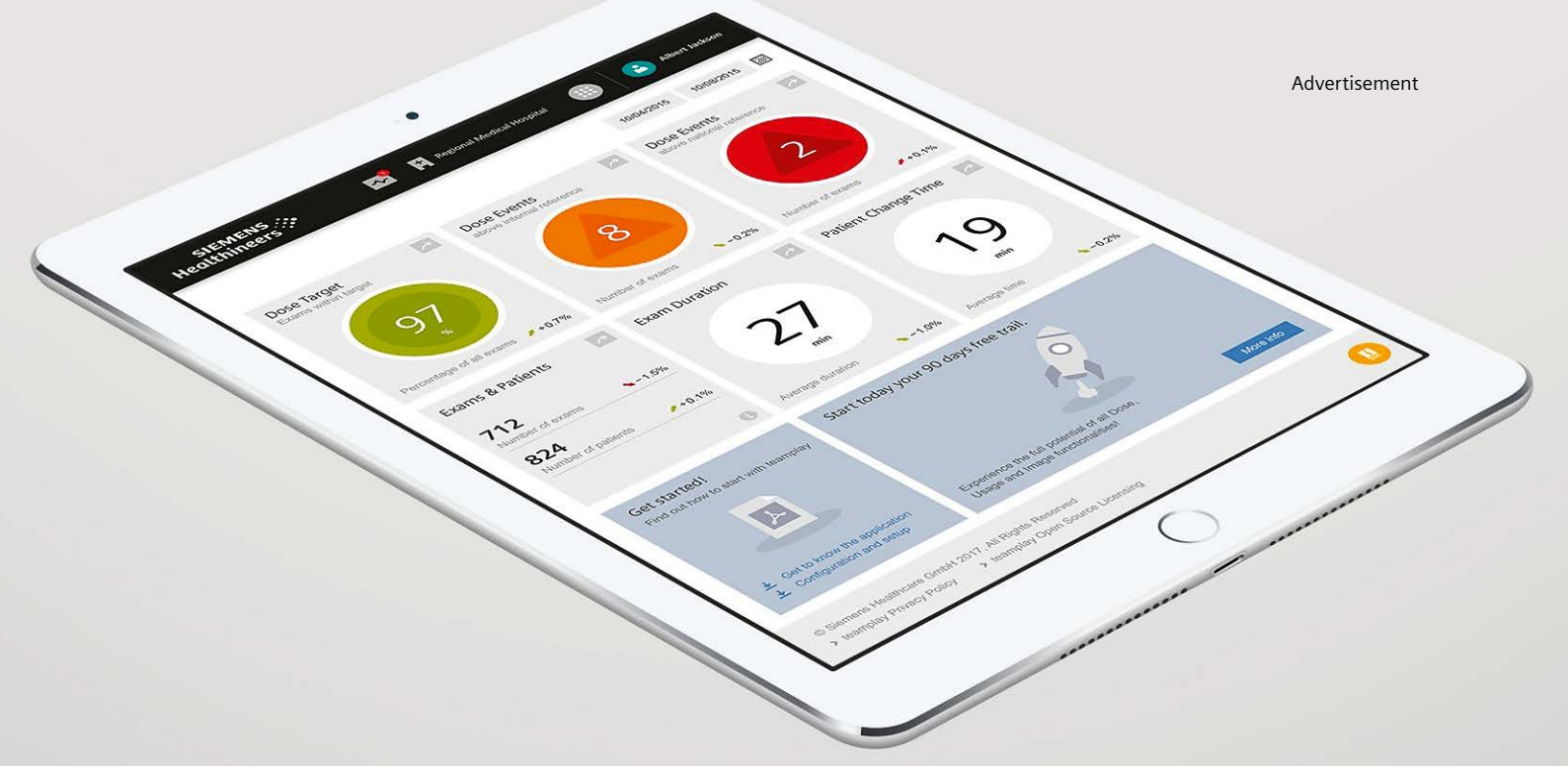

teamplay – Get the most out of your data in radiology and cardiology

healthcare.siemens.de/healthineers-digital-ecosystem/teamplay

To advance digitalization in healthcare, teamplay[1] is a departmental performance management solution that brings together healthcare professionals in a team effort. By connecting medical institutions and their imaging devices, teamplay apps aspire to create the biggest radiology and cardiology team in the world and provide its members with tools to tackle big data and the challenges of increasing cost pressure.

The cloud-based solution teamplay with its apps will help you make prompt and well-informed decisions by offering an intelligible overview of your performance data.

It monitors quantities such as imaging throughput or dose levels, utilization of staff, rooms and resources of your whole department down to every device and procedure, simplifying your reporting and showing you where workflows need adjustments. It links you to other users of teamplay and their data to offer comparable benchmarks[2] and an effortless exchange of images and reports with other healthcare providers.

[1] *Please check if teamplay is available in your country.*
[2] *Availability of Benchmarking option depends on a minimum number of considered subscribers to guarantee customer anonymity and data protection.*

SIEMENS Healthineers

Deep Learning for Parallel MRI Reconstruction: Overview, Challenges, and Opportunities

Kerstin Hammernik[1,2]; Florian Knoll[3]; Daniel Rueckert[1]

[1]Department of Computing, Imperial College London, United Kingdom
[2]Institute of Computer Graphics and Vision, Graz University of Technology, Graz, Austria
[3]Department of Radiology, New York University, New York, NY, USA

With the success of parallel imaging [1–4] and compressed sensing [5–7], we have achieved a breakthrough in the field of routine clinical MR imaging to tremendously accelerate the inherently slow acquisition process. However, with the currently available technologies, we have reached a plateau in terms of acquisition speed. The next paradigm shift is already looming: During the past years, we have seen a tremendous development and impressive results of deep learning [8] algorithms in the field of medical imaging. There are many opportunities how deep learning tools can change the world of clinical examinations, ranging from precision medicine, computer aided diagnosis, image classification and segmentation to data acquisition and image reconstruction. Deep learning leverages the potential to change the complete workflow of clinical imaging, however, many algorithms have been developed regardless of practical relevance. In this article, we focus on the application of deep learning tools for parallel MR image reconstruction. We show how the limits of acquisition speed in MR imaging can be pushed even further, with improved image quality and reduced image reconstruction times compared to current state-of-the-art methods and we provide insights into this highly demanding, clinical standard application from different perspectives.

Deep learning for image reconstruction

Image reconstruction aims at recovering a clean, high-quality MR image from a set of acquired *k*-space measurements from multiple receiver coils. This process involves inverse Fourier transforms to map the measured *k*-space data to the image space. However, this is an ill-posed problem due to measurement errors, low signal-to-noise ratios, sparsely sampled data and limitations of

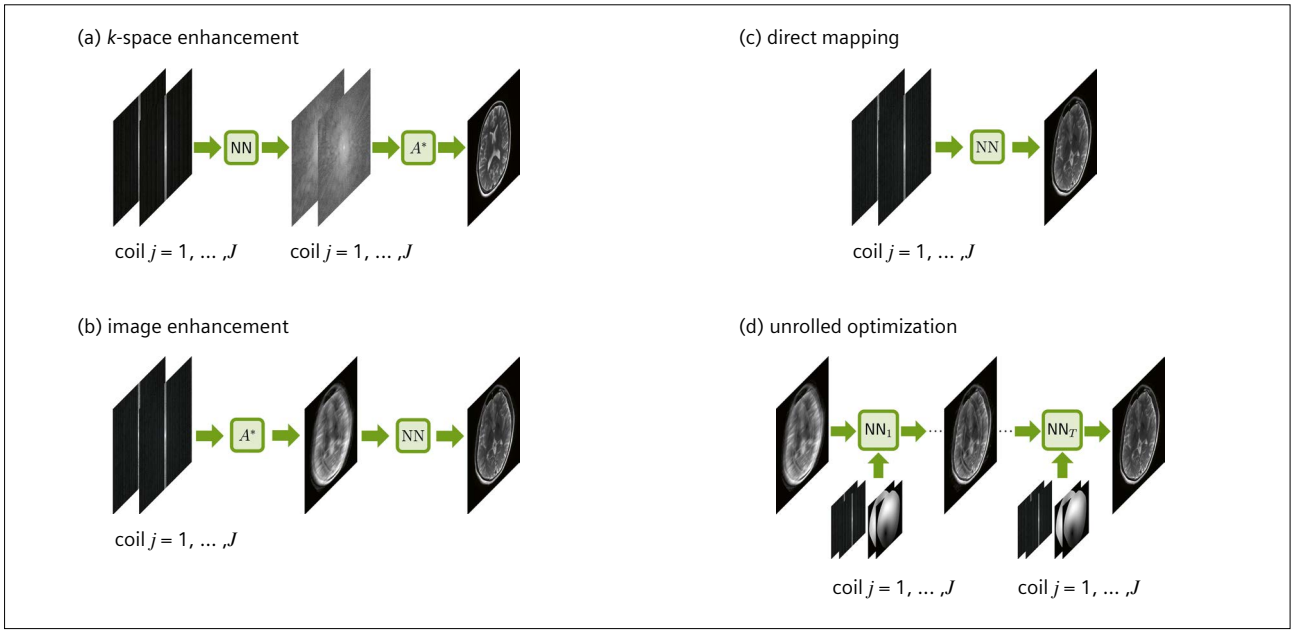

1 Overview of deep learning for parallel MR image reconstruction.

the hardware itself. Two great categories exist for MR image reconstruction, which are in fact closely related: Sensitivity encoding (SENSE) [1, 2] operates in image domain, while generalized autocalibrating partial parallel acquisitions (GRAPPA) [3] fills the missing information of undersampled acquisitions in *k*-space. Similar to the question if one would prefer SENSE or GRAPPA for image reconstruction, deep learning can improve image reconstruction both in *k*-space and image space. In this article, we introduce the basic idea of how deep learning can be used for parallel MR image reconstruction, which is illustrated in Figure 1. We refer the interested reader to [9, 10] for a more detailed insight into this topic.

Learning *k*-space enhancement

To learn improved *k*-space enhancement, both supervised learning methods that depend on training data and self-supervised methods, that learn an interpolation function from the fully sampled autocalibration lines, are reported. DeepSPIRiT [11] is based on *k*-space convolutional neural networks (CNN) that are trained on a reference database and does not depend on explicit coil sensitivity maps, *k*-space interpolation kernels or collection of autocalibration lines. In contrast, GRAPPA-based methods learn a relationship between the coils from an autocalibration signal. While GRAPPA, which is the most clinically used reconstruction method, is based on linear kernel methods and known to suffer from severe noise amplification at higher acceleration rates, it was improved by non-linear kernel methods (RAKI) [12]. RAKI is based on training a CNN from the autocalibration signal to interpolate missing *k*-space lines, resulting in less severe noise amplification compared to GRAPPA as illustrated in Figure 2.

Learning image enhancement

The first group of image-based algorithms learns to enhance a, possibly coil-sensitivity-weighted, zero-filling solution [13–18]. The zero-filling solution is mapped to a fully-sampled reference and does not require any further prior knowledge, hence, consistency to the measured *k*-space data is not ensured. To train these architectures successfully, large amounts of training samples and huge network architectures are required.

Learning the direct transform

The second group of image-based algorithms directly learn a transformation from the undersampled *k*-space data to the fully sampled image. This approach was presented as AUTOMAP by Zhu et al. [19] and is especially useful to overcome errors in the physical model, i.e., imperfect forward operator. The AUTOMAP architecture is characterized by a combination of fully-connected layers with convolutional layers on top and can be applied to any sampling trajectory in MR. The training requires a huge amount of memory due to the fully connected layers, hence, AUTOMAP is limited to small image size. This scaleability issue can be improved by decomposing AUTOMAP as shown in [20]. Although preliminary results are promising, it is practically not applicable yet as the trained networks are limited to specific input sizes which do not meet the requirements for heterogeneous training data in clinical practise.

Learning unrolled optimization

The third and largest group of image-based algorithms learns a fixed unrolled scheme in a supervised end-to-end manner. These fixed, unrolled schemes alternately update the image and impose data consistency. Data consistency can be realized in various ways: By performing gradient steps as in Variational Networks [21] or by solving the proximal mapping [22, 23]. We also find various other optimization schemes, not only for parallel MRI reconstruction, but for medical imaging in general. These schemes range from ADMM-net [24] to variable-splitting schemes [25] and primal-dual optimization [26].

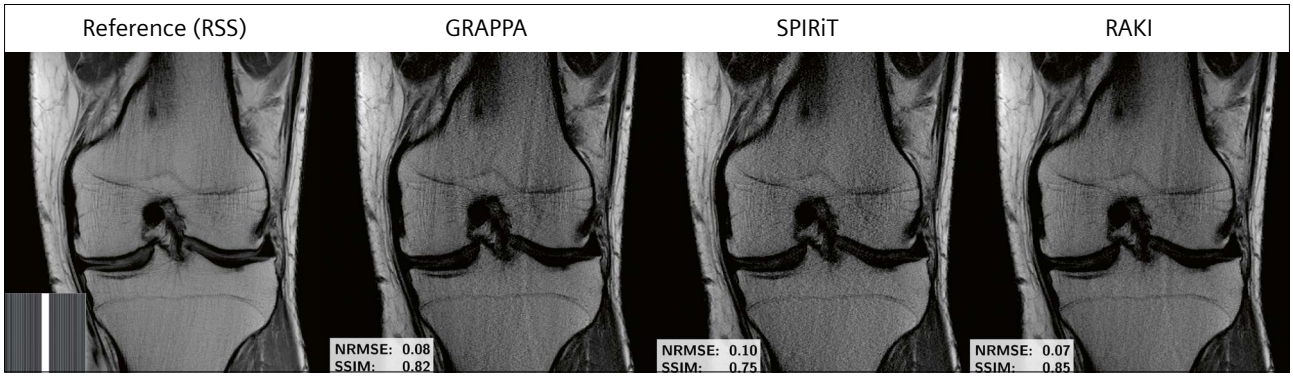

2 GRAPPA-type reconstructions for 4-fold Cartesian undersampling: Comparison of classic GRAPPA, SPIRiT [32] and learning-based RAKI [12] to the root-sum-of-squares (RSS) reference. While GRAPPA suffers from residual artifacts and SPIRiT from noise amplification, RAKI reconstructions achieve both better noise suppression and less residual artifacts. This observation is supported by the quantitative values.

An example for the impact of learning unrolled optimization for accelerated Cartesian imaging is depicted in Figure 3. Here, a variational network reconstruction [21] is compared to a linear CG-SENSE reconstruction [1] and a combined parallel-imaging-compressed sensing (PI-CS) approach [27]. We can clearly see the benefits of the learning-based reconstruction algorithm.

Another question which arises at this stage is if it is really necessary to incorporate the original *k*-space data into the learning-based reconstruction process or if learning image enhancement is enough. A first answer to this question is depicted in Figure 4. Here, a Unet [28] architecture is trained to enhance an initial sensitivity-combined zero-filling solution [16]. This architecture has about 14 million parameters. In comparison, a simple variational network with 140,000 parameters was trained as an unrolled gradient descent scheme with 10 iterations according to [21]. Indeed, we observe that the learned unrolled scheme outperforms the image enhancing network, hence, it is beneficial to include any available prior knowledge in the reconstruction process, which makes the learning task easier and might require less training data to achieve descent results.

High demands for learning-based MRI reconstruction approaches

Many research papers show promising results for learning-based MR image reconstruction, however, these results are often presented for a specific sequence and a simulated environment, e.g., single-coil MR data. We also feel that the image content for a specific sequence is very similar over a wide range of data. In fact, the data is highly inhomogenous and the radiologists' expectations differ from the researchers' perspective in terms of evaluation.

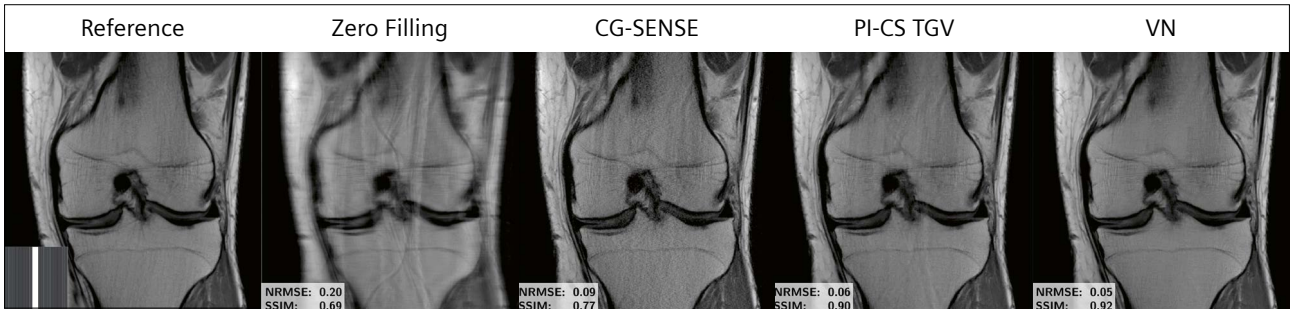

3 SENSE-type reconstructions for 4-fold Cartesian undersampling. Comparison of linear CG-SENSE reconstruction, a parallel imaging-compressed sensing combined Total Generalized Variation (PI-CS TGV) reconstruction [27], and a learning-based Variational Network (VN) reconstruction [21]. The learning-based VN approach reaches superior image quality and reduced artifacts.

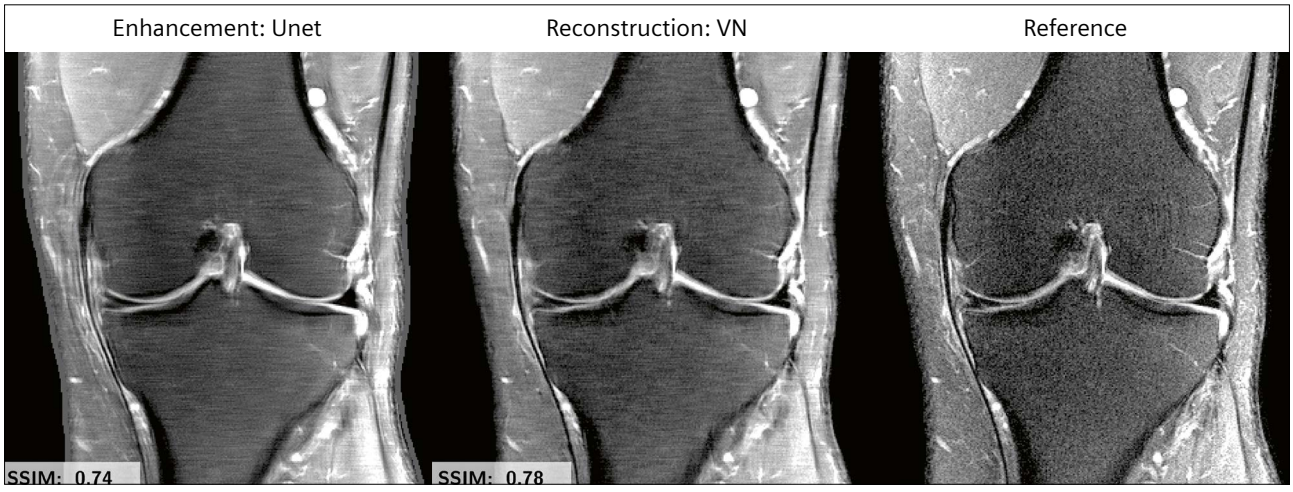

4 Comparison of learning-based image enhancement with a Unet to learning-based image reconstruction with a variational network (VN). The VN that uses the acquired *k*-space data achieves better SSIM scores and has only a fraction (1%) of the parameters compared to the Unet.

More than inverse Fourier transforms

When addressing MR data we often have a simplified picture in mind, telling us that we just have to perform an inverse Fourier transform to obtain the reconstructed image. Indeed, inverse Fourier transforms are the main ingredient for image reconstruction, however, many more aspects have to be considered when building learing-based solutions. The data are acquired in Fourier domain, hence, are complex-valued, which has to be addressed. A common approach here is to handle the complex-valued images as a two-channel real image. Further research points towards addressing the complex-valued issue by complex convolutions and complex activations [29].

In the case of SENSE-based approaches, the explicit estimation of coil sensitivity maps is still a pre-processing step and the final reconstruction quality highly depends on the quality of the coil sensitivity maps. The joint estimation of reconstructed image and coil sensitivity maps is still an open question in deep learning.

Heterogenous MRI data acquisition

Case study

A 42-year-old female patient had to undergo a clinical knee examination. The patient was referred to institution A, where a full clinical protocol (consisting of coronal PDw, coronal PDw with fat saturation, sagittal PDw, sagittal T2w with fat-saturation, axial T2w with fat saturation) was acquired using a 3T MAGNETOM Skyra (Siemens Healthcare, Erlangen, Germany) and a 15-channel knee coil. The patient moved to another country and had to undergo further treatment due to reappearing medical issues at institution B, where the same clinical protocol was acquired using a 1.5T MAGNETOM Aera (Siemens Healthcare, Erlangen, Germany) and a 15-channel knee coil. The patient, who is a computer scientist, was astonished when comparing the two protocols: Why do the images have different size? Why are some parts of the knee cropped and folded back on the other side in certain images of institution A? Why is so much noise in the images of institution B? You can hardly see anything! Why are there some artifacts in the images of institution A?

Using this case study, we can already identify common challenges in every day clinical MRI examinations: There is no universal acquisition scheme and even standard acquisition protocols vary not only from institution to institution, but also within the institution. These variations include changes in sequence parameters, matrix size, and base resolution. Furthermore, the radiographers acquiring the images have to adapt characteristic parameters individually for each patient. This includes for example the setting for phase encoding oversampling to ensure that the entire field-of-view is considered during acquisition and no backfolding occurs. Not only the sequence setting but also the hardware setting itself has a huge impact on the final image quality. The image quality depends on the coil load and the field strength of the MRI scanner. Other sources that influence the image quality are any kind of artifacts, including patient motion. The fastMRI dataset [16] is a great example for a heterogeneous dataset. The protocols for this dataset were adapted to fit the individual scanner hardware and imaged patient as optimal as possible. Figure 5 shows examples from this dataset for varying field strengths, noise levels and artifacts. The images have a different dimension in phase encoding (x) direction. The number of phase encoding steps are individually adjusted during acquisition, hence, introduce another degree of inhomogeneity for learning-based reconstruction approaches.

We see that learning-based approaches have to deal with highly heterogeneous data. Most of the currently available approaches are tested on high SNR data of the same scanner and sequence. Furthermore, for supervised learning approaches, we have to define a "ground truth" reconstruction. This becomes even more challenging, when an additional dynamic component is added or quantitative imaging is performed using learning-based approaches.

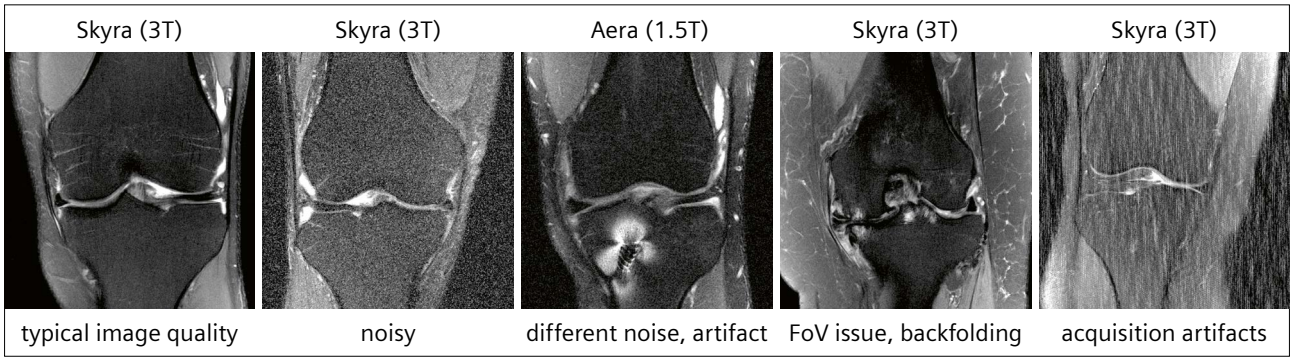

5 Examples of coronal PD-weighted knee scans with fat saturation from the fastMRI dataset [16]. The dataset contains heterogeneous data in terms of varying field strength, number of phase encoding steps and artifacts.

Researchers' evaluation
From a researchers' perspective, quantitative evaluation metrics are required to benchmark different approaches objectively. Common evaluation metrics here are the Peak-Signal-to-Noise ratio (PSNR) or the Structural Similarity Index (SSIM) [30]. Furthermore, supervised machine learning approaches require a qualitative image metric for network training which is reflected in the final image quality. The major drawback of most commonly used quantitative image metrics is their over-smoothing behaviour and the incapability to reflect small, subtle details in the metric. The images might have high quantitative scores, but appear unpleasant from a radiologists' perspective, hence, the insights into the true nature of MR images are still limited. Another obvious issue is to compare GRAPPA-based and SENSE-based algorithms, especially when no additional noise measurement is available to obtain the optimal weighting between the individual coils. Although Figures 2 and 3 show the same image slice, they cannot be compared directly as in this case the SENSE-based algorithms require explicit coil sensitivity maps and GRAPPA-based methods use implicit coil sensitivities for reconstruction. Hence, it is still an open question how to compare these algorithms from a researchers' perspective and it might require a more thorough evaluation of radiologists.

Radiologists' evaluation
In a diagnostic setting, the evaluation of diagnostic content, hence, the presence or absence of small subtle structures is inevitable. This requires large-scale studies to prove if all information are still available for the correct diagnosis if the acquisitions are accelerated. This includes a subjective evaluation of the image quality itself: Many learning-based approaches suffer from blurred images and residual artifacts, however, are these degraded images sufficient for correct diagnosis? Up to now, only small-scale studies in terms of image quality [21] and diagnostic content [31] were performed. Future opportunities include an evaluation on more diverse MR data, sample size and imaging exams.

Opportunities

A major concern in deep learning for medical imaging in general is the need for big data itself. While for computer vision applications, large databases and benchmarks exist, big data are only slowly arriving in medical imaging, mostly associated with dedicated image challenges. In the field of image reconstruction, the fastMRI dataset [16] provides a huge step towards a more generalized raw data archive, currently containing about 1000 fully sampled knee training datasets acquired with different Siemens Healthineers scanners. This rises the questions if we can train a universal network that is able to deal with the heterogeneous data, various anatomies and intra-/inter-vendor hardware settings. Are we able to train a universal network? Or might semi-supervised and unsupervised approaches provide a way to adapt to patient- and acquisition-specific clinical scenarios?

We experience that deep learning, and artificial intelligence in general, have the capability to change the complete imaging workflow in radiology. However, many of the existing approaches so far are based on simulated scenarios and have limited clinical value. Considering parallel imaging in image reconstruction provides a first step towards clinical applicability. While we focus here only on imaging data, there is also a vast amount of medical records, patients' history and even other sensor data available, which might be included and improve the image acquisition and reconstruction workflow.

Conclusion

The current developments in deep learning for medical image reconstruction reminds one of the hype we have experienced with compressed sensing. While compressed sensing started to change image reconstruction almost 20 years ago, it is only now a commercial product and established in clinical routine. Similarly, deep learning approaches for image reconstruction are not yet established in clinical examinations and will require a thorough evaluation, but they already provide a huge potential for the future of MR image reconstruction.

Acknowledgements
We want to thank Jo Schlemper for providing the Unet reconstruction and Mehmet Akçakaya for providing the GRAPPA, SPIRiT, and RAKI reconstructions. We also acknowledge research support by the EPSRC Programme Grant EP/P001009/1 and the National Institutes of Health under grants R01EB024532 and P41EB017183.

References

1 Klaas P Pruessmann, Markus Weiger, Markus B Scheidegger, and Peter Boesiger. SENSE: Sensitivity encoding for fast MRI. Magn Reson Med, 42(5):952–962, 1999.
2 K P Pruessmann, M Weiger, P Boernert, and P Boesiger. Advances in sensitivity encoding with arbitrary k-space trajectories. Magn Reson Med, 46(4):638–651, 2001.
3 Mark A Griswold, Peter M Jakob, Robin M Heidemann, Mathias Nittka, Vladimir Jellus, Jianmin Wang, Berthold Kiefer, and Axel Haase. Generalized autocalibrating partially parallel acquisitions (GRAPPA). Magn ResonMed, 47(6):1202–1210, 2002.
4 D K Sodickson and W J Manning. Simultaneous Acquisition of Spatial Harmonics (SMASH): Fast Imaging with Radiofrequency Coil Arrays. Magn ResonMed, 38(4):591–603, 1997.
5 Michael Lustig, David Donoho, and John M Pauly. Sparse MRI: The application of compressed sensing for rapid MR imaging. Magn Reson Med, 58(6):1182–1195, 2007.

6 Kai Tobias Block, Martin Uecker, and Jens Frahm. Undersampled radial MRI with multiple coils. Iterative image reconstruction using a total variation constraint. Magn Reson Med, 57(6):1086–1098, 2007.

7 Michael Lustig, David L. Donoho, Juan M. Santos, and John M. Pauly. Compressed Sensing MRI. IEEE Signal Processing Magazine, 25(2):72–82, 2008.

8 Yann LeCun, Yoshua Bengio, and Geoffrey Hinton. Deep Learning. Nature,521(7553):436–444, 2015.

9 Kerstin Hammernik and Florian Knoll. Machine learning for image reconstruction. In S. Kevin Zhou, Daniel Rueckert, and Gabor Fichtinger, editors, Handbook of Medical Image Computing and Computer Assisted Intervention. Academic Press, 2019.

10 Florian Knoll, Kerstin Hammernik, Chi Zhang, Steen Moeller, Thomas Pock, Daniel K. Sodickson, and Mehmet Akcakaya. Deep Learning Methods for Parallel Magnetic Resonance Image Reconstruction. Accepted for publication in IEEE Signal Processing Magazine, 2019.

11 Joseph Y. Cheng, Morteza Mardani, Marcus T. Alley, John M. Pauly, and Shreyas S. Vasanawala. Deep-SPIRiT: Generalized parallel imaging using deep convolutional neural networks. In Proc. 26th Annual Meeting of the ISMRM, Paris, France, 2018.

12 Mehmet Akçakaya, Steen Moeller, Sebastian Weingärtner, and Kâmil Uğurbil. Scan-specific robust artificial-neural-networks for k-space interpolation (RAKI) reconstruction: Database-free deep learning for fast imaging. Magn Reson Med, 81(1):439–453, 2019.

13 Yoseob Han, Jaejun Yoo, Hak Hee Kim, Hee Jung Shin, Kyunghyun Sung, Jong Chul Ye. Deep learning with domain adaptation for accelerated projection-reconstruction MR. Magn Reson Med, 80:1189–1205, 2018.

14 Chang Min Hyun, Hwa Pyung Kim, Sung Min Lee, Sungchul Lee, and Jin KeunSeo. Deep learning for undersampled MRI reconstruction. Physics in Medicine and Biology, 63(13), 2018.

15 Guang Yang, Simiao Yu, Hao Dong, Greg Slabaugh, Pier Luigi Dragotti, Xu-jiong Ye, Fangde Liu, Simon Arridge, Jennifer Keegan, Yike Guo, and David Firmin. DAGAN: Deep De-Aliasing Generative Adversarial Networks for Fast Compressed Sensing MRI Reconstruction. IEEE Transactions on Medical Imaging, 2018.

16 Florian Knoll, Jure Zbontar, Anuroop Sriram, Matthew J. Muckley, Mary Bruno, Aaron Defazio, Marc Parente, Krzysztof J. Geras, Joe Katsnelson, Hersh Chandarana, Zizhao Zhang, Michal Drozdzal, Adriana Romero, Michael Rabbat, Pascal Vincent, James Pinkerton, Duo Wang, Nafissa Yakubova, ErichOwens, C. Lawrence Zitnick, Michael P. Recht, Daniel K. Sodickson, and Yvonne W. Lui. fast MRI: a publicly available raw *k*-space and DICOM dataset for accelerated MR image reconstruction using machine learning. Radiology AI, page in press, 2019.

17 Jong Chul Ye, Yoseob Han, and Eunju Cha. Deep Convolutional Framelets: A General Deep Learning Framework for Inverse Problems. SIAM Journal in Imaging Sciences, 11(2):991–1048, 2018.

18 Kyong Hwan Jin, Michael T. McCann, Emmanuel Froustey, and Michael Unser. Deep convolutional neural network for inverse problems in imaging. IEEE Trans Image Proc, 26(9):4509–4522, 2017.

19 Bo Zhu, Jeremiah Z. Liu, Stephen F. Cauley, Bruce R. Rosen, and Matthew S. Rosen. Image reconstruction by domain-transform manifold learning. Nature 555 (7697), pp. 487-492, 2018.

20 Jo Schlemper, Ilkay Oksuz, James Clough, Jinming Duan, Andrew King, Julia Schnabel, Joseph Hajnal, and Daniel Rueckert. dautomap: Decomposing automap to achieve scalability and enhance performance. In ISMRM 27th Annual Meeting, page 0658, 2019.

21 Kerstin Hammernik, Teresa Klatzer, Erich Kobler, Michael P Recht, Daniel K Sodickson, Thomas Pock, and Florian Knoll. Learning a variational network for reconstruction of accelerated MRI data. Mag Reson Med, 79:3055–71, 2018.

22 Jo Schlemper, Jose Caballero, Joseph Hajnal, Anthony Price, and Daniel Rueckert. A deep cascade of convolutional neural networks for MR image reconstruction. In Proceedings of the International Society of Magn Reson Med (ISMRM), page 643, 2017.

23 Hemant K. Aggarwal, Merry P. Mani, and Mathews Jacob. MoDL: Model-Based Deep Learning Architecture for Inverse Problems. IEEE Transactions on Medical Imaging, 2019.

24 Yan Yang, Jian Sun, Huibin Li, and Zongben Xu. Deep ADMM-Net for Compressive Sensing MRI. In Advances in Neural Information Processing Systems (NIPS), pages 10–18, 2016.

25 Jinming Duan, Jo Schlemper, Chen Qin, Cheng Ouyang, Wenjia Bai, Carlo Biffi, Ghalib Bello, Ben Statton, Declan P O'Regan, and Daniel Rueckert. Vs-net: Variable splitting network for accelerated parallel mri reconstruction. Medical Image Computing and Computer Assisted Intervention (MICCAI), pp. 713-722, 2019.

26 Jonas Adler and Ozan Öktem. Learned Primal-Dual Reconstruction. IEEE Transactions on Medical Imaging, 37(6):1322–1332, 2018.

27 Florian Knoll, Kristian Bredies, Thomas Pock, and Rudolf Stollberger. Second order total generalized variation (TGV) for MRI. Magnetic Resonance in Medicine, 65(2):480–491, 2011.

28 Olaf Ronneberger, Philipp Fischer, and Thomas Brox. U-Net: Convolutional Networks for Biomedical Image Segmentation. Medical Image Computing and Computer-Assisted Intervention (MICCAI), pp 234-241, 2015.

29 Chiheb Trabelsi, Olexa Bilaniuk, Dmitriy Serdyuk, Sandeep Subramanian, João Felipe Santos, Soroush Mehri, Negar Rostamzadeh, Yoshua Bengio, and Christopher J. Pal. Deep complex networks. arXiv preprint arXiv:1705.09792,2017.

30 Zhou Wang, Alan Conrad Bovik, Hamid Rahim Sheikh, and Eero P. Simoncelli. Image quality assessment: From error visibility to structural similarity. IEEE Trans Image Proc, 13(4):600–612, 2004.

31 Florian Knoll, Kerstin Hammernik, Elisabeth Garwood, Anna Hirschmann, Leon Rybak, Mary Bruno, Tobias Block, James Babb, Thomas Pock, Daniel Sodickson, and Michael Recht. Accelerated Knee Imaging Using a Deep Learning Based Reconstruction. In Proceedings of the International Society of Magn Reson Med (ISMRM), page 645, 2017.

32 Michael Lustig and John M Pauly. SPIRiT: Iterative self-consistent parallel imaging reconstruction from arbitrary *k*-space. Magn Reson Med, 64(2):457–471, 2010.

Contact

Kerstin Hammernik
Imperial College London
Department of Computing
South Kensington Campus
London SW7 2AZ
United Kingdom
k.hammernik@imperial.ac.uk

Introducing 3T MR Imaging with the new MAGNETOM Lumina

Corentin Mauris[1]; Graça Fernandes[2]; Nicolas Dechâtre[3]; Adrien Jaccoud[1]

[1]GIE IRM74, Groupement d'Intérêt Economique Imagerie par Résonance Magnétique, Annecy, France
[2]Siemens Healthineers, Saint Priest, France
[3]Clinial Application Specialist MR, Medical Professionals, France

With three locations located in eastern France, our facilities are home to over eighty radiologists who have access to our six 1.5T MAGNETOM MRIs, which include three MAGNETOM Aera, one MAGNETOM Avanto Fit, one MAGNETOM Amira with BioMatrix, and one MAGNETOM Altea. Our MR imaging staff perform all types of examinations with the exception of fetal imaging and research MRI. In September 2019, we installed a MAGNETOM Lumina 3T BioMatrix MRI; one of the first to be installed in France and the first 3T magnet in our facility. This particular MRI scanner will be used for oncological and neurological examinations to cater for the many patients referred to us for diagnosis and follow-up from the cancer treatment units (neurological, ENT, abdominal, pelvic, breast, etc.).

Motivation for choosing a 3T MRI system

A key driver for the installation of this 3T system in our economic interest grouping (GIE) was to provide MR imaging with a higher magnetic field, since previously we had only been using 1.5T systems. Our patients will benefit from oncological and neurological examinations in a shorter timeframe and higher spatial resolution, allowing us to replace conventional radiological examinations, such as CT scans, with MRI.

In the decision process, we therefore aimed to select a system with excellent capabilities for fast high-resolution neuro imaging and robust and consistent oncological imaging in all our patients. We selected a 70 cm open bore to avoid any constraints with respect to patient positioning or the performance of the examination. With a compact length of just 186 cm cover-to-cover, patient comfort is optimized. Furthermore, we can advance our neurological imaging beyond what was possible at 1.5T, thanks to the higher field strength and the XK gradients with a slew rate of 200 T/m/sec and a maximum amplitude of 36 mT/m. Our oncological examinations are also free of constraints, thanks to a wide field of view (FOV) of 55 x 55 x 50 cm^3 and the possibility to connect up to 180 channels. Overall, our staff are able to deliver improved patient outcomes thanks to the addition of BioMatrix Technology, the new *syngo* MR XA interface, and the innovative Turbo Suite features.

The planned implementation of the new 3T MRI system impacted our choice of coils: Rather than dedicated MSK coils, such as those for knee, shoulder, or foot/ankle that are already available on almost all our 1.5T systems, we opted for the 20-channel Head/Neck Coil, the 32-channel Head Coil, the 24-channel BioMatrix Spine, the 18-channel Breast, the 12-channel BioMatrix Body, and the 4-channel Flex Small and Large. Our aim is also to make use of the full capabilities of this new system by using PCASL, SVS, and CSI spectroscopy, tractography, and a functional activity project.

1 New Select&Go touchscreen tablets in the room.

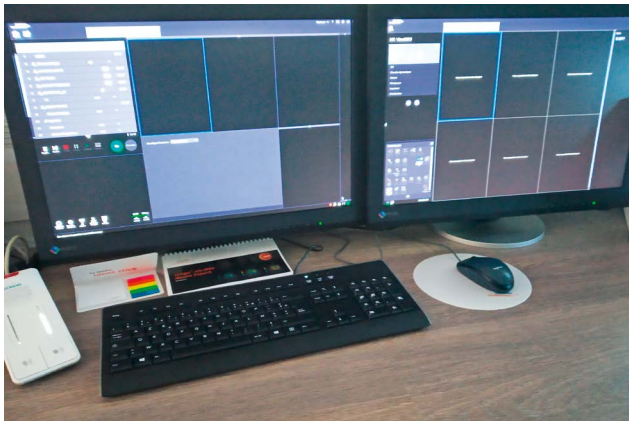

2 New interface for the acquisition console.

Innovative features of the system

With BioMatrix and GO Technologies, MAGNETOM Lumina provides significant benefits for users: Inside the room, the two Select&GO touchscreen tablets (Fig. 1), one on each side of the table, provide the technician with access to comprehensive information about the patient and the examination, which is displayed on the console. Based on a generalized body model, which has been trained with artificial intelligence, and by automatically taking into account the connected coils, it is possible to position the patient quickly and accurately. Without having to use the laser cross-hair the technician only has to click on the area to be scanned on the touch screen. The software automatically auto-centers the region-of-interest, adapted to body size and shape of the individual patient.

The acquisition workplace is equipped with two large screens (Fig. 2), enabling a clear separation of different workflow steps: one monitor on the left to register the patient and examination. The other monitor on the right to display and postprocess the images (View&GO). This time-saving advancement reduces the workload on the technician since it is no longer necessary to switch between the different modules, as it was with the *syngo* MR E11 interface. The intercom has also changed entirely; it is now possible to hear the patient while we are talking to them. Volume adjustments are also made using a touchpad, making use and operation far easier.

The new *syngo* MR XA11B interface allows the technician to access the data quickly and resembles the *syngo*.via interface. Although significant changes have been made compared to the *syngo* MR E11 software version, handling is still relatively fast and simple.

The Dot Cockpit has been retained and has not undergone major changes. We continue to optimize our various protocols in order to guarantee examinations of reproducible quality that are minimally dependent on the technician (implementation of strategies/decisions/interactions). New functionalities help simplify the programming work. For example, it is possible to replace an existing sequence in a Dot engine using simple drag and drop, to easily compare the parameters of two different sequences (Fig. 3A), or even to record a history of modifications as they are carried out for a given sequence (Fig. 3B).

The different Dot engines have been retained and facilitate examination management, such as the labeling of vertebrae, which improves the overall workflow and saves time.

Via Respiratory Sensors in the Spine Coil, the BioMatrix Technology enables the acquisition of sequences during free breathing without the use of a belt or navigator (Fig. 4). Not only does this improve patient comfort, it decreases the number of nondiagnostic images thereby improving our workflow.

The tiltable 20-channel Head/Neck Coil is a great improvement in terms of patient comfort, with possible inclinations of 0°, 9°, or 18° (Fig. 5).

With CoilShim (active shim) built into the Head/Neck Coil, the Fat Sat provides better quality in axial sequences with fat saturation at the ENT-cervical level. In abdominal diffusion-weighted imaging SliceAdjust allows slice-by-slice shimming; for DWI with better quality and less distortions.

Another improvement in the scanner suite is the patient table and its operation. Without any pedals and with a semiautomated (motorized) driving support the new table can be easily moved and is very user friendly.

3 New sequence comparison features **(3A)** and history of changes carried out in real time for one sequence **(3B)**.

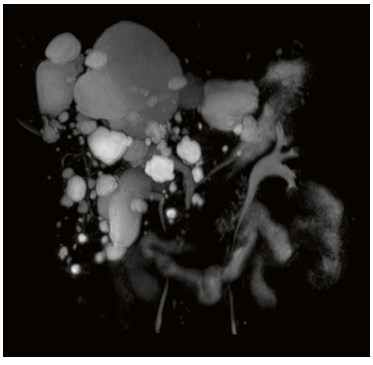

4 Biliary MR MIP – 3D T2w SPACE acquisition – free breathing with expiration detection with the BioMatrix Respiratory Sensor. Multiple hepatic cystic formations containing clear fluid, not suspicious.

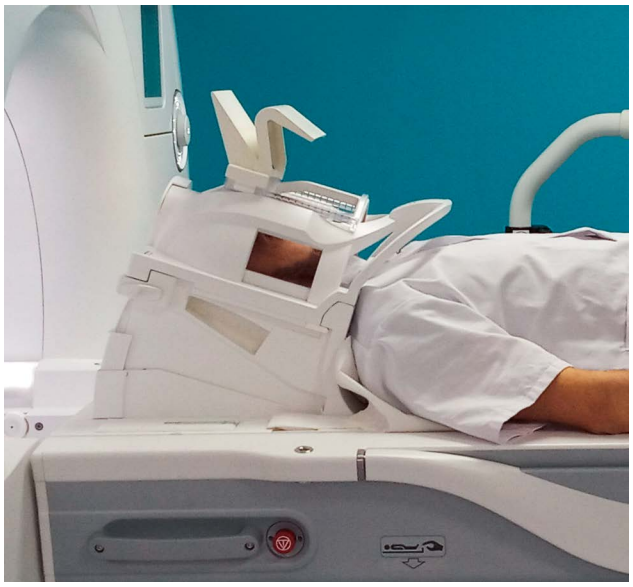

5 Tiltable head coil permitting maximum patient comfort.

Clinical benefits of 3T MRI

While the technological innovations and numerous advantages of the newly installed MAGNETOM Lumina represent a huge advancement, we must also achieve image reproducibility and high quality with our six existing 1.5 T MRI systems at our facility.

Given the advantage of the signal benefits made possible by the 32-channel Head Coil, we decided to use the new 3T MRI for the majority of neurological studies, regardless of whether the examination was routine (Figs. 6 and 7) or more advanced (Fig. 8). It should be noted that the handling and implementation of the ASL and the postprocessing of spectroscopy using *syngo*.via were uncomplicated.

We were able to compare the benefits of the 3T versus the 1.5T when monitoring patients with neurological pathologies (Fig. 9).

The benefits provided by the 3T MRI system led us to review our practice with respect to prostate imaging. We had been working with T2 TSE or with BLADE on the 1.5T.

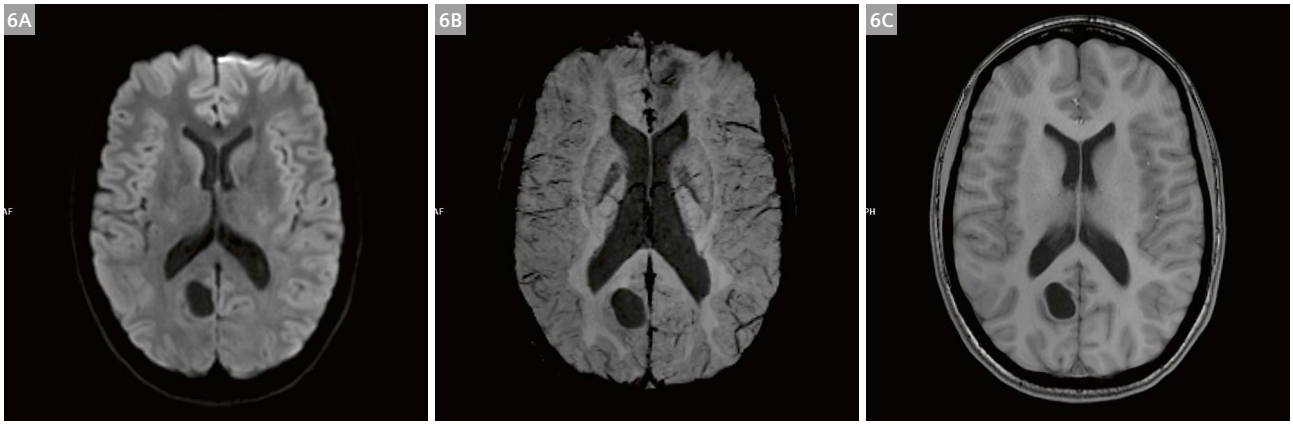

6 Report on a cephalic cystic lesion discovered by chance during a CT scan. RESOLVE **(6A)**, MIP SWI **(6B)**, and T1w GRE **(6C)** transverse diffusion images. Probable arachnoid cyst of the right temporal convexity.

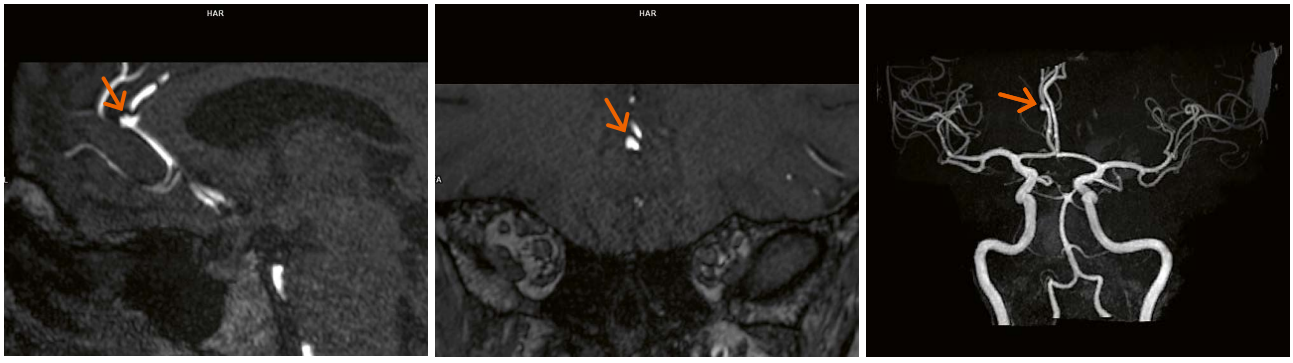

7 Chance discovery of a 2.5 mm aneurysm in the end of the right anterior cerebral artery on the TOF sequence.

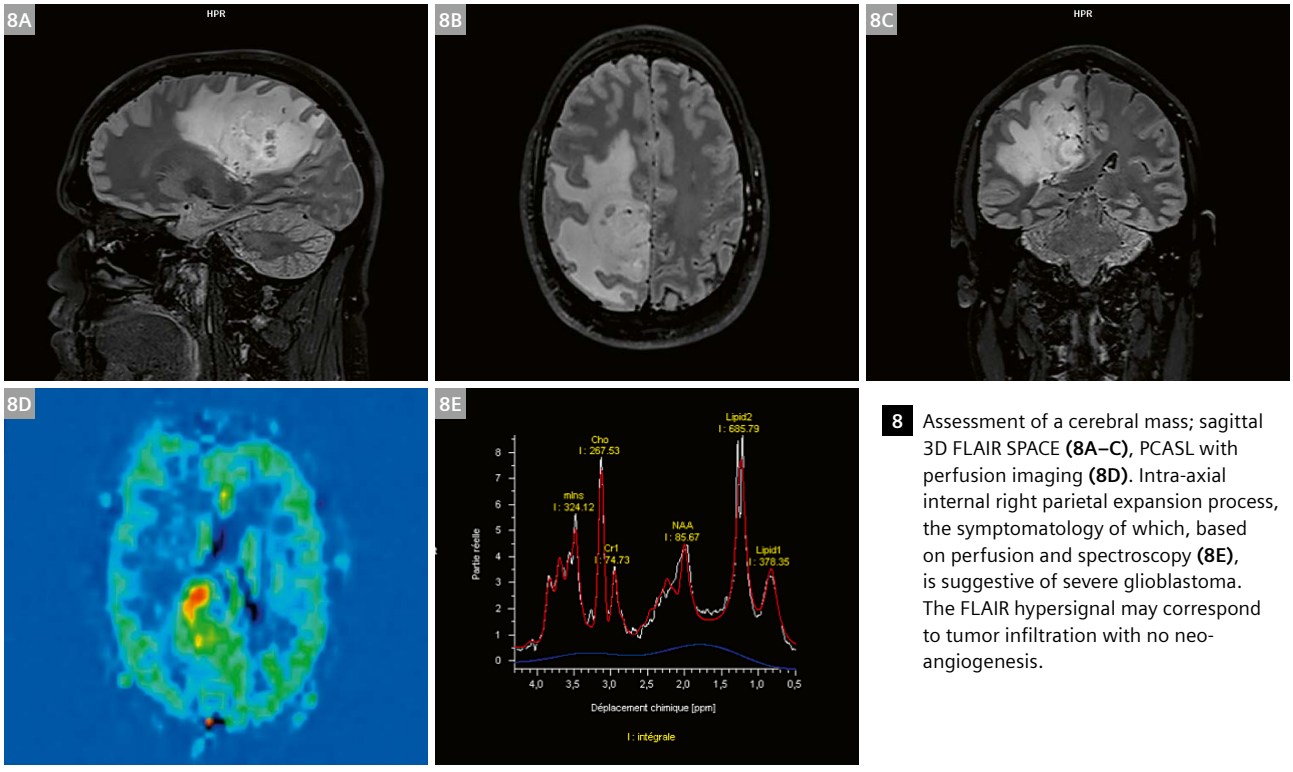

8 Assessment of a cerebral mass; sagittal 3D FLAIR SPACE **(8A–C)**, PCASL with perfusion imaging **(8D)**. Intra-axial internal right parietal expansion process, the symptomatology of which, based on perfusion and spectroscopy **(8E)**, is suggestive of severe glioblastoma. The FLAIR hypersignal may correspond to tumor infiltration with no neo-angiogenesis.

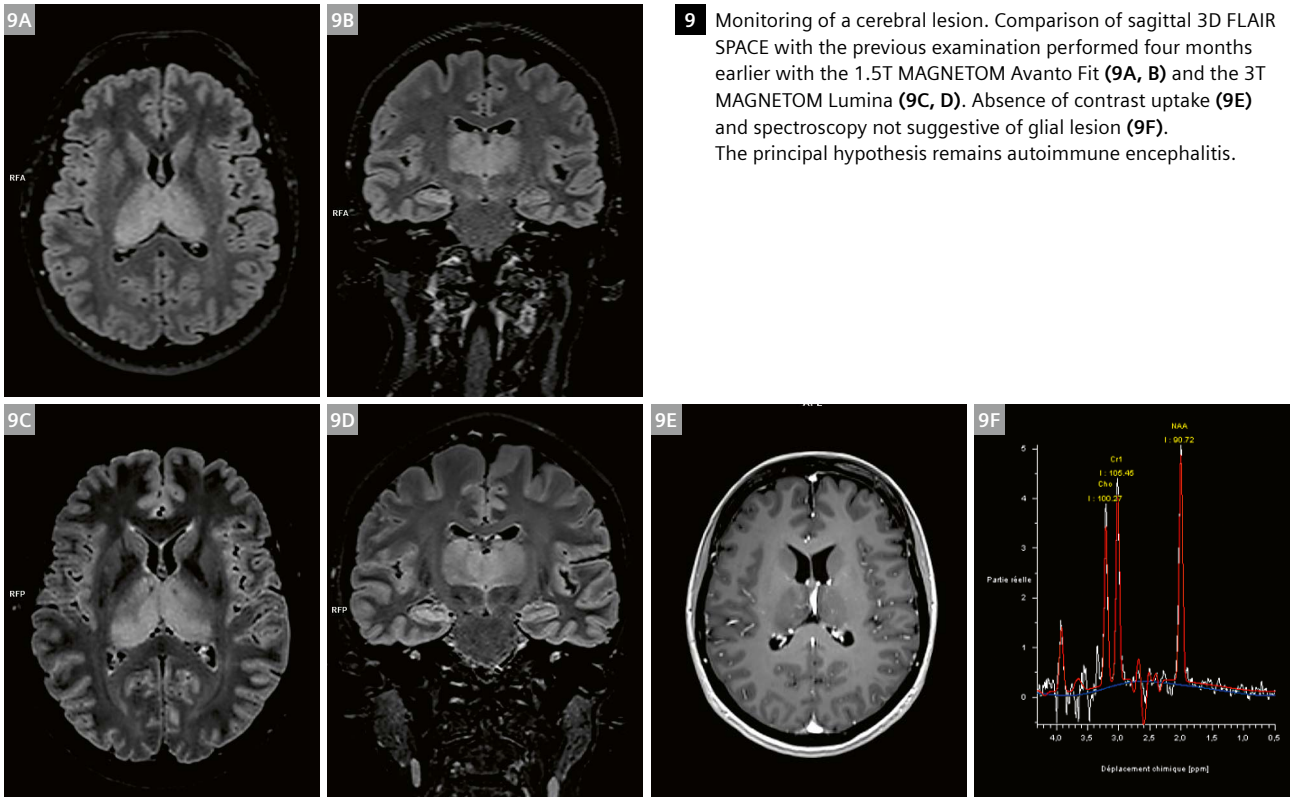

9 Monitoring of a cerebral lesion. Comparison of sagittal 3D FLAIR SPACE with the previous examination performed four months earlier with the 1.5T MAGNETOM Avanto Fit **(9A, B)** and the 3T MAGNETOM Lumina **(9C, D)**. Absence of contrast uptake **(9E)** and spectroscopy not suggestive of glial lesion **(9F)**. The principal hypothesis remains autoimmune encephalitis.

The first acquisition tests using 3D T2 SPACE were conclusive (Fig. 10) and showed better contrast. We continue to use axial T2 2D acquisition, allowing the radiologists to integrate this new approach. In terms of dynamic acquisition using contrast media, we prefer the TWIST-VIBE DIXON method, which has been installed on the entire range of MRI systems at our facility for several months now (Figs. 11, 12).

In breast imaging, we have achieved better resolution by changing the fat saturation technique during dynamic phases using Dixon fat-water separation in order to achieve better reproducibility of fat saturation (Fig. 13).

The benefits were also remarkable in pelvic (Fig. 14) and abdominal (Fig. 15) imaging.

Initially, we decided not to perform a 3T medullary MRI following the various feedback on the practices of other sites that we received before making our choice (i.e., problems with image quality and B_1 artifacts). However, the image quality proved to be more than satisfactory so we decided to perform the medullary examination using our MAGNETOM Lumina (Figs. 16, 17).

The benefits of the 2D simultaneous multi-slice (SMS) acceleration technique were exploited in order to invest the time saved in increasing the image resolution (Fig. 18).

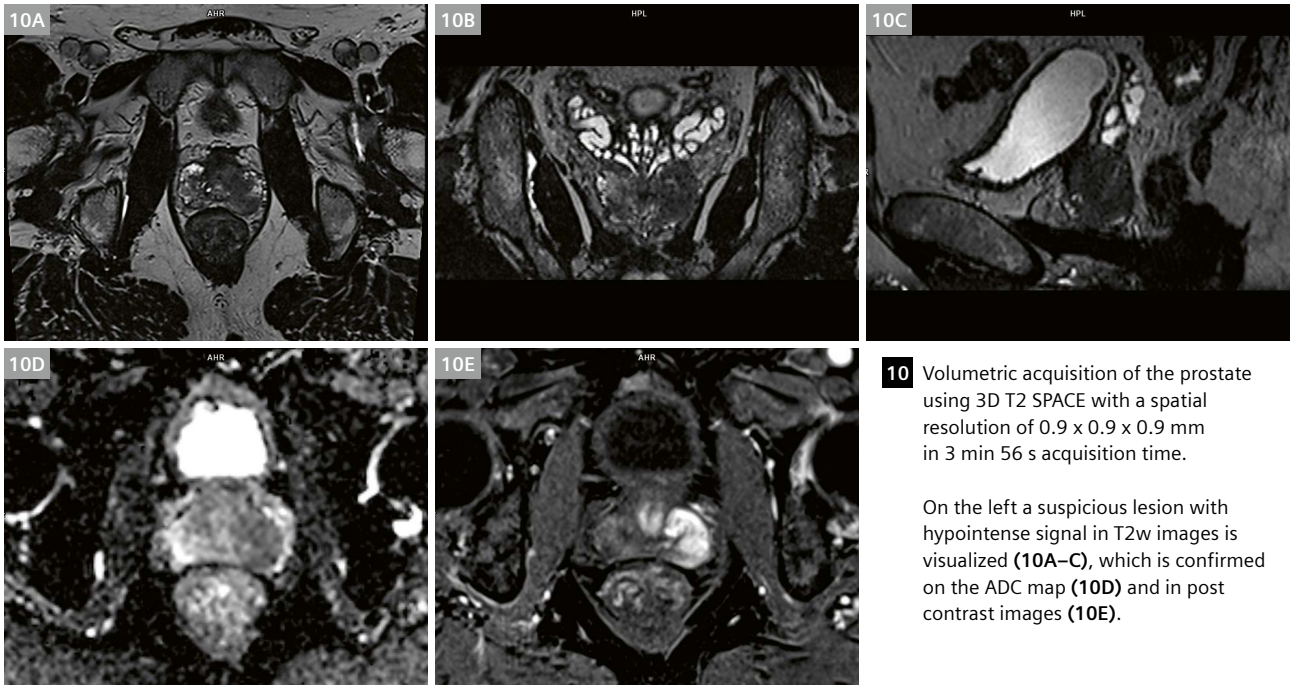

10 Volumetric acquisition of the prostate using 3D T2 SPACE with a spatial resolution of 0.9 x 0.9 x 0.9 mm in 3 min 56 s acquisition time.

On the left a suspicious lesion with hypointense signal in T2w images is visualized **(10A–C)**, which is confirmed on the ADC map **(10D)** and in post contrast images **(10E)**.

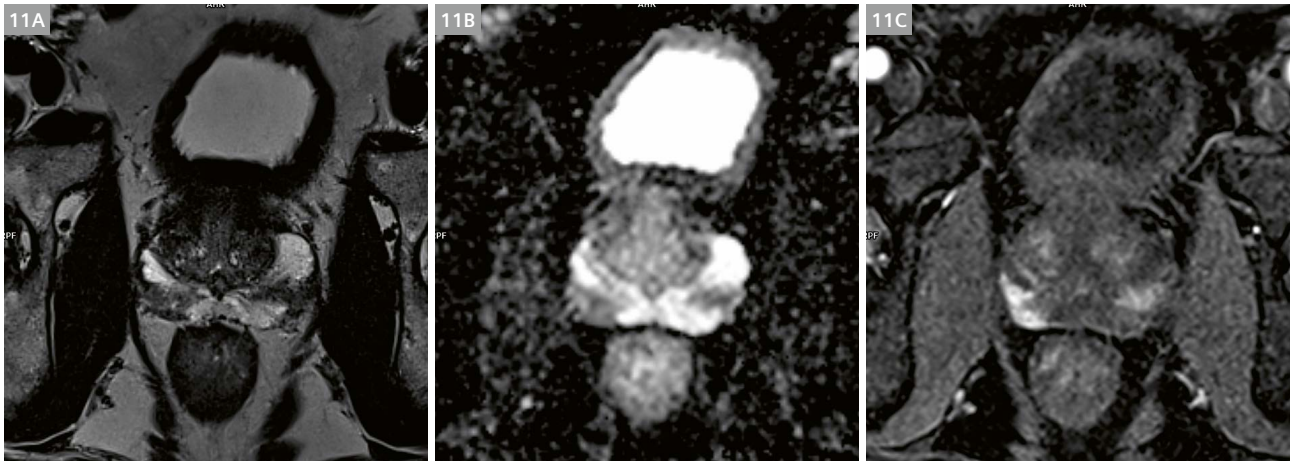

11 In a patient with increased PSA values, two nodular lesions were found. One lesion in the posteriaor and lateral peripheral zone of the base and right middle with a size of 18 x 8 mm, and another lesion in the peripheral zone of the left middle lateral with a size of 15 x 9 mm. Both lesions were clearly visualized using T2w TSE **(11A)**, on the ADC map **(11B)**, and in post contrast images **(11C)**. Both lesions were rated PI-RADS 5.

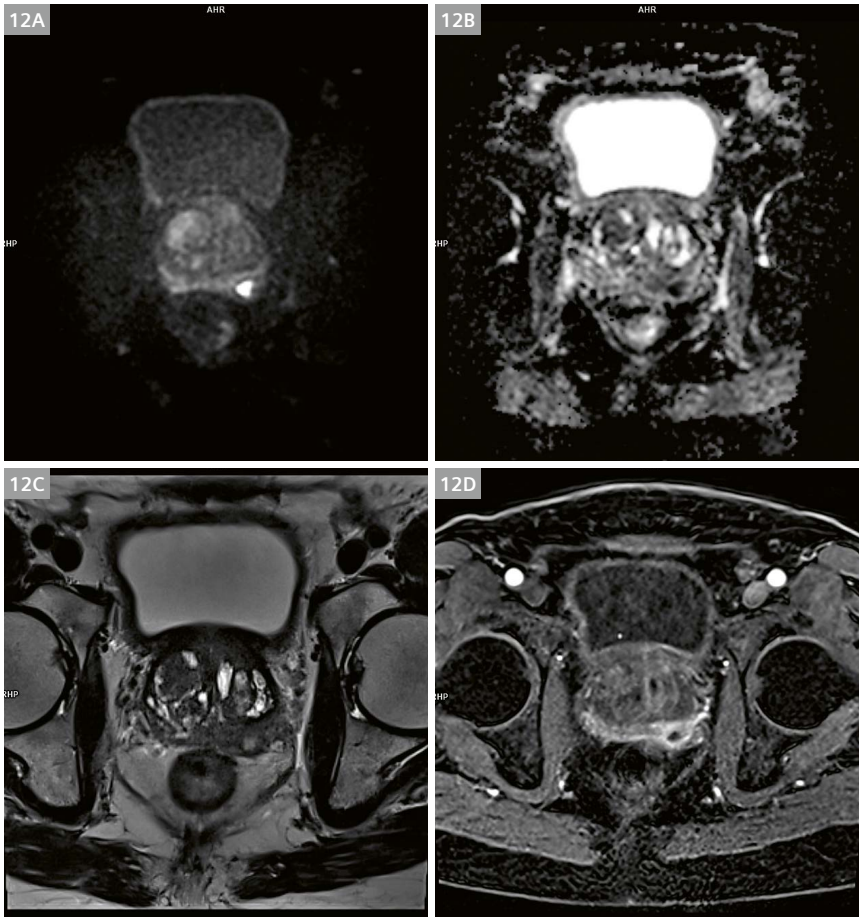

12 In a patient with increased PSA levels a left periprostatic micro-abscess of 8 mm length was found. The abscess showed hyperintensity in b800 s/mm² diffusion-weighted images **(12A)**, restricted diffusivity in the ADC map **(12B)**, hyperintensity in the axial T2 w TSE images **(12C)**, and was non-perfused in post contrast images **(13D)**.

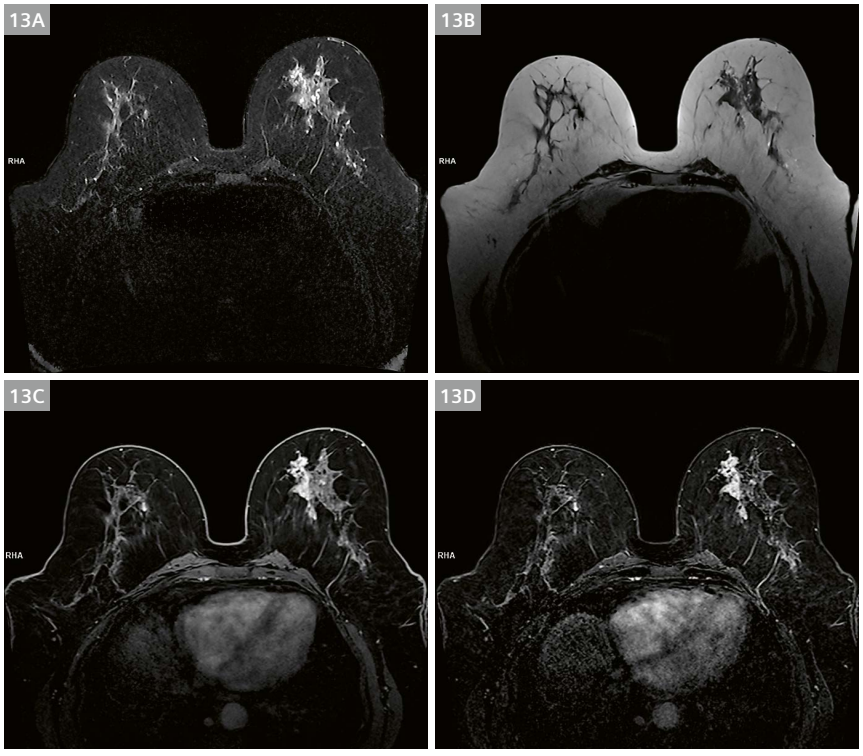

13 Study following diagnosis of suspicious mass during mammography: Confirmation of an ACR4 lesion in the left breast on the axial T2w Dixon fat sat images **(13A)**, axial T1w TSE images (pre-contrast) **(13B)** and corresponding findings in the dynamic axial T1w 3D Dixon **(13C)** series, and on subtraction after contrast media injection **(13D)**.

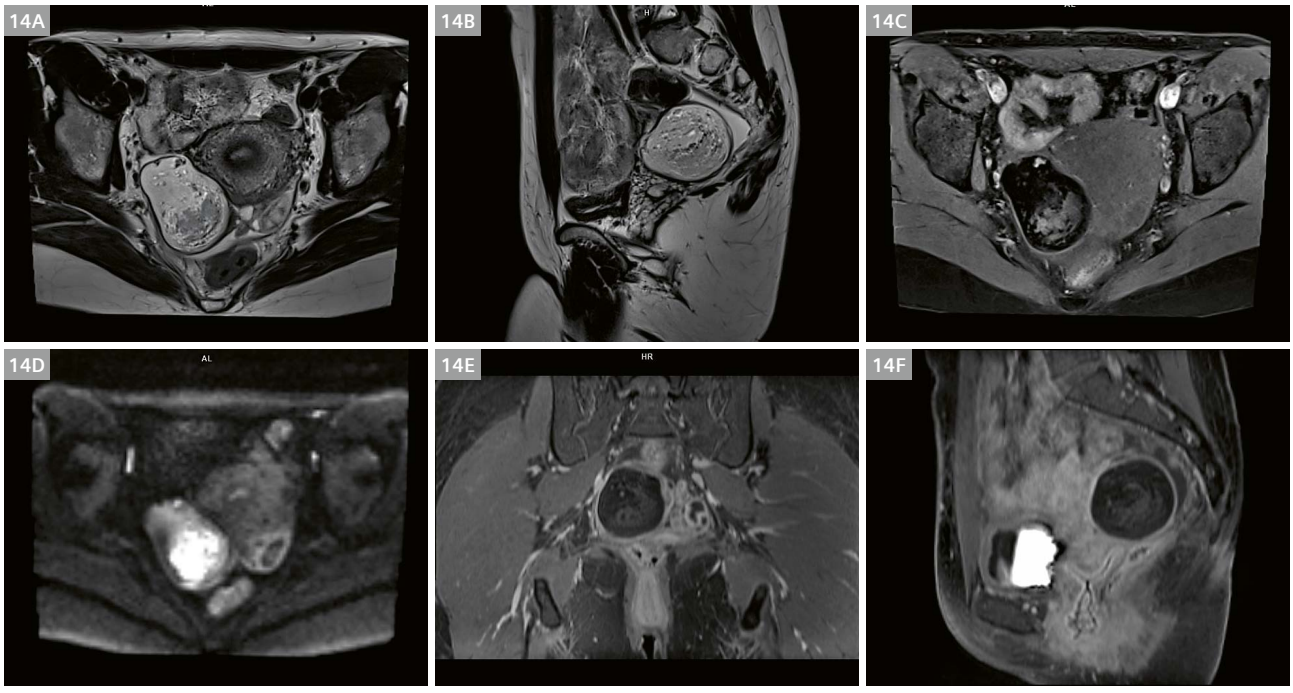

14 Discovery of a pelvic cyst: Right ovarian lesion with a fleshy part and a fatty part using T2w TSE **(14A, B)** and T1w Dixon **(14C)**, DWI with RESOLVE **(14D)**, no enhancement on the post-contrast 3D StarVIBE FS sequence **(14E, F)**. Image primarily suggestive of a right ovarian dermoid cyst.

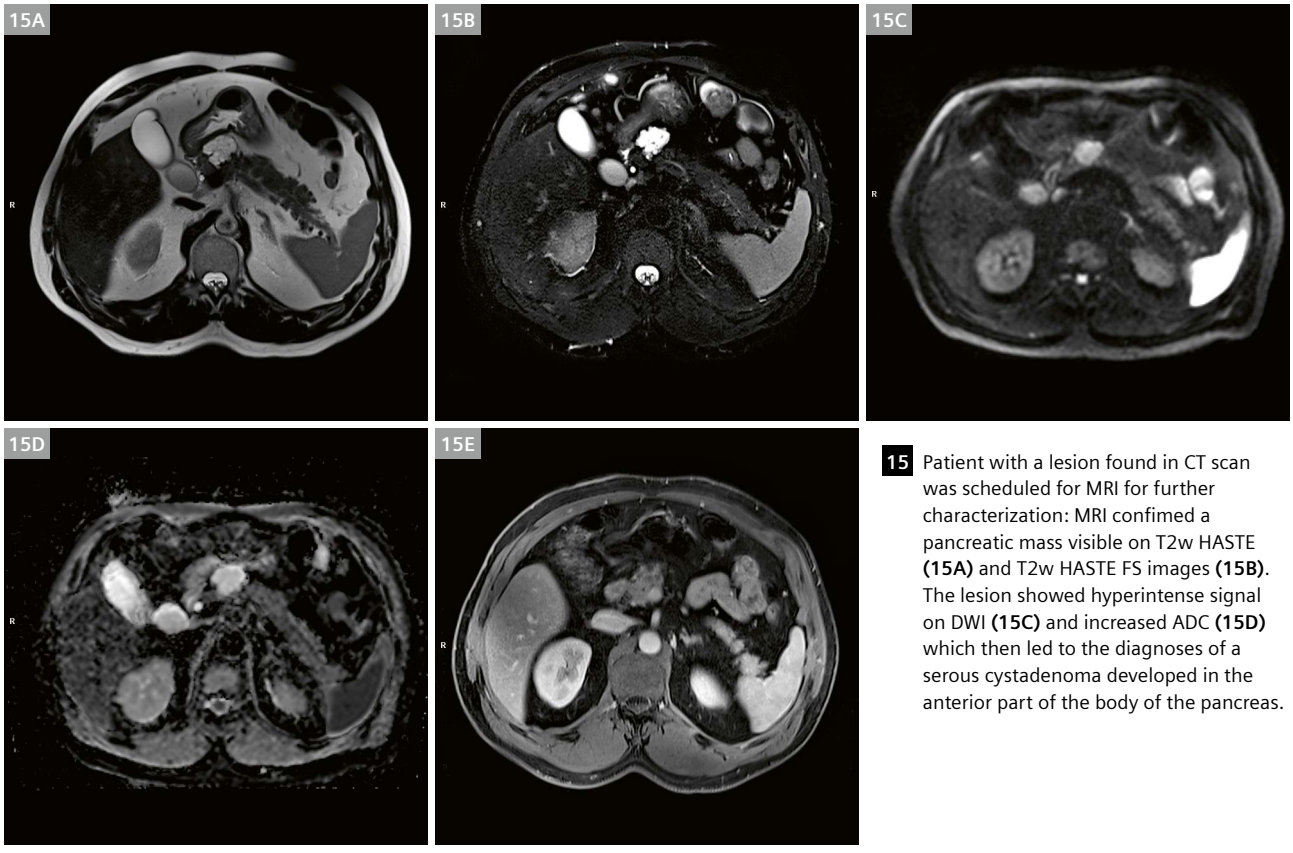

15 Patient with a lesion found in CT scan was scheduled for MRI for further characterization: MRI confimed a pancreatic mass visible on T2w HASTE **(15A)** and T2w HASTE FS images **(15B)**. The lesion showed hyperintense signal on DWI **(15C)** and increased ADC **(15D)** which then led to the diagnoses of a serous cystadenoma developed in the anterior part of the body of the pancreas.

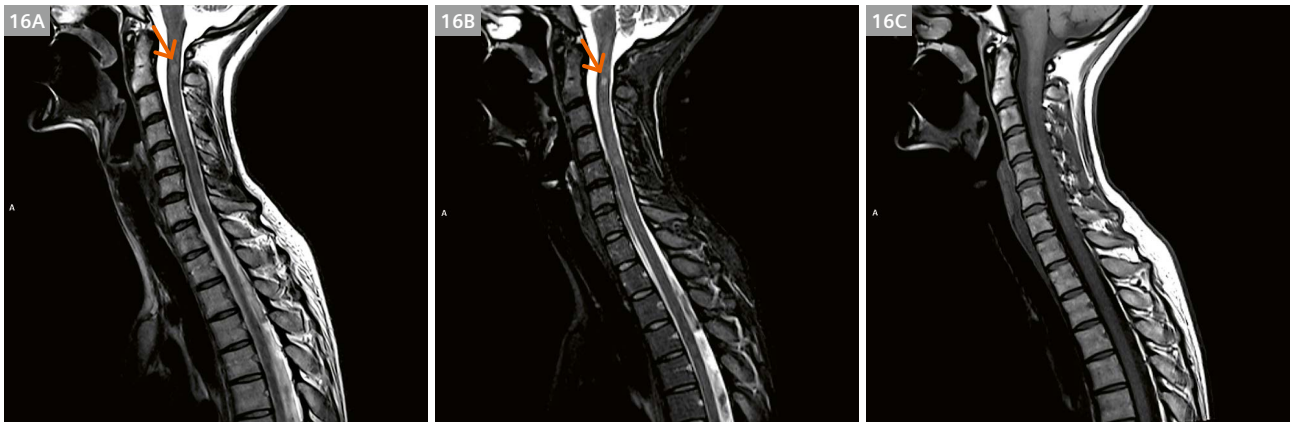

16 Reassessment of a demyelinating disease.
Appearance of a centromedullary hypersignal of 5 mm at C1–C2 level on sagittal T2w TSE **(16A)** and T2w STIR **(16B)** sequences.

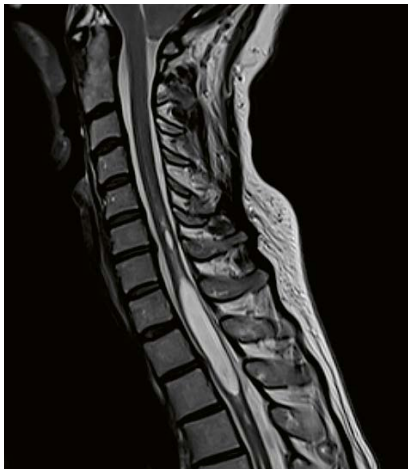

17 Presence of a syringomyelic cavity in T2w TSE images.

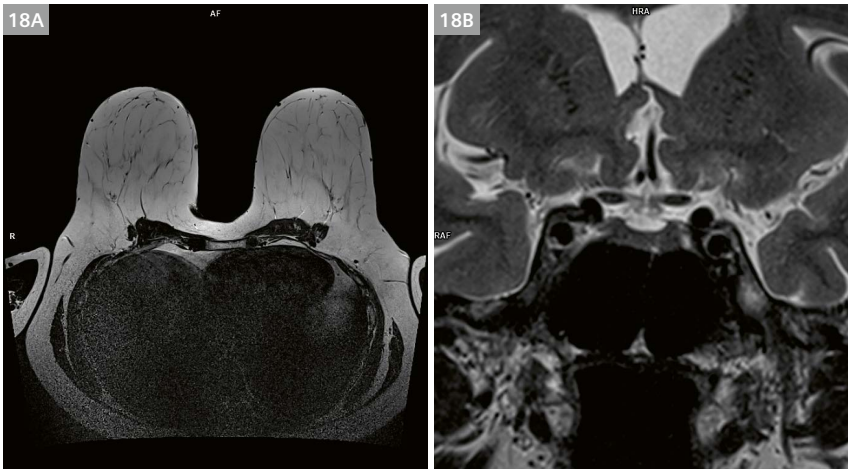

18 Axial T2 SMS TSE breast MRI, 2 mm thick joined slices, 592 x 592, 3 min 23 s **(18A)**.
Coronal T2w SMS TSE in pituitary MRI, 2 mm thick joined slices, 384 x 384, 2 min 36 s **(18B)**.

Conclusions

Following extensive research, we elected to install a 3T MRI system at GIE IRM74. As a result, we have benefitted from superior image quality with equal, or even shorter, examination time compared to the 1.5T systems. This has been made possible thanks to the new protocol optimization tools provided by BioMatrix Technology, the user-friendliness for technicians of the XA interface, and enhanced patient comfort thanks to a reassuring environment and multiple improvements, including the Head/Neck Coil that can be adapted to the patient. The benefits of the new acceleration techniques, such as Simultaneous Multi-Slice and CAIPIRINHA SPACE, are unquestionable in terms of shortening the time the patient spends in the scanner, while at the same time offering remarkable diagnostic image quality.

Contact

Corentin Mauris
Medical Electroradiology Technician
Medical-technical advisor
GIE IRM74
18, Rue de la Césière
74000 Annecy
France
Tel.: +33 4 50 51 81 75
c.mauris@irm74.org

Structured Reports for Communicating with Hepatobiliary Surgeons

Roberto Cannella; Adele Taibbi; Salvatore Pardo; Giuseppe Lo Re; Ludovico La Grutta; Tommaso Vincenzo Bartolotta

Section of Radiology – BiND., University Hospital "Paolo Giaccone", Palermo, Italy

Introduction

Clear and effective communication of imaging findings should be the main goal of an interpreting radiologist. Most physicians rely on radiological reports to plan patient management and treatment, and unclear communication may hinder appropriate treatment, even when the diagnosis is correct.

Traditional nonstructured reports are composed of free narrative text, with variable information, terminology, and recommendations [1]. Such free-text reports may be difficult to interpret for the referring physicians, and often lead to a second radiological consultation for clarification [1]. Moreover, free-text reports may lack clinically relevant information essential for surgical planning.

In hepatobiliary surgery, a major objective for the abdominal radiologist interpreting a liver study is to determine the eligibility for surgery of patients with malignant hepatic lesions. Reporting liver imaging is not an easy task. Reports are challenging given the possible presence of underlying chronic liver disease with multiple hepatic findings, coexistence of benign and malignant lesions, sequela of locoregional treatments, and the complex appearance of images. Moreover, radiologists are required to summarize the main findings according to several guidelines systems, such as the Liver Imaging Reporting and Data System (LI-RADS) for assessing the probability that a lesion is a hepatocellular carcinoma (HCC) in high-risk patients [2], or RECIST criteria to evaluate the treatment response in solid neoplasm after chemotherapy [3]. Given this complexity, it is easy to omit relevant findings requested by hepatobiliary surgeons, such as the absence of vascular invasion in a patient with multiple hepatic lesions.

Prior literature and scientific societies have introduced structured reports for many clinical circumstances [4, 5]. Despite these advances, communicating imaging findings to hepatobiliary surgeons remains challenging for radiologists.

The purpose of this article is to illustrate the main benefits, challenges, and caveats of structured reporting, with particular attention to preoperative hepatobiliary imaging evaluation in patients with malignant hepatic lesions in cirrhotic and non-cirrhotic livers.

The new era of structured reporting

The ultimate goal of structured reporting is to impact clinical care by improving the communication of imaging findings to referring physicians. In recent years, growing evidence has supported the use of structured reports in clinical practice to achieve higher quality and more reproducible communication with clinicians [6–9].

Structured reports decrease the incidence of syntactic and grammatical errors, which are encountered in 22–33% of conventional dictations [10, 11]. A structured template drastically reduces the use of subjective terms for communicating impressions, preventing interpretation ambiguities [12, 13]. Terms such as "consistent with", "compatible with", or "may represent" have significantly different interpretations among radiologists and clinicians regarding the intended level of certainty for imaging diagnosis [14]. In liver imaging, Corwin et al. [15] reported that up to sixteen different terms were adopted in nonstructured reports to describe the same lesions at risk of being HCC, which may have been more simply classified as LR-4 or LR-5 according to the LI-RADS lexicon [2]. Several radiologists also report significantly improved workflow efficiency with reduced dictation time when using standardized reporting [16, 17]. In academic centers, the implementation of structured reports has been proposed for residents training [18, 19]. Lastly, structured reports facilitate better assessability for automated retrospective data analysis for research purposes.

Several studies have shown that, compared with free-text reports, structured templates result in higher satisfaction and improved clarity for referring physicians [7, 20–24]. The greatest improvements were in readability, easier interpretation, increased detail, adherence with current practical guidelines [7, 25–27] and, most importantly, higher rates of management recommendations suggested by radiologists [7, 20].

There is no unique template for a structured report. A template should be designed together with the referring physicians to address a distinct disease and focus on answering specific clinical questions [13]. It also needs to change over time, with constant updates taking into account current evidence and guidelines as well as feedback from interpreting radiologists and referring physicians [23, 28–30].

Most templates are organized in paragraphs including clinical history, technique, comparison, findings and impressions. The "techniques" paragraph should briefly document the main phases/sequences acquired as well as the administration of intravenous contrast agent and the presence of any adverse or allergic reaction. Comparison with prior imaging studies evaluating the target organs should always be reported. The "findings" section is usually organized with subheadings relating to the specific relevant lesions or various imaged organs or anatomical structures [1]. Each subheading may be followed by narrative text or by a standardized text with checkboxes containing options for describing specific findings [16]. Impressions should be concise, including answers to the clinical questions, unexpected relevant findings as well as suggestions for further evaluation, follow-ups, or treatment options according to specific guidelines [16]. Differential diagnosis may be provided if the described observations have uncertain interpretation.

The caveat is to adopt structured reporting only when appropriate according to the clinical context. The systematic use of structured reporting should not prevent the radiologist to switch or customize the template with free-text in more complex or unusual cases, where the standard template is insufficient for describing all the relevant information [8]. Templates should simplify and improve the radiology workflow, so rigid and inefficient reports may need to be revised or abandoned if there are no advantages in specific clinical scenarios.

In hepatobiliary imaging few authors have assessed the effects of structured reporting for the assessment of hepatic lesions [12, 15, 31]. At the University of Palermo, we have introduced structured reports for several clinical applications in abdominal imaging, with promising feedback for the screening and diagnosis of HCC, and pre-operative staging of colorectal liver metastasis and pancreatic ductal adenocarcinoma.

Structured reporting for cirrhotic patients

In cirrhotic patients, hepatocellular carcinoma is the most common liver malignancy, and the leading cause of mortality in compensated cirrhosis [32]. According to the European Association for the Study of the Liver (EASL) and the American Association for the Study of Liver Disease (AASLD), surgical resection is recommended for single HCC, even large lesions (diameter greater than 2 cm), when hepatic function is preserved [33–35].

Structured reports for cirrhosis must clearly communicate the imaging diagnosis to the hepatobiliary surgeons (Fig. 1). Each suspicious lesion should be described individually, including location according to Couinaud segments, maximum diameter with series and image number in which the lesion is measured, the presence of typical major imaging features of HCC (i.e. arterial phase hyperenhancement, washout, peripheral capsule and growth over time), and significant changes from prior exams [35]. When using LI-RADS for the non-invasive diagnosis of HCC, the final categorization should be reported individually for each untreated observation suspicious of malignancy [2]. The spread of LI-RADS templates has been supported by the American College of Radiology website, with sample reports and guidance for concise reporting according to LI-RADS recommendations [36].

One major task for the radiologist is to communicate to hepatobiliary surgeons the presence of macroscopic vascular invasion of HCC or other non-HCC malignancies, which remains one of the main contraindications for surgery [33, 35]. Findings suggestive of tumor in a vein, such as enhancing thrombus, vessel expansion, and restricted diffusion on MRI, must be scrutinized and described in each lesion [37].

In cirrhotic patients, eligibility for surgery depends not only on tumor burden but also on the stage of the chronic liver disease [34]. A structured report should include a detailed description of liver morphology, presence of oesophageal and/or gastric varices, reanalyzed paraumbilical vein, splenomegaly, and ascites [35]. When a major resection is planned, the report should include quantification of future liver remnant (FLR) to ensure that it is sufficient [35].

Radiological reports are crucial to determine organ allocation in patients referred for liver transplant. Eligibility for orthotropic liver transplant is based on the number and maximum diameter of lesions diagnosed as definitive HCC. Templates in candidates for orthotopic liver transplant may be integrated with the OPTN (Organ Procurement and Transplantation Network) classification, which assigns exception points in the United States for transplant for lesions that are unequivocally diagnosed as HCC using imaging [38]. Particularly the OPTN encourages a

structured summary at the end of the report, describing number, size, location, and classification of lesions meeting the criteria for HCC [38].

Some recent studies have investigated the relevance of structured reporting in cirrhosis [12, 15, 31, 39, 40]. Flusberg et al. [12] demonstrated that structured templates using LI-RADS for diagnosis of HCC were significantly associated with more "comprehensive and consistent" reporting of LI-RADS category and description of major features of HCC, as well as size and location of the observations. Poullos et al. [31] analyzed the performance of structured reports in patients with HCC eligible for orthotopic liver transplant, finding significantly improved communication of imaging findings, OPTN class, and eligibility for transplant.

Structured reporting for non-cirrhotic patients

In a non-cirrhotic liver, the most common malignant lesions are metastases, especially of colorectal origin. Hepatic metastases are the primary cause of mortality in patients with other abdominal neoplasms [35]. Although HCC may also arise in patients without evident risk factors for chronic liver disease, its diagnosis usually requires a histopathological confirmation. Another primary hepatic malignancy commonly occurring in non-cirrhotic patients is intra-hepatic mass-forming cholangiocarcinoma. Surgical resection of tumors limited to the liver remains the only potential curative treatment to provide longer survival times [41]. Communicating imaging findings to hepatobiliary surgeons should take into account possible surgical treatments [42–44].

Clinical history: [age]-year-old [female/male] with cirrhosis.

Locoregional treatment: [none – TACE/RFTA in segment…].

Technique: MRI of the liver was performed with the following sequences [sequence type]. Images were obtained prior and following the uneventful administration of [volume] ml of [contrast type].

Comparison: MRI dated [MM/DD/YY].

Findings

Liver morphology: [Cirrhosis].

Lesion #1: In the hepatic segment [segment number] there is a [dimension] cm observation (series [number], image [number]) showing [nonrim arterial phase hyperenhancement] and [washout – enhancing capsule] on portal venous and delayed phases. Threshold growth is [present – absent]. The lesion is classifiable as LR-[classification].

Lesion #2: In the hepatic segment [segment number] there is a [dimension] cm observation (series [number], image [number]) showing [nonrim arterial phase hyperenhancement] and [washout – enhancing capsule] on portal venous and delayed phases. Threshold growth is [present – absent]. The lesion is classifiable as LR-[classification].

Lesion #3: In the hepatic segment [segment number] there is a [dimension] cm observation (series [number], image [number]) showing [nonrim arterial phase hyperenhancement] and [washout – enhancing capsule] on portal venous and delayed phases. Threshold growth is [present – absent]. The lesion is classifiable as LR-[classification].

Hepatic vessels: [patency – nontumoral thrombosis – tumor in vein] of [portal vein – hepatic vein].

Anatomical variants of hepatic vasculature: [none – present (describe)].

Bile duct: [non dilated – dilated].

Extra-hepatic findings: [none, splenomegaly, varices, ascites].

Other organs: [describe other findings].

Impression:

- Lesion #1: [dimension] cm observation in segment [number], classifiable as LR-[LI-RADS classification].
- Lesion #2: [dimension] cm observation in segment [number], classifiable as LR-[LI-RADS classification].
- Lesion #3: [dimension] cm observation in segment [number], classifiable as LR-[LI-RADS classification].
- [patent – nontumoral thrombosis – tumor in vein] of [portal vein – hepatic vein].

1 Example of a structured report template for HCC screening with MRI in cirrhotic patients.

At Palermo, we have adopted structured reports for preoperative hepatic staging of patients with colorectal liver metastasis imaged with MRI (Fig. 2), with significant improvements in communication with hepatobiliary surgeons. The template should include all the surgically relevant anatomical factors needed to plan the resection, and evaluate extra-hepatic disease, background liver parenchyma, and changes after neoadjuvant chemotherapy [45].

Each report should accurately describe the size and number of lesions, the number of involved and uninvolved segments, as well as the relationship and degree of tumor contact with arterial and venous hepatic vessels [35, 45, 46]. Vascular invasion of the main portal vein or hepatic artery often prevents tumor eradication [46]. Ideally, the report should also provide a clear description of anatomical biliary and vascular variants that may significantly influence the resectability or increase the risk of iatrogenic injuries during resection.

The presence of extra-hepatic disease is another significant contraindication for liver resection. Extra-hepatic lesions suspicious of malignancy should be always carefully described in the structured report in both findings and impressions [45]. The size and location of enlarged suspicious abdominal lymph nodes should also be reported.

Up to 60% of patients receive neoadjuvant chemotherapy before resection of hepatic metastases [47], so the report should include comparison with prior exam, with description of size changes, and evidence of treatment response or stability of the disease [3]. Olthof et al. [48] demonstrated that structured reporting for patients receiving neoadjuvant treatment improves report quality

Clinical history: [age]-year-old [female/male] with colorectal adenocarcinoma.

Chemotherapy: [none – number cycles of …].

Locoregional treatment: [none – resection of segment … – left/right hepatectomy].

Technique: MRI of the liver was performed with the following sequences [sequence type]. Images were obtained prior and following the uneventful administration of [volume] ml of [contrast type].

Comparison: MRI dated [MM/DD/YY].

Findings

Liver morphology: [Normal – Dysmorphic liver - Cirrhosis].

Lesion #1: In the hepatic segment [segment number] there is a [dimension] cm lesion (series [number], image [number]) showing [hyperenhancement – rim enhancement – no enhancement] on hepatic arterial phase [with – without] washout on portal venous phase and hypointensity on hepatobiliary phase. The lesion is [increased in size – stable – decreased in size] compared to prior exam, previously measuring [dimension] cm. The lesion is [probably metastasis – indeterminate – probably benign].

Lesion #2: In the hepatic segment [segment number] there is a [dimension] cm lesion (series [number], image [number]) showing [hyperenhancement – rim enhancement – no enhancement] on hepatic arterial phase [with – without] washout on portal venous phase and hypointensity on hepatobiliary phase. The lesion is [increased in size – stable – decreased in size] compared to prior exam, previously measuring [dimension] cm. The lesion is [probably metastasis – indeterminate – probably benign].

Lesion #3: In the hepatic segment [segment number] there is a [dimension] cm lesion (series [number], image [number]) showing [hyperenhancement – rim enhancement - no enhancement] on hepatic arterial phase [with – without] washout on portal venous phase and hypointensity on hepatobiliary phase. The lesion is [increased in size – stable – decreased in size] compared to prior exam, previously measuring [dimension] cm. The lesion is [probably metastasis – indeterminate – probably benign].

Hepatic vessels: [patency – nontumoral thrombosis – tumor in vein] of [portal vein – hepatic vein].

Anatomical variants: [none – present (describe)].

Bile duct: [non dilated – dilated].

Other organs: [describe other findings].

Impression:

- Lesion #1: [dimension] cm lesion in segment [number], [new – increased in size – stable – decreased in size] compared to prior exam.
- Lesion #2: [dimension] cm lesion in segment [number], [new – increased in size – stable – decreased in size] compared to prior exam.
- Lesion #3: [dimension] cm lesion in segment [number], [new – increased in size – stable – decreased in size] compared to prior exam.
- [patent – nontumoral thrombosis – tumor in vein] of [portal vein – hepatic vein].

2 Example of a structured report template for MRI acquired in the preoperative evaluation of non-cirrhotic patients with colorectal liver metastasis.

and adherence to RECIST guidelines for assessing treatment response. Attention should be paid to possible liver confounders caused by chemotherapy-induced hepatotoxicity. In particular, oxaliplatin treatment of colorectal metastasis has been associated with sinusoidal obstruction syndrome [49] and in some cases with the appearance of focal nodular hyperplasia-like nodules [50].

Although structured reporting is recommended by several societies for preoperative evaluation of focal liver lesions in non-cirrhotic liver, there is a lack of evidence in the radiological literature supporting its value.

Conclusions

We have illustrated the major strengths and limitations of structured reporting in liver imaging, focusing on communicating imaging findings to hepatobiliary surgeons for treatment of malignant liver lesions in cirrhotic and non-cirrhotic patients. Implementation of structured report templates may improve the quality and completeness of reports, focusing them on relevant clinical questions that are crucial for surgical planning.

References

1 Ganeshan D, Duong PT, Probyn L, Lenchik L, McArthur TA, Retrouvey M, Ghobadi EH, Desouches SL, Pastel D, Francis IR. Structured Reporting in Radiology. Acad Radiol. 2018;25:66-73.
2 American College of Radiology. Liver imaging reporting and data system. Available from: https://www.acr.org/Clinical-Resources/Reporting-and-Data-Systems/LI-RADS. Accessed on February 2019.
3 Eisenhauer EA, Therasse P, Bogaerts J, Schwartz LH, Sargent D, Ford R, Dancey J, Arbuck S, Gwyther S, Mooney M, Rubinstein L, Shankar L, Dodd L, Kaplan R, Lacombe D, Verweij J. New response evaluation criteria in solid tumours: revised RECIST guideline (version 1.1). Eur J Cancer. 2009;45:228-47.
4 Radiological Society of North America website. RSNA RadReport Template Library. Available from: www.radreport.org. 2018. Accessed on February 2019.
5 Society of Abdominal Radiology. Disease-Focused Panels. Available from: https://www.abdominalradiology.org/page/DFP. Accessed on February 2019.
6 Faggioni L, Coppola F, Ferrari R, Neri E, Regge D. Usage of structured reporting in radiological practice: results from an Italian online survey. Eur Radiol. 2017;27:1934-1943.
7 Heye T, Gysin V, Boll DT, Merkle EM. JOURNAL CLUB: Structured Reporting: The Voice of the Customer in an Ongoing Debate About the Future of Radiology Reporting. AJR Am J Roentgenol. 2018;211:964-970.
8 Powell DK, Silberzweig JE. State of structured reporting in radiology, a survey. Acad Radiol. 2015;22:226-33.
9 Goldberg-Stein S, Walter WR, Amis ES Jr, Scheinfeld MH. Implementing a Structured Reporting Initiative Using a Collaborative Multistep Approach. Curr Probl Diagn Radiol. 2017;46:295-299.
10 Quint LE, Quint DJ, Myles JD. Frequency and spectrum of errors in final radiology reports generated with automatic speech recognition technology. J Am Coll Radiol. 2008;5:1196-9.
11 Hawkins CM, Hall S, Zhang B, Towbin AJ. Creation and implementation of department-wide structured reports: an analysis of the impact on error rate in radiology reports. J Digit Imaging. 2014;27:581-7.
12 Flusberg M, Ganeles J, Ekinci T, Goldberg-Stein S, Paroder V, Kobi M, Chernyak V. Impact of a Structured Report Template on the Quality of CT and MRI Reports for Hepatocellular Carcinoma Diagnosis. J Am Coll Radiol. 2017;14:1206-1211.
13 European Society of Radiology (ESR). ESR paper on structured reporting in radiology. Insights Imaging. 2018;9:1-7.
14 Lee B, Whitehead MT. Radiology Reports: What YOU Think You're Saying and What THEY Think You're Saying. Curr Probl Diagn Radiol. 2017;46:186-195.
15 Corwin MT, Lee AY, Fananapazir G, Loehfelm TW, Sarkar S, Sirlin CB. Nonstandardized Terminology to Describe Focal Liver Lesions in Patients at Risk for Hepatocellular Carcinoma: Implications Regarding Clinical Communication. AJR Am J Roentgenol. 2018;210:85-90.
16 Manoonchai N, Kaewlai R, Wibulpolprasert A, Boonpramarn U, Tohmee A, Phongkitkarun S. Satisfaction of imaging report rendered in emergency setting: a survey of radiology and referring physicians. Acad Radiol. 2015;22:760-70.
17 Hanna TN, Shekhani H, Maddu K, Zhang C, Chen Z, Johnson JO. Structured report compliance: effect on audio dictation time, report length, and total radiologist study time. Emerg Radiol. 2016;23:449-53.
18 Johnson TF, Brinjikji W, Doolittle DA, Nagelschneider AA, Welch BT, Kotsenas AL. Structured Head and Neck CT Angiography Reporting Reduces Resident Revision Rates. Curr Probl Diagn Radiol. 2018 Apr 12. pii: S0363-0188(17)30311-0. doi: 10.1067/j.cpradiol.2018.04.003.
19 Marcal LP, Fox PS, Evans DB, Fleming JB, Varadhachary GR, Katz MH, Tamm EP. Analysis of free-form radiology dictations for completeness and clarity for pancreatic cancer staging. Abdom Imaging. 2015;40:2391-7.
20 Nguyen Q, Sarwar A, Luo M, Berkowitz S, Ahmed M, Brook OR. Structured Reporting of IR Procedures: Effect on Report Compliance, Accuracy, and Satisfaction. J Vasc Interv Radiol. 2018;29:345-352.
21 Sabel BO, Plum JL, Kneidinger N, Leuschner G, Koletzko L, Raziorrouh B, Schinner R, Kunz WG, Schoeppe F, Thierfelder KM, Sommer WH, Meinel FG. Structured reporting of CT examinations in acute pulmonary embolism. J Cardiovasc Comput Tomogr. 2017;11:188-195.
22 Nörenberg D, Sommer WH, Thasler W, D'Haese J, Rentsch M, Kolben T, Schreyer A, Rist C, Reiser M, Armbruster M. Structured Reporting of Rectal Magnetic Resonance Imaging in Suspected Primary Rectal Cancer: Potential Benefits for Surgical Planning and Interdisciplinary Communication. Invest Radiol. 2017;52:232-239.
23 Magnetta MJ, Donovan AL, Jacobs BL, Davies BJ, Furlan A. Evidence-Based Reporting: A Method to Optimize Prostate MRI Communications With Referring Physicians. AJR Am J Roentgenol. 2018;210:108-112.
24 Schwartz LH, Panicek DM, Berk AR, Li Y, Hricak H. Improving communication of diagnostic radiology findings through structured reporting. Radiology. 2011;260:174-81.
25 Griffin AS, Mitsky J, Rawal U, Bronner AJ, Tessler FN, Hoang JK. Improved Quality of Thyroid Ultrasound Reports After Implementation of the ACR Thyroid Imaging Reporting and Data System Nodule Lexicon and Risk Stratification System. J Am Coll Radiol. 2018;15:743-748.
26 Buckley BW, Daly L, Allen GN, Ridge CA. Recall of structured radiology reports is significantly superior to that of unstructured reports. Br J Radiol. 2018;91:20170670.
27 Marcovici PA, Taylor GA. Journal Club: Structured radiology reports are more complete and more effective than unstructured reports. AJR Am J Roentgenol. 2014;203:1265-71.

28 Larson DB, Towbin AJ, Pryor RM, Donnelly LF. Improving consistency in radiology reporting through the use of department-wide standardized structured reporting. Radiology. 2013;267:240-50.
29 Larson DB. Strategies for Implementing a Standardized Structured Radiology Reporting Program. Radiographics. 2018;38:1705-1716.
30 Pinto Dos Santos D, Hempel JM, Mildenberger P, Klöckner R, Persigehl T. Structured Reporting in Clinical Routine. Rofo. 2019;191:33-39.
31 Poullos PD, Tseng JJ, Melcher ML, Concepcion W, Loening AM, Rosenberg J, Willmann JK. Structured Reporting of Multiphasic CT for Hepatocellular Carcinoma: Effect on Staging and Suitability for Transplant. AJR Am J Roentgenol. 2018;210:766-774.
32 Ferlay J, Soerjomataram I, Dikshit R, Eser S, Mathers C, Rebelo M, Parkin DM, Forman D, Bray F. Cancer incidence and mortality worldwide: sources, methods and major patterns in GLOBOCAN 2012. Int J Cancer. 2015;136:E359-86.
33 Galle PR, Forner A, Llovet JM, Mazzaferro V, Piscaglia F, Raoul JL, Schirmacher P, Vilgrain V. EASL Clinical Practice Guidelines: Management of hepatocellular carcinoma. J Hepatol. 2018;69:182-236.
34 Marrero JA, Kulik LM, Sirlin CB, Zhu AX, Finn RS, Abecassis MM, Roberts LR, Heimbach JK. Diagnosis, Staging, and Management of Hepatocellular Carcinoma: 2018 Practice Guidance by the American Association for the Study of Liver Diseases. Hepatology. 2018;68:723-750.
35 Shin DS, Ingraham CR, Dighe MK, Wang C, Vaidya S, Moshiri M, Lall C, Park JO, Bhargava P. Surgical resection of a malignant liver lesion: what the surgeon wants the radiologist to know. AJR Am J Roentgenol. 2014;203:W21-33.
36 Chernyak V, Fowler KJ, Kamaya A, Kielar AZ, Elsayes KM, Bashir MR, Kono Y, Do RK, Mitchell DG, Singal AG, Tang A, Sirlin CB. Liver Imaging Reporting and Data System (LI-RADS) Version 2018: Imaging of Hepatocellular Carcinoma in At-Risk Patients. Radiology. 2018;289:816-830.
37 Cannella R, Fowler KJ, Borhani AA, Minervini MI, Heller M, Furlan A. Common pitfalls when using the Liver Imaging Reporting and Data System (LI-RADS): lessons learned from a multi-year experience. Abdom Radiol (NY). 2019;44:43-53.
38 Wald C, Russo MW, Heimbach JK, Hussain HK, Pomfret EA, Bruix J. New OPTN/UNOS policy for liver transplant allocation: standardization of liver imaging, diagnosis, classification, and reporting of hepatocellular carcinoma. Radiology. 2013;266:376-82.
39 Clark TJ, McNeeley MF, Maki JH. Design and implementation of handheld and desktop software for the structured reporting of hepatic masses using the LI-RADS schema. Acad Radiol. 2014;21:491-506.
40 Pinto Dos Santos D, Arnhold G, Mildenberger P, Düber C, Kloeckner R. Guidelines Regarding §16 of the German Transplantation Act - Initial Experiences with Structured Reporting. Rofo. 2017;189:1145-1151.
41 Bertens KA, Hawel J, Lung K, Buac S, Pineda-Solis K, Hernandez-Alejandro R. ALPPS: challenging the concept of unresectability – a systematic review. Int J Surg. 2015;13:280-7.
42 Torzilli G, Adam R, Viganò L, Imai K, Goransky J, Fontana A, Toso C, Majno P, de Santibañes E. Surgery of Colorectal Liver Metastases: Pushing the Limits. Liver Cancer. 2016;6:80-89.
43 Idrees JJ, Bagante F, Gani F, Rosinski BF, Chen Q, Merath K, Dillhoff M, Cloyd J, Pawlik TM. Population level outcomes and costs of single stage colon and liver resection versus conventional two-stage approach for the resection of metastatic colorectal cancer. HPB (Oxford). 2018 Sep 25. pii: S1365-182X(18)33937-6. doi: 10.1016/j.hpb.2018.08.007.
44 Khan AS, Garcia-Aroz S, Ansari MA, Atiq SM, Senter-Zapata M, Fowler K, Doyle MB, Chapman WC. Assessment and optimization of liver volume before major hepatic resection: Current guidelines and a narrative review. Int J Surg. 2018;52:74-81.
45 Zerial M, Lorenzin D, Risaliti A, Zuiani C, Girometti R. Abdominal cross-sectional imaging of the associating liver partition and portal vein ligation for staged hepatectomy procedure. World J Hepatol. 2017;9:733-745.
46 Frankel TL, Gian RK, Jarnagin WR. Preoperative imaging for hepatic resection of colorectal cancer metastasis. J Gastrointest Oncol. 2012;3:11-8.
47 Regimbeau JM, Cosse C, Kaiser G, Hubert C, Laurent C, Lapointe R, Isoniemi H, Adam R. Feasibility, safety and efficacy of two-stage hepatectomy for bilobar liver metastases of colorectal cancer: a LiverMetSurvey analysis. HPB (Oxford). 2017;19:396-405.
48 Olthof AW, Borstlap J, Roeloffzen WW, Callenbach PMC, van Ooijen PMA. Improvement of radiology reporting in a clinical cancer network: impact of an optimised multidisciplinary workflow. Eur Radiol. 2018;28:4274-4280.
49 Brancatelli G, Furlan A, Calandra A, Dioguardi Burgio M. Hepatic sinusoidal dilatation. Abdom Radiol (NY). 2018;43:2011-2022.
50 Furlan A, Brancatelli G, Dioguardi Burgio M, Grazioli L, Lee JM, Murmura E, Lucidarme O, Strauss C, Rode A, Ronot M, Vilgrain V. Focal Nodular Hyperplasia After Treatment With Oxaliplatin: A Multiinstitutional Series of Cases Diagnosed at MRI. AJR Am J Roentgenol. 2018;210:775-779.

Roberto Cannella

Tommaso Vincenzo Bartolotta

Contact

Professor Tommaso Vincenzo Bartolotta, M.D., Ph.D.
Section of Radiology – BiND.
University Hospital "Paolo Giaccone"
Via del Vespro 129
90127 Palermo
Italy
tommasovincenzo.bartolotta@unipa.it

Prospective Motion Correction in Pediatric Neuroimaging with KinetiCor

Camilo Jaimes, M.D.[1, 3, 4]; Onur Afacan, Ph.D.[1,2,4]; Tess Wallace, Ph.D.[1,2,4]; Kristina Pelkola, RT (R) MR[1,2]; Lisa Chuah, Ph.D.[5]; Jenna Weldon, RT (R) MR[1]; Simon K. Warfield, Ph.D.[1,2,4]; Richard L. Robertson, M.D.[1,2]

[1]Department of Radiology, Boston Children's Hospital, Boston, MA, USA
[2]Computational Radiology Laboratory, Boston Children's Hospital, Boston, MA, USA
[3]Fetal-Neonatal Neuroimaging and Developmental Science Center, Boston, MA, USA
[4]Harvard Medical School, Boston, MA, USA
[5]KinetiCor Inc., Honolulu, HI, USA

During MRI, unwanted motion can displace or destroy image encoding, leading to non-diagnostic images. The problem of motion in MRI is particularly prevalent in clinical pediatric[1] imaging. In addition to challenges related to comfort, scanner-induced anxiety, and length of the exam, which affect patients of all ages, children may be unable to cooperate either as a result of a medical condition (e.g., autism spectrum disorder) or because they are too young to follow instructions [1, 2]. To obtain diagnostic images, many hospitals have a low threshold for imaging patients with sedation or general anesthesia. In fact, the rate of sedation for MRI in children between the ages

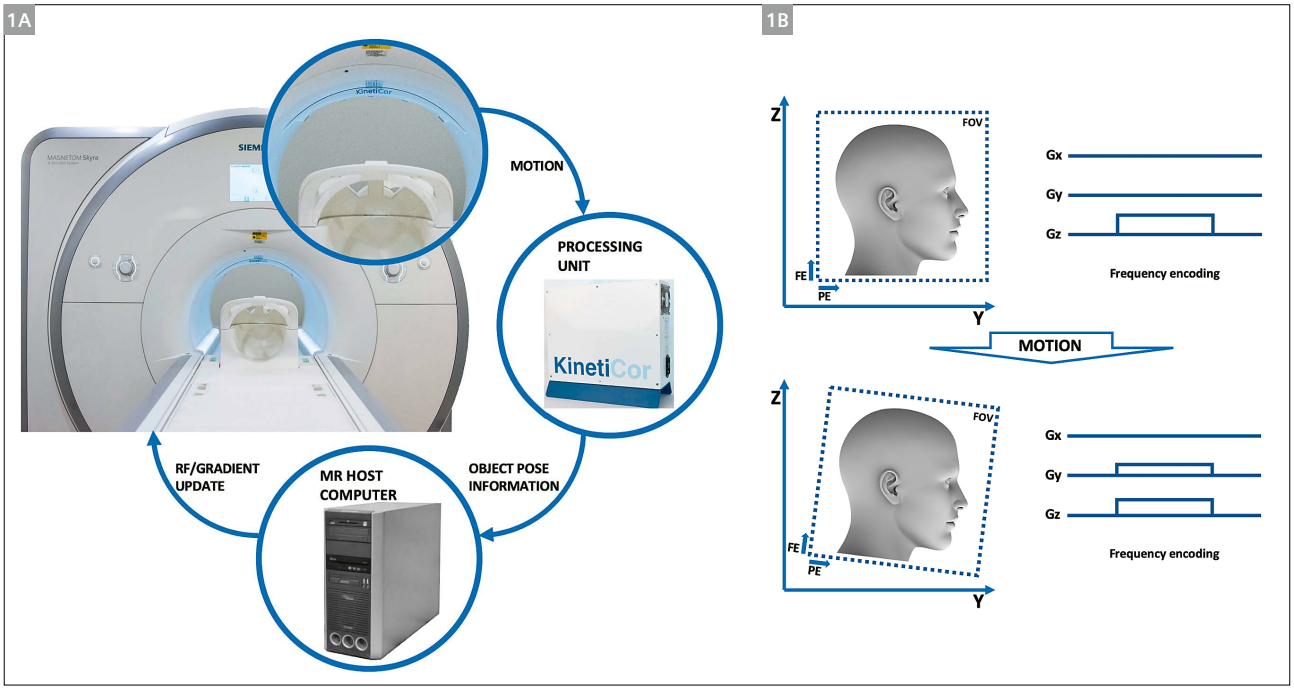

1 Schematic illustration of the KinetiCor system[2]. **(1A)** Illustrates the main components including the quad-camera, processing unit, MR Host computer, and feedback loop to the scanner. **(1B)** Illustrates prospective motion correction (PMC) based on updating coordinate positions, scanner gradients, and adjusting the field of view.

[1]MR scanning has not been established as safe for imaging fetuses and infants less than two years of age. The responsible physician must evaluate the benefits of the MR examination compared to those of other imaging procedures. Note: This Siemens Healthineers disclaimer does not represent the opinion of the author.
[2]The BioMatrix Kinetic Sensor is released with 3T MAGNETOM Vida and 1.5T MAGNETOM Sola. With MAGNETOM Skyra and MAGNETOM Prisma the KinetiCor system is work in progress, it is currently under development and is not for sale in the U.S. and in other countries. Its future availability cannot be ensured.

of 6 months and 6 years exceeds 90% [3, 4]. Although sedation and general anesthesia are an effective means of reducing patient motion they are not devoid of risks. Acute medical complications associated with sedation and anesthesia may occur and can range from mild medication reactions to severe life threating cardiopulmonary events [5]. Recently, concerns for long-term of effects of anesthetic medication on cognitive function also have been raised [6–8]. Finally, the cost of sedation and its effect on workflow also need to be considered, as the use of sedation can nearly triple the cost of the exam [9].

Recent advances in MRI hardware and pulse sequences have enabled faster acquisition of images. In conjunction with child-life specialists and other behavioral techniques, these have contributed to increasing the success rate of awake MRI in children [3]. However, these techniques have limited impact in some of our most vulnerable patients, including younger children and those with developmental disabilities. Motion correction strategies have therefore emerged as promising alternatives to mitigate motion artifacts in these patients. In particular, prospective motion correction (PMC) strategies are well suited for clinical practice, since they avoid delays that can result from "off line" processing of images and are therefore easy to integrate into the clinical workflow [1].

Prospective motion correction with KinetiCor

The MRI-compatible KinetiCor tracking system consists of a quad-camera that is embedded in a plastic molding and affixed securely to the bore of the MRI system. The camera is connected to the processing unit which is located in the equipment room alongside the scanner electronic cabinets. The camera system is connected to the processing unit through a shielded twisted power cable and 4 pairs of optical fibers (Fig. 1). For motion tracking in adults, KinetiCor provides a two-winged marker that is designed to be placed on the bridge of the nose. When the marker is visible, the tracking system continuously records rigid head motion with six degrees of freedom (translations in x, y, and z axes and rotations around x, y, and z axes). The camera system has been tested to have a spatial tracking accuracy of at least 100 microns for translation and 0.1 degrees for rotation with a recording rate of 60 Hz (60 frames per second). The motion estimates from the camera system are sent in real time to a motion correction framework that uses these data to update the field of view, RF pulses, and gradients, so that the imaging volume coincides with the new head position [10, 11].

Tailoring solutions to the needs of every patient

Simply put, one size doesn't fit all. Pediatric imaging, and certainly pediatric neuroimaging, illustrates this principle. The size of the brain of a term born infant is approximately 25% of the size of an adult. Brain growth is the fastest in the first year of life, resulting in doubling of brain volume (and head size) by 12 months of age [12]. During infancy and early childhood, fast growth will continue until the head reaches approximately 90% of its adult size by the age of 6 years [13, 14]. In practical terms, this means that the conventional two-winged marker that is used for PMC in adults is not suitable for imaging our youngest patients. The two-winged marker would cover most of the face of a newborn and would not couple appropriately with the facial structure of newborns or young infants. To address this, we have modified the two-winged nasal marker to a single flat marker than can be placed on the forehead (Fig. 2). A fortuitous advantage to the use of a single marker is that it can be used to track motion when patients use MRI-compatible video goggles which obscure the eyes and nose of the patient. In doing so, the single marker has enabled us to perform PMC in some of the most challenging patients we encounter (ages 3–7 years), who are at very high-risk for non-diagnostic examinations when imaged without sedation or anesthesia.

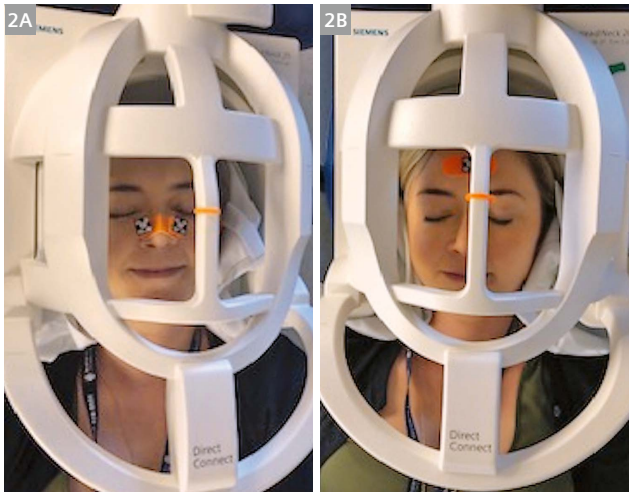

2 Images of an adult volunteer using the 64-channel head coil with the **(2A)** two-winged nose marker and the **(2B)** single-forehead marker.

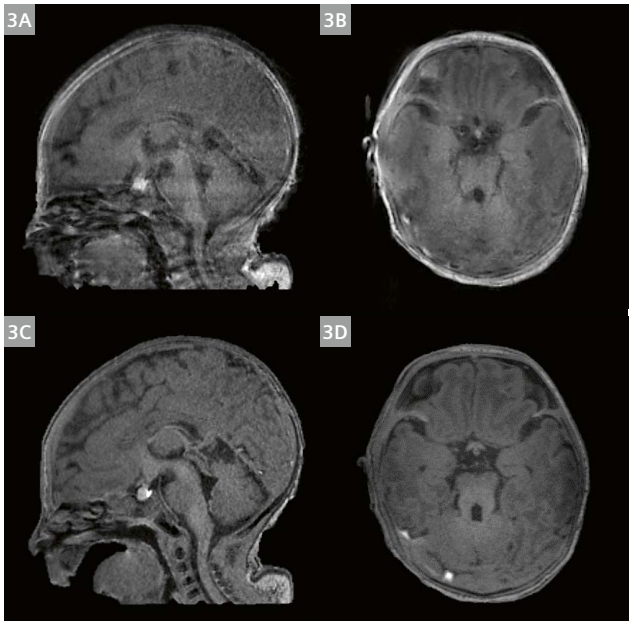

3 PMC in a 4-week-old infant[1] with abnormal prenatal head ultrasound who underwent MRI with feed and wrap technique. **(3A)** Sagittal and **(3B)** axial MPRAGE images show moderate motion artifacts. **(3C)** Sagittal and **(3D)** axial MPRAGE with PMC show substantial improvement in image quality, allowing for clear identification of hypoplasia and dysgenesis of the superior cerebellar vermis (3C) and a "molar tooth configuration" of the superior cerebellar peduncles (3D).

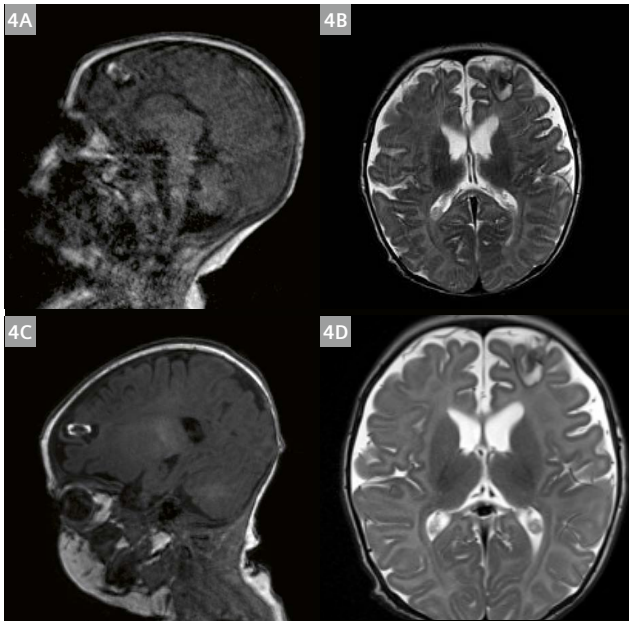

4 PMC in a 12-week-old infant[1] who obtained an MRI for follow-up of a perinatal intraparenchymal hemorrhage. **(4A)** Sagittal MPRAGE shows severe motion artifact; while a region of T1 shortening is identified at the site of the hematoma, anatomic detail is distorted and is overall non-diagnostic. **(4B)** Axial T2 image through the site of the hemorrhage shows mild motion artifact, with acceptable depiction of the region of encephalomalacia and chronic blood products. **(4C)** Sagittal MPRAGE with PMC and **(4D)** axial T2 obtained with PMC show virtually no motion artifacts and provide superior evaluation of the site of the hemorrhage as well as the rest of the brain parenchyma.

Special population: newborns and young infants

A patient population that is frequently imaged at children's hospitals are infants less than 12 months of age[1]. Imaging during natural sleep using the "feed and swaddle technique" has a high success rate, approaching 80% [15]. Despite the overwhelming success, some infants have trouble falling asleep or are intermittently disrupted by the sound of the MRI scanner. Other patients are jittery or have slow "bobbing" head movements, which introduces artifacts. The small size of the brain and the subtle nature of some abnormalities in this age range, such as some congenital malformations, may require high-resolution imaging that is highly susceptible to motion. With the use of the pediatric marker, we have successfully improved quality of scans in newborns and young infants imaged during natural sleep (Figs. 3 and 4). Images have been acquired using a 3T MR scanner (MAGNETOM Prisma, Siemens Healthcare, Erlangen, Germany)[2].

High resolution imaging

Protocols that rely on high-resolution sequences with lengthy acquisitions, such as epilepsy and neuro-oncology protocols, stand to benefit the most from PMC. These protocols are often degraded by motion even in reasonably compliant children and adolescents, resulting in repeat acquisitions and low-quality images. The epilepsy protocol for instance takes approximately 30 minutes of gradient time and includes: 3D MPRAGE, 3D T2 SPACE FLAIR, (35 direction) diffusion tensor imaging, high-resolution 2D T2 TSE and 2D TSE fat-suppressed FLAIR, with acquisitions that require 6 minutes, 6 minutes, 4 minutes, 5 minutes, and 4 minutes, respectively. Since the differential diagnosis for pediatric epilepsy is broad high-quality imaging is crucial, as the radiologist needs to exclude tumors, prior injury, and brain malformations as potential causes. Some of these, in particular cortical malformations, can be difficult to detect and present as subtle areas of blurring of the gray-white junction or other alterations of the gray-white interface that can easily be obscured by motion artifacts (Fig. 5) [16].

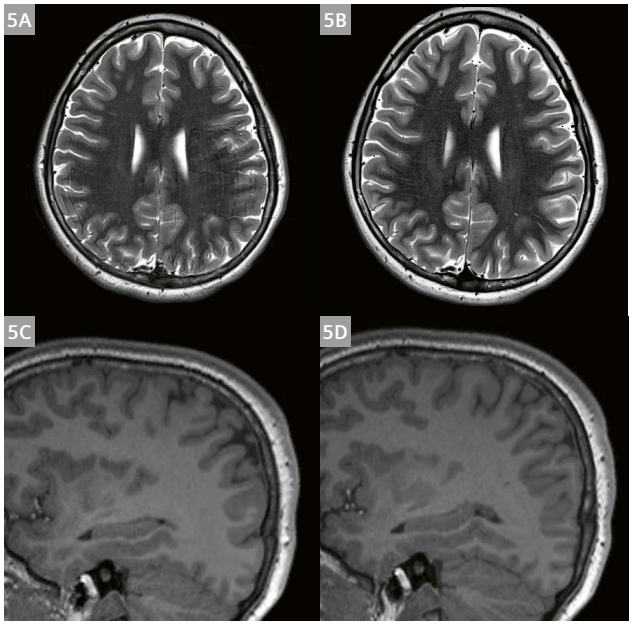

5 PMC in a 10-year-old patient with new onset generalized seizures obtained with the aid of MRI compatible video goggles. No abnormality was identified. **(5A)** T2-weighted image shows mild ringing which decreases image quality, while remaining borderline diagnostic. Repeat **(5B)** axial T2 image with PMC shows resolution of artifacts, allowing for better evaluation of the parenchyma. **(5C)** Sagittal MPRAGE shows overall good image quality although mild ringing artifact noted in the posterior parietal lobe. Repeat **(5D)** MPRAGE with PMC shows resolution of ringing artifact.

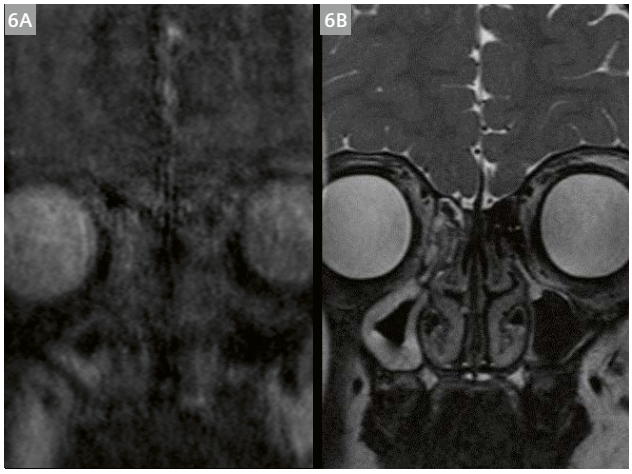

6 PMC in high-resolution cranial nerve imaging with T2 SPACE in a 5-year-old girl with poor sense of smell. **(6A)** Coronal reformat from T2 SPACE image through the anterior cranial fossa is non diagnostic. **(6B)** Coronal reformat from a repeat T2 SPACE acquisition with PMC shows substantial improvement and shows absence of the olfactory bulbs.

Cranial nerve imaging also relies on high-resolution sequences. At Boston Children's Hospital, we use a high-resolution 3D T2 SPACE or CISS sequences to outline cranial nerves or small lesions that are located at the interface of the parenchyma and cerebrospinal fluid. Despite routine utilization of targeted regions of interest (e.g., specific cranial nerves) the acquisitions often exceed 6 minutes and are frequently motion degraded. Since cranial nerves move rigidly with the skull, PMC works well to improve anatomic detail (Fig. 6). We are currently undergoing optimization of PMC for other high-resolution 2D spin-echo acquisitions used for imaging orbits, skull base, and skull.

A final niche application of PMC is to maximize the chances of obtaining diagnostic images after the administration of gadolinium-based contrast agents. Gadolinium-enhanced T1-weighted images are often obtained last on brain MRI protocols, to avoid the possible confounding effects of contrast (T1 shortening and the T2* effects) on other pulse sequences. Even compliant children can become restless during long scans and their ability to cooperate with crucial post-contrast images is often suboptimal. In recent years, there has been a growing concern regarding the long-term effects of gadolinium deposition in tissues, including the brain [16]. PMC can help obtain high-quality post-contrast images, ensuring that the administration of contrast serves its purpose and is not in vain. At Boston Children's Hospital we use T1-SPACE and occasionally T1-MPRAGE for our gadolinium-enhanced whole-brain imaging, both of which profit from PMC. Given that contrast-enhanced images are often obtained to monitor disease activity of serious conditions (tumors, infection, demyelination), improving image quality directly affects patient care.

Challenges

Despite a successful initial experience with the KinetiCor system several challenges remain to be addressed. PMC with KinetiCor is more effective in 3D-sequences; artifacts resulting from through-plane motion on 2D sequences remain a challenge, particularly when acquiring sequences in the coronal plane. The system is unable to correct non-rigid motion, which precludes utilization in the infra-hyoid neck, cranio-cervical junction, and spine. Another

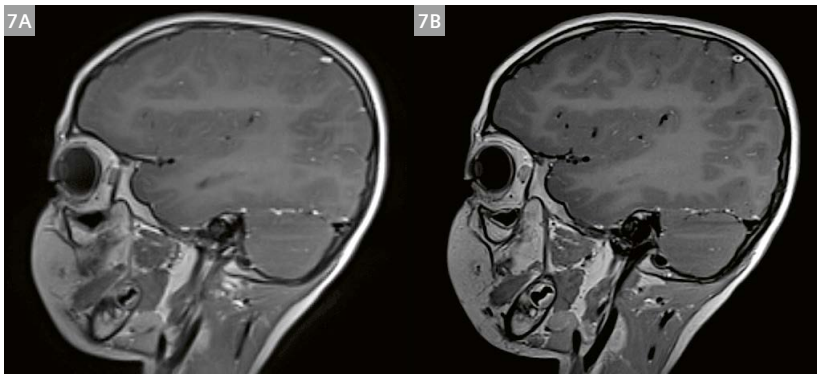

7 PMC in postcontrast sagittal T1 SPACE in a 10-year-old boy with concern for meningitis. No abnormal enhancement was seen. **(7A)** Sagittal T1 SPACE is of diagnostic quality and shows only mild motion artifact (subtle blurring and mild ringing). **(7B)** Repeat sagittal T1 SPACE with PMC shows resolution of ringing and blurring.

important limitation is that the skin marker is susceptible to skin motion and can result in spurious motion estimates that do not reflect true head motion. Improved filtering algorithms and markerless detection are under development, which are expected to mitigate or resolve this issue.

Conclusion

PMC is emerging as a promising technique to improve image quality in pediatric neuroradiology. In conjunction with child-life specialists, faster sequences, and audio-visual/behavioral techniques, PMC could contribute to decreasing the need for sedation and general anesthesia in vulnerable populations, including young children and those with cognitive disabilities who are unable to remain motionless during MR imaging acquisitions.

References

1 Robertson RL, Silk S, Ecklund K, et al. Imaging Optimization in Children. J Am Coll Radiol 2018;15:440-443.
2 Afacan O, Erem B, Roby DP, et al. Evaluation of motion and its effect on brain magnetic resonance image quality in children. Pediatr Radiol 2016;46:1728-1735.
3 Jaimes C, Gee MS. Strategies to minimize sedation in pediatric body magnetic resonance imaging. Pediatr Radiol 2016;46:916-927.
4 Jaimes C, Murcia DJ, Miguel K, et al. Identification of quality improvement areas in pediatric MRI from analysis of patient safety reports. Pediatr Radiol 2018;48:66-73.
5 Sanborn PA, Michna E, Zurakowski D, et al. Adverse cardiovascular and respiratory events during sedation of pediatric patients for imaging examinations. Radiology 2005;237:288-294.
6 Wilder RT, Flick RP, Sprung J, et al. Early exposure to anesthesia and learning disabilities in a population-based birth cohort. Anesthesiology 2009;110:796-804.
7 Creeley C, Dikranian K, Dissen G, et al. Propofol-induced apoptosis of neurones and oligodendrocytes in fetal and neonatal rhesus macaque brain. Br J Anaesth 2013;110 Suppl 1:i29-38.
8 Pediatric anesthesia and neurotoxicity: what the radiologist needs to know, PMID 28470388.
9 Vanderby SA, Babyn PS, Carter MW, et al. Effect of anesthesia and sedation on pediatric MR imaging patient flow. Radiology 2010;256:229-237.
10 Maclaren J, Herbst M, Speck O, et al. Prospective motion correction in brain imaging: a review. Magn Reson Med 2013;69:621-636.
11 Zaitsev M, Dold C, Sakas G, et al. Magnetic resonance imaging of freely moving objects: prospective real-time motion correction using an external optical motion tracking system. Neuroimage 2006;31:1038-1050.
12 Knickmeyer RC, Gouttard S, Kang C, et al. A structural MRI study of human brain development from birth to 2 years. J Neurosci 2008;28:12176-12182.
13 Reiss AL, Abrams MT, Singer HS, et al. Brain development, gender and IQ in children. A volumetric imaging study. Brain 1996;119 (Pt 5):1763-1774.
14 Stiles J, Jernigan TL. The basics of brain development. Neuropsychol Rev 2010;20:327-348.
15 Antonov NK, Ruzal-Shapiro CB, Morel KD, et al. Feed and Wrap MRI Technique in Infants. Clin Pediatr (Phila) 2017;56:1095-1103.
16 Knake S, Triantafyllou C, Wald LL, et al. 3T phased array MRI improves the presurgical evaluation in focal epilepsies: a prospective study. Neurology 2005;65:1026-1031.
17 Flood TF, Stence NV, Maloney JA, et al. Pediatric Brain: Repeated Exposure to Linear Gadolinium-based Contrast Material Is Associated with Increased Signal Intensity at Unenhanced T1-weighted MR Imaging. Radiology 2017;282:222-228.

Contact

Camilo Jaimes, M.D.
Instructor of Radiology
Harvard Medical School
Staff Neuroradiologist
Boston Children's Hospital
Camilo.jaimescobos@childrens.harvard.edu

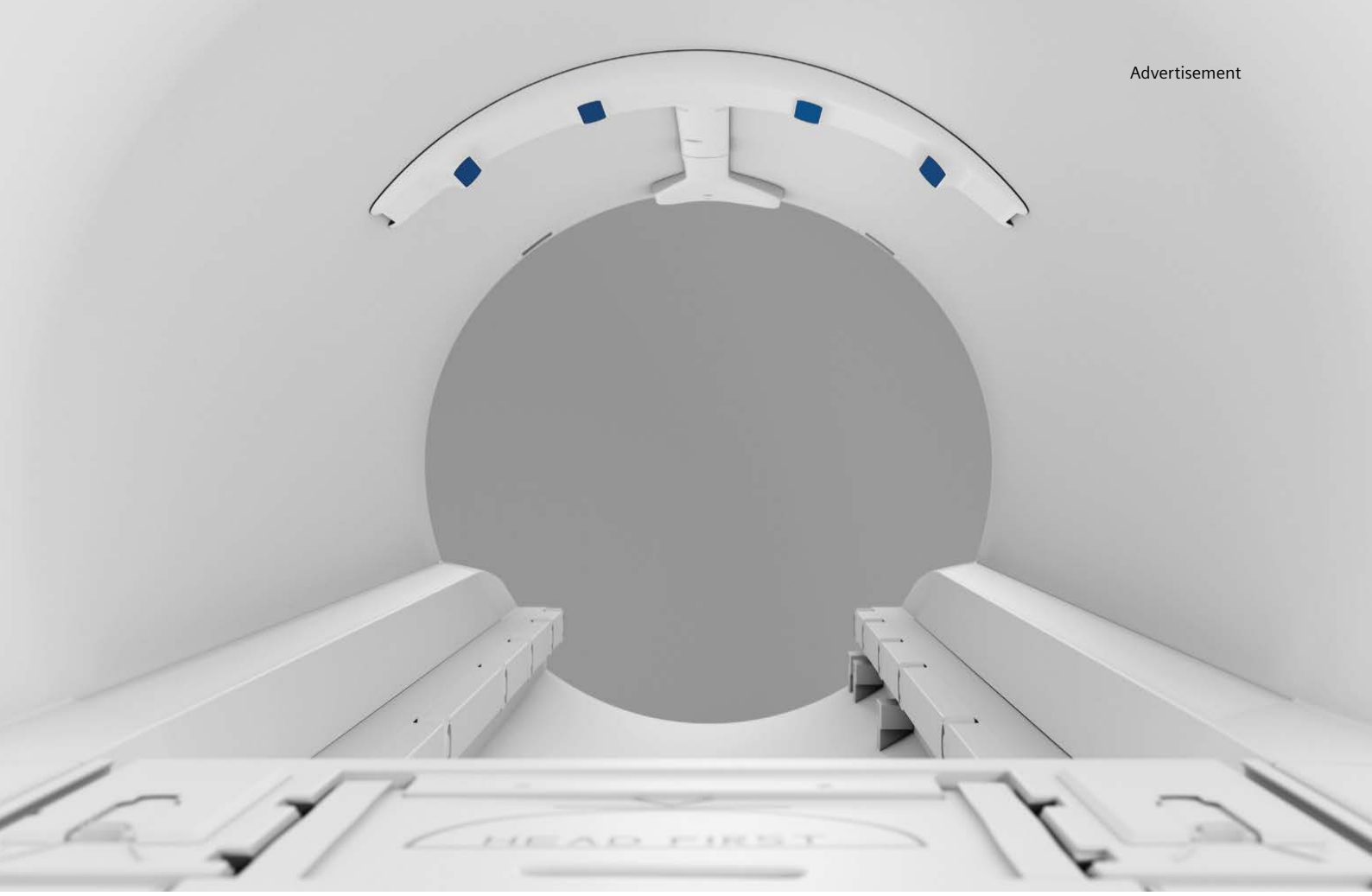

Bringing new clarity to imaging

Enhancing Imaging. Improving Care. Reducing Costs.

MR imaging is the gold standard for the imaging of most neurological diseases. However, being motionless throughout the exam is a challenge for many patients and almost impossible for some, such as the young and those with motor or cognitive challenges.

The BioMatrix Kinetic Sensor, jointly developed by Siemens Healthineers and KinetiCor, brings close-up patient monitoring and prospective motion correction to MR imaging. Mimimizing motion artifacts and enabling diagnostic imaging for all patients – to reduce the need for recalls, rescans and sedation.

Learn more at www.siemens-healthineers.com/biomatrix

Strategic Partner

KINETICOR
BIOMETRIC INTELLIGENCE

SIEMENS
Healthineers

Experience after One Year with MRgFUS

Marta Vidorreta, Ph.D.[1]; Miguel Fernández, MSc.[2]; Pablo D. Domínguez, M.D.[2]; Arantza Gorospe, M.D.[3]; Iciar Avilés-Olmos, M.D., Ph.D.[3]; María Cruz Rodríguez-Oroz, M.D., Ph.D.[3]; Jorge Guridi, M.D., Ph.D.[4]

[1]Siemens Healthineers, Madrid, Spain
[2]Department of Radiology, Clínica Universidad de Navarra, Pamplona, Spain
[3]Department of Neurology, Clínica Universidad de Navarra, Pamplona, Spain
[4]Department of Neurosurgery, Clínica Universidad de Navarra, Pamplona, Spain

Introduction

Essential tremor [1] is the most common neurological movement disorder. It causes involuntary and uncontrollable rhythmic shaking, most frequently in the hands, but other body parts can also be affected.

Severe tremor can seriously impair quality of life. It usually appears while doing everyday activities such as writing, eating or tying a shoelace – interfering with a patient's ability to live an independent and active lifestyle.

Essential tremor is a progressive disorder, and until very recently surgical treatment was the last resort when medication becomes ineffective. The preferred surgical method is Deep Brain Stimulation (DBS), in which electrodes are implanted into the target brain region and are controlled by a subcutaneous Implantable Pulse Generator (IPG) implanted at the subclavicular region. Albeit effective, this procedure requires extensive post-operative care, and incurs the risks of any open surgical procedure.

MR-guided Focused Ultrasound (MRgFUS) [2] is a novel, groundbreaking technology that allows incisionless surgery. Insightec's Exablate Neuro™ (Insightec, Tirat Carmel, Israel)[1] (Fig. 1) uses up to 1024 High-Intensity

[1] *The information shown herein refers to products of 3rd party manufacturers and thus are in their regulatory responsibility. Please contact the 3rd party manufacturer for further information.*

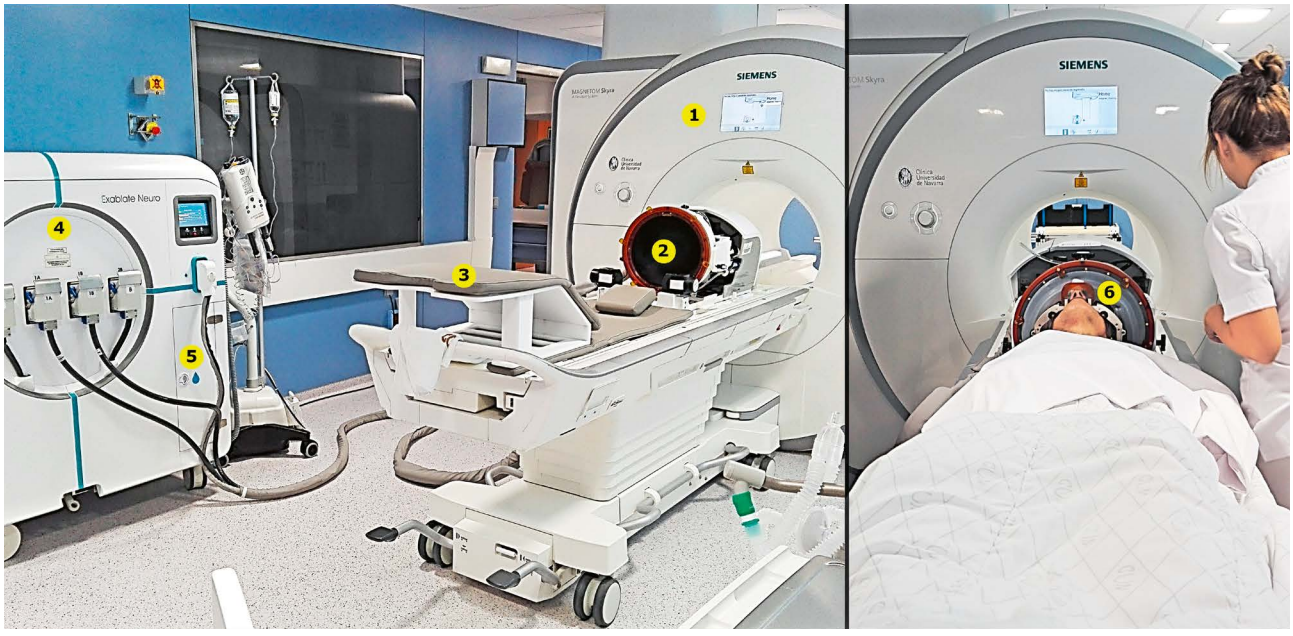

1 **MRgFUS setup**
In the MR room, MRgFUS treatment requires: **(1)** The MRI system, **(2)** the HIFU transducer helmet with its positioning system, **(3)** the patient's leg positioner, **(4)** the Exablate Neuro frontend cabinet, containing the power amplifiers that drive the transducer, **(5)** the water system cabinet that provides degassed, cold water at 15 °C, to serve as interface between the patient's head and the transducer, and **(6)** the silicon membrane that seals the transducer and permits water filling. Additional elements outside the MR room are the Exablate Neuro console, from which the neurosurgeon operates the procedure, and the equipment cabinet, containing the control PC and other electronics.

Focused Ultrasound waves (HIFU waves) to heat and precisely ablate the target spot with no surgical incisions or burr holes. Integration with the MRI system allows precise, patient-specific treatment planning and real-time monitoring. Moreover, MR temperature mapping is essential for careful temperature control of the target spot. At first the target area is heated gently, remaining below the 55–60 °C threshold that would produce irreversible effects, allowing a neurologist to evaluate patient response including tremor relief and potential side effects. This information is used by the treating physician to perform adjustments if necessary. Once the target is confirmed, the heating is gradually increased to create a highly accurate and controllable lesion. As a result, most patients experience immediate reduction of tremor with minimal complications.

Pre-treatment protocol

Patients diagnosed with severe essential tremor, which is incapacitating and resistant to medication, may be candidates for DBS or MRgFUS treatment. Depending on age and the physical state of the patient, MRgFUS may be recommended over DBS. As in any MRI scan, contraindications to MRgFUS include:

- Claustrophobia
- Inability to lie still for a long time
- Presence of non-MRI-compatible metallic/electronic objects in body

Subjects must also undergo a high-resolution head CT-scan prior to the procedure, to estimate their skull density ratio (SDR), defined as the averaged ratio between the skull's cancellous and cortical bones mean Hounsfield units. Patients with very low SDR scores, as determined by the Exablate Neuro's algorithm, are not suitable for MRgFUS, as the energy required to complete a successful treatment would be too high for existing safety standards.

Cardiovascular diseases must also be considered before recommending MRgFUS, as it can cause deep vein thrombosis due to the long immobilization time, and carries other CV risks.

A pre-treatment MRI scan is always performed to discard other neurological diseases and plan the MRgFUS ablation target. The MRI scan is done in our 3T intra-operative MAGNETOM Skyra (Siemens Healthcare, Erlangen, Germany), software version *syngo* MR E11C-AP03, with 32-channel head coil. The imaging protocol includes a high-resolution T1 MPRAGE, T2 FLAIR, T2 SPACE, and a DTI scan.

In essential tremor, the target spot is the Ventralis Intermidius Thalamic (Vim) nucleus, located in the hemisphere contralateral to the affected body part.

Vim planning can be performed on the T1 or T2 anatomical MR images, following these steps [3]:

- Find the intercommisural plane, i.e. the axial plane including both the anterior commissure (AC) and posterior commissure (PC)
- Draw the midline, and calculate the AC-PC distance, i.e. the length of the third ventricle
- Locate the Vim starting from the PC, measuring 25% of this distance in the anterior direction, 14–17 mm lateral from the midline, and 0–2 mm above the intercommissural plane

In our center, the Vim location calculation also uses information from the DTI scan [4]. The neuroradiologist processes this data at the *syngo*.via station and extracts the dentato-rubro-thalamic and cortico-thalamic tracts, which connect the motor centers from cerebellum and cortex, through the Vim nucleus in the thalamus. The tract information is fused with the anatomical image, to visualize the tract crossing at the AC-PC plane (Fig. 2). The final target is selected by the neurosurgeon based on all this information.

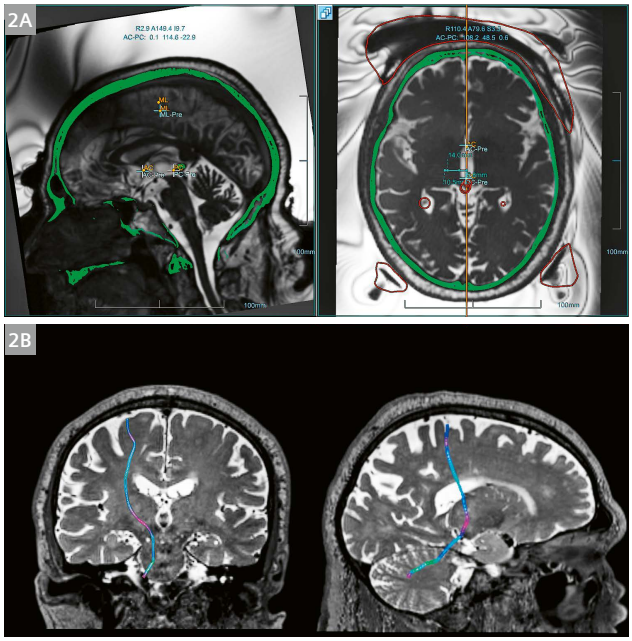

2 Target planning
Target planning is performed at the Exablate Neuro console, after the CISS sequence is acquired **(2A)**. The anterior and posterior commissures (AC and PC) are located on the sagittal and axial views, and the image is reformatted to the AC-PC plane. The Vim area is then identified 25% anterior to the PC and typically 14 mm lateral from the midline [3], although the third-ventricle wall can also be used as reference. If information about the crossing of the dentato-rubro-thalamic tract on the AC-PC plane is available, it can help refine the target location. The coronal and sagittal projections of the tract **(2B)** are extracted from pre-scan DTI data and postprocessed using *syngo*.via's Neuro 3D workflow. The tract can be exported as a DICOM series to be used at the time of planning.

Treatment day

Patients must be fully awake and responsive during treatment. Before starting, the only medications that may be administered are corticosteroids (dexamethasone), as a preventive measure, and analgesics in case of reported back pain or headache.

MRgFUS is a multi-departmental activity. On the day of treatment, the first thing to be done is the Daily Quality Assurance (DQA) scan at our 3T MAGNETOM Skyra. Communication between the MR and Exablate Neuro's console (Model Exablate 4000 Type 1.1, software version 7.2) is performed through the Access-i remote control feature, which allows the MR system to be operated from another client.

The DQA scan is performed on a special DQA phantom gel provided by Insightec. This checks that all functionalities are running smoothly (B_1 calibration, geometric alignment, temperature control, steering verification and cavitation control). The DQA protocol lasts about 15 minutes and is always performed by one of our team MR techs, trained and certified by Insightec's neuro application specialists.

Once the DQA is completed successfully, patient preparation begins. The scalp is shaved to prevent trapping of air that could absorb heat during treatment, causing skin burns. Then the neurosurgeon places the stereotactic frame on the patient's head. Compression stockings are recommended to reduce the chances of deep vein thrombosis. Finally, a silicon membrane is placed on the head. This seals the transducer, which is then filled with cold water at 15 °C, preventing skin damage during high-energy sonications. In between imaging and sonications this water is constantly circulating to keep the temperature low.

Once the patient is lying on the MR table, the frame is attached to the transducer to ensure no head motion during treatment.

Before starting the procedure, the anesthesiology team ensures that vital signs will be monitored at all times. Their main goal is to control potential symptoms. To this end, an intravenous line is placed in the non-treated arm in case medication needs to be administered during treatment. The most commonly used medications are:

- Antiemetics, if nausea is reported by the patient
- Steroids, to prevent and control edema
- Opioids, occasionally, for pain management
- Dexmedetomidine, an optional sedative administered always in low doses to perform Monitored Anesthesia Care (MAC) to manage anxiety

Prior to treatment, the patient's CT scan is loaded onto the Exablate Neuro's console. The neuroradiologist tags all air sinuses and calcifications as "no-pass" regions, as they can dissipate and deflect energy. The tagged CT scan will later be fused with the intra-operative MR images, using Exablate's semi-automatic registration method (Fig. 3). As a safety measure, transducer elements with orientations that cross the no-pass regions are automatically detected and switched off.

The complete MR procedure is carried out using the Tx-Rx body coil, as the Exablate Neuro transducer does not currently allow for a dedicated receive coil. After careful shimming and B_1 calibration, the planning scan is acquired using a 3D CISS sequence with the following parameters:

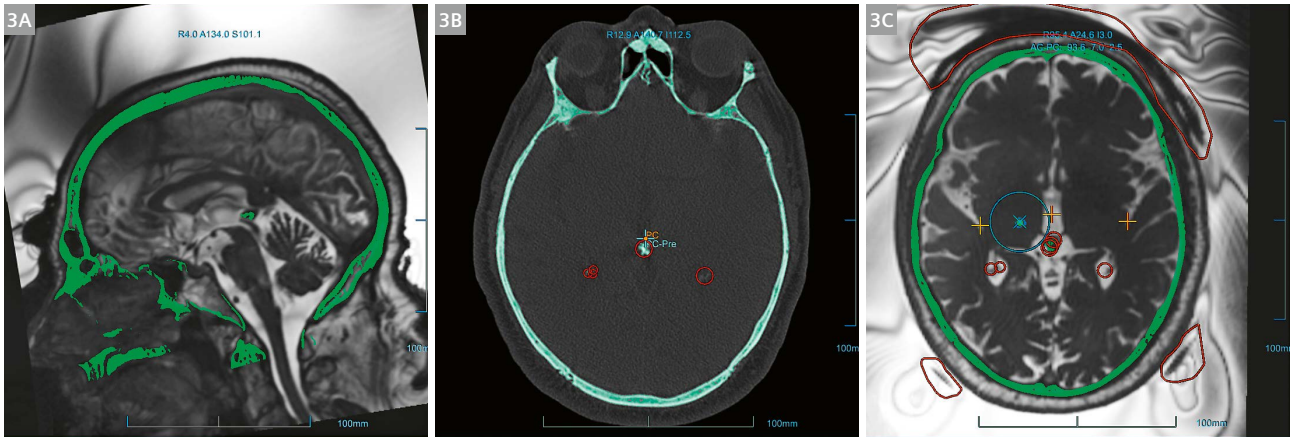

3 **Additional pre-planning steps**
Before proceeding to target planning, the CT and MRI scans must be fused **(3A).** This is performed using Insightec's semi-automatic method, and the result is always verified and corrected if necessary by the neurosurgeon. Calcium spots must be marked on the CT scan as "no-pass" regions **(3B)**, as they can dissipate and deflect energy. Membrane folds must be marked as they can contain trapped air bubbles **(3C)**. Motion trackers (orange crosses in 3C) are also placed throughout the brain at high-contrast interface areas to detect patient movement during treatment.

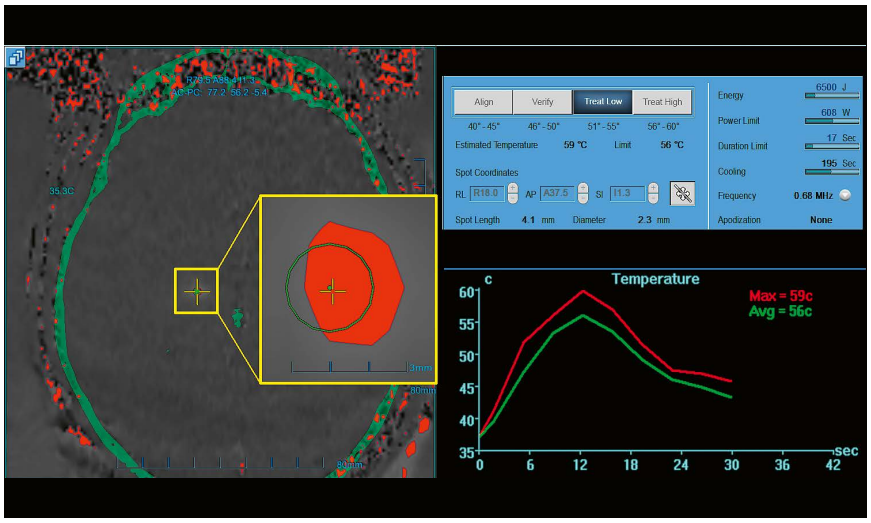

4 Sonication control
There are four sonication modes to choose from during a MRgFUS treatment: **Align** (40–45 °C), **Verify** (46–50 °C), **Treat-low** (51–55 °C) and **Treat-high** (56–60 °C). The total energy, maximum power and maximum duration of a sonication can be chosen by the neurosurgeon. Sonication stops automatically if the maximum temperature (determined by the chosen mode) is reached before the total energy is delivered. Real-time mean and maximum temperature graphs at the target spot are displayed for evaluation. After each sonication, there is a cooling pause of variable length, depending on the total energy applied.

TE/TR 2.4/5.6 ms, BW 300 Hz/px, FA 35–40°, FOV 240 x 240 mm², matrix 218 x 256, 144 sagittal slices, 1.35 mm slice thickness, 22%/50% slice/phase oversampling, slab-selective excitation, TA 8.5 min. MR frequency adjustment, critical to minimize imaging and thermal shifts, is also controlled in the Exablate's console.

The next steps are CISS image reformatting, MR-CT fusion, MR image screening of membrane folds (which also need to be avoided by the HIFU waves), motion tracker placement and target spot location. Once these are done, the transducer position is manually updated to bring the target center coordinates to the magnet's isocenter in order to minimize distortions.

At least four sonications are needed to complete a MRgFUS treatment (Fig. 4):

- **Align:** 40–45 °C sonication for target location
- **Verify:** 46–50 °C sonication for target localization and shape verification
- **Treat-low:** 51–55 °C sonication for clinical evaluation of the patient response to the stimulated target
- **Treat-high:** 56–60 °C sonication for permanent target ablation

In between each sonication there is a cooling pause of variable length. A specialized neurologist assesses the patient during these breaks, right at the bore of the MR, to ensure the effectiveness of the treatment. For instance, the patient may be asked to lift the affected limb and keep it still, write their name on a piece of paper, or mimic a drinking movement. Potential adverse effects, such as other limbs' numbness, are closely monitored. In case of side effects or insufficient clinical response, the target may be relocated and the sonication chain repeated.

Real-time temperature monitoring is carried out during each sonication by MR thermometry (Fig. 4). MR temperature maps are acquired with a time resolution of 3.5 s by means of a 2D FLASH phase image, with the following parameters: TE/TR 12.7/27.1 ms, BW 44 Hz/px, FA 30°, FOV 280 x 280 mm², matrix 128 x 256, 1 mm slice thickness. Real-time mean and maximum temperature graphs at the target spot are displayed at the Exablate's console for evaluation.

The desired power, duration and total energy delivered during a sonication can be freely chosen by the neurosurgeon. Each of the four sonication modes has a maximum threshold temperature, and real-time MR thermal mapping ensures that the sonication is automatically stopped if this temperature is reached before the total energy is delivered.

The whole treatment can last between 2 and 3 hours, depending on many factors including the patient's skull density score, the duration of the cooling pauses, and the number of sonications needed for successful treatment.

Post-treatment evaluation

A post-treatment MRI scan is always performed immediately after completing the HIFU procedure. This is done to evaluate lesion location and volume, before post-procedural symptoms appear as a result of the disrupted blood-brain barrier. Increased edema and petechial hemorrhage around the lesion area are common transitory symptoms that appear a few hours after treatment and gradually disappear in the following weeks [5].

The water is emptied from the system, the plastic membrane and stereotactic frame are removed from the patient, and the Exablate's transducer is replaced by the

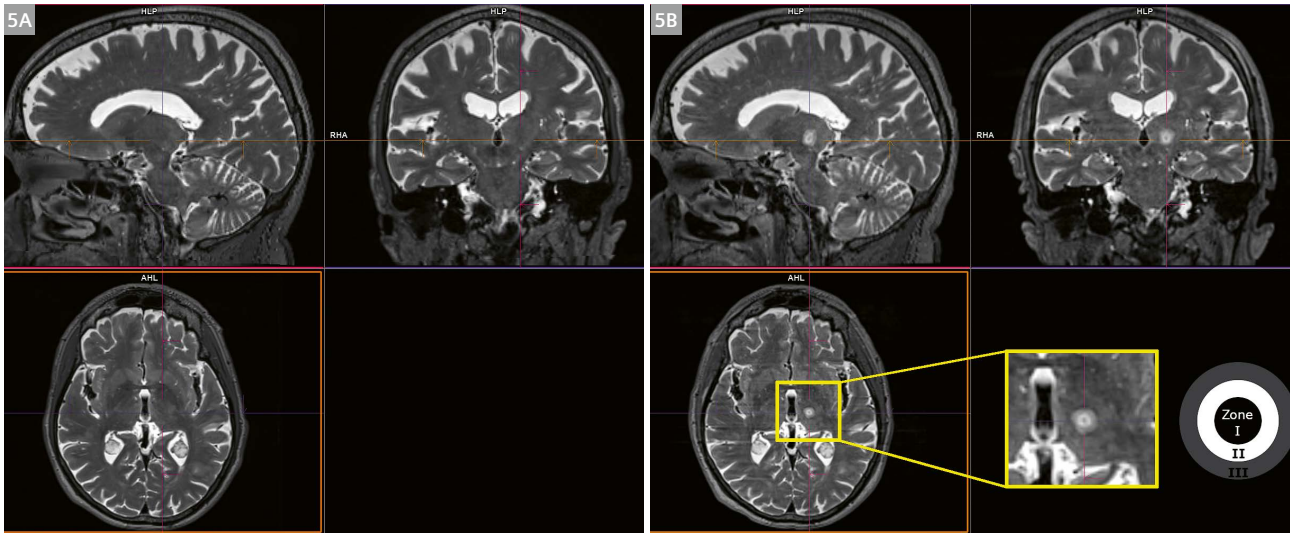

5 **Lesion evaluation**
T2-weighted SPACE images obtained from a representative patient pre- **(5A)** and 30 minutes post- MRgFUS treatment **(5B)**. Note the three concentric regions that appear in the treated hemisphere at the target spot, each with a distinct T2 contrast. The inner, hypointense region represents zone I, indicating necrosis; the mid, hyperintense region represents zone II, indicating cytotoxic edema; and the outer, mid-intense concentric region is zone III, and indicates the area of vasogenic edema [4].

32-channel coil on the MR table. Then the patient gets back in the scanner for approximately 30 minutes. As in the pre-treatment scan, the post-treatment examination consists of an anatomical 3D T1 MPRAGE, a 3D T2 SPACE, 2D T2 TSE, SWI, and a DTI scan.

The T2-weighted images are key to evaluate the extent of the lesion (Fig. 5). Typically, the lesion will show a circular shape of 3–6 mm diameter. We can distinguish up to three concentric zones in the T2 images [5]:

- **Zone I, necrotic:** the inner, T2 hypointense region shows the necrotic core
- **Zone II, cytotoxic:** the mid, T2 hyperintense region is cytotoxic edema
- **Zone III, vasogenic:** the outer, moderately T2 hyperintense ring shows the vasogenic portion of the edema

The lesion will extend through zones I and II, as cytotoxic edema is a premorbid cellular process, and thus irreversible. This process is confirmed in the diffusion scan, as cytotoxic edema causes increased restricted diffusion on MRI due to the cellular swelling and extracellular volume reduction.

Most patients stay overnight for further observation and are discharged the next day after receiving positive clinical evaluation from both the neurology and neurosurgery teams.

Personal experience

Looking back, we are proud to be the first institution worldwide to start treating patients with a Siemens Healthineers MRI scanner compatible with Exablate Neuro. This highly precise, minimally invasive treatment presents a great opportunity to improve many people's quality of life. As proof we have performed over 100 MRgFUS treatments within a year, with highly satisfactory results in most cases, and only a small percentage of patients with procedure-related complications, mostly transient.

Evolving from traditional surgery methods to MR-guided therapy was a challenge that we are happy to have successfully overcome as a team. During the first few procedures, Insightec's application specialists were with us on site, as well as our local Siemens Healthineers MR clinical scientist, to provide support.

Our close relationship with both Insightec and Siemens Healthineers allows us to solve any arising issues quickly, and we have now formed an effective multidisciplinary team that can perform much shorter, faster and safer procedures.

Future directions

Although essential tremor patients are the largest target group for this kind of therapies, MRgFUS is not limited to this condition. We will soon start treating Parkinson's disease tremor by targeting the subthalamic nucleus (STN).

The STN is proven as a beneficial therapeutic target [6], although its use for MRgFUS poses a challenge as it is difficult to reliably image even with 3T MRI. Other targets, including the internal globus pallidus, will also be explored.

Acknowledgments

MRgFUS is a multidisciplinary effort, and our treatments required a tight collaboration between the neurosurgeon and neurologist. But it could not be completed without the cooperation of the MR tech team, who were specifically trained for this procedure, the engineer on site, and the valuable contribution of the anesthesiologists Dr. Cristina Honorato and Dr. Antonio Martínez-Simón, who ensured the patient's well-being throughout the whole time.

We also thank the Insightec neuro apps team, led by Paul Wragg in Europe, for their valuable help during the training process.

References

1 Zesiewicz TA, Chari A, Jahan I, et al. Overview of essential tremor. Neuropsychiatr Dis Treat. 2010;6:401-408.
2 Lipsman N, Schawartz M, Huang Y, et al. A MR-guided focused ultrasound thalamotomy for essential tremor; A proof of concept study. Lancet Neurol. 2013;12:462-468.
3 Moser D, Zadicario E, Schiff G et al. MR-guided focused ultrasound technique in functional neurosurgery: targetic accuracy. J Ther Ultrasound. 2013;1:17.
4 Ezponda et al. Mapping the cortical connections of the ventral intermediate nucleus (VIM) with tractography in patients undergoing MRI-guided intensity focused ultrasound (HIFU) thalamotomy. RSNA. 2019;19008221.
5 Wintermark M, Druzgal DS, Huss MA et al. Imaging findings in MR imaging-guided focused ultrasound treatment for patients with essential tremor. Am J Neuroradiol. 2014;35:891-896.
6 Magara A, Bühler R, Moser D, et al. First experience with MR-guided focused ultrasound in the treatment of Parkinson's Disease. J Ther Ultrasound. 2014;2:11.

Contact

Jorge Guridi, M.D., Ph.D.
Head of the Neurosurgery Department
Clínica Universidad de Navarra
Avda. Pío XII, 36
31008 Pamplona (Navarra), Spain
+34 948 255 400
jguridi@unav.es

Application of Magnetic Resonance Fingerprinting in Epilepsy

Siyuan Hu[1]; Joon Yul Choi[4]; Debra McGivney[1]; Stephen Jones[3]; Imad Najm[4]; Mark Griswold[2]; Irene Wang[4]; Dan Ma[1]

[1]Biomedical Engineering, Case Western Reserve University, Cleveland, OH, USA
[2]Radiology, Case Western Reserve University, Cleveland, OH, USA
[3]Imaging Institute, Cleveland Clinic, Cleveland, OH, USA
[4]Epilepsy Center, Cleveland Clinic, Cleveland, OH, USA

Introduction

Afflicting 3.4 million patients, epilepsy is one of the most common neurological diseases in the US [1]. Presurgical evaluation of epilepsy strongly relies on diagnostic magnetic resonance imaging (MRI) for accurate identification of epileptogenic lesions. In particular, it is crucial to visualize and detect subtle lesions such as small focal cortical dysplasias (FCDs). The diagnosis of mesial temporal lobe epilepsy (MTLE) benefits from precise evaluation of the hippocampal volume and contrast for detection of hippocampal sclerosis (HS). In cases where multifocal and widespread lesions exist, such as periventricular nodular heterotopias (PVN) and tuberous sclerosis complexes (TSC) [2], characterization of each lesion also provides helpful information for surgical planning. However, there is much room for improvement for the routine MRI scans currently implemented in most clinical settings to reach the above expectations [3]. Over the past year, several studies have proposed magnetic resonance fingerprinting (MRF) as an alternative imaging method. This quantitative MR imaging technique has shown promising efficacy to provide additional, clinically relevant information as compared to conventional MRI for patients with epilepsy [4–6].

Here we present a review of previous studies on the application of MRF in epilepsy. Discussion will first start with conventional MRI methods as well as the challenges of these methods in epilepsy. Then we will briefly introduce the basic concept and implementation of MRF, followed by an explanation of its benefits and advantages compared to standard MRI protocol. Lastly, improvements of epilepsy diagnosis by using MRF will be described in sections for FCD, PVN/TSC, and MTLE.

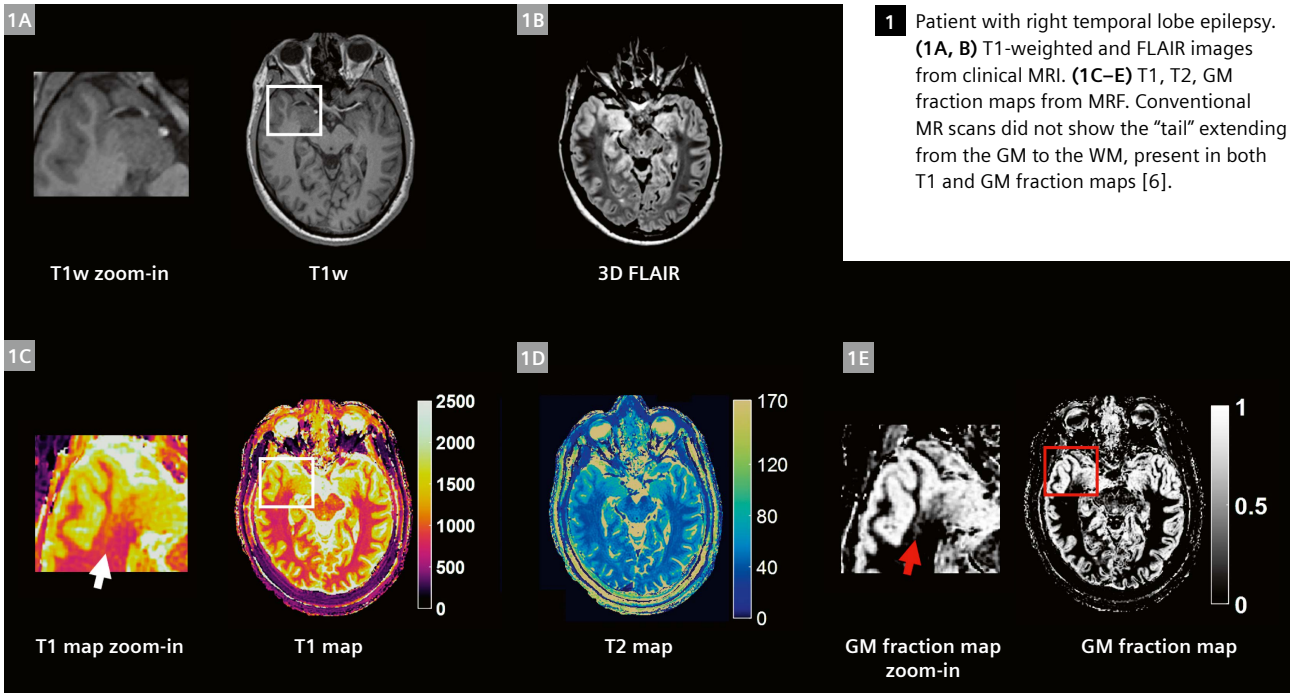

1 Patient with right temporal lobe epilepsy. **(1A, B)** T1-weighted and FLAIR images from clinical MRI. **(1C–E)** T1, T2, GM fraction maps from MRF. Conventional MR scans did not show the "tail" extending from the GM to the WM, present in both T1 and GM fraction maps [6].

Challenges of conventional MRI methods

MR imaging for epilepsy can be challenging and time consuming. Firstly, the structural and morphological changes of epileptogenic lesions can be as subtle as in the scale of millimeters, and these lesions can occur in any cerebral lobe or spread across different lobes. This requires the epilepsy MRI protocol to have high image resolution (submillimeter) and whole brain coverage. Secondly, for detection of subtle lesions, images with multiple contrasts are typically acquired. A typical epilepsy MRI protocol consists of multiple scans running a series of multislice imaging sequences, including fluid-attenuated inversion recovery (FLAIR), T1- and T2-weighted imaging [7], which altogether usually takes more than half an hour.

More importantly, conventional MR scans generate qualitative images, in which visualization of tissue abnormalities is highly dependent on image contrast. Take the T1- and T2-weighted images for example, these two contrasts are mostly but not completely governed by T1 or T2 values. As a result, signal intensities and contrasts of MR images are the product of mixture of multiple underlying tissue properties, which could cancel out contrast signatures and obscure lesion features in images. This may explain why some subtle FCD and HS lesions were not detectable by conventional MRI. The qualitative nature also confines its abilities in multicenter/longitudinal studies, since signal contrast may vary due to the type and setup of scanners. In the case of multifocal lesions such as PVN and TSC, although conventional MRI could visualize them well, it is not capable of recognizing which one of the lesions is the most relevant to the epilepsy. Additionally, diagnosis of lesions based on qualitative MRI adopts comparative strategies; thus the accuracy of such approach strongly depends on the expertise of the reviewing neuroradiologist. For example, routine MRI examines bilateral MTLE by comparing volume and signal of both hippocampi, assuming that the contralateral hippocampus is healthy. Erroneous conclusions are likely made for patients with bilateral volume loss/signal changes, and patients with subtle unilateral signal variations [4].

Quantitative MRI, by providing tissue property maps such as T1, T2 maps, could inherently detect subtle tissue changes with enhanced sensitivity and specificity. Quantitative maps depict pure tissue properties, which avoids mixing of contrast as in the case of weighted signals and helps clearly present lesion signatures. Since absolute values are measured, the resulting maps are immune to the impact of variations in scanner setup. These advantages make the T1 and T2 maps more reliable and objective for clinical diagnosis, as compared to the weighted images. Previous studies have shown both T1 and T2 values of epileptogenic foci are longer than in healthy tissue controls, which is relevant to cytological abnormalities, gliosis and neuronal cell loss [8–10].

Despite its advantages, conventional quantitative MRI is rarely adopted in a clincial setting, due to its great consumption of time, low spatial resolution and low robustness.

MR Fingerprinting scan

As a state-of-the-art quantitative MR imaging method, MRF provides multiple tissue property maps from a single scan within clinical tolerable time. The underlying concept of MRF is that different tissues could generate unique signal evolutions under appropriate data acquisition schemes, which are achieved by pseudo-randomly varying acquisition parameters. By incorporating possible tissue property values, a dictionary containing all foreseeable signal evolutions is constructed, signals from each pixel can be assigned to an entry of the dictionary by signal pattern recognition. This scenario is analogous to matching unique human fingerprints with existing records, in order to retrieve information from a database. Similarly, once an entry of signal vectors is selected, information such as tissue types, T1 and T2 values in a pixel could be retrieved from the dictionary altogether [11].

MRF yields many benefits allowing it to overcome limitations in clinical applications. For example, results of MRF are highly repeatable and reproducible in human brain imaging [12]. Although signal fingerprints could be influenced by imperfections in scanning systems, the processing algorithms could account and compensate for it during dictionary construction. T1 and T2 relaxation times measured by MRF using different scanners are consistent, especially for solid compartments of brain [12]. Another significant advantage of MRF is its ability to fully extract multiple tissue property values from one scan within clinically feasible time [11]. This process is highly efficient, as it substantially shortens scanning time while examining more tissue parameters than traditional quantitative imaging methods. These quantitative maps can also be used to synthesize clinical standard MR images, such as T1-weighted, T2-weighted and FLAIR, without additional scan time.

Moreover, maps are perfectly coregistered, which facilitates multiparametric analysis of tissue maps. Comprehensive analysis across multiple of MR parameters could expose complex morphological tissue changes with increased sensitivity and specificity in previous studies. For example, T1 and T2 maps generated from MRF was reported to distinguish different types of intra-axial brain tumors [13]. In prostate cancer applications, multiparametric analysis combining T1, T2 maps and apparent diffusion coefficient (ADC) mapping has been proven to differentiate normal peripheral zone from transition zone [14, 15].

MRF is robust in rejecting acquisition and motion errors due to its pattern matching algorithm. Acquisition and reconstruction artifacts are suppressed in MRF images due to spatial and temporal incoherence between measurement errors and predicted signals. Images obtained from a motion-corrupted scan with random motion happened during the last ¼ of the scan time demonstrate almost the same quality and anatomical structure as motion-free images [11]. Advanced image reconstruction algorithms, such as Motion insensitive MRF (MORF)[1] is able to recover maps while tolerating 54% of motion corruption in data [16]. Besides, strategies have been developed in many aspects to further avoid image and map corruption of MRF with reduced scan time, such as incorporating more efficient sequences [17–19], and advanced reconstruction algorithms before pattern matching [20, 21].

MRF in epilepsy

In a number of studies, MRF scans and conventional MR images were reviewed separately and independently for diagnosis of different types of epileptogenic lesions. These studies provided encouraging data that MRF could provide additional findings in detection and characterization of epileptogenic lesions, assisting presurgical evaluation.

Focal cortical dysplasia (FCD)

MRF was shown to be able to reveal subtle FCD lesions that were not obvious when reviewing clinical MR scans. Since T1 and T2 maps particularly reflect cell structure, myelin/water content and microenvironment, they are in principle more sensitive to tissue malformation than the weighted

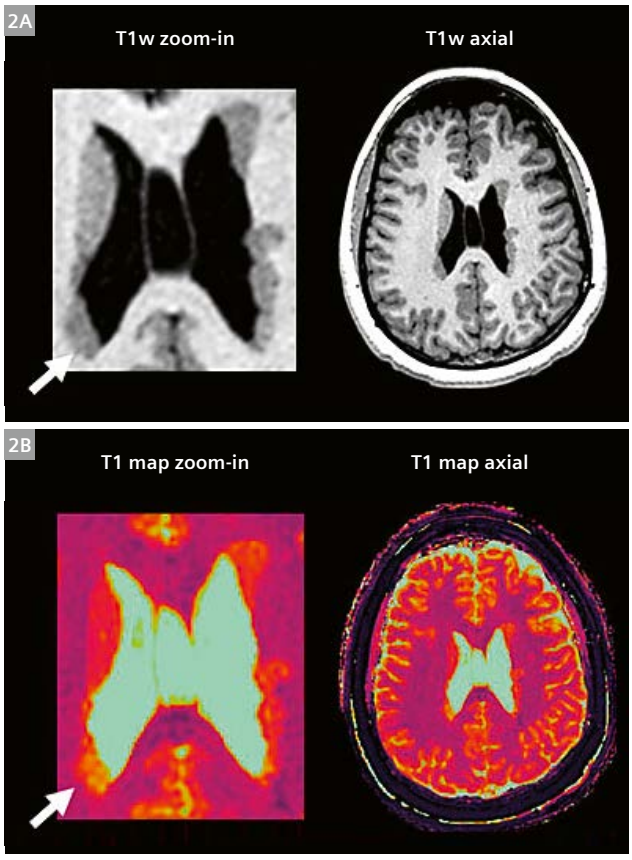

2 Patient with bilateral PVN. **(2A)** Axial T1-weighted image from the conventional scan. **(2B)** T1 map from MRF. T1 map showed increased values of the nodules at the right occipital horn, where signal intensity was uniform among all the nodules on the T1-weighted scan [6].

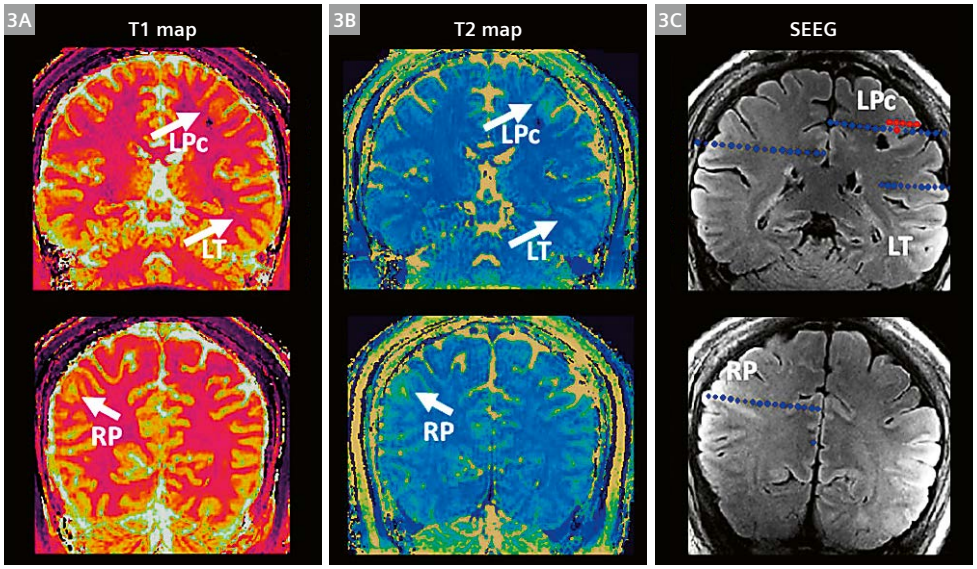

3 Patient with multiple TSC tubers (three lesions shown). **(3A, B)** T1 and T2 maps from MRF. **(3C)** Invasive stereo-EEG electrode locations (blue spheres) shown on T2-weighted FLAIR image, with red spheres showing ictal onset. Characterization from T1 and T2 maps were consistent with the invasive evaluation results of the three lesion areas [6].

[1] *Work in progress: the application is currently under development and is not for sale in the U.S. and in other countries. Its future availability cannot be ensured.*

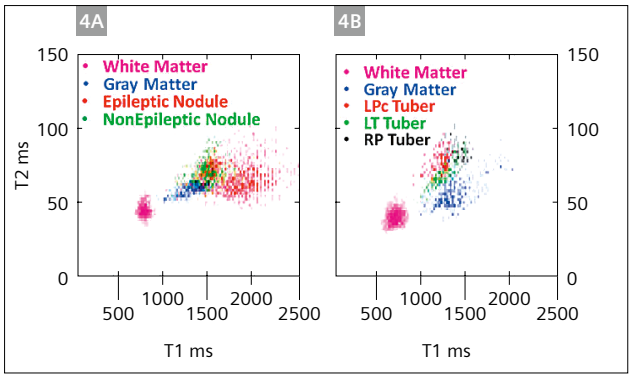

4 ROI analysis of **(4A)** the PVN patient in Figure 2 and **(4B)** the TSC patient in Figure 3. Lesions, normal gray matter and normal white matter form distinct clusters [6].

measures provided by clinical MRI [6]. Also, GM and WM fraction maps which segment brain tissue structures are useful in lesion detection at the GM/WM boundary.

Figure 1 illustrated an examplary patient with right temporal lobe epilepsy [6]. Conventional MRI (Fig. 1A, B) showed hyperintensity of the right amygdala in the FLAIR scan, and no noticeable abnormalities in the temporal lobes otherwise. MRF maps (Figs. 1C–E) visualized an additional tail-like tissue alternation on the right temporal lobe besides the amygdala hyperintensity. This "tail" had an increased T1 value and higher GM fraction implying a potential epileptic abnormality. Subsequent interictal and ictal EEG monitoring was consistent with the location of the abnormality. Resective surgery completely included the abnormality. Histopathology revealed mild malformation of cortical development. The patient remained seizure-free after surgery.

Periventricular nodular heterotopias (PVN)/ tuberous sclerosis complexes (TSC)

For multifocal lesions such as PVN and TSC, clinical MRI scans were able to map their distribution and boundaries, but no signal differences manifested to distinguish one lesion from another. Through multiparametric quantitative ROI analyses, quantitative T1 and T2 maps from MRF could enable the characterization of these lesions [6]. This was illustrated in Figure 2, which showed a patient diagnosed with bilateral PVN. T1 map highlighted an extraordinary increase of T1 value from the nodules at the right occipital horn, which exhibited little signal differences with other heterotopias on conventional T1-weighted scan. The ROI analysis (Fig. 4A) demonstrated a significant shift of T1 values in the right occipital horn as compared to the left-sided nonepileptic nodules. This patient underwent stereo-EEG (SEEG) monitoring to verify the epileptogenic zone, and the separation of lesion clusters was concordant with their individual epileptogenicity [6].

Figure 3 was an example of a patient with three TSC lesions, located in the left precentral (LPc), right parietal (RP) and left temporal (LT) lobes of the brain respectively. MRF maps indicated variations of quantitative T1 and T2 values among these TSC lesions. In the ROI analysis (Fig. 4B), the LPc tuber formed a distinct cluster with a significantly different T2 value from the other clusters. The following SEEG evaluation targeting all the tubers proved the highest epileptogenicity was indeed from the LPc tuber.

Mesial temporal lobe epilepsy (MTLE)

Accuracy of MTLE diagnosis could be further improved by MRF through quantitative comparison of T1 and T2 values in the hippocampus between patients and healthy controls. HS lesions showed higher values of both T1 and T2 than normal contralateral hippocampus and healthy control groups [4]. For unilateral MTLE patients who received negative MRI results on conventional scans (due to the very subtle T1/T2 signal changes in the HS lesions), MRF maps were sensitive and effective in detecting such tiny differences via statistical analysis. MRF also facilitated quantitative comparison among both sides of hippocampus and healthy controls, which reduced incorrect diagnosis of bilateral HS as unilateral and elevated diagnosis rate of MTLE from 69.7% to 96.9% [4].

Table 1 listed the statistics of average T1 and T2 values for unilateral MTLE patient group and healthy control group. Tissue properties of atrophic hippocampus were compared against both healthy controls and the contralateral regions. Mean T1 and T2 values of HS lesions were at least one standard deviation higher than the other two reference groups, which confirmed the existence of unilateral HS. No difference was seen between contralateral hippocampus regions and healthy controls.

Figure 5 illustrated the clinical images and MRF maps in coronal and axial views from a patient with bilateral HS. While lesion signatures were vague on conventional scans, MRF demonstrated significantly higher T1 and T2 values of the hippocampi on both sides, as compared to healthy controls, which supported the diagnosis of this patient as bilateral HS. In this case, the quantitative nature of MRF allowed for lesion recognition in MTLE, independent of the condition (normal or pathologic) of the contralateral side, which had been impossible with conventional MRI [4].

Besides diagnosis purposes, MRF was also useful in investigating the structural changes outside of the hippocampus caused by MTLE, such as temporal lobe white matter. Longer T2 values were detected in temporopolar white matter and temporal stem on both sides of unilateral MTLE-HS patients, but only ipsilateral white matter had higher T1 value [5]. This finding might extend our understandings of the pathology, neuronal malformation, and microstructure alternation in MTLE.

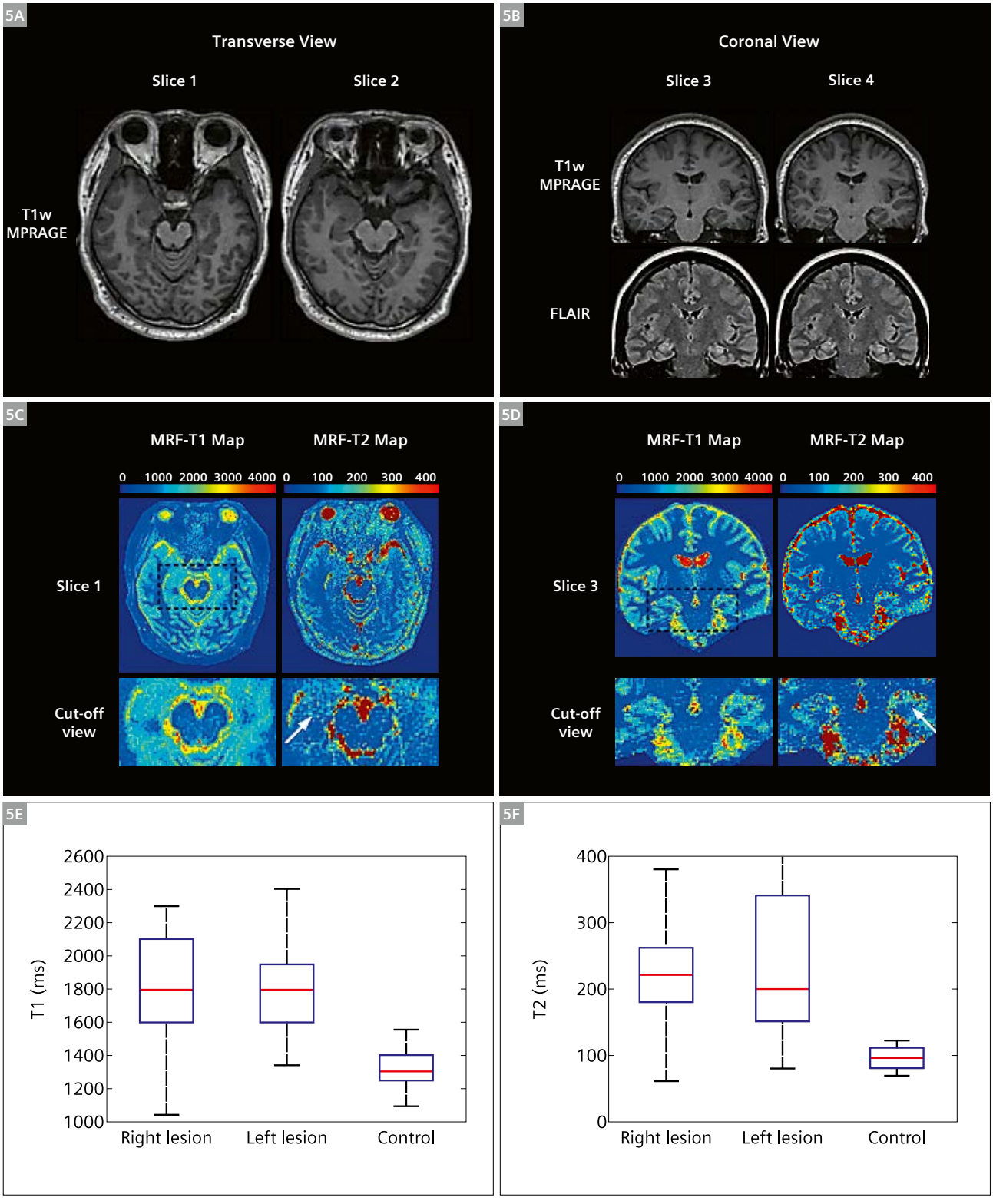

5 Patient with bilateral HS-MTLE. **(5A, B)** T1-weighted and FLAIR scans in axial views and coronal views. **(5C, D)** T1 and T2 maps (axial and coronal views) from MRF **(5E, F)** Box-and-whisker plots of both sides of HS lesions as compared to healthy hippocampi [4].

Participant	T1 (msec)	T2 (msec)
Atrophic hippocampus (n = 28)*	1361 ± 85	135 ± 15
Contralateral hippocampus (n = 28)*	1255 ± 68	103 ± 11
Healthy control participants (n = 30)	1249 ± 59	104 ± 9

*Patients with unilateral mesial temporal lobe epilepsy.

Table 1: T1 and T2 values of HS lesions and contralateral hippocampus.

Conclusion

In epilepsy applications, MRF has been shown to provide additional information to improve diagnosis accuracy and assist surgical planning. It has the potential to detect subtle tissue abnormalities that is invisible on clinical MR scans with high sensitivity and specificity. Lesion characterization based on epileptogenicity could benefit from multiparametric analysis of tissue properties maps. The diagnosis could thus become more objective and less biased because no contrast comparison from apparent health tissue is needed. With enhanced efficiency and reliability, MRF offers great opportunities of improving the current clinical MRI examination for epilepsy patients.

References

1 Zack MM, Kobau R. National and state estimates of the numbers of adults and children with active epilepsy — United States, 2015. Morb Mortal Wkly Rep. 2017;66(31):821-825. doi:10.15585/mmwr.mm6631a1

2 Leventer RJ, Guerrini R, Dobyns WB. Malformations of cortical development and epilepsy. Dialogues Clin Neurosci. 2008;10(1):47-62. http://www.ncbi.nlm.nih.gov/pubmed/18472484. Accessed September 12, 2019.

3 Bernasconi A, Bernasconi N, Bernhardt BC, Schrader D. Advances in MRI for "cryptogenic" epilepsies. Nat Rev Neurol. 2011;7(2):99-108. doi:10.1038/nrneurol.2010.199

4 Liao C, Wang K, Cao X, et al. Detection of lesions in mesial temporal lobe epilepsy by using MR fingerprinting. Radiology. 2018;288(3):804-812. doi:10.1148/radiol.2018172131

5 Wang K, Cao X, Wu D, et al. Magnetic resonance fingerprinting of temporal lobe white matter in mesial temporal lobe epilepsy. Ann Clin Transl Neurol. July 2019. doi:10.1002/acn3.50851

6 Ma D, Jones SE, Deshmane A, et al. Development of high-resolution 3D MR fingerprinting for detection and characterization of epileptic lesions. J Magn Reson Imaging. 2019;49(5):1333-1346. doi:10.1002/jmri.26319

7 Bernasconi A, Cendes F, Theodore WH, et al. Recommendations for the use of structural magnetic resonance imaging in the care of patients with epilepsy: A consensus report from the International League Against Epilepsy Neuroimaging Task Force. Epilepsia. 2019;60(6):1054-1068. doi:10.1111/epi.15612

8 Bernasconi A, Bernasconi N, Caramanos Z, et al. T2 relaxometry can lateralize mesial temporal lobe epilepsy in patients with normal MRI. Neuroimage. 2000;12(6):739-746. doi:10.1006/nimg.2000.0724

9 Woermann FG, Barker GJ, Birnie KD, Meencke HJ, Duncan JS. Regional changes in hippocampal T2 relaxation and volume: A quantitative magnetic resonance imaging study of hippocampal sclerosis. J Neurol Neurosurg Psychiatry. 1998;65(5):656-664. doi:10.1136/jnnp.65.5.656

10 Rugg-Gunn FJ, Boulby PA, Symms MR, Barker GJ, Duncan JS. Whole-brain T2 mapping demonstrates occult abnormalities in focal epilepsy. Neurology. 2005;64(2):318-325. doi:10.1212/01.WNL.0000149642.93493.F4

11 Ma D, Gulani V, Seiberlich N, et al. Magnetic Resonance Fingerprinting. Nature. 2013;495(7440):187-192.

12 Körzdörfer G, Kirsch R, Liu K, et al. Reproducibility and Repeatability of MR Fingerprinting Relaxometry in the Human Brain. Radiology. 2019;292(2):429-437. doi:10.1148/radiol.2019182360

13 Badve C, Yu A, Dastmalchian S, et al. MR fingerprinting of adult brain tumors: Initial experience. In: American Journal of Neuroradiology. Vol 38. American Society of Neuroradiology; 2017:492-499. doi:10.3174/ajnr.A5035

14 Yu AC, Badve C, Ponsky LE, et al. Development of a combined Mr Fingerprinting and Diffusion examination for Prostate cancer. Radiology. 2017;283(3):729-738. doi:10.1148/radiol.2017161599

15 Panda A, Obmann VC, Lo W-C, et al. MR Fingerprinting and ADC Mapping for Characterization of Lesions in the Transition Zone of the Prostate Gland. Radiology. July 2019:181705. doi:10.1148/radiol.2019181705

16 Mehta BB, Ma D, Pierre EY, Jiang Y, Coppo S, Griswold MA. Image reconstruction algorithm for motion insensitive MR Fingerprinting (MRF): MORF. Magn Reson Med. 2018;80(6):2485-2500. doi:10.1002/mrm.27227

17 Jiang Y, Ma D, Seiberlich N, Gulani V, Griswold MA. MR fingerprinting using fast imaging with steady state precession (FISP) with spiral readout. Magn Reson Med. 2015;74(6):1621-1631. doi:10.1002/mrm.25559

18 Ehses P, Seiberlich N, Ma D, et al. IR TrueFISP with a golden-ratio-based radial readout: Fast quantification of T1, T2, and proton density. Magn Reson Med. 2013;69(1):71-81. doi:10.1002/mrm.24225

19 Ben-Eliezer N, Sodickson DK, Shepherd T, Wiggins GC, Block KT. Accelerated and motion-robust in vivo T 2 mapping from radially undersampled data using bloch-simulation-based iterative reconstruction. Magn Reson Med. 2016;75(3):1346-1354. doi:10.1002/mrm.25558

20 Pierre EY, Ma D, Chen Y, Badve C, Griswold MA. Multiscale reconstruction for MR fingerprinting. Magn Reson Med. 2016;75(6):2481-2492. doi:10.1002/mrm.25776

21 Davies M, Puy G, Vandergheynst P, Wiaux Y. A compressed sensing framework for magnetic resonance fingerprinting. SIAM J Imaging Sci. 2014;7(4):2623-2656. doi:10.1137/130947246

Contact

Dan Ma
Department of Biomedical Engineering
Case Western Reserve University
11100 Euclid Ave
Cleveland, OH 44106
USA
Tel.: +1 2168445935
dxm302@case.edu

Perfusion and Metabolism Mismatch in a Cerebral Arteriovenous Malformation: A PET-MR Case

Diego Cecchin[1,2]; Mariagiulia Anglani[3]; Giacomo Cester[3]; Pietro Zucchetta[1]; Simeone Rossella[1]; Francesco Causin[3]; Franco Bui[1]

[1]Nuclear Medicine Unit, Department of Medicine – DIMED, University Hospital of Padova, Italy
[2]Padova Neuroscience Center, University of Padova, Italy
[3]Neuroradiology Unit, University Hospital of Padova, Italy

Background

In resting state conditions, there is a well-established and tight coupling between neuronal activity, brain perfusion, and metabolism. During neuronal activation, there is an increase in energy demand and a hemodynamic response that increases cerebral blood flow (CBF). It has been possible to use both magnetic resonance imaging (MRI) and positron emission tomography (PET) to evaluate different aspects of the CBF metabolism coupling. In a number of pathologies, especially in non-resting state conditions, an uncoupling of cerebral blood flow and metabolism might be present and could explain clinical symptoms.

In this article, we present a case of cerebral arteriovenous malformation (MAV) where PET-MR imaging has proven to be a valuable tool to assess a perfusion/metabolism mismatch.

Case report

A 57-year-old woman with a history of hypertension presented at the University Hospital of Padova with continuous (15-day) cephalalgia (frontal pain radiating out to the right side of the face and associated with blurred vision) not responsive to non-steroid anti-inflammatory drugs. No history of cephalalgia was reported.

A CT scan revealed a suspected cerebral, occipital arteriovenous malformation (AVM) with suspicion of active bleeding (no anticoagulant or antiaggregant drugs had been taken). The patient was hemodynamically and neurologically stable and was admitted to the neurological department.

On the same day, a contrast-enhanced MR was performed, which confirmed the diagnosis of supratentorial parieto-occipital AVM. The following day, the patient underwent a digital subtraction angiography (DSA), which revealed a Spetzler-Martin [1] grade 4 AVM (Fig.1) with a 6 mm intra-nidus aneurysm and small aneurisms of other small arterial branches.

During hospitalization, the patient developed left hemianopsia and therefore underwent a visual acuity examination that was reported as negative but was not completely reliable due to decreased fixation.

To better assess the clinical symptoms and possibly correlate them with areas of metabolic impairment, an ^{18}F-FDG PET-MR scan (Biograph mMR, Siemens Healthcare, Erlangen, Germany; funded by the Fondazione Cassa di Risparmio di Padova e Rovigo and co-funded by the University Hospital of Padova) was performed ten days later.

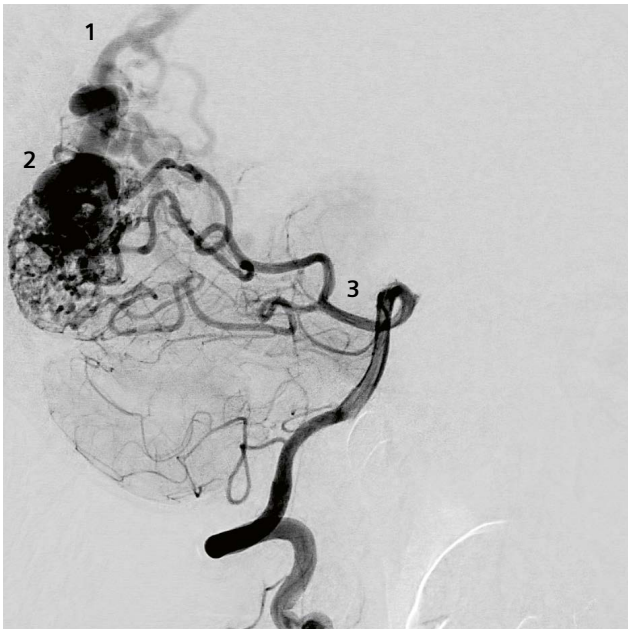

1 Digital subtraction angiography (DSA) in a lateral projection demonstrating the presence of a large cerebral, occipital AVM (2) sustained by branches deriving from the right posterior cerebral artery (3) and draining into enlarged cortical veins (1).

	TR/TE (ms)	FA (°)	voxel size (mm)	BW (Hz/pix)
T1-weighted 3D MPRAGE	2400 / 3.24 / TI: 1000	8	1 x 1 x 1	210
T2 TSE (t2_tse_tra)	5000 / 105	150	0.5 x 0.5 x 4	223
T2-weighted 3D FLAIR (t2_spc_da-fl_iso)	5000 / 394	–	1 x 1 x 1	781
TOF 3D multislab	24 / 4.16	18	0.4 x 0.4 x 1	184
SWI	27 / 20	–	0.6 x 0.6 x 2.5	170
DWI	4500 / 57	–	0.8 x 0.8 x 4	1488
DWI RESOLVE	5000 / 57 / TE1: 72 / TE2: 122	–	1 x 1 x 4	620
DSC	1510 / 25	–	1.8 x 1.8 x 4	1466

Table 1: MR protocol (Biograph mMR)

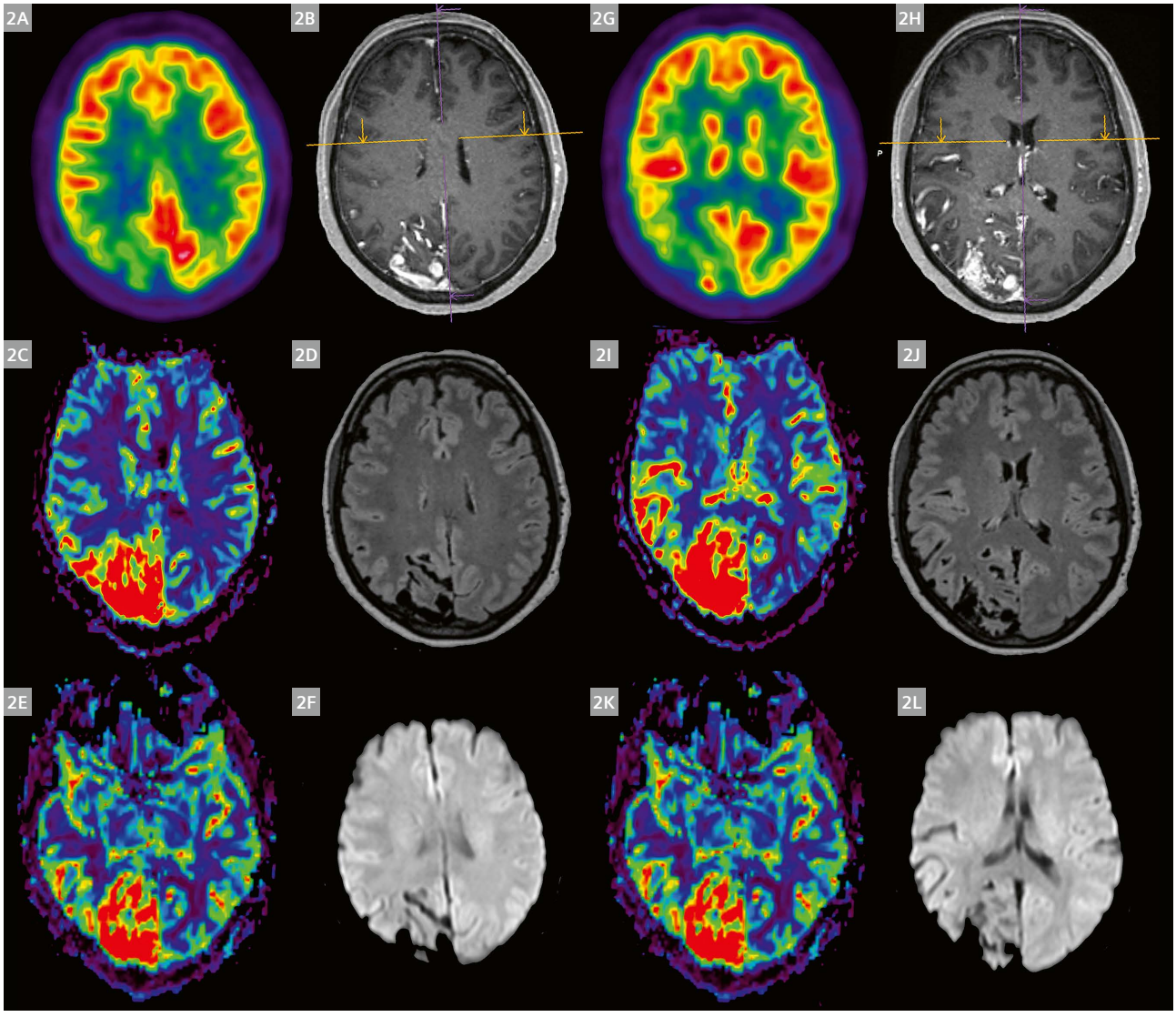

2 Pre-embolization and pre-surgical ^{18}F-FDG PET-MR scan demonstrating **(2A, G)** hypometabolism in the superficial portion of the right calcarine cortex and part of the ipsilateral parieto-temporal cortex (the two columns on the left **2A–2F** on a level passing through the upper portion of the ventricles and the two columns on the right **2G–2L** on a level passing through the head of the caudate).
In the same areas, DSC perfusion demonstrates increased rCBV **(2C, I)** and rCBF **(2E, K)**. Image **2B, H** (1 mm isotropic MPRAGE) show contrast enhancement in the nidus of the AVM. Image **2D**, **J** (isotropic 1 mm FLAIR) show no areas of increased signal surrounding the AVM, suggesting absence of edema or gliosis. Image **2F**, **L** show no significant restriction on DWI with b-value 1000 s/mm^2.

The PET-MR protocol included T1-weighted 3D MPRAGE (1 mm isotropic), T2-weighted 3D FLAIR (1 mm isotropic), T2 TSE (4 mm), susceptibility-weighted imaging (SWI), diffusion-weighted imaging (DWI RESOLVE) (b50, b1000), TOF 3D multislab and dynamic susceptibility contrast (DSC) perfusion.

An area of moderate hypometabolism (Fig. 2A, G) surrounding the AVM nidus (clearly hypometabolic) was observed, including the superficial portion of the right calcarine cortex (explaining visual deficits) and part of the ipsilateral parieto-temporal cortex, which did not show any kind of MR signal alteration related to gliosis (Fig. 2D, J) or cortical atrophy.

The DSC perfusion sequence demonstrated a marked augmentation of rCBV (Fig. 2C, I) and rCBF (Fig. 2E, K) values corresponding with the nidus of the AVM and a smaller increase in the cortical areas characterized by moderate hypometabolism. Interestingly, these areas

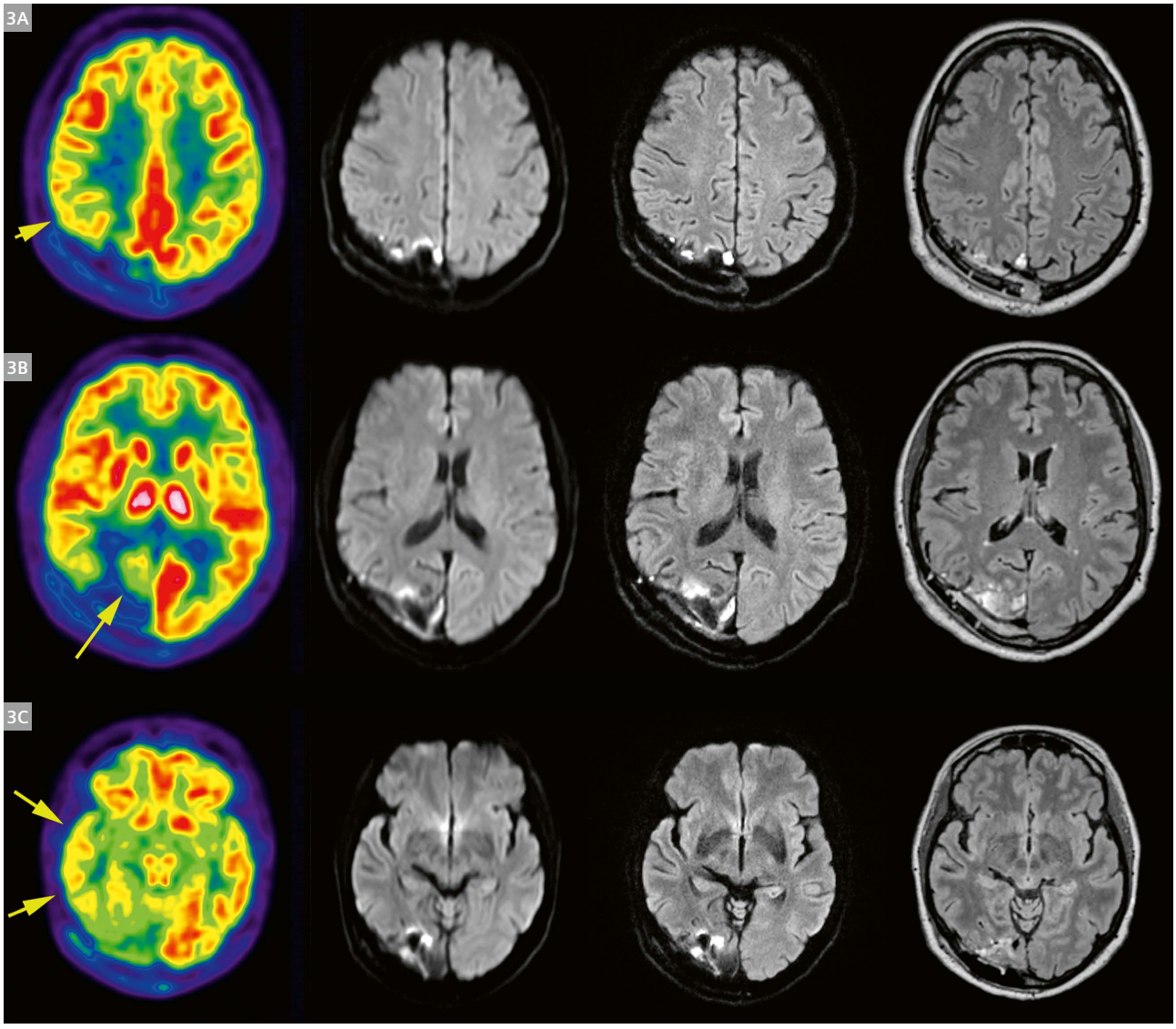

3 Post-embolization and post-surgical ^{18}F-FDG PET-MR scan demonstrating hypometabolism in the superficial and deep portion of the right calcarine cortex and in the ipsilateral parieto-temporal and temporal cortex (first row, **3A**, on a level passing above the lateral ventricles; second row, **3B**, on a level passing through the caudate head; third row, **3C**, on a level passing through the temporal and inferior frontal lobes). The second and third columns from the left show a comparison between the single-shot EPI b1000 DWI (second column) and the multi-shot EPI b1000 DWI (RESOLVE). Despite a comparable acquisition time, the increase in resolution [3] is clearly visible. No significant restriction of the DWI was noted in the areas of ^{18}F-FDG hypometabolism.The last column on the right (isotropic 1 mm, contrast-enhanced T1-MPRAGE) shows the post-surgical outcome at the AVM site.

of increased rCBV and rCBF and decreased metabolism (mismatch) surrounding the nidus, in our experience, seem to clearly correlate with the clinical symptoms reported, especially when located in an eloquent area. The possible physio-pathological explanation could be increased 'luxury' perfusion in these areas of dissociation between vaso-constrictive and vasodilatory reactivity [2], which did not lead to normal compensation of the metabolism.

The patient then underwent an endovascular embolization procedure to remove the aneurysms and some of the arteriovenous shunts, which relieved the pain and partially improved the hemianopia symptoms.

The patient was discharged with an appointment for another session of endovascular embolization and indication for a subsequent neurosurgical intervention to completely remove the AVM. Approximately one month later, a second endovascular embolization was performed leading to reduction of arteriovenous shunts and shrinkage of the nidus of the AVM. A further ten days later, the patient underwent a right parieto-occipital craniotomy and complete dissection and removal of the AVM. A post-surgical DSA confirmed the complete removal of the AVM with initial reduction of the diameter of afferent arteries and no residual arteriovenous shunts.

One month later, the ^{18}F-FDG PET-MR scan (Fig. 3) was repeated due to worsened visual deficits in the absence of new morphological alterations at a follow-up MR scan. The exam revealed decreased FDG metabolism in the residual portion of the right calcarine cortex (Fig. 3A, first column) and decreased parieto-temporal and temporal metabolism without anatomical and DWI alterations on MR.

Conclusions

Hybrid ^{18}F-FDG PET-MR imaging may prove to be a valuable tool for the simultaneous assessment of perfusion and metabolism in clinical situations, such as arteriovenous malformations, where a perfusion/metabolism mismatch might be present and, as in our experience, may help to better explain clinical symptoms.

References

1 Spetzler RF, Martin NA. A proposed grading system for arteriovenous malformations. J Neurosurg. 1986 Oct;65(4): 476–83.
2 Tyler JL, Leblanc R, Meyer E, Dagher A, Yamamoto YL, Diksic M, Hakim A. Hemodynamic and metabolic effects of cerebral arteriovenous malformations studied by positron emission tomography. Stroke. 1989 Jul;20(7): 890–8.
3 Porter DA, Heidemann RM. High resolution diffusion-weighted imaging using readout-segmented echo-planar imaging, parallel imaging and a two-dimensional navigator-based reacquisition. Magn Reson Med. 2009 Aug;62(2): 468–75. doi: 10.1002/mrm.22024.

Contact

Professor Diego Cecchin
University Hospital of Padova
Nuclear Medicine Unit
Department of Medicine – DIMED
Via Giustiniani 2
35128 Padova
Italy
diego.cecchin@unipd.it

HIGHLIGHTS OF PRESCRIBING INFORMATION

These highlights do not include all the information needed to use Fludeoxyglucose F 18 Injection safely and effectively. See full prescribing information for Fludeoxyglucose F 18 Injection. Fludeoxyglucose F 18 Injection, USP For intravenous use Initial U.S. Approval: 2005

RECENT MAJOR CHANGES

Warnings and Precautions (5.1, 5.2)	7/2010
Adverse Reactions (6)	7/2010

INDICATIONS AND USAGE

Fludeoxyglucose F18 Injection is indicated for positron emission tomography (PET) imaging in the following settings:

- Oncology: For assessment of abnormal glucose metabolism to assist in the evaluation of malignancy in patients with known or suspected abnormalities found by other testing modalities, or in patients with an existing diagnosis of cancer.
- Cardiology: For the identification of left ventricular myocardium with residual glucose metabolism and reversible loss of systolic function in patients with coronary artery disease and left ventricular dysfunction, when used together with myocardial perfusion imaging.
- Neurology: For the identification of regions of abnormal glucose metabolism associated with foci of epileptic seizures (1).

DOSAGE AND ADMINISTRATION

Fludeoxyglucose F 18 Injection emits radiation. Use procedures to minimize radiation exposure. Screen for blood glucose abnormalities.

- In the oncology and neurology settings, instruct patients to fast for 4 to 6 hours prior to the drug's injection. Consider medical therapy and laboratory testing to assure at least two days of normoglycemia prior to the drug's administration (5.2).
- In the cardiology setting, administration of glucose-containing food or liquids (e.g., 50 to 75 grams) prior to the drug's injection facilitates localization of cardiac ischemia (2.3).

Aseptically withdraw Fludeoxyglucose F 18 Injection from its container and administer by intravenous injection (2).

The recommended dose:

- for adults is 5 to 10 mCi (185 to 370 MBq), in all indicated clinical settings (2.1).
- for pediatric patients is 2.6 mCi in the neurology setting (2.2).

Initiate imaging within 40 minutes following drug injection; acquire static emission images 30 to 100 minutes from time of injection (2).

DOSAGE FORMS AND STRENGTHS

Multi-dose 30mL and 50mL glass vial containing 0.74 to 7.40 GBq/mL (20 to 200 mCi/mL) Fludeoxyglucose F 18 Injection and 4.5mg of sodium chloride with 0.1 to 0.5% w/w ethanol as a stabilizer (approximately 15 to 50 mL volume) for intravenous administration (3).

CONTRAINDICATIONS

None

WARNINGS AND PRECAUTIONS

- Radiation risks: use smallest dose necessary for imaging (5.1).
- Blood glucose adnormalities: may cause suboptimal imaging (5.2).

ADVERSE REACTIONS

Hypersensitivity reactions have occurred; have emergency resuscitation equipment and personnel immediately available (6).

To report SUSPECTED ADVERSE REACTIONS, contact PETNET Solutions, Inc. at 877-473-8638 or FDA at 1-800-FDA-1088 or www.fda.gov/medwatch.

USE IN SPECIFIC POPULATIONS

Pregnancy Category C: No human or animal data. Consider alternative diagnostics; use only if clearly needed (8.1).

- Nursing mothers: Use alternatives to breast feeding (e.g., stored breast milk or infant formula) for at least 10 half-lives of radioactive decay, if Fludeoxyglucose F 18 Injection is administered to a woman who is breast-feeding (8.3).
- Pediatric Use: Safety and effectiveness in pediatric patients have not been established in the oncology and cardiology settings (8.4).

See 17 for PATIENT COUNSELING INFORMATION

Revised: 1/2011

FULL PRESCRIBING INFORMATION: CONTENTS*

*Sections or subsections omitted from the full prescribing information are not listed.

FULL PRESCRIBING INFORMATION

1 INDICATIONS AND USAGE

Fludeoxyglucose F 18 Injection is indicated for positron emission tomography (PET) imaging in the following settings:

1.1 Oncology

For assessment of abnormal glucose metabolism to assist in the evaluation of malignancy in patients with known or suspected abnormalities found by other testing modalities, or in patients with an existing diagnosis of cancer.

1.2 Cardiology

For the identification of left ventricular myocardium with residual glucose metabolism and reversible loss of systolic function in patients with coronary artery disease and left ventricular dysfunction, when used together with myocardial perfusion imaging.

1.3 Neurology

For the identification of regions of abnormal glucose metabolism associated with foci of epileptic seizures.

2 DOSAGE AND ADMINISTRATION

Fludeoxyglucose F 18 Injection emits radiation. Use procedures to minimize radiation exposure. Calculate the final dose from the end of synthesis (EOS) time using proper radioactive decay factors. Assay the final dose in a properly calibrated dose calibrator before administration to the patient [see Description (11.2)].

2.1 Recommended Dose for Adults

Within the oncology, cardiology and neurology settings, the recommended dose for adults is 5 to 10 mCi (185 to 370 MBq) as an intravenous injection.

2.2 Recommended Dose for Pediatric Patients

Within the neurology setting, the recommended dose for pediatric patients is 2.6 mCi, as an intravenous injection. The optimal dose adjustment on the basis of body size or weight has not been determined [see Use in Special Populations (8.4)].

2.3 Patient Preparation

- To minimize the radiation absorbed dose to the bladder, encourage adequate hydration. Encourage the patient to drink water or other fluids (as tolerated) in the 4 hours before their PET study.
- Encourage the patient to void as soon as the imaging study is completed and as often as possible thereafter for at least one hour.
- Screen patients for clinically significant blood glucose abnormalities by obtaining a history and/or laboratory tests [see Warnings and Precautions (5.2)]. Prior to Fludeoxyglucose F 18 PET imaging in the oncology and neurology settings, instruct patient to fast for 4 to 6 hours prior to the drug's injection.
- In the cardiology setting, administration of glucose-containing food or liquids (e.g., 50 to 75 grams) prior to Fludeoxyglucose F18 Injection facilitates localization of cardiac ischemia

2.4 Radiation Dosimetry

The estimated human absorbed radiation doses (rem/mCi) to a newborn (3.4 kg), 1-year-old (9.8 kg), 5-year-old (19 kg), 10-year-old (32 kg), 15-year-old (57 kg), and adult (70 kg) from intravenous administration of Fludeoxyglucose F 18 Injection are shown in Table 1. These estimates were calculated based on human[2] data and using the data published by the International Commission on Radiological Protection[4] for Fludeoxyglucose ^{18}F. The dosimetry data show that there are slight variations in absorbed radiation dose for various organs in each of the age groups. These dissimilarities in absorbed radiation dose are due to developmental age variations (e.g., organ size, location, and overall metabolic rate for each age group). The identified critical organs (in descending order) across all age groups evaluated are the urinary bladder, heart, pancreas, spleen, and lungs.

Table 1. Estimated Absorbed Radiation Doses (rem/mCi) After Intravenous Administration of Fludeoxyglucose F-18 Injection[a]

Organ	Newborn (3.4 kg)	1-year-old (9.8 kg)	5-year-old (19 kg)	10-year-old (32 kg)	15-year-old (57 kg)	Adult (70 kg)
Bladder wall[b]	4.3	1.7	0.93	0.60	0.40	0.32
Heart wall	2.4	1.2	0.70	0.44	0.29	0.22
Pancreas	2.2	0.68	0.33	0.25	0.13	0.096
Spleen	2.2	0.84	0.46	0.29	0.19	0.14
Lungs	0.96	0.38	0.20	0.13	0.092	0.064
Kidneys	0.81	0.34	0.19	0.13	0.089	0.074
Ovaries	0.80	0.8	0.19	0.11	0.058	0.053
Uterus	0.79	0.35	0.19	0.12	0.076	0.062
LLI wall *	0.69	0.28	0.15	0.097	0.060	0.051
Liver	0.69	0.31	0.17	0.11	0.076	0.058
Gallbladder wall	0.69	0.26	0.14	0.093	0.059	0.049
Small intestine	0.68	0.29	0.15	0.096	0.060	0.047
ULI wall **	0.67	0.27	0.15	0.090	0.057	0.046
Stomach wall	0.65	0.27	0.14	0.089	0.057	0.047
Adrenals	0.65	0.28	0.15	0.095	0.061	0.048
Testes	0.64	0.27	0.14	0.085	0.052	0.041
Red marrow	0.62	0.26	0.14	0.089	0.057	0.047
Thymus	0.61	0.26	0.14	0.086	0.056	0.044
Thyroid	0.61	0.26	0.13	0.080	0.049	0.039
Muscle	0.58	0.25	0.13	0.078	0.049	0.039
Bone surface	0.57	0.24	0.12	0.079	0.052	0.041
Breast	0.54	0.22	0.11	0.068	0.043	0.034
Skin	0.49	0.20	0.10	0.060	0.037	0.030
Brain	0.29	0.13	0.09	0.078	0.072	0.070
Other tissues	0.59	0.25	0.13	0.083	0.052	0.042

[a] MIRDOSE 2 software was used to calculate the radiation absorbed dose. Assumptions on the biodistribution based on data from Gallagher et al.1 and Jones et al.[2]

[b] The dynamic bladder model with a uniform voiding frequency of 1.5 hours was used.

*LLI = lower large intestine; **ULI = upper large intestine

2.5 Radiation Safety – Drug Handling

- Use waterproof gloves, effective radiation shielding, and appropriate safety measures when handling Fludeoxyglucose F 18 Injection to avoid unnecessary radiation exposure to the patient, occupational workers, clinical personnel and other persons.
- Radiopharmaceuticals should be used by or under the control of physicians who are qualified by specific training and experience in the safe use and handling of radionuclides, and whose experience and training have been approved by the appropriate governmental agency authorized to license the use of radionuclides.
- Calculate the final dose from the end of synthesis (EOS) time using proper radioactive decay factors. Assay the final dose in a properly calibrated dose calibrator before administration to the patient [see Description (11.2)].
- The dose of Fludeoxyglucose F 18 used in a given patient should be minimized consistent with the objectives of the procedure, and the nature of the radiation detection devices employed.

2.6 Drug Preparation and Administration

- Calculate the necessary volume to administer based on calibration time and dose.
- Aseptically withdraw Fludeoxyglucose F 18 Injection from its container.
- Inspect Fludeoxyglucose F 18 Injection visually for particulate matter and discoloration before administration, whenever solution and container permit.
- Do not administer the drug if it contains particulate matter or discoloration; dispose of these unacceptable or unused preparations in a safe manner, in compliance with applicable regulations. Use Fludeoxyglucose F 18 Injection within 12 hours from the EOS.

2.7 Imaging Guidelines

- Initiate imaging within 40 minutes following Fludeoxyglucose F 18 Injection administration.
- Acquire static emission images 30 to 100 minutes from the time of injection.

3 DOSAGE FORMS AND STRENGTHS

Multiple-dose 30 mL and 50 mL glass vial containing 0.74 to 7.40 GBq/mL (20 to 200 mCi/mL) of Fludeoxyglucose F 18 Injection and 4.5 mg of sodium chloride with 0.1 to 0.5% w/w ethanol as a stabilizer (approximately 15 to 50 mL volume) for intravenous administration.

4 CONTRAINDICATIONS

None

5 WARNINGS AND PRECAUTIONS

5.1 Radiation Risks

Radiation-emitting products, including Fludeoxyglucose F 18 Injection, may increase the risk for cancer, especially in pediatric patients. Use the smallest dose necessary for imaging and ensure safe handling to protect the patient and health care worker [see Dosage and Administration (2.5)].

5.2 Blood Glucose Abnormalities

In the oncology and neurology setting, suboptimal imaging may occur in patients with inadequately regulated blood glucose levels. In these patients, consider medical therapy and laboratory testing to assure at least two days of normoglycemia prior to Fludeoxyglucose F 18 Injection administration.

6 ADVERSE REACTIONS

Hypersensitivity reactions with pruritus, edema and rash have been reported in the post-marketing setting. Have emergency resuscitation equipment and personnel immediately available.

7 DRUG INTERACTIONS

The possibility of interactions of Fludeoxyglucose F 18 Injection with other drugs taken by patients undergoing PET imaging has not been studied.

8 USE IN SPECIFIC POPULATIONS

8.1 Pregnancy

Pregnancy Category C

Animal reproduction studies have not been conducted with Fludeoxyglucose F 18 Injection. It is also not known whether Fludeoxyglucose F 18 Injection can cause fetal harm when administered to a pregnant woman or can affect reproduction capacity. Consider alternative diagnostic tests in a pregnant woman; administer Fludeoxyglucose F 18 Injection only if clearly needed.

8.3 Nursing Mothers

It is not known whether Fludeoxyglucose F 18 Injection is excreted in human milk. Consider alternative diagnostic tests in women who are breast-feeding. Use alternatives to breast feeding (e.g., stored breast milk or infant formula) for at least 10 half-lives of radioactive decay, if Fludeoxyglucose F 18 Injection is administered to a woman who is breast-feeding.

8.4 Pediatric Use

The safety and effectiveness of Fludeoxyglucose F 18 Injection in pediatric patients with epilepsy is established on the basis of studies in adult and pediatric patients. In pediatric patients with epilepsy, the recommended dose is 2.6 mCi. The optimal dose adjustment on the basis of body size or weight has not been determined. In the oncology or cardiology settings, the safety and effectiveness of Fludeoxyglucose F 18 Injection have not been established in pediatric patients.

11 DESCRIPTION

11.1 Chemical Characteristics

Fludeoxyglucose F 18 Injection is a positron emitting radiopharmaceutical that is used for diagnostic purposes in conjunction with positron emission tomography (PET) imaging. The active ingredient 2-deoxy-2-[^{18}F]fluoro-D-glucose has the molecular formula of $C_6H_{11}{}^{18}FO_5$ with a molecular weight of 181.26, and has the following chemical structure:

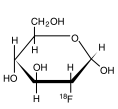

Fludeoxyglucose F 18 Injection is provided as a ready to use sterile, pyrogen free, clear, colorless solution. Each mL contains between 0.740 to 7.40GBq (20.0 to 200 mCi) of 2-deoxy-2-[^{18}F]fluoro-D-glucose at the EOS, 4.5 mg of sodium chloride and 0.1 to 0.5% w/w ethanol as a stabilizer. The pH of the solution is between 4.5 and 7.5. The solution is packaged in a multiple-dose glass vial and does not contain any preservative.

11.2 Physical Characteristics

Fluorine F 18 decays by emitting positron to Oxygen O 16 (stable) and has a physical half-life of 109.7 minutes. The principal photons useful for imaging are the dual 511 keV gamma photons, that are produced and emitted simultaneously in opposite direction when the positron interacts with an electron (Table 2).

Table 2. Pricipal Radiation Emission Data for Fluorine F18		
Radiation/Emission	% Per Disintegration	Mean Energy
Positron (b+)	96.73	249.8 keV
Gamma (±)*	193.46	511.0 keV

*Produced by positron annihilation

From: Kocher, D.C. Radioactive Decay Tables DOE/TIC-I 1026, 89 (1981)

The specific gamma ray constant (point source air kerma coefficient) for fluorine F 18 is 5.7 R/hr/mCi (1.35 x 10-6 Gy/hr/kBq) at 1 cm. The half-value layer (HVL) for the 511 keV photons is 4 mm lead (Pb). The range of attenuation coefficients for this radionuclide as a function of lead shield thickness is shown in Table 3. For example, the interposition of an 8 mm thickness of Pb, with a coefficient of attenuation of 0.25, will decrease the external radiation by 75%.

Table 3. Radiation Attenuation of 511 keV Photons by lead (Pb) shielding	
Shield thickness (Pb) mm	Coefficient of attenuation
0	0.00
4	0.50
8	0.25
13	0.10
26	0.01
39	0.001
52	0.0001

For use in correcting for physical decay of this radionuclide, the fractions remaining at selected intervals after calibration are shown in Table 4.

Table 4. Physical Decay Chart for Fluorine F18	
Minutes	Fraction Remaining
0*	1.000
15	0.909
30	0.826
60	0.683
110	0.500
220	0.250

*calibration time

12 CLINICAL PHARMACOLOGY

12.1 Mechanism of Action

Fludeoxyglucose F 18 is a glucose analog that concentrates in cells that rely upon glucose as an energy source, or in cells whose dependence on glucose increases under pathophysiological conditions. Fludeoxyglucose F 18 is transported through the cell membrane by facilitative glucose transporter proteins and is phosphorylated within the cell to [^{18}F] FDG-6-phosphate by the enzyme hexokinase. Once phosphorylated it cannot exit until it is dephosphorylated by glucose-6-phosphatase. Therefore, within a given tissue or pathophysiological process, the retention and clearance of Fludeoxyglucose F 18 reflect a balance involving glucose transporter, hexokinase and glucose-6-phosphatase activities. When allowance is made for the kinetic differences between glucose and Fludeoxyglucose F 18 transport and phosphorylation (expressed as the ‚lumped constant" ratio), Fludeoxyglucose F 18 is used to assess glucose metabolism. In comparison to background activity of the specific organ or tissue type, regions of decreased or absent uptake of Fludeoxyglucose F 18 reflect the decrease or absence of glucose metabolism. Regions of increased uptake of Fludeoxyglucose F 18 reflect greater than normal rates of glucose metabolism.

12.2 Pharmacodynamics

Fludeoxyglucose F 18 Injection is rapidly distributed to all organs of the body after intravenous administration. After background clearance of Fludeoxyglucose F 18 Injection, optimal PET imaging is generally achieved between 30 to 40 minutes after administration.

In cancer, the cells are generally characterized by enhanced glucose metabolism partially due to (1) an increase in activity of glucose transporters, (2) an increased rate of phosphorylation activity, (3) a reduction of phosphatase activity or, (4) a dynamic alteration in the balance among all these processes. However, glucose metabolism of cancer as reflected by Fludeoxyglucose F 18 accumulation shows considerable variability. Depending on tumor type, stage, and location, Fludeoxyglucose F 18 accumulation may be increased, normal, or decreased. Also, inflammatory cells can have the same variability of uptake of Fludeoxyglucose F 18.

In the heart, under normal aerobic conditions, the myocardium meets the bulk of its energy requirements by oxidizing free fatty acids. Most of the exogenous glucose taken up by the myocyte is converted into glycogen. However, under ischemic conditions, the oxidation of free fatty acids decreases, exogenous glucose becomes the preferred myocardial sub strate, glycolysis is stimulated, and glucose taken up by the myocyte is metabolized immediately instead of being converted into glycogen. Under these conditions, phosphorylated Fludeoxyglucose F 18 accumulates in the myocyte and can be detected with PET imaging.

In the brain, cells normally rely on aerobic metabolism. In epilepsy, the glucose metabolism varies. Generally, during a seizure, glucose metabolism increases. Interictally, the seizure focus tends to be hypometabolic.

12.3 Pharmacokinetics

Distribution: In four healthy male volunteers, receiving an intravenous administration of 30 seconds in duration, the arterial blood level profile for Fludeoxyglucose F 18 decayed triexponentially. The effective half-life ranges of the three phases were 0.2 to 0.3 minutes, 10 to 13 minutes with a mean and standard deviation (STD) of 11.6 (±) 1.1 min, and 80 to 95 minutes with a mean and STD of 88 (±) 4 min. Plasma protein binding of Fludeoxyglucose F 18 has not been studied.

Metabolism: Fludeoxyglucose F 18 is transported into cells and phosphorylated to [^{18}F]-FDG-6-phosphate at a rate proportional to the rate of glucose utilization within that tissue. [F18]-FDG-6-phosphate presumably is metabolized to 2-deoxy-2-[F18]fluoro-6-phospho-D-mannose([F 18]FDM-6-phosphate).

Fludeoxyglucose F 18 Injection may contain several impurities (e.g., 2-deoxy-2-chloro-D-glucose (ClDG)). Biodistribution and metabolism of ClDG are presumed to be similar to Fludeoxyglucose F 18 and would be expected to result in intracellular formation of 2-deoxy-2-chloro-6-phospho-D-glucose (ClDG-6-phosphate) and 2-deoxy-2-chloro-6-phospho-D-mannose (ClDM-6-phosphate). The phosphorylated deoxyglucose compounds are dephosphorylated and the resulting compounds (FDG, FDM, ClDG, and ClDM) presumably leave cells by passive diffusion. Fludeoxyglucose F 18 and related compounds are cleared from non-cardiac tissues within 3 to 24 hours after administration. Clearance from the cardiac tissue may require more than 96 hours. Fludeoxyglucose F 18 that is not involved in glucose metabolism in any tissue is then excreted in the urine.

Elimination: Fludeoxyglucose F 18 is cleared from most tissues within 24 hours and can be eliminated from the body unchanged in the urine. Three elimination phases have been identified in the reviewed literature. Within 33 minutes, a mean of 3.9% of the administrated radioactive dose was measured in the urine. The amount of radiation exposure of the urinary bladder at two hours post-administration suggests that 20.6% (mean) of the radioactive dose was present in the bladder.

Special Populations: The pharmacokinetics of Fludeoxyglucose F 18 Injection have not been studied in renally-impaired, hepatically impaired or pediatric patients. Fludeoxyglucose F 18 is eliminated through the renal system. Avoid excessive radiation exposure to this organ system and adjacent tissues. The effects of fasting, varying blood sugar levels, conditions of glucose intolerance, and diabetes mellitus on Fludeoxyglucose F 18 distribution in humans have not been ascertained [see Warnings and Precautions (5.2)].

13 NONCLINICAL TOXICOLOGY

13.1 Carcinogenesis, Mutagenesis, Impairment of Fertility

Animal studies have not been performed to evaluate the Fludeoxyglucose F 18 Injection carcinogenic potential, mutagenic potential or effects on fertility.

14 CLINICAL STUDIES

14.1 Oncology

The efficacy of Fludeoxyglucose F 18 Injection in positron emission tomography cancer imaging was demonstrated in 16 independent studies. These studies prospectively evaluated the use of Fludeoxyglucose F 18 in patients with suspected or known malignancies, including non-small cell lung cancer, colo-rectal, pancreatic, breast, thyroid, melanoma, Hodgkin's and non-Hodgkin's lymphoma, and various types of metastatic cancers to lung, liver, bone, and axillary nodes. All these studies had at least 50 patients and used pathology as a standard of truth. The Fludeoxyglucose F 18 Injection doses in the studies ranged from 200 MBq to 740 MBq with a median and mean dose of 370 MBq. In the studies, the diagnostic performance of Fludeoxyglucose F 18 Injection varied with the type of cancer, size of cancer, and other clinical conditions. False negative and false positive scans were observed. Negative Fludeoxyglucose F 18 Injection PET scans do not exclude the diagnosis of cancer. Positive Fludeoxyglucose F 18 Injection PET scans can not replace pathology to establish a diagnosis of cancer. Non-malignant conditions such as fungal infections, inflammatory processes and benign tumors have patterns of increased glucose metabolism that may give rise to false-positive scans. The efficacy of Fludeoxyglucose F 18 Injection PET imaging in cancer screening was not studied.

14.2 Cardiology

The efficacy of Fludeoxyglucose F 18 Injection for cardiac use was demonstrated in ten independent, prospective studies of patients with coronary artery disease and chronic left ventricular systolic dysfunction who were scheduled to undergo coronary revascularization. Before revascularization, patients underwent PET imaging with Fludeoxyglucose F 18 Injection (74 to 370 MBq, 2 to 10 mCi) and perfusion imaging with other diagnostic radiopharmaceuticals. Doses of Fludeoxyglucose F 18 Injection ranged from 74 to 370 MBq (2 to 10 mCi). Segmental, left ventricular, wall-motion assessments of asynergic areas made before revascularization were compared in a blinded manner to assessments made after successful revascularization to identify myocardial segments with functional recovery. Left ventricular myocardial segments were predicted to have reversible loss of systolic function if they showed Fludeoxyglucose F 18 accumulation and reduced perfusion (i.e., flow-metabolism mismatch). Conversely, myocardial segments were predicted to have irreversible loss of systolic function if they showed reductions in both Fludeoxyglucose F 18 accumulation and perfusion (i.e., matched defects). Findings of flow-metabolism mismatch in a myocardial segment may suggest that successful revascularization will restore myocardial function in that segment. However, false-positive tests occur regularly, and the decision to have a patient undergo revascularization should not be based on PET findings alone. Similarly, findings of a matched defect in a myocardial segment may suggest that myocardial function will not recover in that segment, even if it is successfully revascularized. However, false-negative tests occur regularly, and the decision to recommend against coronary revascularization, or to recommend a cardiac transplant, should not be based on PET findings alone. The reversibility of segmental dysfunction as predicted with Fludeoxyglucose F 18 PET imaging depends on successful coronary revascularization. Therefore, in patients with a low likelihood of successful revascularization, the diagnostic usefulness of PET imaging with Fludeoxyglucose F 18 Injection is more limited.

14.3 Neurology

In a prospective, open label trial, Fludeoxyglucose F 18 Injection was evaluated in 86 patients with epilepsy. Each patient received a dose of Fludeoxyglucose F 18 Injection in the range of 185 to 370 MBq (5 to 10 mCi). The mean age was 16.4 years (range: 4 months to 58 years; of these, 42 patients were less than 12 years and 16 patients were less than 2 years old). Patients had a known diagnosis of complex partial epilepsy and were under evaluation for surgical treatment of their seizure disorder. Seizure foci had been previously identified on ictal EEGs and sphenoidal EEGs. Fludeoxyglucose F 18 Injection PET imaging confirmed previous diagnostic findings in 16% (14/87) of the patients; in 34% (30/87) of the patients, Fludeoxyglucose F 18 Injection PET images provided new findings. In 32% (27/87), imaging with Fludeoxyglucose F 18 Injection was inconclusive. The impact of these imaging findings on clinical outcomes is not known. Several other studies comparing imaging with Fludeoxyglucose F 18 Injection results to subsphenoidal EEG, MRI and/or surgical findings supported the concept that the degree of hypometabolism corresponds to areas of confirmed epileptogenic foci. The safety and effectiveness of Fludeoxyglucose F 18 Injection to distinguish idiopathic epileptogenic foci from tumors or other brain lesions that may cause seizures have not been established.

15 REFERENCES

- 1. Gallagher B.M., Ansari A., Atkins H., Casella V., Christman D.R., Fowler J.S., Ido T., MacGregor R.R., Som P., Wan C.N., Wolf A.P., Kuhl D.E., and Reivich M. "Radiopharmaceuticals XXVII. ^{18}F-labeled 2-deoxy-2-fluoro-d-glucose as a radiopharmaceutical for measuring regional myocardial glucose metabolism in vivo: tissue distribution and imaging studies in animals," J Nucl Med, 1977; 18, 990-6.
- 2. Jones S.C., Alavi, A., Christman D., Montanez, I., Wolf, A.P., and Reivich M. "The radiation dosimetry of 2 [F-18] fluoro-2-deoxy-D-glucose in man," J Nucl Med, 1982; 23, 613-617.
- 3. Kocher, D.C. "Radioactive Decay Tables: A handbook of decay data for application to radiation dosimetry and radiological assessments," 1981, DOE/TIC-I 1026, 89.
- 4. ICRP Publication 53, Volume 18, No. I-4,1987, pages 75-76.

16 HOW SUPPLIED/STORAGE AND DRUG HANDLING

Fludeoxyglucose F 18 Injection is supplied in a multi-dose, capped 30 mL and 50 mL glass vial containing between 0.740 to 7.40 GBq/mL (20 to 200 mCi/mL), of no carrier added 2-deoxy-2-[F 18] fluoro-D-glucose, at end of synthesis, in approximately 15 to 50 mL.
The contents of each vial are sterile, pyrogen-free and preservative-free.
NDC 40028-511-30; 40028-511-50

Receipt, transfer, handling, possession, or use of this product is subject to the radioactive material regulations and licensing requirements of the U.S. Nuclear Regulatory Commission, Agreement States or Licensing States as appropriate.

Store the Fludeoxyglucose F 18 Injection vial upright in a lead shielded container at 25°C (77°F); excursions permitted to 15-30°C (59-86°F).

Store and dispose of Fludeoxyglucose F 18 Injection in accordance with the regulations and a general license, or its equivalent, of an Agreement State or a Licensing State.

The expiration date and time are provided on the container label. Use Fludeoxyglucose F 18 Injection within 12 hours from the EOS time.

17 PATIENT COUNSELING INFORMATION

Instruct patients in procedures that increase renal clearance of radioactivity.
Encourage patients to:

- drink water or other fluids (as tolerated) in the 4 hours before their PET study.
- void as soon as the imaging study is completed and as often as possible thereafter for at least one hour.

Manufactured by: PETNET Solutions Inc. 810 Innovation Drive Knoxville, TN 37932

Distributed by: PETNET Solutions Inc.^ 810 Innovation Drive Knoxville, TN 37932^

PETNET Solutions

PN0002262 Rev. A

Marcg 1, 2011

Indications

Fludeoxyglucose F18 Injection is indicated for positron emission tomography (PET) imaging in the following settings:

Oncology: For assessment of abnormal glucose metabolism to assist in the evaluation of malignancy in patients with known or suspected abnormalities found by other testing modalities, or in patients with an existing diagnosis of cancer.

Cardiology: For the identification of left ventricular myocardium with residual glucose metabolism and reversible loss of systolic function in patients with coronary artery disease and left ventricular dysfunction, when used together with myocardial perfusion imaging.

Neurology: For the identification of regions of abnormal glucose metabolism associated with foci of epileptic seizures.

Important Safety Information

Radiation Risks: Radiationemitting products, including Fludeoxyglucose F18 Injection, may increase the risk for cancer, especially in pediatric patients. Use the smallest dose necessary for imaging and ensure safe handling to protect the patient and healthcare worker.

Blood Glucose Abnormalities: In the oncology and neurology setting, suboptimal imaging may occur in patients with inadequately regulated blood glucose levels. In these patients, consider medical therapy and laboratory testing to assure at least two days of normoglycemia prior to Fludeoxyglucose F18 Injection administration.

Adverse Reactions: Hypersensitivity reactions with pruritus, edema and rash have been reported; have emergency resuscitation equipment and personnel immediately available.

Dosage Forms and Strengths: Multiple-dose 30 mL and 50 mL glass vial containing 0.74 to 7.40 GBq/mL (20 to 200 mCi/mL) of Fludeoxyglucose F^{18} injection and 4.5 mg of sodium chloride with 0.1 to 0.5% w/w ethanolas a stabilizer (approximately 15 to 50 mL volume) for intravenous administration. Fludeoxyglucose F^{18} injection is manufactured by Siemens' PETNET Solutions, 810 Innovation Drive, Knoxville, TN 39732, USA.

Clinical fMRI: Where do I start?

Victoria Sherwood, Ph.D.; and Tina Pavlin, Ph.D.

NordicNeuroLab AS, Bergen, Norway

Introduction

There have been many developments in technology in recent years which have seen functional MRI gain popularity and acceptance within clinical practice. The most common use for functional MRI (fMRI) remains to be pre-surgical mapping of motor and language areas of the brain, which can help guide the neurosurgeon in their approach. Despite its steadily increasing use, many clinicians still see fMRI as a tool for the large teaching hospital, and something unachievable for a smaller center with less of a support network. Although expertise in neuroradiology is paramount to success, there are fewer barriers to setting up an fMRI service than is often believed. Sites equipped with a motivated multi-disciplinary team can easily navigate the learning curve with support from equipment manufacturers. Increasing the number of centers performing fMRI will aid hugely in future standardization. Siemens Healthineers and NordicNeuroLab provide an easy to use system of hardware and stimulus presentation software, which can ease users into this subject with confidence.

The BOLD signal

fMRI is based on the detection of a Blood Oxygenation Level Dependent (BOLD) signal change when a person is presented with a stimulus. Rapid imaging using a T2*-weighted sequence allows an increased signal to be detected due to the increase in blood flow in the stimulated brain area. An experiment, or paradigm, is based on stimuli which target a certain neurological process, such as language production. These measurements make it possible to both lateralize and localize the part of the brain controlling that process on an individual basis. This is incredibly important for planning an approach for tumor resection, or temporal lobectomy in epilepsy, for example. There is a vast amount of literature available for the interested reader [1–4]. This article outlines the requirements for reliable paradigm delivery and measurement of the BOLD response.

Use cases

In the first instance, a clinical referral guides the choice of paradigms to be used. In tumor or stroke cases, the location of the pathology will dictate which functions the clinician would choose to map. Temporal lobe epilepsy is a rapidly growing area in terms of fMRI referrals, and in this case lateralizing the patient's language function has historically been the most important motivation [5]. Recently more and more groups are investigating the possibility of directly mapping memory centers [6], although memory activation is somewhat more difficult to achieve. In addition, there are a surprising number of topics in research where fMRI is of interest, relating to myriad

1 fMRI hardware (left to right): *SyncBox*, *InRoomViewingDevice*, *VisualSystem HD (VSHD)*, and *ResponseGrips*.

neurological disorders [7–11] and extending to psychology, economics and marketing, to name but a few [12–16]. Resultingly there is a demand for facilities that can conduct high quality fMRI.

Standardization

As with many quantitative MRI techniques, standardization is a difficult subject due to a lack of sufficient clinical evidence. A brief search of the literature will uncover so many paradigm designs and discussions of post processing approaches that it can be overwhelming to a clinician who is looking into the possibility of setting up a service [17]. However, there are some basic motor and language paradigms that are very commonly used, such as tapping the fingers on one or the other hand to activate the primary motor area, and asking the patient to think of words starting with a given letter to activate the Broca's area associated with language production. Typically, multiple motor and language paradigms would be run within a session. For the motor cortex, this might be due to the need to map areas associated with different motor functions such as feet, toes, even the tongue. With regards to language, it is useful to overlap results from at least three paradigms to gain further confidence in the results. The American Society for Functional Neuroradiology have published recommendations for language [18] and motor [19] paradigms where they also address the need for some flexibility depending on the patient. It is crucial that the radiographer understands each patient and their capabilities and can adapt accordingly (see "Patient preparation and setup").

Basic requirements

Hardware overview
An fMRI system normally consists of 5 components:

1. A device for synchronization of stimulus presentation with MR image acquisition
2. A high-resolution MR compatible visual display (screen or goggles) for presenting visual stimuli inside the MR scanner
3. A powerful PC running stimulus presentation SW, such as NordicNeuroLab's *nordicAktiva* solution
4. High-precision pneumatic, electrostatic, or piezoelectric headphones/earplugs for auditory stimulus presentation, along with a communication console in the MR control room
5. A pair of hand-held button devices or grips for collecting subject feedback during the fMRI experiment

These are described in more detail below, and are shown in Figure 1.

Synchronization
One of the challenges in fMRI is synchronizing stimulus presentation with MR image acquisition. The accuracy and verification of timing information is critical to the validity of results. The synchronization device from NordicNeuroLab is called a *SyncBox* (Fig. 1). It detects the optical trigger pulse (or alternatively, the TTL pulse or the RS 485/422 signal) from the MRI scanner at the start of each acquisition and then sends the signal (either ASCII code or key press) to the stimulus-presentation computer via a USB connection (green connection Fig. 2). One useful feature of NNL's *SyncBox* is a so-called simulation mode: by simulating trigger signals coming from the MR scanner during image acquisition, paradigms can be developed and tested outside the MR environment, thus minimizing the need for expensive scanner time.

Visual display
The most common clinical solution for presenting visual stimuli to a patient inside the MR scanner is a shielded LCD screen mounted on a stand ideally at the back of the scanner, allowing for a large visual field and unobstructed view of the patient from the MR control room. If space is limited, the LCD screen can alternatively be placed at patient's feet. The patient can see the display through mirrors mounted on the head coil assembly, and the placement of the LCD screen and the mirror configuration will determine the required orientation of the visual display. The display orientation of the *InRoomViewingDevice* from NordicNeuroLab (Fig. 1), can be adjusted via an in-built settings menu. However, a much more user-friendly solution is to adjust the screen rotation remotely from the control room. NordicNeuroLab has developed a *nordicComfort* software that not only enables the radiographer to control the LCD functionality (display orientation and an in-built camera) remotely, but also includes a library of content-appropriate entertainment for adult and pediatric[1] patient populations, as well as the possibility to stream entertainment content from a number of popular streaming services. Although the patient entertainment functionality cannot be utilized during a task-based fMRI scan, it is a very beneficial feature to use during the structural and DTI acquisitions as it helps to ease patient anxiety or even claustrophobia, minimizing patient motion and scan interruptions [20–21].
An alternative to a shielded LCD screen is a coil-mounted display in the form of goggles, for example NordicNeuroLab's high-definition *VisualSystem* (*VSHD*, Fig. 1). These use dual HD OLED technology to display the visual stimuli to the patient. One advantage is full visual immersion, with

[1] *MR scanning has not been established as safe for imaging fetuses and infants less than two years of age. The responsible physician must evaluate the benefits of the MR examination compared to those of other imaging procedures.*

a large field-of-view. This can be especially beneficial for patients with claustrophobia or children who often resist being prepped for scanning due to the unfamiliar environment. Another advantage of the *VSHD* is that it allows dioptric correction of patient vision, which is often a problem in the aging population. Finally, the integrated eye-tracking functionality provides feedback to the radiographer on the patient's level of alertness as well as stress. Despite these advantages, the LCD screen may be preferable in clinical settings due to its ease-of-use which allows for high patient throughput.

As shown in Figure 2, the paradigm is first transmitted from the stimulus PC using an HDMI (video) output. To avoid RF interference inside the MR room, a *Fiber Transmitter* converts the digital video signal into an optical signal which is then fed through the waveguide (red connection Fig. 2) and connected to either the LCD screen or the coil-mounted goggles. The LCD and *VSHD* both require a power source. NordicNeuroLab uses a *Shielded Interface Unit* which resides in the far-corner of the MR room to convert the AC voltage to a DC voltage required to power the displays without producing RF interference.

Audible stimulus presentation

There are several MR-compatible audio solutions on the market today, utilizing different technology for providing the auditory stimuli to the patient. The most common are pressure waveguide headphones that keep speakers outside of the magnet bore and the sound is carried through semi-rigid tubing into the headphones [22]. Although robust and integrated with the scanner's communication console in the control room, the downside is the inability to provide a stereo input and a rather compromized sound quality due to signal losses along the waveguide. A better sound quality is achieved using either electrostatic or piezoelectric headphones. Furthermore, space restrictions within the latest head coils can be prohibitive, therefore in-ear headphones can be advantageous.

Response devices

Visual and auditory stimuli are used to instruct the patient to perform a task during MR acquisition. The patient may be asked to perform a simple motor or language task, such as finger-tapping or word generation, in which case there is little need to monitor patient responses. However, in instances when the patient is performing a task which requires a decision, such as a rhyming or a verbal memory task, then the fMRI hardware should also include a set of Button Response Devices (BRD). NordicNeuroLab supplies *ResponseGrips* (Fig. 1) for this purpose. These consist of a pair of ergonomically made 2-button grips, and a *ResponseGrip Interface* which converts each button press, detected as an interruption of optical signal (light blue connection Fig. 2), into a distinct ASCII character code output. This is detected by the stimulus-presentation software, *nordicAktiva* (black connection Fig. 2), and stored in a log file of the fMRI experiment.

Stimulus presentation workstation

The stimulus-presentation software should be installed on a dedicated workstation in the control room. This workstation must have at least one HDMI video port (or equivalent), an audio port, and one or more USB ports for detecting the ASCII character code input from the trigger box and the BRD. In addition, it must have a powerful graphics card for fast video transmission and a fast processor to minimize signal delays.

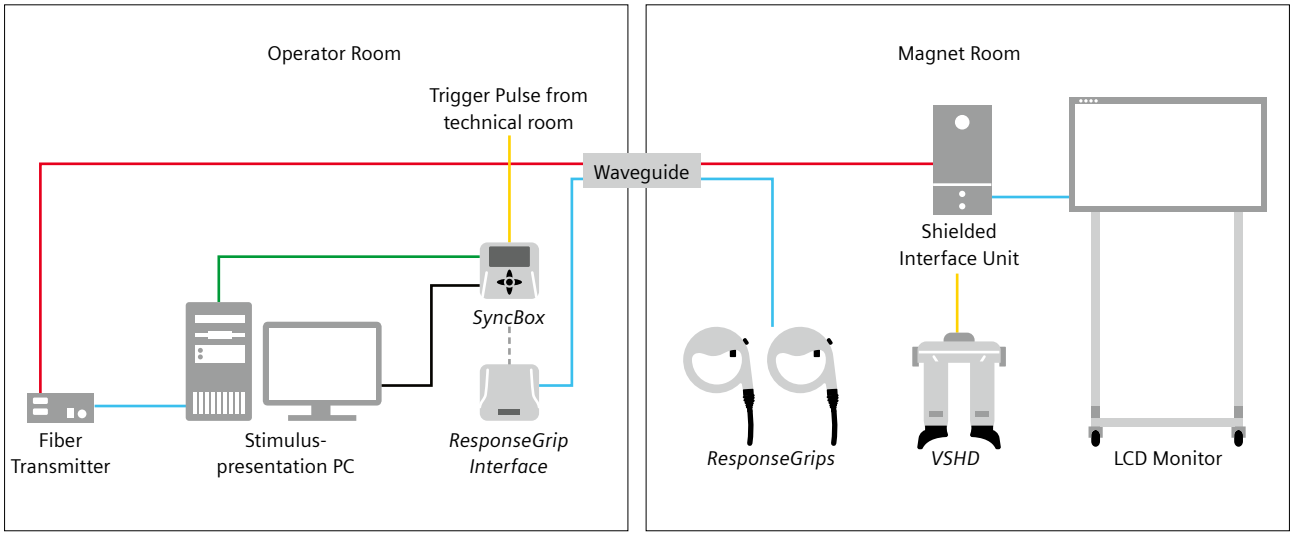

2 Connection diagram of fMRI hardware in the control room and magnet room.

Stimulus-presentation software

Stimulus-presentation software controls the selection and timing of paradigms. Paradigms used in clinical fMRI are most commonly based on a block design, which means periods of active tasks are interlaced with periods of either rest or non-relevant tasks (Fig. 3), and the fMRI analysis then looks at the BOLD signal differences between the two conditions.

The most basic solution for paradigm display is Microsoft PowerPoint®. Slides containing text, video or audio content can be designed easily, and slide timing can be controlled using the slide-timing feature. However, using PowerPoint has its limitations – the biggest one being that it is challenging to detect the scanner trigger signal from within the software, so the presentation and the MRI acquisition must be started simultaneously by the radiographer. In addition, the internal clock of the PowerPoint presentation is not as accurate as in a dedicated SW, so the presentation can over time become out-of-sync with the MRI acquisition. Finally, PowerPoint cannot detect patient responses.

There exist more powerful and flexible paradigm-presentation software options including E-prime® (Psychology Software Tools, Sharpsburg, PA, USA), Presentation® (Neurobehavioral Systems, Albany, CA, USA), PsychoPy (based on Python language) and Psychophysics Toolbox (based on Matlab). These packages are designed for research use and require some effort and time to learn. *nordicAktiva* from NordicNeuroLab, on the other hand, is a clinically approved software designed specifically for pre-surgical motor and language assessment in the treatment of patients with brain tumors, epilepsy and other conditions. *nordicAktiva* is delivered with a library of ready-to-use standard clinical paradigms that are designed according to ASFNR recommendations [18–19]. Although these recommendations need constant revision and improvement due to developments in the field, they provide a common frame of reference by which inter-institutional standardization of clinical fMRI becomes a possibility. This in turn can lead to meaningful comparison of clinical fMRI outcomes between institutions and, eventually, to advancement of our knowledge and improved patient care.

Even though the standardization of fMRI paradigms is at the core of *nordicAktiva*, the user can modify the paradigms to better suite their needs. A typical modification could be to shorten the TR within the paradigm to make it compatible with acquisition protocols utilizing Simultaneous Multi-Slice (SMS; see "Scanning protocol") or to make simple changes to the slide content, such as changing the text, picture, or sound presented to the patient. *nordicAktiva* also includes patient and operator instructions in multiple languages and allows the user to easily add new languages to the standard paradigm library.

Post-processing software (BOLD and DTI)

After the functional data are acquired, they must be processed through calculations of statistical *t*-maps using the General Linear Model (GLM). This model compares the signal time course in each voxel with what is expected based on the paradigm design and hemodynamic response (see "Processing") to determine whether signal changes during stimulation are significantly greater than those at rest. These maps are examined by neuroradiologists before being passed on to neurosurgeons. The user has a plethora of post-processing software packages to choose from, such as *syngo*.via Neuro 3D and NordicNeurolab's *nordicBrainEx*, each with its strengths and limitations. In the context of clinical fMRI and DTI, it is essential to choose a software that allows for the export of BOLD overlays and diffusion fiber groups to presurgical planning stations and neuronavigational systems used by neurosurgeons, such as BrainLab (Munich, Germany), Stryker (Kalamazoo, MI, USA), Medtronic (Dublin, Ireland) or Surgical Theatre (Los Angeles, CA, USA). Furthermore, the software should have an intuitive workflow for easy adoption in the clinics, and fast processing capabilities to handle large data

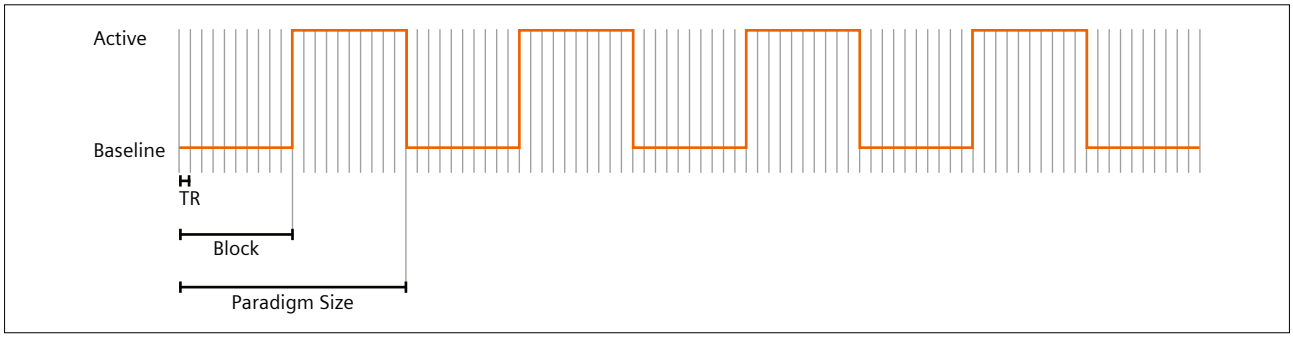

3 Schematic representation of a block design paradigm: Red curve represents blocks of active (Task ON) and baseline (Task OFF) state. Periods between vertical lines represent measurements of brain volumes which take one TR time to acquire. Here there are ten measurements per block, a total of 90 measurements. Paradigm Size is a vector parameter in the BOLD sequence tab card representing an OFF+ON state. In the example above, the Paradigm Size would contain ten baseline measurements and ten active measurements (= 20).

throughput as well as the increasing need to examine the data shortly after scanning. Most importantly, it should be based on modern post-processing algorithms that have been validated against existing gold standards, such as cortical mapping using electrocortical stimulation, and which aim at minimizing the number of false positive and false negative findings [23].

Patient preparation and setup

One of the most important factors determining success of an fMRI examination is proper patient preparation which relies on good and efficient communication between patient and radiographer. It is paramount that the radiographer evaluates the patient's functional capacity and ability to perform a specific task. Very often, stroke or tumor patients have functional deficits, for instance difficulty reading, speaking, and/or understanding instructions, or compromized motor function. Epilepsy patients can be sensitive to certain colors or color combinations which can trigger an epileptic seizure. Older patients often have compromized vision and/or hearing, while children have a large spread of reading proficiency. Basic useful information can be gathered via a standard questionnaire. Patients should be asked what their mother tongue is, whether they are left/right-handed for certain tasks, whether they wear glasses or contact lenses, whether they suffer from seizures, and whether they have issues with particular colors. Furthermore, patients should be asked whether they take any medication (such as sedation, relaxant), whether they have taken any medication on the day of the scan, and whether they feel tired.

It is very beneficial to do a 'practice-run' through the paradigms in the patient preparation room. The patient can be given a document describing the paradigms and asked to rehearse each task, then shown the paradigms on a workstation or laptop as they will appear on the screen during the MRI scan. *nordicAktiva* can be run in a so-called Simulate Mode, without requiring a trigger from the scanner. This way the patient can see the entire paradigm before the actual exam. The patient should also be told explicitly that they should not read the text on the slides out load, but silently in their head.

Adapting to your patient

In case a patient has difficulties executing a task, adaptations should be considered. For visually impaired patients, a simple solution could be to increase font sizes; if a patient cannot read, their language function can be tested using picture naming or auditory stimuli (such as a Story Listening paradigm); if they cannot tap each finger individually for a motor task, they can tap all the fingers at the same time, or clench them into a fist; if they are completely paralyzed on one side, then one can test their sensory input by stroking their hand. Having a range of different paradigms based on written text, pictures or audible stimuli, and accounting for varying levels of proficiency, can go a long way to ensuring the success of the examination.

Positioning

Once prepared, the patient is positioned on the MR scanner table with the appropriate head coil. Immobilization of their head using memory foam is recommended, and they should be made as comfortable as possible (e.g., padding their knees, covering them with a blanket). An appropriate mirror should then be attached to the head coil, and the patient instructed to look at the LCD screen. Are the letters oriented correctly (up/down, left/right)? Can they see sharply or are the words blurred? Can they see the entire screen? At this point it might be necessary to modify the size of the letters, re-orient the LCD display or reposition the LCD screen (Fig. 4).

Communication during the scanning session is key. The radiographer should encourage and motivate the patient by giving positive feedback, thereby relaxing the patient, increasing their confidence and improving task performance. Specific task instructions should be repeated before each paradigm, as these can easily be forgotten.

After the completion of the scan, the patients should be asked about their performance, whether they felt they executed the tasks well, and whether they remained alert during the scan. This information can be very useful for quality control purposes.

All patients are unique, and radiographers are faced with new and unforeseen challenges almost daily. However, with proper training they can become experts in evaluating patient's ability and needs, and thus greatly contribute to the success of an fMRI session.

4 Patient positioned with double mirror and LCD screen behind the scanner. At this point correct orientation of the screen should be confirmed by the patient.

Scanning protocol

Suggested core sequences for a functional study and important parameters to consider can be found in Table 1. These are by no means hard and fast rules, but should be considered as a starting point for optimization.

Anatomical data

A high-quality 3D isotropic structural scan of the whole brain is the first step. This will provide a detailed anatomical reference for the statistical activation maps and tractography data. Functional data will be co-registered to and overlaid on the structural data, providing a sense check that the fibers and areas of activation are in the expected locations and aiding in localization.

The BOLD sequence

BOLD images are usually obtained using a gradient-echo EPI sequence. The BOLD tab card (Fig. 5) contains information relevant to the paradigm design and preprocessing steps.

A whole-brain volume is acquired within each TR, and each volume makes up one measurement (Fig. 5, A) within the experiment. Continuous measurements are made for the entirety of the paradigm duration (Fig. 3). When setting up each BOLD sequence, the TR and the total number of measurements must match exactly the paradigm. These can be compared with *nordicAktiva* before starting the paradigm. Note: the scanning time will be a few seconds longer than the duration of the paradigm due to the acquisition of dummy scans. It is recommended

Sequence	Resolution, mm	TR, ms	TE, ms	Acceleration	Directions	b-value, s/mm^2
T1 MPRAGE	1 x 1 x 1 (Distance factor = 0)	As per Siemens Healthineers library protocol	As per Siemens Healthineers library protocol	As per Siemens Healthineers library protocol	–	–
BOLD (EP2D) (without SMS)	3 x 3 x 3 (Distance factor = 0)	3000	20–30	GRAPPA 2–3	–	–
BOLD (EP2D) (with SMS)	2 x 2 x 2 (Distance factor = 0)	2000	20–30	GRAPPA 2, SMS 3	–	–
DTI (EP2D MDDW) (with or without SMS)	2.5 x 2.5 x 2.5 (Distance factor = 0) or as close as possible, remaining isotropic	Depending on SMS, coverage, etc.	Lowest possible	GRAPPA 2, SMS 3 where possible	≥ 32	1000–2000

Table 1: Recommendations of core sequences and various scanning parameters for an fMRI examination.

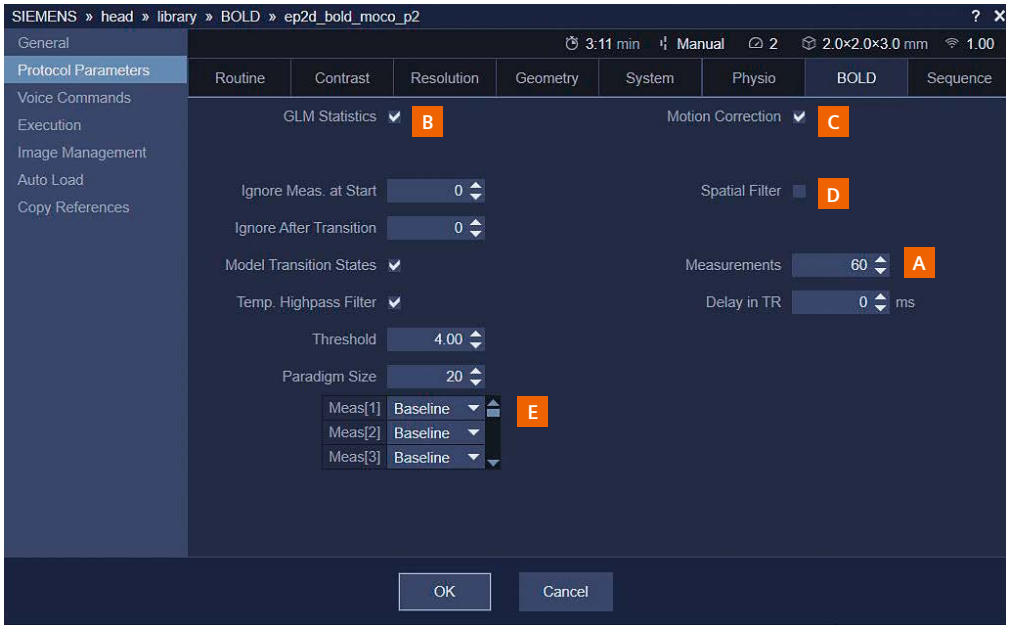

5 BOLD tab card in *syngo* MR XA11 software, including most important parameters: Number of measurements (A), GLM statistics for inline processing (B), motion correction (C), spatial smoothing filter activation (D), and paradigm block design specification (E).

that the 'Introduction' feature is switched off to avoid further confusion about the timings. Spatial resolution is also an important consideration, particularly for pre-surgical planning where visualization in 3D is the endpoint, and isotropic acquisitions with no slice gap are highly recommended.

Additional parameters in the BOLD tab card allow for optimal inline processing, which has two main benefits. Firstly, statistical *t*-maps are created automatically (GLM series), so for sites where pre-processing requirements are well known and tested, it is possible to avoid any offline processing of the data beyond a visual check and thresholding of the maps, for example in the fMRI tab of the *syngo*.via Neuro 3D workflow. Secondly, and perhaps more importantly, thumbnails of the inline statistical maps can be viewed in real time during the scan. Although these do not provide the complete picture available after post-processing, they can make a useful guide for the radiographer to indicate that some activation is visible in the relevant brain areas. The 'GLM Statistics' check box (Fig. 5, B) should be used to provide the inline statistical processing. Retrospective motion correction is available here (C), as are some other pre-processing options.
For ease of inline visualization of activations by the radiographer, it is recommended that a spatial (smoothing) filter (D) of at least 1.5 times the in-plane resolution of the sequence is used (see "Processing"). Defining the extent of spatial smoothing is possible once the box is checked. Finally, the BOLD tab card contains details of the block design of the paradigm (E). 'Paradigm size' refers to one full cycle (active and rest) of the paradigm (Fig. 3). For example, a simple 'On/Off' paradigm with ten measurements per block would have a paradigm size of 20. Each measurement must be specified as 'Baseline' or 'Active' via a series of drop-down tabs. A more complex paradigm with two different active conditions such as Rest – Right-hand finger tapping – Left-hand finger tapping, also with ten measurements per block, would have a total paradigm size of 30. Note: Inline processing only accounts for a single active condition, so the GLM series must be re-calculated for any experiment involving multiple different active conditions.

It is advisable to create a library protocol with correct parameters for all required paradigms, to minimize the potential for errors during a session.

The impact of SMS

Simultaneous multi-slice (SMS) sequences can have a big impact on fMRI. The additional acceleration can be used in a number of ways:

- If the paradigm timings are kept the same, a larger slice coverage or higher spatial resolution can be achieved within the same TR.
- Maintaining the same spatial resolution, the TR can be significantly reduced. Either this can provide time savings by making the entire experiment shorter, or the total number of measurements can be increased accordingly to improve statistical power [24, 25].

In the latter case, the paradigm itself will require modification. *nordicAktiva* v1.3 includes different TR options to cater for customers with or without SMS capabilities.

Motion correction

There are two options in the Siemens library for inline motion correction of BOLD EPI data. 'Moco' is a retrospective motion correction using *k*-space interpolation to correct for motion after the acquisition of data and can be activated using a check box in the BOLD tab card (Fig. 5, C). PACE is a prospective technique where motion is detected, and the image position shifted in real time for the next measurement. The two techniques can be used independently or together, however, it should be noted that for PACE protocols both the motion correction and spatial smoothing (see "Processing") are applied prior to reconstruction of the base EPI images and cannot be removed. With Moco there is a separate motion corrected 'MocoSeries' generated in addition to the original images. For applications where the user may wish to apply their motion correction during the processing stage (a common request for research studies, for example), PACE would not be appropriate, but Moco could still be used to improve the inline maps. Some form of motion correction is of course recommended, however, and in the clinical setting a PACE approach may give a cleaner result in the presence of significant motion [26].

Log and design files

nordicAktiva writes any detected responses from *ResponseGrips* to a log file. This describes all events occurring during the experiment and their exact timings, including details of the slides presented and incoming trigger signals from the scanner. Afterwards, this file can be saved alongside a design file. The design file describes the block design of the presented paradigm for later importing into *nordicBrainEx* post-processing software.

DTI

It is common to use tractography alongside BOLD in pre-surgical planning, and some thought should be given to optimization for this purpose. SMS can provide significant time savings for DTI and should be used where possible.

Processing

An overview of the steps

There are several strategies that may be taken when processing fMRI data, depending on the preferences of the site. The main recommended steps are summarized in Table 2.

Conditions and contrasts

For statistical calculations one must specify whether a paradigm block should represent an active condition (e.g., 1) or baseline (e.g., 0). Next, the required contrasts are specified. In a basic On/Off paradigm such as unilateral finger tapping with one active and one baseline condition, one would specify a contrast of [1 0] to compare the active condition with baseline. If two active conditions are included (such as right hand (condition 1) and left hand (condition -1) finger tapping), there are a few options. One can compare each hand separately with the baseline condition, resulting in contrasts of [1 0] and [-1 0], and/or one can compare each hand with the other, resulting in contrasts of [1 -1] or [-1 1]. In the latter case, any brain regions which are activated by both stimuli will be cancelled out, so for inclusion of the supplementary motor area, the two hands should be analysed separately.

The use of inline processing

Using the BOLD tab card, it is possible to specify pre-processing steps and the block design. This allows for inline calculation of statistical maps, in which case the post processing may only involve thresholding and exporting the maps. Although this process is the most streamlined, it removes the ability to explore different pre-processing options and adapt them to the patient. Variability between seemingly similar patients can be extremely high, and for patients with low activation, particularly in language paradigms, visualization can be difficult. Increasing the spatial filter and applying clustering can greatly help in these cases, especially for lateralization. The user has a lot

Processing step	Description
Co-registration	3D rigid registration of BOLD and DTI data with structural data.
Motion correction	Registration of each frame in the functional series to the first. Applies to both BOLD and DTI data.
Slice timing correction	A correction for BOLD data to account for the fact that slices are not all acquired simultaneously. This cannot be applied to SMS data.
Spatial filtering	A smoothing kernel is commonly applied to help improve visualization of activation over noise. This does also reduce the spatial localization accuracy so should be used appropriately depending on the importance of localization versus laterality.
Temporal high pass filtering	High pass filtering can be applied to remove slow signal drifts over time.
Temporal smoothing	Data can be smoothed in the time domain to reduce inherent rapid noise fluctuations. This should also be used with caution to prevent smearing out of the responses over time.
Convolution of the stimulus with the hemodynamic response function	The effect of a stimulus on the blood flow in the brain is not immediate but is characterized by a hemodynamic response function (HRF). A model of the HRF should be included in the analysis (Fig. 6).
Calculation of statistical maps using the General Linear Model	The statistical significance of signal changes is calculated based on knowledge of the expected signal change due to the paradigm. Pixelwise maps of the *t*-statistic are created for overlay onto the structural data.
Thresholding of *t*-maps	Whilst viewing as an overlay, a threshold is applied to each *t*-map and adjusted manually such that only pixels above a certain value are displayed. This is a subjective process and requires knowledge of the neuroanatomy involved. Thresholding can significantly impact the apparent size of activation regions, so radiologists should be involved in this process. *nordicBrainEx* provides automated thresholding to 40% of the maximum *t*-value as a starting point to assist with standardization [27].
Clustering	To remove small regions of noise from the *t*-maps, clustering can be applied such that activation regions are only displayed when x number of adjacent voxels are above the chosen threshold (Fig. 7). Clustering is applied in 3D and may typically be set to 20 or 30 voxels.

Table 2: A summary of common processing parameters used in fMRI.

of flexibility in their choice of pre-processing parameters, depending on the chosen software, and this can sometimes be overlooked. The Neuro3D workflow in Numaris X or *syngo*.via will automatically load the maps produced inline and display them for thresholding and will assume

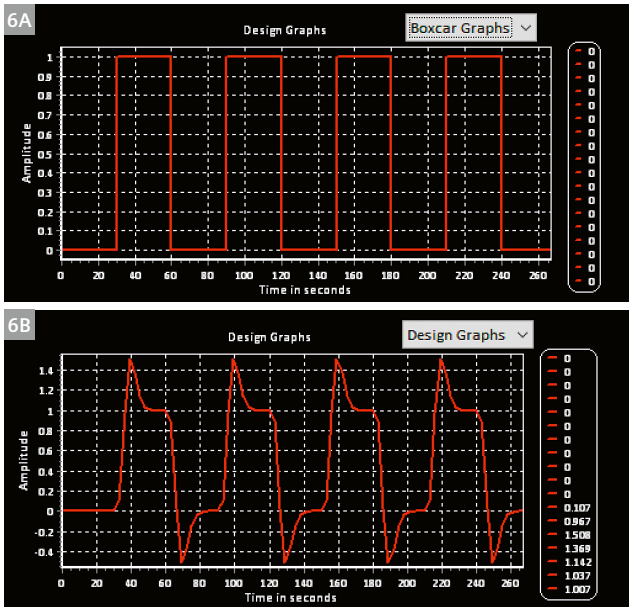

6 **(6A)** Boxcar diagram of a straightforward On/Off paradigm, and **(6B)** the design graph incorporating a model of hemodynamic response function.

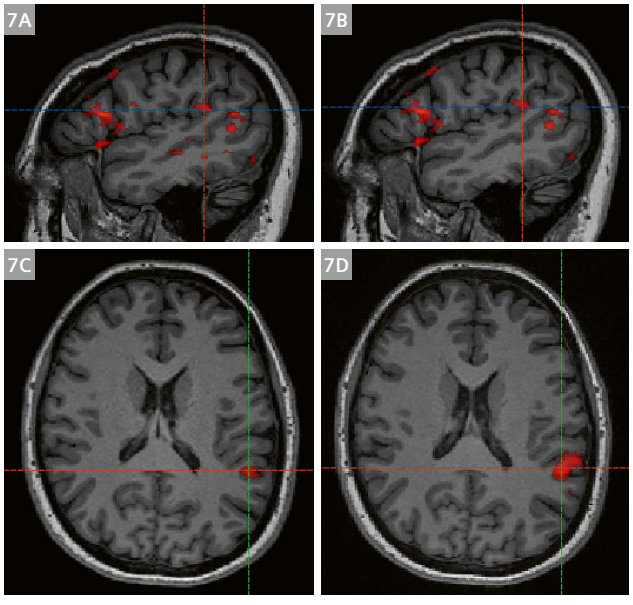

7 Visualization of language areas **(7A)** without and **(7B)** with clustering of 30 voxels, showing the ability to remove spurious noisy areas of false positive activation. Wernicke's area with **(7C)** no spatial smoothing filter and **(7D)** with 6 x 6 x 6 mm smoothing.

the paradigm followed the block design specified in the BOLD tab card. However, it also includes an optional 'BOLD Calculation' step which can be used to change the paradigm design, add contrasts, change pre-processing parameters and implement clustering. As mentioned, this feature is required in the case of multiple active conditions (e.g., rest – left hand – right hand) which the inline processing cannot facilitate.

The use of design files and *nordicBrainEx*

nordicBrainEx provides an automated GLM calculation using a design file. Firstly, a design file can be sent to *nordicBrainEx* from *nordicAktiva* which describes exactly the paradigm design that was displayed during the experiment, thus removing the potential for error. It also contains default values for the pre-processing steps and contrasts, which are then easily editable prior to calculation, if desired. Once a design file has been imported, it will be saved and can be selected for subsequent patients for whom the same paradigm has been used. Either the original EPI images can be imported, or the MocoSeries – in the latter case, both motion correction and spatial filtering can be switched off in *nordicBrainEx*.

Multiple overlapping activation maps

Particularly for language or memory paradigms, it can be difficult to clearly visualize the areas of true activation over and above false positive regions. Overlapping multiple *t*-maps from different paradigms can really increase confidence in the true positive results, and it is recommended that for language area mapping, at least three paradigms are used.

Processing of DTI data alongside BOLD

Where DTI data is desired, it can be very useful to display both BOLD and DTI simultaneously. Importantly BOLD activation regions can be used to guide tractography.

Conclusions – Setting up an fMRI service

Most commonly fMRI is used for neurosurgical planning/navigation. This requires a multi-disciplinary team, within which the importance of communication cannot be underestimated. Central to this team is a motivated radiologist with the time, interest, and support to develop the service. Another key person is the neurosurgeon, both as the end user of the information, and potentially as a source of funding. Neurosurgeons should be educated on the capabilities of the software to produce data sets of various formats (both from BOLD and DTI data), to optimize the integration with the neuronavigational system. Feedback from the neurosurgeon on the format, quality, and usefulness of the data should be sought regularly to aid further optimization. The responsibility for feedback on image

quality lies with the radiologist, and often it takes several trial sessions to ensure the available scanning tools are being used to their fullest. Practically the scanning is up to the radiographers, who should be specifically designated staff members who have undergone appropriate training to build confidence in patient preparation, image sequences and paradigms. Whilst the support of an MR physicist with knowledge of fMRI is not essential, it can help both the radiographers and radiologists become more proficient in their respective roles more quickly.

When getting started, support from applications specialists is paramount, for sequence and workflow optimization as well as paradigm delivery. It can be beneficial for the multi-disciplinary team to discuss with the applications specialists the plans and possibilities for the service, to ensure every person is clear about the overall goals, and to set expectations. Variability in equipment, paradigms, sequence parameters and patients themselves all impact on the success of an investigation. There may be instances where little or no activation is seen simply due to the patient. Accepting occasional failure and learning how to adapt to difficult situations are important steps in the learning curve.

Even once the service is up and running, additional applications support should be sought, even as far as sharing data for discussion. It is within everyone's best interests to establish an efficient workflow using equipment which integrates and communicates effectively.

References

1 Castellano A et al. (2017), Functional MRI for Surgery of Gliomas. Current Treatment Options in Neuroradiology, 19:34.
2 Orringer D et al. (2012), Clinical Applications and Future Directions of Functional MRI. Seminars in Neurology, 32(4):466-475.
3 Bizzi A (2009), Presurgical Mapping of Verbal Language in Brain Tumours with Functional MR Imaging and MR Tractography. Neuroimaging Clinics of North America, 19:573-596.
4 Tieleman A et al. (2009), Preoperative fMRI in tumour surgery. European Radiology, 19:2523-2534.
5 van Heereden J et al. (2014), Functional MRI in clinical practice: A pictorial essay. Journal of Medical Imaging and Radiation Oncology, 58:320-326.
6 Towgood K et al. (2015), Bringing Memory fMRI into the Clinic: A Comparison of Seven Memory fMRI Protocols in Temporal Lobe Epilepsy, Human Brain Mapping, 36:1595-1608.
7 Sirnsek F et al. (2017), Neural activation during cognitive reappraisal in girls at high risk for depression. Prog Neuropsychopharmacol Biol Psychiatry, 77:49-56.
8 Zhang B et al. (2017), Altered task-specific deactivation in the default mode network depends on valence in patients with major depressive disorder. Journal of Affective Disorders, 207:377-383.
9 Wang X et al. (2017), Early Changes in Cortical Emotion Processing Circuits after Mild Traumatic Brain Injury from Motor Vehicle Collision. Journal of Neurotrauma, 34(2):273-280.
10 Szabo AG et al. (2017), Impaired mixed emotion processing in the right ventrolateral prefrontal cortex in schizophrenia: an fMRI study. BMC Psychiatry, 17(1):391.
11 Amgrim N et al. (2019), Effect of hypoxia on BOLD fMRI response and total cerebral blood flow in migraine with aura patients. Journal of Cerebral Blood Flow and Metabolism, 39(4):680-689.
12 Dimoka A et al. (2012), How to conduct a functional magnetic resonance (fMRI) study in social science research. MIS Quarterly, 36(3):811-840.
13 Lambert B et al. (2017), A functional MRI study on how oxytocin affects decision making in social dilemmas: Cooperate as long as it pays off, aggress only when you think you can win. Hormones and Behaviour; 94:145-152.
14 Bethlehem R et al. (2013), Oxytocin, brain physiology, and functional connectivity: a review of intranasal oxytocin fMRI studies. Psychoneuroendocrinology; 38(7):962-74.
15 Gawda B et al. (2017), Valence of Affective Verbal Fluency: fMRI Studies on Neural Organization of Emotional Concepts Joy and Fear. Journal of Psycholinguistic Research, 46(3):731-746.
16 Hsu CT et al. (2018), How mimicry influences the neural correlates of reward: An fMRI study. Neuropsychologica, 116(Pt A):61-67.
17 Amaro E & Barker GJ et al. (2006), Study design in fMRI: Basic principles. Brain and Cognition, 60:220-232.
18 Black DF et al. (2017), American Society of Functional Neuroradiology-Recommended fMRI Paradigm Algorithms for Presurgical Language Assessment. American Journal of Neuroradiology, 38:E65-E73.
19 American Society for Functional Neuroradiology. Available: https://www.asfnr.org/wp-content/uploads/ASFNR-BOLD-Paradigms.pdf
20 Siemens Healthineers (2019), MRI Patient Experience Accessories. Available: https://static.healthcare.siemens.com/siemens_hwem-hwem_ssxa_websites-context-root/wcm/idc/groups/public/@global/@imaging/documents/download/mda4/oty4/~edisp/siemens-healhineers_mri-patient-experience-accessories-06286879.pdf
21 Lemaire C et al. (2009), Impact of audio/visual systems on pediatric sedation in magnetic resonance imaging. Journal of Magnetic Resonance Imaging, 30(3):649-655.
22 fMRI Techniques and Protocols, 2nd ed. Ed. Massimo Filippi, Neuromethods 119, Springer Protocols.
23 Unadkat P et al. (2019), Functional MRI Task Comparison for Language Mapping in Neurosurgical Patients. Journal of Neuroimaging, 29:348-356.
24 Hoge R et al. (2015), Improving Sensitivity and Specificity in BOLD fMRI Using Simultaneous Multi-Slice Acquisition. MAGNETOM Flash, 63: 65-69.
25 Bouchard LO et al. (2017), Simultaneous Multi-Slice: a Case-based Presentation of Pre-Operative Brain Tumor Evaluation. MAGNETOM Flash, 68:19-21.
26 Zaitsev M et al. (2017), Prospective Motion Correction in Functional MRI. Neuroimage, 154:33-42.
27 Voyvodic JT (2012), Reproducibility of single-subject fMRI language mapping with AMPLE normalization. Journal of Magnetic Resonance Imaging, 36(3):569-580.

Contact

Vicky Sherwood, Ph.D.
Application Specialist
NordicNeuroLab AS
Møllendalsveien 1
N-5009 Bergen
Norway
Mobile: +44 7367 190 271
vicky@nordicneurolab.com

Vicky Sherwood

Tina Pavlin

Taking the Complexity out of Brachial Plexus MRI

Adrien Jaccoud[1]; Graça Maria Fernandes[2]; Marie-Françoise Favre-Felix[3]; Corentin Mauris[1]; Nicolas Dechâtre[4]; Jean-Luc Montazel[5]; Alexandre Lesage[5]; Pierre Pottecher[5]

[1]GIE IRM74, Groupement d'Intérêt Economique Imagerie par Résonance Magnétique, Annecy, France
[2]Siemens Healthineers, Saint Priest, France
[3]Directrice d'établissement de santé, retraitée, GIE IRM74, Annecy, France
[4]Spécialiste Application Clinique IRM, Medical Professionals, Annecy, France
[5]Radiologues, Groupe IMARA, Clinique générale, Annecy, France

Introduction

Brachial plexus MRI scans are diagnostically highly relevant. However, the routine examination of the brachial plexus is made difficult by its structure and anatomy. Since imaging staff rarely perform such examinations, they often do so with trepidation and, as a result, may make errors. Moreover, the examination is most often described using a 3T MRI system [3–6]. In our multi-site structure in Annecy, France, consisting of 7 MRI scanners from Siemens Healthineers, this type of imaging, which was previously performed infrequently (0.06% in 2017), is requested and performed more often (0.13% in 2018 and 0.18% in 2019 [2]). Given the strong demographic pressure and subsequent growing demand for brachial plexus imaging [1], the optimization of protocols via the use of Dot engines, as well as new 3D acquisition techniques such as CAIPIRINHA SPACE, are required to better structure this examination, to reproduce it over time, and to homogenize it for our various MRI systems. In short, these protocols take the complexity out of brachial plexus imaging.

In this article, we share with you how we introduced brachial plexus MRI at 1.5T to cover 100% of indications by simplifying the work of radiology technologists, strengthening the analysis by radiologists (who do not perform this type of examination very often), and responding to the high demand for our activity.

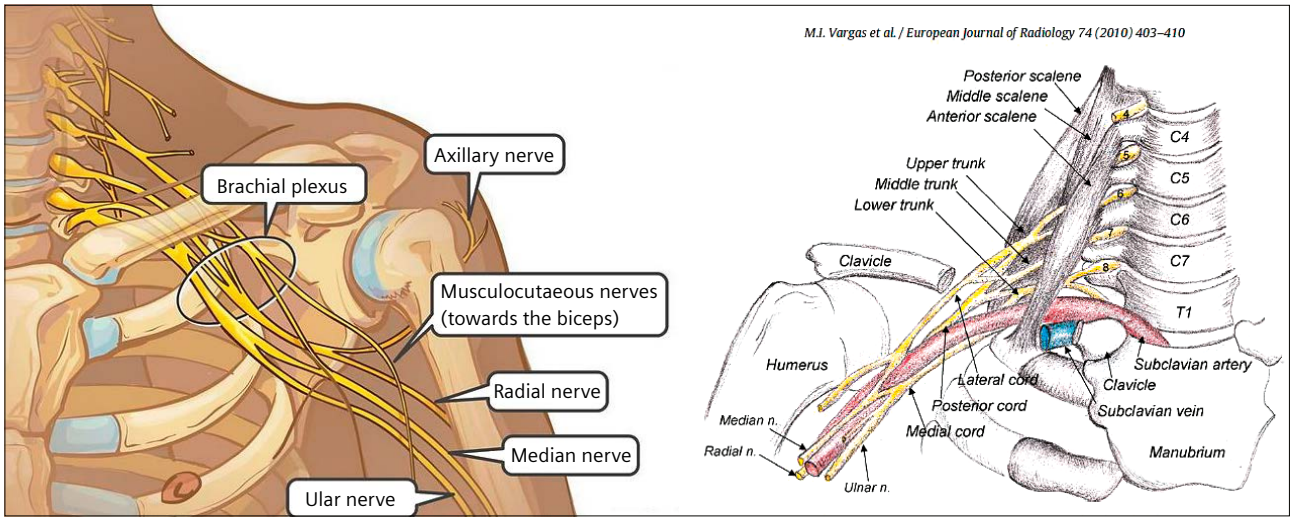

1 **Anatomical diagrams.** [6]
The brachial plexus is formed by the union of the anterior branches of the last four cervical nerves (C5, C6, C7, C8) and the first thoracic nerve (T1). The union of these nerves contributes to the creation of the three primary trunks that form three secondary trunks and culminate in the terminal branches. Functionally, the posterior segment of the plexus largely corresponds to the plane of extension of the upper limb (shoulder, elbow, and wrist) and the anterior segment to the plane of flexion (elbow, wrist, and fingers).

Anatomical overview / indications

The indications for brachial plexus MRI are:
- **Trauma** (investigation of root avulsion): see Figures 7A, B.
- **Primary or secondary tumors**: see Figures 8A, B.
- **Inflammation** (radiculoplexus neuropathy, etc.): see Figure 9.
- **Thoracobrachial outlet syndrome**: see Figures 14, 15.

Investigation using MRI is complex:
- Multiple anatomical structures: arteries and veins, fat, bones, muscles, tendons, nerves;
- Inhomogeneities in the B_0 field related to air – neck – shoulders interfaces leading to difficulties in carrying out efficient B_0 adjustment (shimming); and,
- Proximity of the lungs: presence of motion artifacts related to breathing.

Robust acquisition techniques must therefore be applied.

Historically, our protocols have always been dependent on technologists/radiologists, who must choose from these options: T2w TSE 2D in 3 planes; or STIR TSE 2D or 3D; or T2w Dixon in 3 planes; or T1w TSE in 3 planes; CISS; postcontrast T1w TSE with fat saturation or water excitation; or T1w TSE Dixon; or T1w 3D Dixon VIBE.

The literature largely recommends the use of 3D TSE STIR (SPACE). However, such an application can be time consuming (8 to 12 minutes) [3, 4, 8] and is generally recommended for 3T. It would therefore appear to be inappropriate for our work, due to its impact in terms of time. In our structure, a 3T field only became available in September 2019, with the delivery of a MAGNETOM Lumina system, which is principally oriented toward neurological, abdominal, and pelvic imaging. Recent improvements in 3D techniques in general and the benefits of the CAIPIRINHA algorithm in particular, along with the systematic investigation protocol in the Dot Cockpit makes 3T MRI especially efficient and effective.

Brachial plexus investigation protocol

Equipment

The strategies described for each stage are applied and reproduced on our six 1.5T MRI scanners and our 3T MRI scanner, taking into account the technical constraints of each device.

The ergonomic quality of the coils from Siemens Healthineers, the ability to pool them at each site, their similar interfaces equipped with the Dot Cockpit (*syngo* MR E11A, E11C, XA11), the two *syngo*.via servers covering the entire range of MRIs, and the three geographical sites allow a high level of convenience.

- Choice of coils: Head/Neck 20ch/16ch + Body 18ch/12ch + Spine 24ch/32ch
- Investigation exclusively in 3D sequences: SPACE, FLASH, and Dixon VIBE techniques
- Creation of a Dot workflow dedicated to acquisition consoles
- Creation of a dedicated workflow on *syngo*.via

Our three MAGNETOM Aera systems use GRAPPA. For all the other MRIs, we were easily able to use the CAIPIRINHA technique for every 3D SPACE sequence.

Patient positioning

The patient is supine with their arms at their sides. The anterior element of the Head/Neck Coil can be removed with no loss of diagnostic quality. The Body Coil is placed contiguous to the NE1 element of the Head/Neck Coil.

In the case of brachial plexus pathologies originating in the last cervical vertebrae and following a path toward the arms, we apply cervical centering with an automatic movement of the table (for *syngo* MR E11 software) or "Select&GO" (for *syngo* XA software) cervical centering.

We routinely use three anterior elements and three posterior elements of the activated coils, which is ideal for CAIPIRINHA (high density of elements in the acquisition area).

As a first-line approach, we regularly use comparative bilateral anatomical coverage with a FOV of 300 mm, Phase FOV 125%, 120 slices at 1 mm thickness, and 20% phase oversampling to create reproducible images regardless of the patient, the user, or the system used.

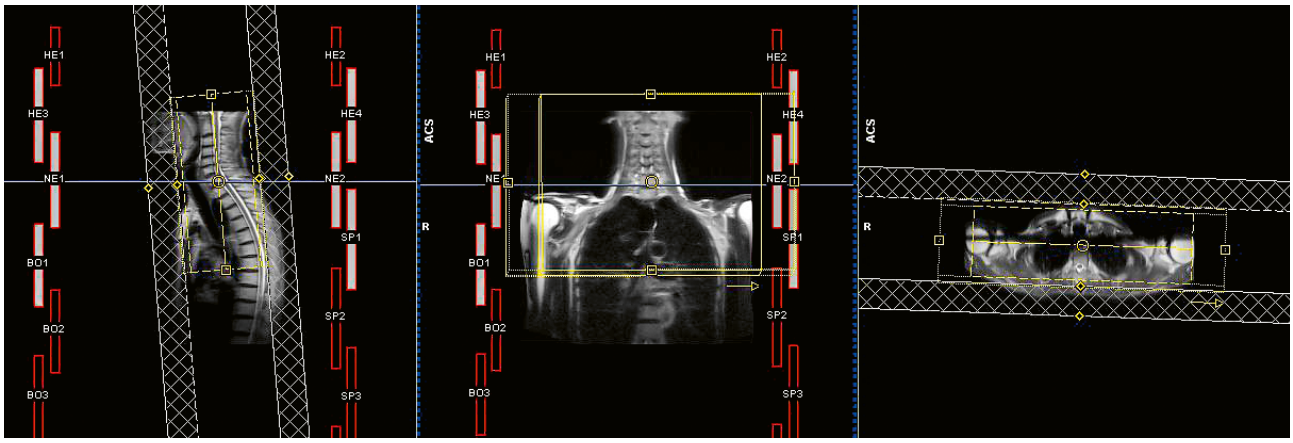

2 Anatomical positioning, activated coils, elements involved

Acquisition

1. Dot Cockpit: Creating a Dot workflow for brachial plexus analysis

The Dot Cockpit enables the establishment of different workflows to support the technologist and is fundamental in supporting this particular examination with the creation of strategies, alternatives, and the use of generic views for real-time reminders. Since 2014 (*syngo* MR E11), this tool adds real measurable value. Our Brachial Plexus Dot contains just a single strategy with a common core leading to four clinical decision points covering all medical indications for this anatomy (see Figure 3).

- On patient registration, our RIS Xplore (EDL, La Seyne Sur Mer, France) defines an examination label: "Brachial Plexus."

All MRI systems from Siemens Healthineers are able to identify this label and to automate the selection of the dedicated Dot Engine. The starting protocol is, therefore, always the same with no time wasted on selection, while the likelihood of choosing an inappropriate protocol is reduced.

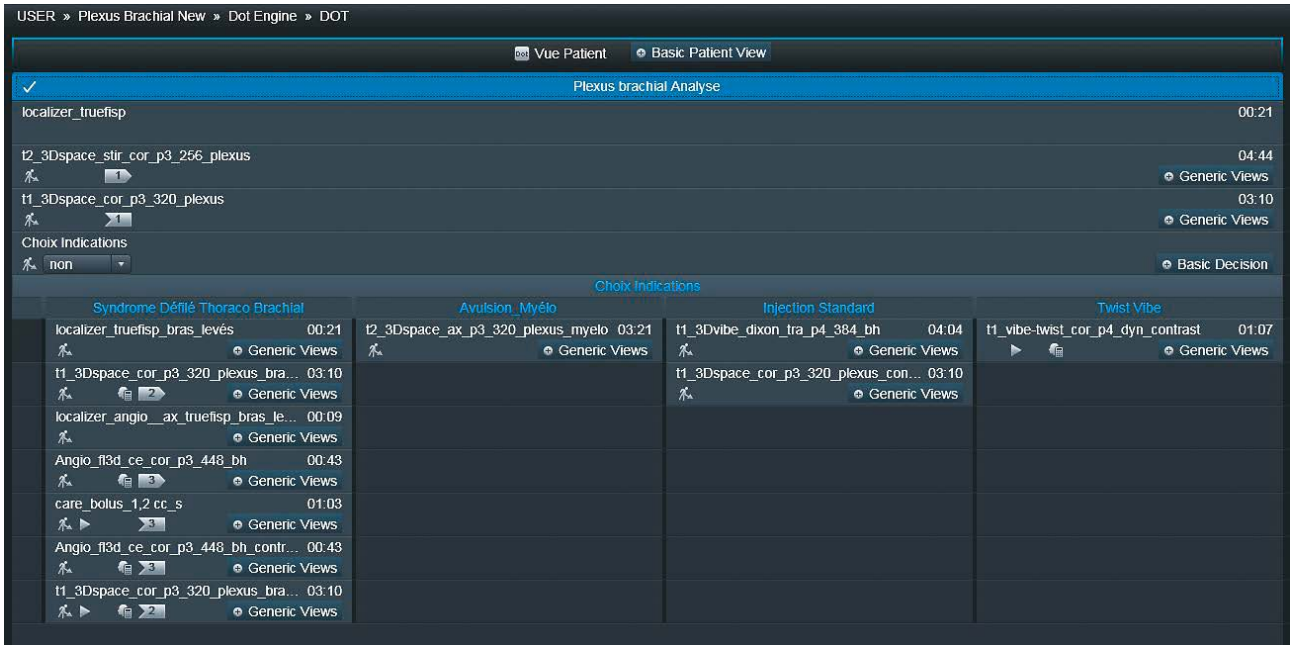

3 Brachial Plexus Dot

- For technologists, the anatomical positioning of a 3D sequence is simple compared with the alternative positioning for the multiple 2D series required for this complex anatomical area.

All the copy references and automatic subtractions are enabled in the Dot Cockpit, resulting in a significant reduction in clicks.

Depending on the radiologist or the indication, the technologist merely has to follow the internally validated scheme: This is a single strategy with four alternatives defined as clinical decision points linked to the medical indication.

2. Choice of sequences

3D SPACE TSE technique

The 3D SPACE TSE technique is the most robust and reproducible [7] and is therefore indispensable. The main advantages are:

- Fine slice planes, possibility to map lesions or follow nerve paths in a mass;
- Choice of T2 or T1 weighting;
- Ability to use inversion recovery (IR) for homogeneous fat suppression;
- Image creation acceleration algorithms (GRAPPA and, especially, CAIPIRINHA);
- Not very sensitive to movement, i.e., acquisition with free breathing;
- No flow artifacts; arteries appear as a hypointense signal (black vessels);
- Possibility of wide anatomical coverage.

We use it with STIR, T1, and T2 weighting.

Coronal 3D SPACE STIR

In T2 weighting with fat suppression, the nerve roots appear hyperintense. A 3D STIR sequence is widely recommended for imaging the brachial plexus. The acquisition times are, however, often very long (8 to 10 minutes) [3, 4, 6, 8]. Our optimized MR imaging protocols on the 1.5T scanner are shown in Figure 4. They were defined in order to obtain optimal quality while keeping the acquisition time sequence below 5 minutes.

The benefits of CAIPIRINHA have enabled us to apply more qualitative parameters without compromises in terms of time, or actually to reduce the acquisition time for improved patient comfort and to limit movement during the examination.

Our radiologists have therefore been reassured about using the 3D STIR sequence. This sequence has also been spread across the whole fleet of MRI systems in order to improve our examinations of this anatomy (see Figure 5).

The next step is to work on suppressing some of the surrounding venous flows that appear as a hyperintense signal and can sometimes affect the radiologist's analysis. The application of "black blood" gradients is an interesting option [5]. The flows are not suppressed completely and the signal of all tissues appears a little bit flat, although the differentiation of the roots is good (see Figure 6A–C).

Otherwise, there is a simple technique that makes it possible to obtain a satisfactory result: the injection of gadolinium [6]. When the injection of a contrast agent is anticipated for an investigation of the brachial plexus, we use the 3D SPACE STIR sequence post contrast. In fact, after injecting a gadolinium contrast agent, the T1 relaxation time of the surrounding vessels becomes similar to the T1 relaxation time of the fatty tissues; the vessel signal is therefore flattened [6].

Comparative parameters of 3D SPACE STIR for 1.5T and 3T MRI examinations at GIE IRM74, France

MR system	MAGNETOM Aera Tim4G 1.5T	MAGNETOM Altea BioMatrix 1.5T	MAGNETOM Avanto Fit Tim4G 1.5T	MAGNETOM Amira BioMatrix 1.5T	MAGNETOM Lumina BioMatrix 3T
Algorithm	**GRAPPA pat3**	CAIPIRINHA pat4	CAIPIRINHA pat4	CAIPIRINHA pat4	CAIPIRINHA pat4
Time	4 min 44 s	**3 min**	**4 min 2 s**	**3 min**	4 min 33 s
Matrix	320 x 256	320 x 256	**408 x 384**	320 x 256	**448 x 437**
TR (ms)	2000	2000	**3500**	2000	**3000**
TE (ms)	252	252	259	252	332

Figure 4: Table of 3D SPACE STIR parameters used at our facility. The parameters that represent a gain compared with the first base sequences on MAGNETOM Aera 1.5T with GRAPPA are shown in bold.

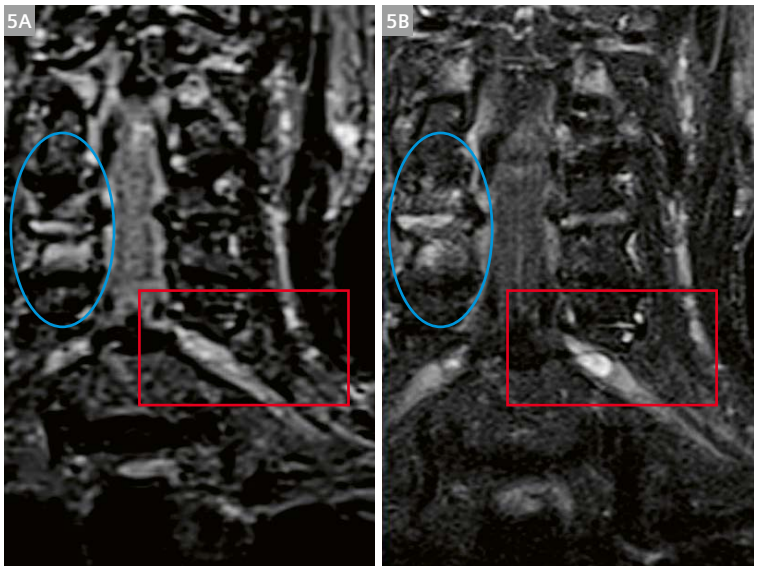

5 Comparison of a coronal 3D SPACE STIR, GRAPPA 3 256 matrix in 4 min 44 s **(5A)** with a coronal 3D SPACE STIR, CAIPI 4, 384 matrix in 4 min 4 s **(5B)** in the same patient. Osseous hyperintense signal (blue circle), root exiting foramen (red rectangle). Images have been acquired using a MAGNETOM Avanto Fit 1.5T system, with Tim4G.

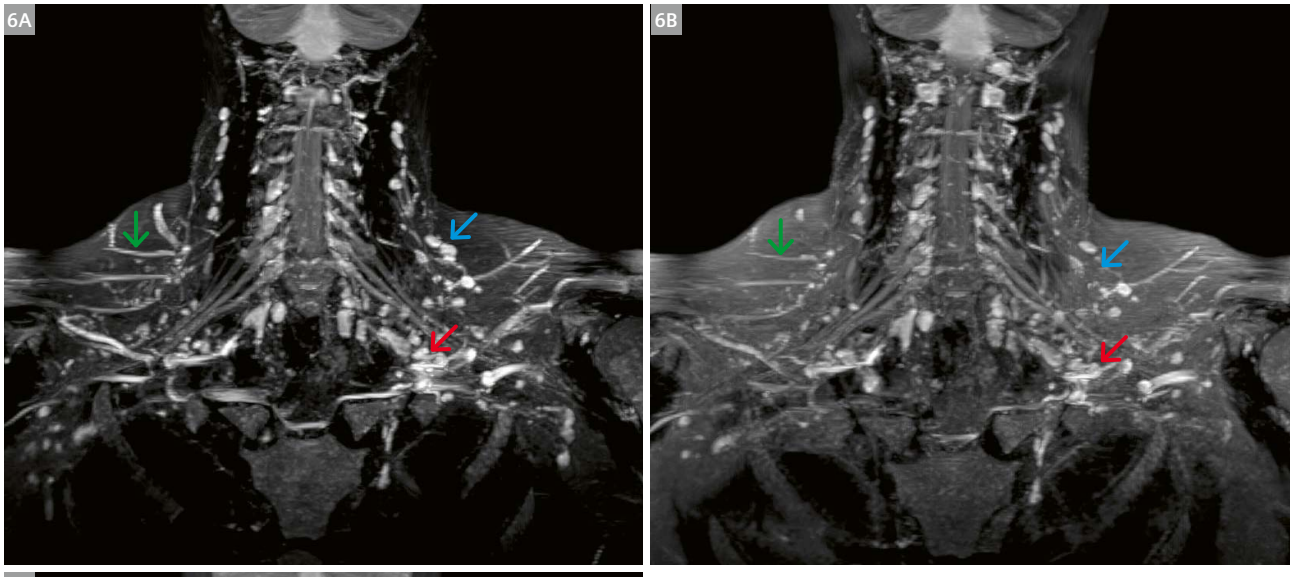

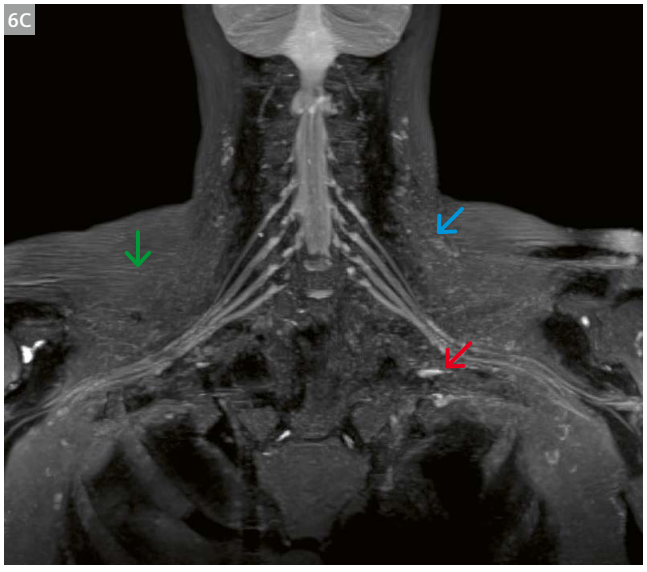

6 3D STIR SPACE performed on the same patient aimed at saturation of the surrounding vascular signals (colored arrows). Avanto Fit 1.5T system, Tim4G.
(6A) 3D CAIPIRINHA SPACE STIR standard: Good analysis of the plexus and surrounding vessels in a T2-weighted series with hyperintense signal.
(6B) 3D CAIPIRINHA SPACE STIR with the application of "black blood" gradients: Analysis of the nerve roots forming the plexus is still satisfactory; the vessels in the T2-weighted series are attenuated. The signal from all tissues is flattened with no loss of quality for the nerve roots.
(6C) 3D CAIPIRINHA SPACE STIR after injection of contrast agent. Almost complete suppression of the surrounding vessels. Very good differentiation of nerve roots.

Various cases on pathologies of the brachial plexus – coronal 3D SPACE STIR sequences

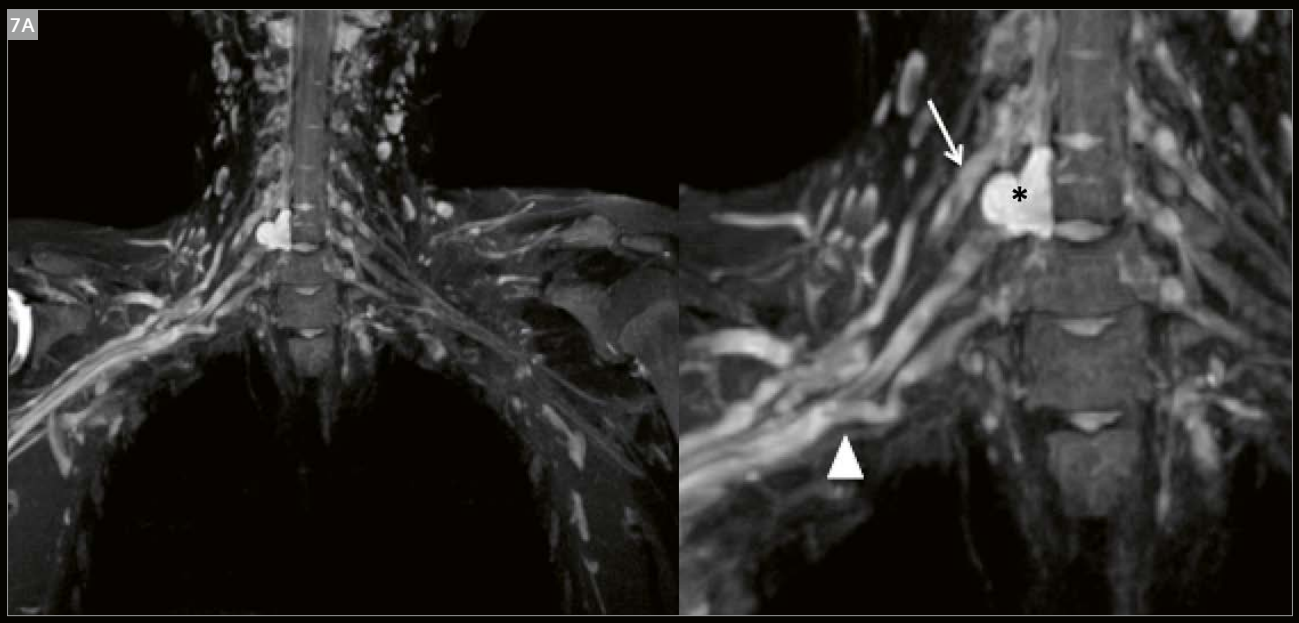

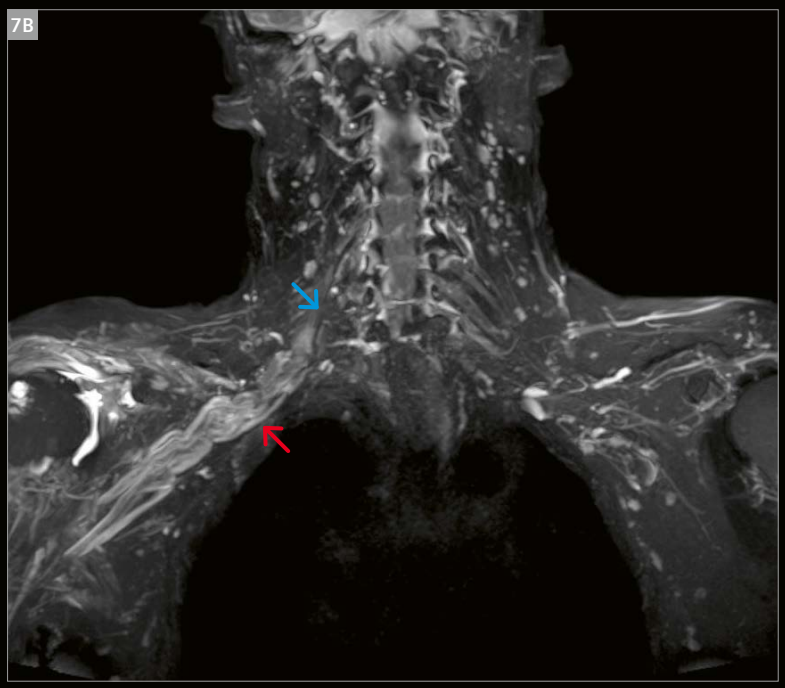

7 **Trauma:**
(7A) A 17-year-old patient with deficit in areas C5–C6 and right C7, in the context of trauma sustained two months prior. 3D STIR SPACE coronal sequences. Results: Thickening in T2 hyperintense signal of C6 root on the right (arrow). Radicular avulsion of C7 root on the right with pseudomeningocele (asterisk). T2 hyperintense signal of C8 root on the right in the interscalene triangle (arrowhead). MAGNETOM Aera 1.5T system, Tim4G.
(7B) Pre-therapeutic assessment of a 53-year-old patient with a history of trauma. 3D STIR SPACE coronal sequence, thick MIP. Results: No visualization of the C6, C7, and C8 roots (blue arrow) of the right brachial plexus suggesting a cervical lesion with distal retraction (red arrow) of the plexus roots at 4 cm from their cervical origin. Edema from Wallerian degeneration of the plexus trunks and fascicules downstream. Edema due to denervation of the supraspinatus, infraspinatus, small circular, larger circular, subscapularis, deltoid, and longissimus muscles.

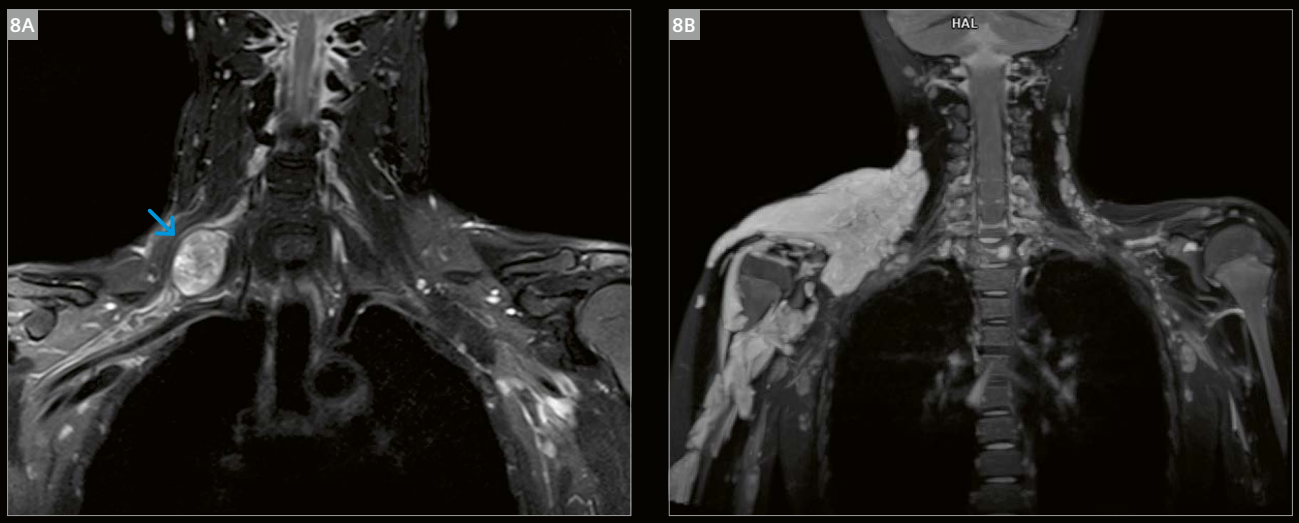

8 Tumor
(8A) Thick MPR. Mapping of a neurofibroma (blue arrow) in contact with the right brachial plexus.
(8B) Thick MIP. Vascular malformation with slow flow.

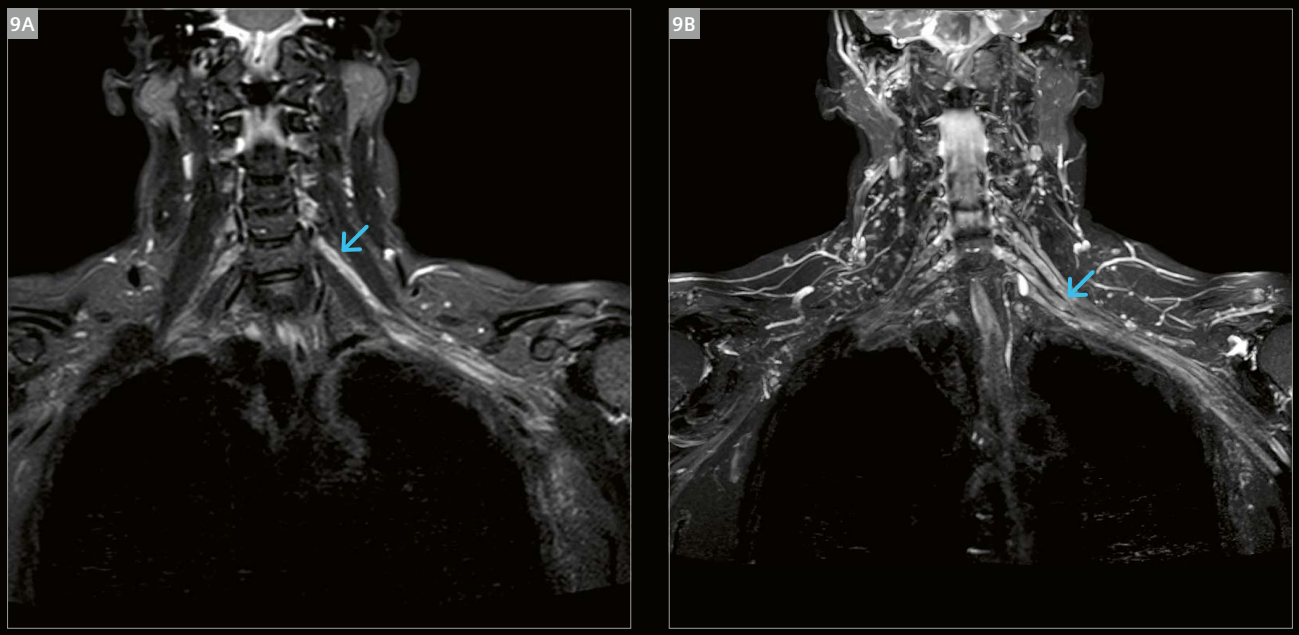

9 Inflammation
A 55-year-old patient monitored due to breast cancer with loss of sensitivity in the left upper limb in the context of radiotherapy. Suspected plexitis. Result: Plexitis in the left root (arrow).

Coronal T1w 3D SPACE

We use this sequence because it enables an excellent anatomical and morphological analysis, (Fig. 10) including analysis of anatomical reports in 3D, assessment of nerve caliber, excellent muscle/fat/bone/nerve/black vessel contrast, and high signal reserve capacity.

The benefits of CAIPIRINHA make the T1w 3D SPACE technique an essential sequence due to its acquisition speed, the image quality, and enhanced patient comfort during the "arms raised" position (indicated for thoracobrachial outlet syndrome, as described below).

We apply it for 2 minutes 30 seconds on MRI systems equipped with the CAIPIRINHA algorithm (see table in Fig. 11).

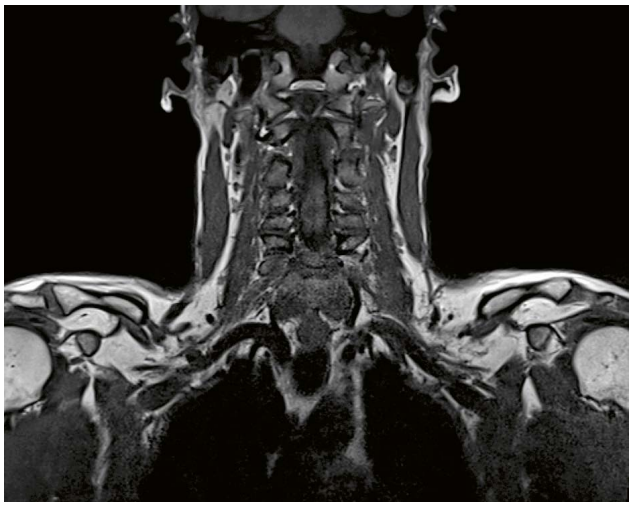

10 Coronal T1w SPACE centered on the brachial plexus.

Comparative T1w 3D SPACE parameters for 1.5T and 3T MRI examinations at GIE IRM74, France					
MR system	MAGNETOM Aera Tim4G 1.5T	MAGNETOM Altea BioMatrix 1.5T	MAGNETOM Avanto Fit Tim4G 1.5T	MAGNETOM Amira BioMatrix 1.5T	MAGNETOM Lumina BioMatrix 3T
Algorithm	GRAPPA pat3	CAIPIRINHA pat4	CAIPIRINHA pat4	CAIPIRINHA pat4	CAIPIRINHA pat4
Time	3 min 10 s	**2 min 33 s**	**2 min 37 s**	2 min 33 s	2 min 42 s
Matrix	360 x 320	360 x 320	**476 x 448**	360 x 320	**389 x 448**
TR (ms)	470	**600**	500	**600**	**600**
TE (ms)	23	15	15	15	23

Figure 11: Table showing T1w 3D SPACE parameters.

Axial T2w 3D SPACE

In indications of avulsions with pseudomeningocele, the benefits of T2w 3D SPACE provide an excellent complement (Fig. 12). It enables a myelographic study, depicting the intradural root segments, particularly in traumatic pathology, visualizing root avulsions. This sequence, which is always based on a basic 3D TSE SPACE with T2 weighting, provides good water (cerebrospinal fluid)/nerve contrast and submillimeter slices with the possibility of reconstructions in all planes [10].

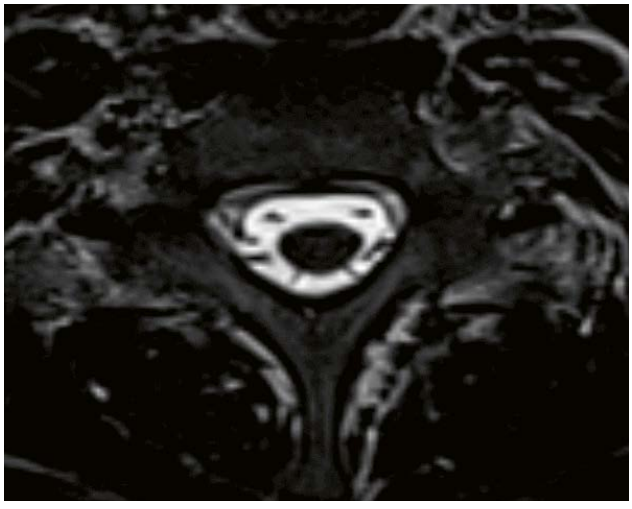

12 Axial T2w 3D SPACE for myelographic analysis.

Contrast-enhanced imaging: T1w SPACE or Dixon VIBE
The indications for contrast-enhanced MRI in the brachial plexus are inflammation, tumor, or angiography of the arteries (see thoracobrachial outlet syndrome below).

Our choice of post-contrast imaging comprises two alternatives: Coronal T1w 3D SPACE with automatic subtraction or T1w 3D Dixon VIBE (Fig. 13) for better management of fat saturation in this anatomy. It is recommended to avoid a fat saturation technique in this anatomical region. The B_0 inhomogeneities are too significant, despite the use of a dedicated shim (Standard Neck).

3. Thoracobrachial outlet syndrome
The objective is to analyze the brachial plexus according to the same 3D SPACE STIR protocol associated with the T1w 3D SPACE, but also to compare the reduction of the costoclavicular space and the associated neurovascular compressions when in the dynamic "arms raised" position. Historically, most investigations have been performed using SAG T1w TSE for this indication [10]. We now have a T1w 3D SPACE sequence that is far more robust with respect to movements and different flows, making analysis possible in all planes (Fig. 15A–C). We systematically complement it with a 3D FLASH arterial angiography series in order to evaluate the caliber of the subclavian artery in the "arms raised" position (see Figures 14 and 15D).

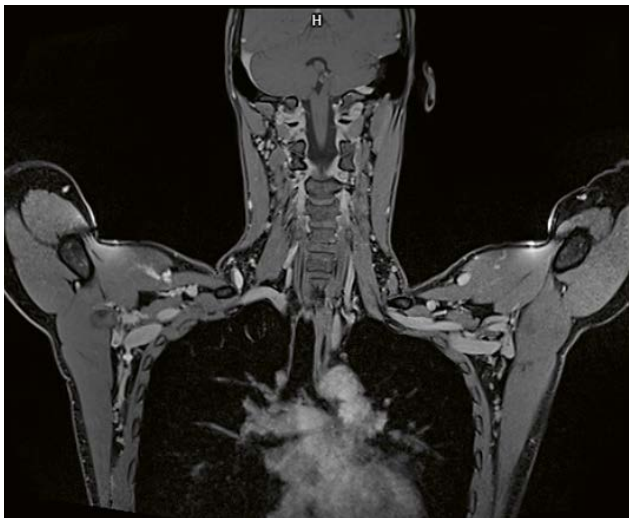

13 Post-contrast coronal 3D Dixon VIBE.

Various cases on pathologies of the brachial plexus – coronal T1w 3D SPACE

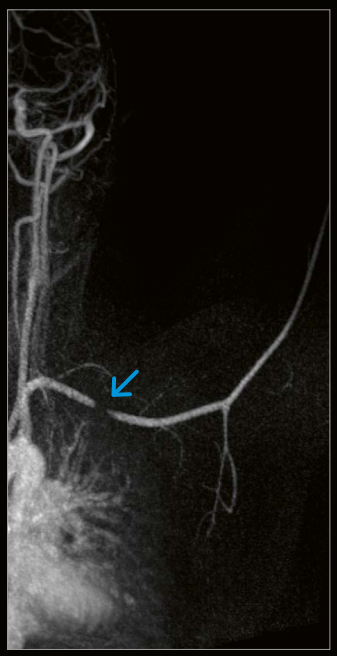

14 Case 1: A 28-year-old patient presenting with left thoracobrachial outlet syndrome. Coronal FLASH 3D angio MIP with arms raised.

Results: Loss of flow in left subclavian artery at the level of the left costoclavicular pinching. The stenosis is evaluated at 90% according to the MRI scan.

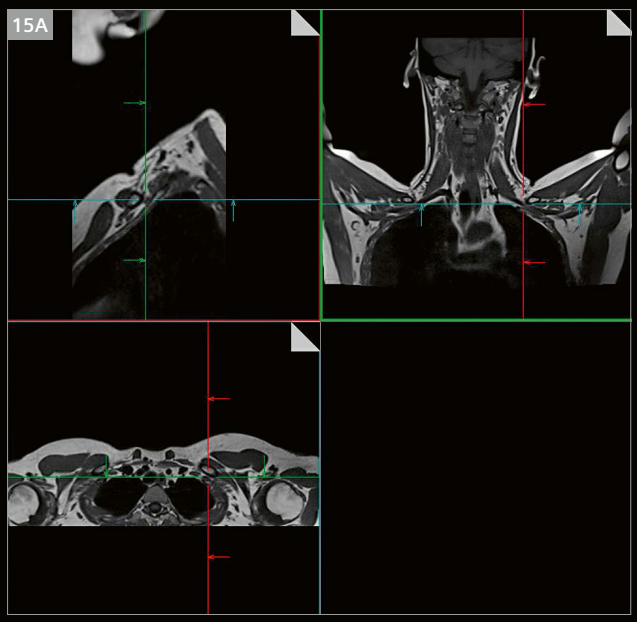

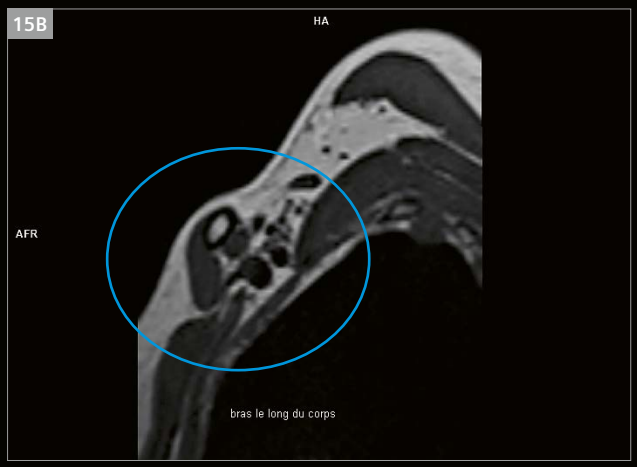

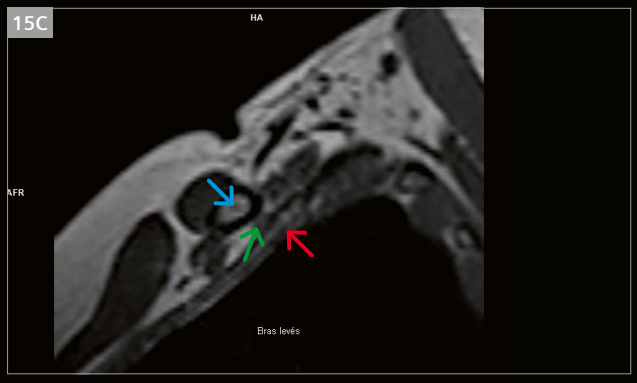

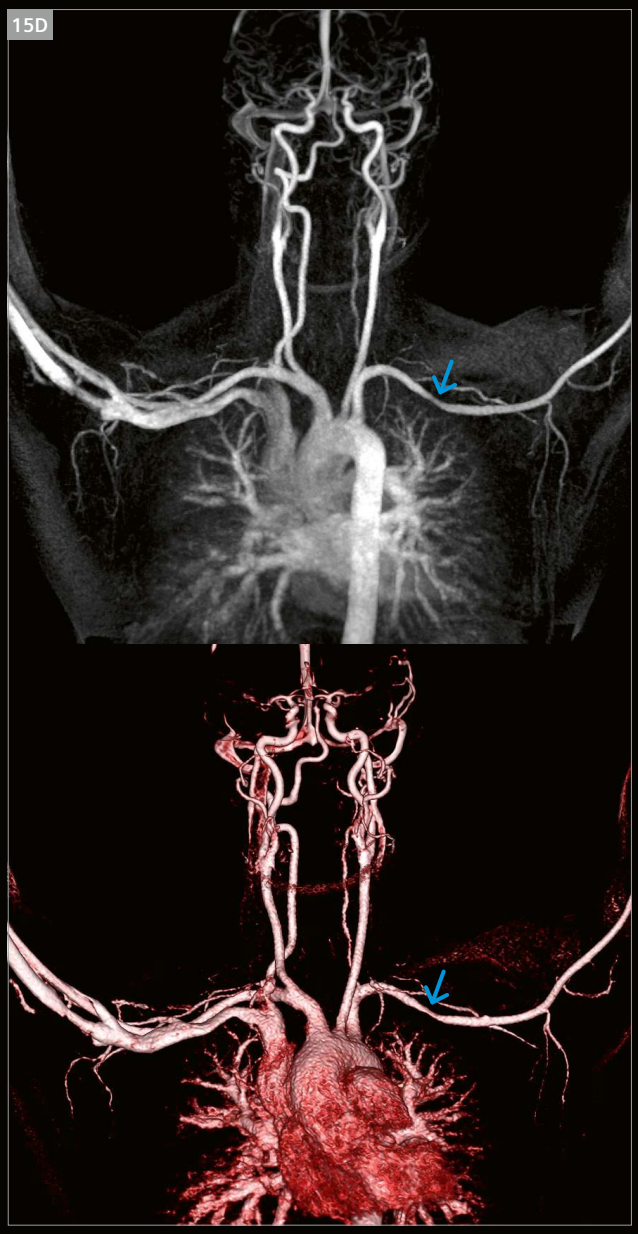

15 Case 2: A 49-year-old patient presenting with left thoracobrachial outlet syndrome, with suspected plexus involvement.
(15A) Coronal T1w 3D SPACE with arms raised, visualized in 3 planes at the level of the left subclavian artery.
(15B) Analyzed area with arms at the side of the body in the sagittal plane (blue circle).
(15C) Visualization with arms raised in the sagittal plane. Observation of the compression of the left subclavian artery (green arrow) between the clavicle (blue arrow) and the rib (red arrow).
(15D) Coronal FLASH 3D Angio MIP (top) and VRT (bottom).

Results: Asymmetry in the caliber of the left subclavian artery (blue arrow) at the level of the costoclavicular pinching. Arms raised, stenosis evaluated at 60% according to the MRI scan.

Postprocessing with *syngo*.via

The benefits of 3D acquisition simplify the work of technologists in terms of anatomical positioning, while yielding a more extensive image volume for interpretation by radiologists. In addition, several image volumes are available for analysis. We have developed a dedicated flow for brachial plexus analysis in 3D. By default, the 3D STIRs are displayed in MIPs 3 mm thick. This flow comprises three main analysis steps:

- **1 morphological step** (see Figure 16): Synchronized visualization of the 3D STIR in comparison with the 3D T1 in the AX, COR, and SAG comparative planes. STIR – T1 – T1 arms raised.

- **1 angiography step** (see Figure 17): Comparative visualization in MIP of the angio performed with arms raised with the T1w morphological acquisition also performed with arms raised.

- **1 fusion angio step** (see Figures 18–20): The FLASH 3D angiography imagery is superimposed with gadolinium onto the morphological T1w 3D SPACE. The angiographic image will automatically be associated with a "hot body" scale look-up table (LUT). The window adjustment by the physician allows a T1 morphological analysis or post-injection angiography. The benefits of this image fusion are relevant for the correlation between the patient's static anatomy and the dynamic angiographic analysis of the vessel of interest.

By configuring this *syngo*.via workflow in connection with the Dot acquisition, the radiologist is therefore automatically and immediately immersed in the image volumes. The differently configured synchronizations are very convenient in terms of the evolution of medical expertise (navigation, windowing, zoom, type of display, slice thickness). Handling becomes very simple and medical input is enhanced.

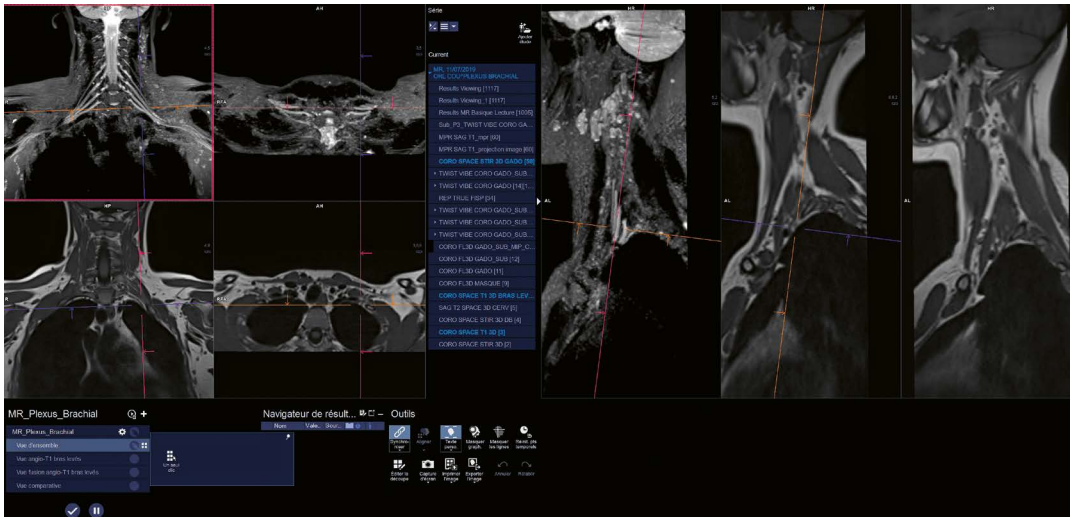

16 First step in the synchronized 3D morphological *syngo*.via analysis.

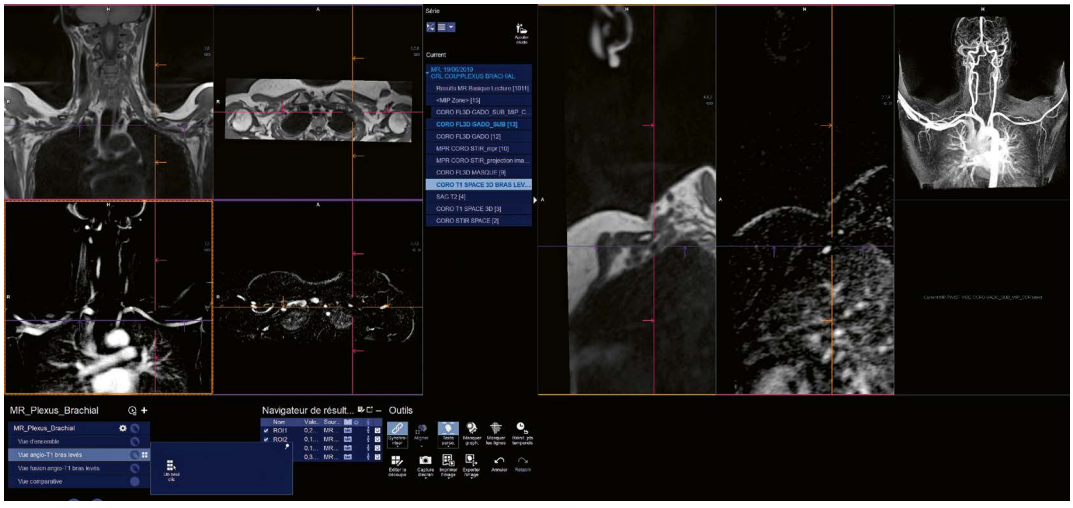

17 Second step in the comparative angiography *syngo*.via analysis with arms raised.

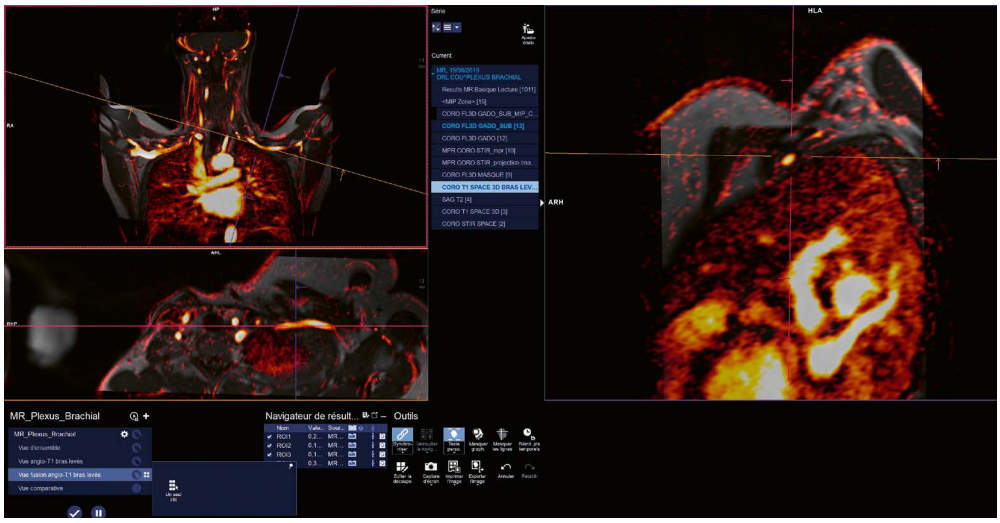

18 Third step in the *syngo*.via analysis with "hot body" T1w 3D SPACE and Angio FLASH 3D fusion window.

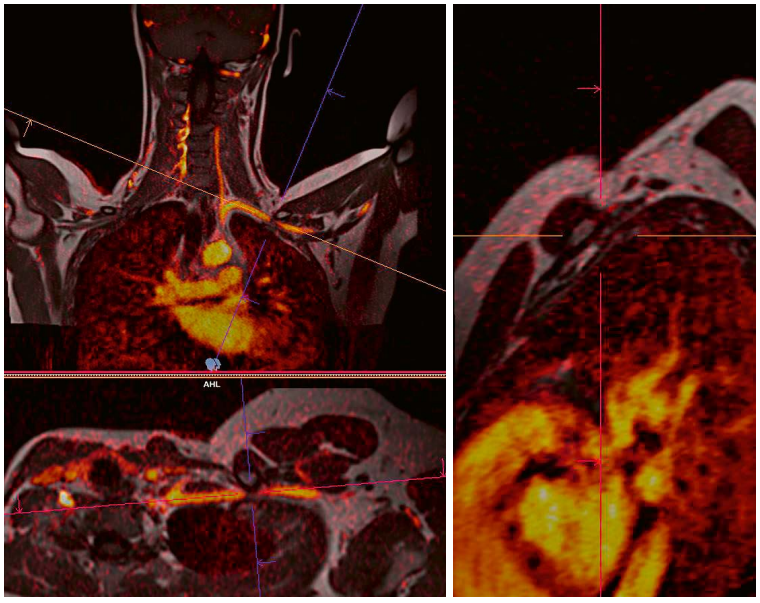

19 Compressive pathology: Fusion of contrast-enhanced angio FLASH 3D "hot body" window and T1w 3D SPACE arms raised images, centered on the compression zone of the left subclavian artery.

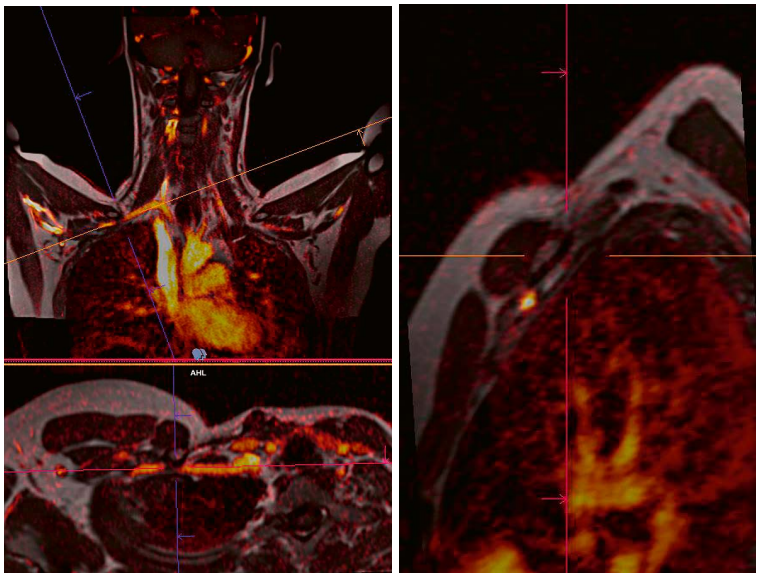

20 Compressive pathology in another patient: Fusion of contrast-enhanced angio 3D FLASH "hot body" window and T1w 3D SPACE images, centered on the compression zone of the right subclavian artery.

Conclusion

Within five years, we have greatly increased our diagnostic accuracy in examinations of the brachial plexus thanks to the new tools offered by Siemens Healthineers (Dot Cockpit, *syngo*.via VB30, the CAIPIRINHA algorithm, and new XA interfaces), we have been able to:

- optimize our patient care time and reduce the amount of time they spend in the MRI scanner;
- systematize a protocol covering 100% of indications for this anatomy;
- simplify this complex application, thus reducing stress for technologists; and,
- improve radiologist's analysis by optimizing and automating a maximum number of *syngo*.via post-processing tools for larger image volumes.

Our group has high expectations with respect to future developments in the field of brachial plexus imaging, and Compressed Sensing (CS SPACE) in particular. Since September 2019, the installation of our MAGNETOM Lumina 70 cm BioMatrix 3T MRI scanner has been the ideal tool to advance this investigation.

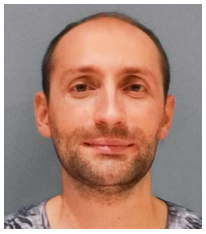

Contact

Adrien Jaccoud
Medical Electroradiology Technician,
multi-site contact
GIE IRM74
18 Rue de la Césière
74000 Annecy, France
a.jaccoud@irm74.org

Pierre Pottecher, M.D.,
Radiologist with Groupe IMARA,
Annecy Clinique Générale
GIE IRM74
18 Rue de la Césière
74000 Annecy
France
pierre.pottecher@gmail.com

Marie-Françoise Favre-Felix

Jean-Luc Montazel

Alexandre Lesage

Acknowledgments

The GIE IRM74 team and Siemens Europe/France would like to thank Marie-Françoise Favre-Felix, director of GIE IRM74, for her 27 years of MRI management work. You have made an enormous contribution to the performance and development of your medical imaging tools, having worked with 15 MRI systems from Siemens Healthineers of different generations. Thank you for your loyalty. Enjoy your retirement, Marie-Françoise!

References

1 Thouilleux C et al. Haute-Savoie: la plus forte croissance démographique de métropole. INSEE FLASH AUVERGNE-RHÔNE-ALPES. January 2019: 53.
2 Internal statistical data, GIE IRM74, Annecy, FRANCE
3 Viallon M et al. High-resolution and functional magnetic resonance imaging of the brachial plexus using an isotropic 3D T2 STIR (Short Term Inversion Recovery) SPACE sequence and diffusion tensor imaging. Eur Radiol. 2008 May;18(5):1018-23. doi: 10.1007/s00330-007-0834-4. Epub 2008 Jan 8.
4 Vargas MI et al. New approaches in imaging of the brachial plexus. Eur J Radiol. 2010 May;74(2):403-10. doi: 10.1016/j.ejrad.2010.01.024. Epub 2010 Mar 12.
5 Klupp E et al. Improved Brachial Plexus Visualization Using an Adiabatic iMSDE-Prepared STIR 3D TSE. Clin Neuroradiol. 2018 Jul 23. doi: 10.1007/s00062-018-0706-0. [Epub ahead of print]
6 Chen WC et al. Value of Enhancement Technique in 3D-T2-STIR Images of the Brachial Plexus. J Comput Assist Tomogr. 2014 May-Jun;38(3):335-9. doi: 10.1097/RCT.0000000000000061.
7 Mugler JP. Optimized Three-Dimensional Fast-Spin-Echo MRI. J Magn Reson Imaging. 2014 Apr;39(4):745-67. doi: 10.1002/jmri.24542. Epub 2014 Jan 8.
8 Singer AD et al. The Multidisciplinary Approach to the Diagnosis and Management of Nonobstetric Traumatic Brachial Plexus Injuries. Neuroradiology/Head and Neck Imaging. AJR Am J Roentgenol. 2018 Dec;211(6):1319-1331. doi: 10.2214/AJR.18.19887. Epub 2018 Sep 24.
9 https://www.plexusbrachial.com/
10 Petit-Lacour MC et al. MRI of the brachial plexus. J Neuroradiol. 2004; 31(3): 198-206.

MR Neurography as a Useful Tool in the Determination and Differentiation of Disorders of the Peripheral Nervous System

Florian Hessenauer and Mirko Pham

Department of Diagnostic and Interventional Neuroradiology, University Hospital of Würzburg, Germany

Introduction

At the core of a clinical MR Neurography protocol are high-resolution T2- or PD-weighted sequences with large longitudinal coverage of the nerve regions of interest [1].

Patients with sensory, motor, or autonomic symptoms specifically attributable to the peripheral nervous system (PNS) tend to have a long journey from their first contact with a healthcare professional to definite diagnosis and, where possible, appropriate therapy for their disease [2].

There are several reasons why the diagnostic determination and differentiation of PNS disease remains difficult [3, 4] and is facilitated by novel PNS imaging methods, particularly MR Neurography but also nerve sonography [5]:

- Individual and thus variable perceptions of body function/dysfunction, particularly with regard to painful and sensory symptoms
- Differentiation between functional orthopedic complaints and neurogenic dysfunction is not always straightforward [6]
- The nervous system itself is a highly sophisticated organ with different organization levels, sensory and motor modalities, and varying symptoms depending on the lesion level [4]
- Complex lesion patterns including partial or fascicular nerve lesions [7, 8]
- Limitations of physical, clinical, and electrophysiological examinations [3]

Consequently, PNS imaging is increasingly in demand in clinical diagnostics, particularly to address the challenge of correctly locating lesion sites spatially (PNS lesion localization) and accurately detecting nerve lesions (lesion determination) [7, 9, 10].

In recent years, several groups have successfully demonstrated that MR Neurography with dedicated receiver coils optimized with regard to signal-to-noise ratio (SNR) and facilitating large nerve coverage at high resolution is capable of significantly improving nerve lesion detection and localization [5–7,11–13]. It combines structural and pathomorphological information not only about topographically related organs such as muscles, tendons, vessels, joints, and bones but, in particular, provides detailed insight into intrinsic structural nerve lesions at their fascicular level [1, 7, 9, 10, 14, 15]. Under experimental conditions, it has even become possible at ultra-high magnetic field strengths not only to visualize nerve stems and fascicles but even to visualize the smallest functional subunits of a peripheral nerve, the axons, or at least the larger (myelinated) axons [16].

Furthermore, MR Neurography can also detect neurogenic muscle injury, such as muscle denervation [15], which is of additive and specific diagnostic value in the PNS. Such denervation patterns alone allow us to improve the accuracy of nerve lesion detection and localization. This can be particularly important when peripheral nerve disease, that is "peripheral neuropathy", has to be differentiated from root pathology (radiculopathy) or plexopathy. Finally, in several scenarios, imaging lesion detection/localization using MR Neurography was proven to yield higher sensitivity and accuracy in detecting nerve and muscle damage than with conventional diagnostic means [14, 17–19]. For example, denervation signs in muscle can be detected as early as 24 hours after damage is induced [15] while they do not become observable in an EMG until much later, typically approximately two weeks after induced damage [10].

In the following, we present two exemplary cases of MR Neurography investigations demonstrating its diagnostic clinical value.

Case 1

This patient presented with dysesthesia in the 4th and 5th finger of his right hand as well as weakness of the right arm which had developed over the course of two years. During this time, the patient consulted three specialists in the neurological and neurosurgical field who confirmed these sensory and motor symptoms in the distribution of the functional territories of the radial and ulnar nerves. A previous MRI scan at a remote outpatient site demonstrated insignificant multisegmental degenerative discopathy of the cervical spine.

From a clinical diagnostic perspective, the structural compression of both the radial and ulnar nerves in their peripheral course at the same time did not seem likely as a possible differential diagnosis. Finally, the first diagnostic assumption was Parsonage-Turner Syndrome (neuralgic shoulder amyotrophy) for which the patient received probatory corticosteroid therapy. This therapy was abandoned after four weeks when symptoms remained refractory.

The patient was referred for large coverage MR Neurography two months later, which was performed at our institution.

The patient was examined in prone, head first position with the symptomatic arm elevated and covered by the flexible NORAS Variety coil [20] in our MAGNETOM Skyra MRI at 3T. Positioning aids and additional weight were used to achieve a comfortable position for the patient and a stable position for the arm, centered to the main magnetic field. The fat-saturated axial T2-weighted sequences demonstrate a strong increase in nerve T2 signal of the radial and ulnar nerves beginning in the distal upper arm (Fig. 1A) with inconspicuous signal of the median nerve. In the distal imaging slabs (Figure 1B and especially 1C), higher signal intensity in the ulnar than in the median nerve can also be determined. In both Figures 1B and 1C, the deep/profundus branch of the radial nerve (syn. posterior interosseous nerve) is depicted within the supinator channel. Furthermore, pathological T2 signal increase in the muscular parenchyma is exhibited as a sign of denervation in most but not all the muscles of the extensor compartment innervated by the radial nerve. Additionally, several muscles innervated by the ulnar nerve, for example the flexor carpi ulnaris muscle, exhibit pathological T2-hyperintense parenchymal signal as evidence of neurogenic injury (i.e., denervation). At the same time, muscles innervated by the median nerve show normal signal. Any compressive etiology associated with these intrinsic T2 signal nerve lesions within the radial and ulnar nerves were not detectable. To summarize, these results strongly suggest a neuritic/autoimmune etiology of the underlying neuropathy and support the exclusion of root disease (radiculopathy or multiple radiculopathies) and plexus disease. Importantly, these findings indicate that the underlying disease is not focal and thus not focally treatable with surgical decompression at the spinal, the plexus, or the peripheral nerve stem levels.

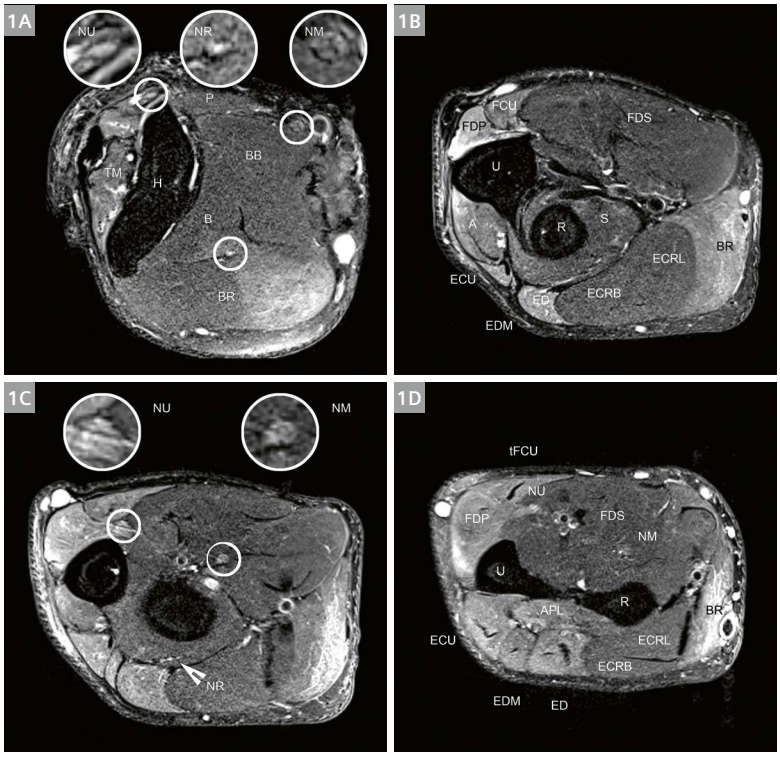

1 Fat-saturated T2-weighted 2D TSE axial slabs of the right arm (TR/TE 4500/65 ms, 60 slices of 3 mm thickness, FOV 220 mm, acquisition time: 5 min 17 s), **(1A)** distal upper arm; **(1B)** proximal forearm; **(1C)** second distal slab of the proximal forearm; **(1D)** distal forearm.

Abbreviations
Nerves and relevant innervated muscles:
Median nerve (NM): P: pronator teres, FDS: flexor digitorum superficialis
Radial nerve (NR): A: anconeus, APL: abductor pollicis longus, BR: brachioradialis, ECRB: extensor carpi radialis brevis, ECRL: extensor carpi radialis longus, ECU: extensor carpi ulnaris, ED: extensor digitorum, EDM: extensor digiti minimi, S: supinator, TM: triceps brachii caput mediale
Ulnar nerve (NU): FCU: flexor carpi ulnaris, tFCU: FCU tendon. FDP: flexor digitorum profundus
Additionally B: musculus brachialis, BB: musculus biceps brachii; H: humerus, R: radius, U: ulna

Digital zoom of nerve diameter in 1A and 1C 2.5x; arrowhead in 1C: Radial nerve within the supinator channel.

Case 2

This patient reported an episode of strong pain followed by prolonged loss of sensation in the shoulder and arms on both sides two weeks after suffering from erythema infectiosum (Parvovirus B19). Suspected diagnosis by the treating neurologist was an associated neuralgic amyotrophy (Parsonage-Turner Syndrome) or a sensory radicular C6 syndrome due to cervical discopathy.

A previously externally acquired MRI scan of the cervical spine shows the beginnings of bilateral herniation of the spinal disc within the C5/6 segment with discrete neuroforaminal confinement of the C6 root on both sides. We were approached to confirm or exclude Parsonage Turner Syndrome with MR Neurography of the brachial plexus.

We performed MR Neurography of the right brachial plexus as shown in (Fig. 2) using a combination of neck coil, inbuilt spine coil, and the 16-channel NORAS Variety coil (MAGNETOM Skyra). It depicts the lower cervical spinal nerves C5–Th1, the supraclavicular level of the brachial plexus with trunci superior, medius, and inferior, the fascicular level of the plexus with lateral, median, and inferior fascicles and infraclavicular level with fascicles, as well as proximal sections of the axillary nerve and nervus musculocutaneus. The close anatomic relationship between the nerves and vessels in particular as well as the inevitable thoracic excursions in the neck and shoulder region during breathing makes this examination prone to artifacts caused by movement or insufficient fat suppression. We examined the patient head first and in supine position, reducing to a minimum, although not completely controlling thoracic excursions and respiration artifacts by adding extra weight on top of the shoulder region and by advising our patient not to breathe heavily.

In our case, the MR Neurography of the brachial plexus reveals normointense nerve signal in the nerve roots C5–Th1 as well as in the proximal trunci superior and medius (Fig. 2B) and inferior (not shown). However, it did detect a strong and therefore unanimously pathological signal increase and thickening at the fascicular/cord level (Fig: 2C), which continues into the distal infraclavicular plexus and could also even be found in the distal origin of the axillary nerve (NA, Fig. 2D). This correlates well with the slightly but homogeneously increased parenchymal signal intensity of the anterior and posterior part of the delta muscle, indicating denervation (D, Fig. 2D).

Thus, given the typical clinical history, with onset of severe pain and nerve dysfunction after viral infection and clear increase in signal intensity beginning in the supraclavicular plexus and traceable into the infraclavicular plexus and the axillary nerve along with denervation edema in the deltoid muscle, we could rule out radicular C6 syndrome and instead were able to confirm the neuralgic amyotrophy (i.e., Parsonage-Turner Syndrome) [10, 21].

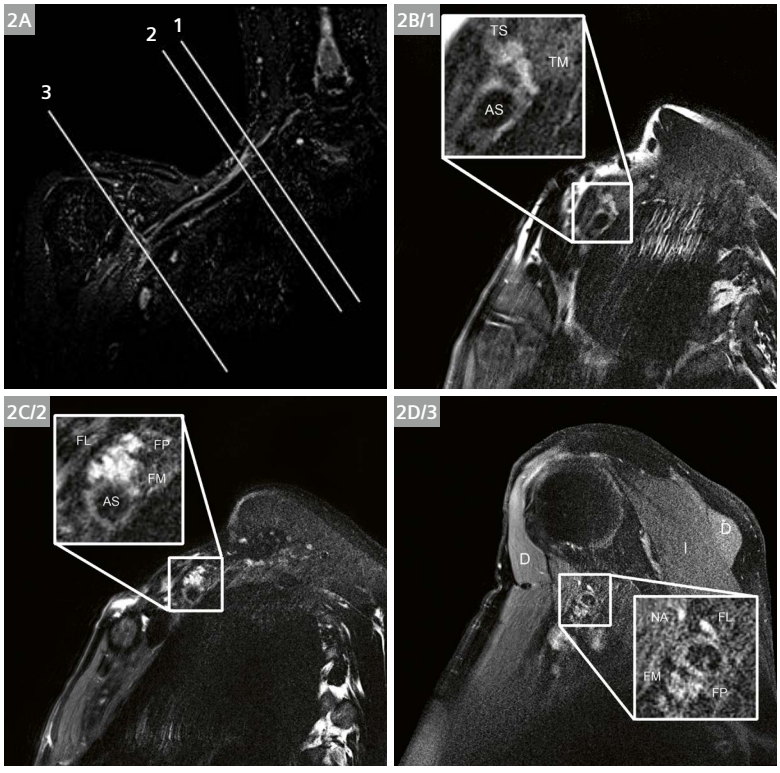

2 Plexus brachialis A: coronal T2 SPACE STIR (TR/TE/TI 2500/208/210 ms, 104 slices of 1 mm thickness, FOV 305 mm, acquisition time 6 min 19 s) showing the topography of the T2-weighted fat-saturated sagittal oblique slices 1–3 (TR/TE 4800/66 ms, 60 slices of 3 mm thickness, FOV 220 mm, acquisition time 5 min 38 s) represented in the images **2B–D**: 2B/1 proximal truncal level; 2C/2 proximal fascicular level; 2D distal fascicular level (infraclavicular).

Abbreviations
AS: arteria subclavia, D: musculus deltoideus, FL: fasciculus lateralis, FM: fasciculus medius, FP: fasciculus posterior, I: musculus infraspinatus, NA: nervus axillaris, TM: truncus medius, TS: truncus superior

References

1 Kollmer J, Bendszus M, Pham M. MR Neurography: Diagnostic Imaging in the PNS. Clin Neuroradiol. 2015;25 Suppl 2283–9. doi:10.1007/s00062-015-0412-0
2 Filler AG, Maravilla KR, Tsuruda JS. MR neurography and muscle MR imaging for image diagnosis of disorders affecting the peripheral nerves and musculature. Neurol Clin. 2004;22(3): 643–82, vi-vii. doi:10.1016/j.ncl.2004.03.005
3 Doughty CT, Seyedsadjadi R. Approach to Peripheral Neuropathy for the Primary Care Clinician. Am J Med. 2018;131(9): 1010–6. doi:10.1016/j.amjmed.2017.12.042
4 Watson JC, Dyck PJB. Peripheral Neuropathy: A Practical Approach to Diagnosis and Symptom Management. Mayo Clin Proc. 2015;90(7): 940–51. doi:10.1016/j.mayocp.2015.05.004
5 Pham M, Bäumer T, Bendszus M. Peripheral nerves and plexus: Imaging by MR-neurography and high-resolution ultrasound. Curr Opin Neurol. 2014;27(4): 370–9. doi:10.1097/WCO.0000000000000111
6 Assmus H, Antoniadis G, Bischoff C. Carpal and cubital tunnel and other, rarer nerve compression syndromes. Dtsch Arztebl Int. 2015;112(1-2): 14-25; quiz 26. doi:10.3238/arztebl.2015.0014
7 Bäumer P, Weiler M, Bendszus M, Pham M. Somatotopic fascicular organization of the human sciatic nerve demonstrated by MR neurography. Neurology. 2015;84(17): 1782–7. doi:10.1212/WNL.0000000000001526
8 Bäumer P, Kele H, Xia A, Weiler M, Schwarz D, Bendszus M, Pham M. Posterior interosseous neuropathy: Supinator syndrome vs fascicular radial neuropathy. Neurology. 2016;87(18): 1884–91. doi:10.1212/WNL.0000000000003287
9 Pham M. MR-Neurographie zur Läsionslokalisation im peripheren Nervensystem. Warum, wann und wie? [MR neurography for lesion localization in the peripheral nervous system. Why, when and how?]. Nervenarzt. 2014;85(2): 221-35; quiz 236-7. ger. doi:10.1007/s00115-013-3951–0
10 Wolf M, Wolf C, Weber M-A. Neurogene Myopathien und Bildgebung der Muskeldenervation [Neurogenic myopathies and imaging of muscle denervation]. Radiologe. 2017;57(12): 1038–51. ger. doi:10.1007/s00117-017-0316-x
11 Kronlage M, Knop KC, Schwarz D, Godel T, Heiland S, Bendszus M, Bäumer P. Amyotrophic Lateral Sclerosis versus Multifocal Motor Neuropathy: Utility of MR Neurography. Radiology. 2019;292(1): 149–56. doi:10.1148/radiol.2019182538
12 Bergmeister KD, Schönle P, Böcker AH, Kronlage M, Godel T, Daeschler S, Bendszus M, Kneser U, Harhaus L, Schwarz D. Gezielte Therapieplanung bei traumatischen Nervenläsionen mittels MR-Neurographie [Improved diagnostics and therapeutic decision-making in traumatic peripheral nerve lesions using MR neurography]. Handchir Mikrochir Plast Chir. 2018;50(4): 232–40. ger. doi:10.1055/s-0044-101833
13 Löscher WN, Wanschitz J, Iglseder S, Vass A, Grinzinger S, Pöschl P, Grisold W, Ninkovic M, Antoniadis G, Pedro MT, König R, Quasthoff S, Oder W, Finsterer J. Iatrogenic lesions of peripheral nerves. Acta Neurol Scand. 2015;132(5): 291–303. doi:10.1111/ane.12407
14 Crim J, Ingalls K. Accuracy of MR neurography in the diagnosis of brachial plexopathy. Eur J Radiol. 2017; 9524–7. doi:10.1016/j.ejrad.2017.07.012
15 Bendszus M., Koltzenburg M., Wessig C., Solymosi L. Sequential MR Imaging of Denervated Muscel: Experimental Study. Am J Neuroradiol;2002(22): 1427–31.
16 Heddings A, Bilgen M, Nudo R, Toby B, McIff T, Brooks W. High-resolution magnetic resonance imaging of the human median nerve. Neurorehabil Neural Repair. 2004;18(2): 80–7. doi:10.1177/0888439004267074
17 Kollmer J, Sahm F, Hegenbart U, Purrucker JC, Kimmich C, Schönland SO, Hund E, Heiland S, Hayes JM, Kristen AV, Röcken C, Pham M, Bendszus M, Weiler M. Sural nerve injury in familial amyloid polyneuropathy: MR neurography vs clinicopathologic tools. Neurology. 2017;89(5): 475–84. doi:10.1212/WNL.0000000000004178
18 Kollmer J, Weiler M, Purrucker J, Heiland S, Schönland SO, Hund E, Kimmich C, Hayes JM, Hilgenfeld T, Pham M, Bendszus M, Hegenbart U. MR neurography biomarkers to characterize peripheral neuropathy in AL amyloidosis. Neurology. 2018;91(7): e625-e634. doi:10.1212/WNL.0000000000006002
19 Pham M, Oikonomou D, Hornung B, Weiler M, Heiland S, Bäumer P, Kollmer J, Nawroth PP, Bendszus M. Magnetic resonance neurography detects diabetic neuropathy early and with Proximal Predominance. Ann Neurol. 2015;78(6): 939–48. doi:10.1002/ana.24524
20 NORAS MRI products GmbH Leibnizstraße 4, 97204 Höchberg, Germany. Variety_16Ch_Multipurpose_Coil_Manual 117234 Variety 16-Channel Multipurpose Coil 3T for Siemens Scanner.
21 van Eijk JJJ, Groothuis JT, van Alfen N. Neuralgic amyotrophy: An update on diagnosis, pathophysiology, and treatment. Muscle Nerve. 2016;53(3): 337–50. doi:10.1002/mus.25008

Prof. Mirko Pham Florian Hessenauer

Contact

Florian Hessenauer
Department of Diagnostic and Interventional Neuroradiology
University Hospital of Würzburg
Josef-Schneider-Str. 11, Haus B1
D-97080 Würzburg
Germany
Hessenauer_F@ukw.de

Cartilage Imaging of the Knee at 3T: Experiences with Different Sequences on a MAGNETOM Skyra Fit MRI System

Marc-André Weber, M.D., M.Sc.; Steve Küster; Bastian Klaan, M.D.

Institute of Diagnostic and Interventional Radiology, Pediatric Radiology and Neuroradiology, University Medical Center Rostock, Rostock, Germany

Abstract

Proton-density-weighted fat-suppressed or intermediately-weighted fat-suppressed turbo spin echo sequences are currently the standard two-dimensional (2D) sequences to delineate the cartilage of the knee. Several three-dimensional (3D) sequences are now available to assess cartilage with isotropic voxels and a reduced scan time thanks to the option of multiplanar reformations. We report here on our experience of cartilage imaging of the knee in clinical daily routine with different sequences on a MAGNETOM Skyra Fit 3-Tesla MRI system.

In order to answer questions on therapy from our clinical partners, we need to have robust and reliable, as well as consistent depiction of articular cartilage. Clinical questions, which need to be answered relate to the extent and depth of cartilage lesions, as well as to the differentiation of cartilaginous from bony components of a lesion and to the lesion's location within the compartments of the knee. To maximize the therapeutic and prognostic relevance of findings from cartilage imaging, radiologists need to be sensitive to often very subtle imaging clues. At the same time, we need to be aware of the limitations of our methods. Any displaced fragments, concomitant meniscal, ligamentous, and/or degenerative lesions that may be present need to be identified. To date, MRI is the workhorse of cartilage imaging and is largely based on moderately T2-weighted or proton-density (PD)-weighted fat-suppressed turbo spin echo (TSE) sequences [1, 2]. Direct MR and CT arthrography are the gold standard for evaluating thin cartilage layers, for instance to delineate the integrity of osteochondral lesions of the ankle joint [3]. Recent advances in coil and MR sequence design, increased availability of 3T MRI systems, and more and more sophisticated acceleration techniques allow for better spatial resolution and more robust image contrast with acceptable scan times. Recent advances in MRI include 3D isotropic joint imaging, which deliver higher signal-to-noise ratios of the cartilage in the ankle joint and fewer partial volume artifacts, for example, when compared with standard 2D sequences [3].

Imaging-based analysis of articular cartilage and its defects, as well as the radiologist who performs it, have to help answer the increasingly specific clinical questions that result from the growing experience with cartilage-dedicated therapies. Local aspects and topographic distribution of bone marrow edema patterns, careful analysis of the cartilage surface and of the subchondral plate, as well as the patient's clinical and biomechanical context are key to image analysis. Formal grading is helpful to communicate imaging findings, but is not sufficient for a comprehensive analysis [4]. It is more important to use the same language as the referring clinician and to have regular face-to-face case discussions; ideally before and after cartilage surgery or arthroscopy. When planning therapy, it is essential to assess the stability of a pure cartilage lesion or an osteochondral lesion. While MR imaging is helpful in this regard, it can be challenging and requires consideration of the arthroscopic and histologic perspective. This is why close communication with the orthopedic and trauma surgeon is critical for quality control in radiology reporting. In the following, we report on cartilage imaging findings using a MAGNETOM Skyra Fit system relevant for lesion analysis based on our experience in clinical routine.

At our MAGNETOM Skyra Fit system (software version *syngo* MR E11C), we use the following protocol for cartilage imaging of the knee with a dedicated 15-channel knee coil from Siemens Healthineers:

Protocol	Acquisition Parameters	TA
Localizer		0:27 min
Sag T1 TSE	Voxel 0.3 x 0.3 x 3 mm, FOV 170 mm, TR 560 ms, TE 12 ms	3:38 min
Sag PD TSE fs	Voxel 0.3 x 0.3 x 3 mm, FOV 170 mm, TR 5030 ms, TE 31 ms	3:43 min
Cor PD TSE fs	Voxel 0.4 x 0.4 x 3 mm, FOV 170 mm, TR 3000 ms, TE 26 ms	3:38 min
Ax PD TSE fs	Voxel 0.4 x 0.4 x 2.5 mm, FOV 140 mm, TR 4550 ms, TE 27 ms	3:58 min
DESS 3D	Voxel 0.6 x 0.6 x 0.6 mm, FOV 150 mm, TR 14.1 ms, TE 5 ms	5:30 min

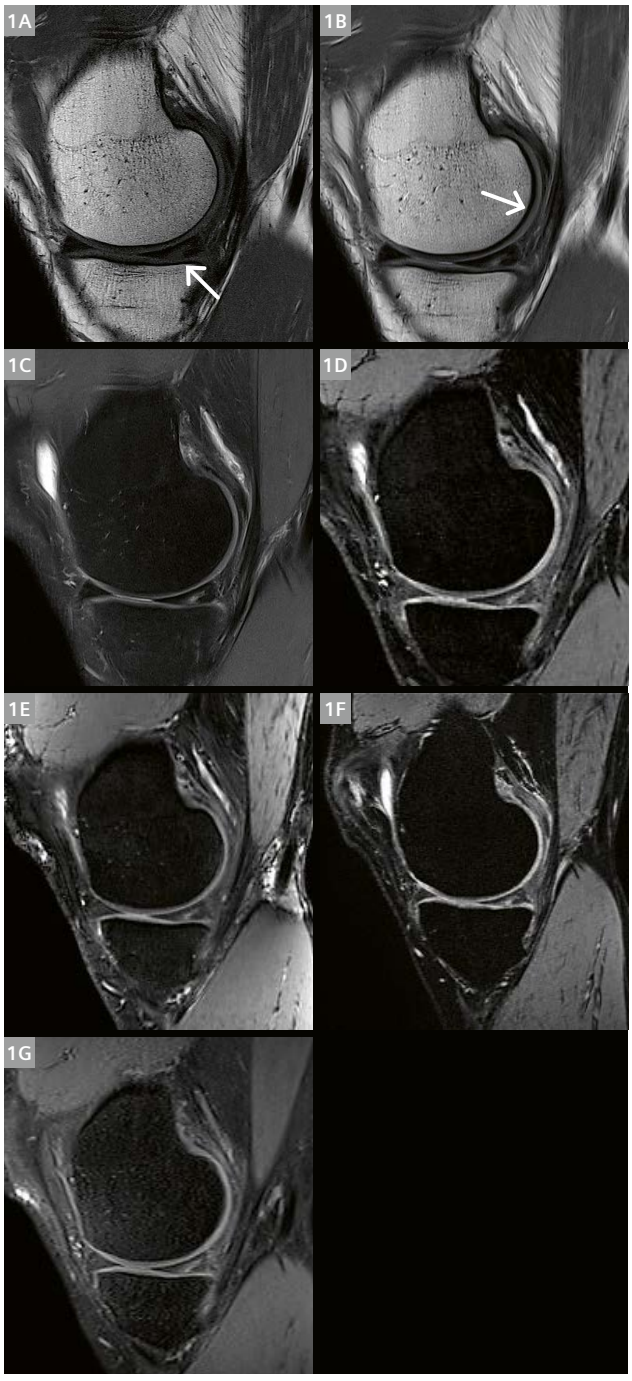

1 35-year-old patient with chronic knee pain. MRI shows a horizontal tear in the medial meniscus (arrow). The cartilage is normal. **(1A)** Sagittal 2D T1-weighted turbo spin echo (TSE), **(1B)** sagittal 2D proton density (PD)-weighted TSE, **(1C)** sagittal 2D PD fat-saturated (fs) TSE – all with 3 mm slice thickness. **(1D)** 3D T2 DESS in sagittal reformation with isotropic 0.6 mm^3 voxel size, **(1E)** 3D T2 TrueFiSP (TR/TE 7.78/3.37 ms, TA 6:25 min) in sagittal reformation with isotropic 0.6 mm^3 voxel size, **(1F)** 3D T2* MEDIC fs (TR/TE 44/16 ms, TA 7:44 min) in sagittal reformation with isotropic 0.6 mm^3 voxel size, **(1G)** 3D T1 SPACE fs (TR/TE 700/11 ms, TA 4:58 min) in sagittal reformation with isotropic 0.6 mm^3 voxel size. The meniscal tear is clearly visible in all 3D sequences.

In our experience, when using conventional 2D sequences for the assessment of morphology with high in plane resolution, the following sequence-specific findings can be observed in the cartilage of a normal knee (Fig. 1). When using a T1-weighted sequence, there is little contrast between cartilage to synovial fluid (Fig. 1A). A PD-weighted TSE sequence shows better contrast between cartilage and the joint fluid but displays chemical-shift artifacts (arrow) that limit the conspicuity of the subchondral bone layer. It also has a low dynamic range regarding the cartilage (Fig. 1B). We prefer to use PD TSE sequences with spectral fat suppression (fs) to achieve suppression of the chemical-shift artifacts (compare the cartilage – subchondral bone transition in Fig. 1B with Fig. 1C) and a higher contrast range due to the spectral fat suppression pulse (Fig. 1C). A similar image impression compared with the PD fs TSE is provided by the 3D DESS (double echo steady state) sequence (Fig. 1D), which enables an isotropic voxel size of 0.6 mm^3 and secondary multiplanar reformations. Likewise, a 3D TrueFISP (true fast imaging with steady state precession) sequence achieves good contrast between cartilage and bone (Fig. 1E). Other 3D sequences for cartilage imaging of the knee joints are the MEDIC (multi-echo data image combination) sequence (Fig. 1F) and the SPACE (sampling perfection with application-optimized contrasts using different flip-angle evolution) sequence (Fig. 1G). A variant of the 3D TSE sequence, the SPACE sequence can be used with different weightings such as PD or T1. SPACE PD fs seems to be a good compromise between known contrast and signal behavior of 2D TSE sequences, and high in-plane and through-plane resolution [5]. Gradient-echo sequences such as FLASH (fast low-angle shot) yield a high cartilage signal (Fig. 2), but these sequences have been shown to be inferior regarding the detection of cartilage lesions when compared with PD fs TSE sequences [6]. A 3D sequence gives us a volume dataset; because of the isotropic voxels, we then have the potential to perform secondary reconstructions in any plane (e.g., along the anterior cruciate ligament). With just one or two 3D sequences instead of the entire knee protocol (usually consisting of at least four 2D sequences) and a compliant patient who does not move significantly, the measurement time can be greatly reduced while retaining high resolution. Moreover, the diagnostic performance of 3D MRI has shown statistically significant improvements over the last three decades: Several studies have demonstrated that 3D and 2D sequences have comparable performance in cartilage imaging of the knee (Figs. 3, 4), including studies with arthroscopic correlation [7].

Furthermore, 3D multiplanar reformation has been associated with higher specificity compared with conventional axial, sagittal, and coronal 2D MRI planes in a recent meta-analysis for depicting cartilage defects in the knee [7]. Currently, 3D MRI provides diagnostic performance comparable to 2D MRI with improvements achieved by using 3T field strength, 3D turbo (TSE), or fast spin echo (FSE) sequences, and multiplanar reformation (MPR) [7, 8].

In conclusion, excellent morphological imaging of knee cartilage is now possible using 3T MRI and dedicated coil technology, allowing for the detection of subtle cartilage pathologies. Besides the standard 2D sequences, a multitude of 3D sequences are available for high-resolution cartilage imaging. In addition, the potential of obtaining thinner slices with a 3D sequence enables better detection of smaller lesions. This option may be chosen on an individual basis, such as in the case of a discrepancy between 2D results and clinical symptoms. In such situations, we recommend the use of an additional 3D sequence. As abundant as current developments in clinical routine cartilage imaging may be, the radiologist must carefully select the approach best suited to answering the clinical question at hand.

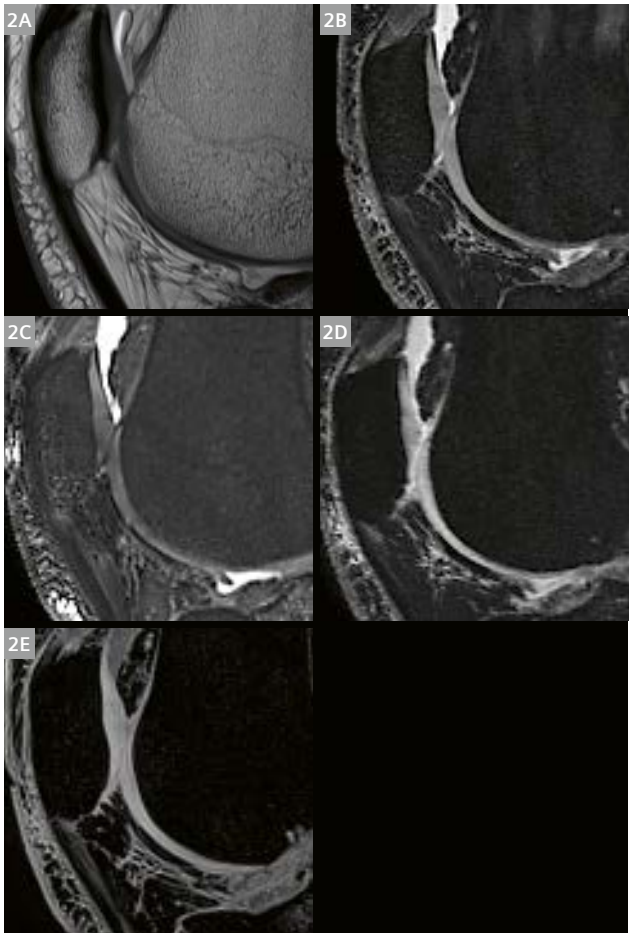

2 Comparison of different sequences for assessing the retropatellar cartilage. **(2A)** 2D PD TSE with 3 mm slice thickness, **(2B)** 3D T2 DESS in sagittal reformation with isotropic 0.6 mm^3 voxel size, **(2C)** 3D T2 TrueFiSP in sagittal reformation with isotropic 0.6 mm^3 voxel size, **(2D)** 3D T2* MEDIC fs in sagittal reformation with isotropic 0.6 mm^3 voxel size, and **(2E)** T1-weighted VIBE (volumetric interpolated breath-hold examination) sequence (TR/TE 11.7/5.38 ms, TA 5:38 min) in sagittal reformation with isotropic 0.6 mm^3 voxel size.

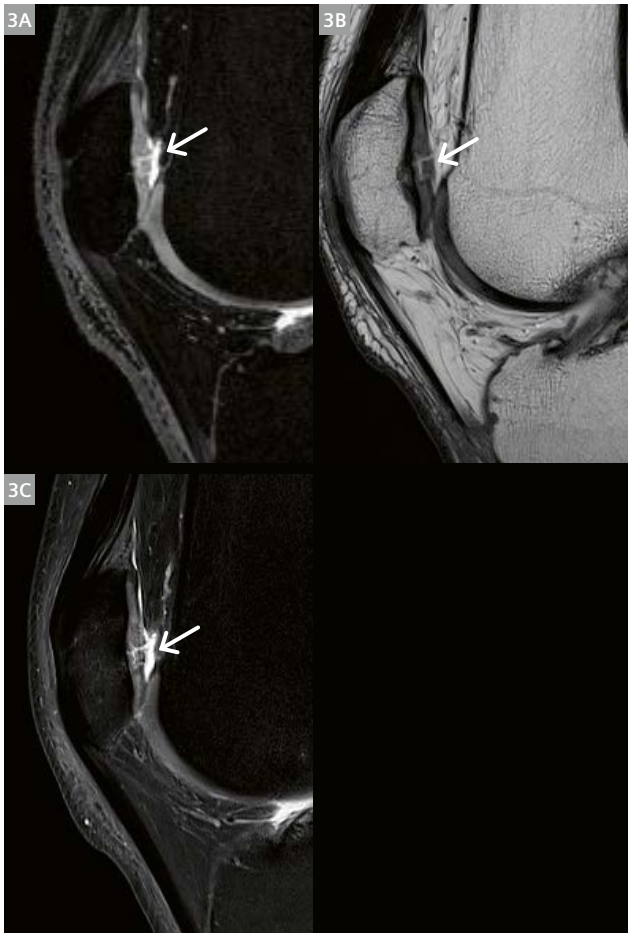

3 37-year-old patient with knee joint distortion and clinically suspected meniscal lesion. **(3A)** Sagittal 3D T2 DESS with isotropic 0.6 mm^3 voxel size, **(3B)** sagittal T2-weighted TSE with 2.5 mm slice thickness (TR/TE 3100/66 ms, TA 3:04 min), and **(3C)** sagittal PD fs TSE with 3 mm slice thickness. All sequences demonstrate the retropatellar chondromalacia with deep tears and a non-displaced flap (arrows).

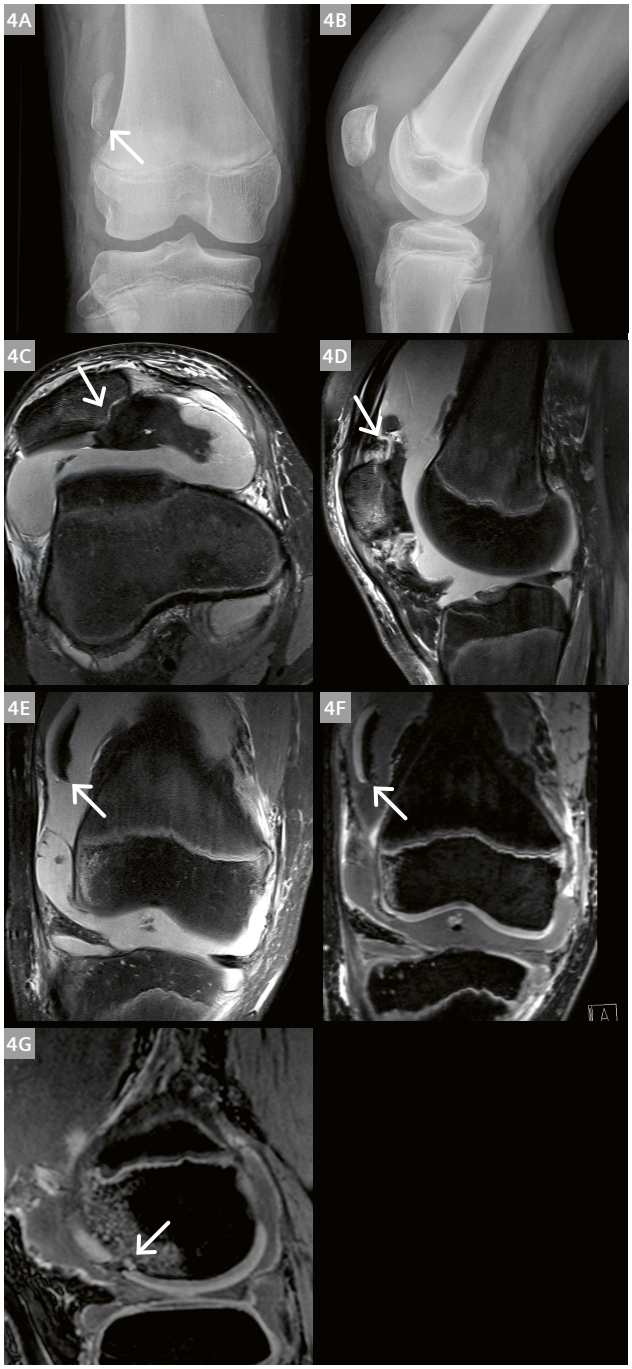

4 13-year-old patient with knee joint distortion and swelling with pain. Radiographs in anteroposterior and lateral projections **(4A, B)**. There was likely trauma to the knee one year prior. Now, the trauma surgeon wants to know whether this displaced fragment is an old flake (arrow). PD TSE fs axial **(4C)** and sagittal **(4D)** sequences show the typical condition after lateral patellar luxation with an osteochondral flake fracture (arrows) and a large hemorrhagic joint effusion. The contrast between bone and cartilage of the osteochondral flake (arrows) is much lower on the coronal standard PD TSE fs **(4E)** compared with the T2 3D DESS (coronal **(4F)** and sagittal reformations **(4G)**). The sagittal DESS also demonstrates additional cartilage damage at the contusion zone of the lateral femoral condyle (arrow).

References

1 Rehnitz C, Weber MA. Morphological and functional cartilage imaging. Orthopäde. 2015 Apr;44(4):317-33; quiz 334-5. doi: 10.1007/s00132-015-3110-3.
2 Glaser C, Heuck A, Horng A. Update: clinical imaging of cartilage-part 1: Technical aspects. Radiologe. 2019 Aug;59(8):692-699. doi: 10.1007/s00117-019-0561-2.
3 Weber MA, Wünnemann F, Jungmann PM, Kuni B, Rehnitz C. Modern cartilage imaging of the ankle. Fortschr Röntgenstr. 2017 Oct;189(10):945-956. doi: 10.1055/s-0043-110861.
4 Glaser C, Heuck A, Horng A. Update: Clinical imaging of cartilage-part 2: Aspects helpful in daily clinical practice. Radiologe. 2019 Aug;59(8):700-709. doi: 10.1007/s00117-019-0554-1.
5 Kloth JK, Winterstein M, Akbar M, Meyer E, Paul D, Kauczor HU, Weber MA. Comparison of 3D turbo spin-echo SPACE sequences with conventional 2D MRI sequences to assess the shoulder joint. Eur J Radiol. 2014 Oct;83(10):1843-9. doi: 10.1016/j.ejrad.2014.06.011.
6 Mohr A. The value of water-excitation 3D FLASH and fat-saturated PDw TSE MR imaging for detecting and grading articular cartilage lesions of the knee. Skeletal Radiol. 2003 Jul;32(7):396-402.
7 Shakoor D, Guermazi A, Kijowski R, Fritz J, Jalali-Farahani S, Mohajer B, Eng J, Demehri S. Diagnostic Performance of Three-dimensional MRI for Depicting Cartilage Defects in the Knee: A Meta-Analysis. Radiology. 2018 Oct;289(1):71-82. doi: 10.1148/radiol.2018180426.
8 Gustas CN, Blankenbaker DG, Rio AM, Winalski CS, Kijowski R. Evaluation of the Articular Cartilage of the Knee Joint Using an Isotropic Resolution 3D Fast Spin-Echo Sequence With Conventional and Radial Reformatted Images. AJR Am J Roentgenol. 2015 Aug;205(2):371-9. doi: 10.2214/AJR.14.14265.

Contact

Marc-André Weber, M.D., M.Sc.
Professor of Radiology and Chairman
Institute of Diagnostic and Interventional Radiology, Pediatric Radiology and Neuroradiology
University Medical Center Rostock
Ernst-Heydemann-Str. 6
18057 Rostock
Germany
Tel: +49 (0)381 494-9201
Fax: +49 (0)381 494-9202
marc-andre.weber@med.uni-rostock.de
http://radiologie.med.uni-rostock.de

Compressed Sensing VIBE – Clinical Applications in the Female Pelvis

Daniel Hausmann, M.D.[1]; Dominik Nickel, Ph.D.[2]; Berthold Kiefer, Ph.D.[2]; Rahel A. Kubik-Huch, M.D.[1]

[1]Department of Radiology, Kantonsspital Baden, Baden, Switzerland
[2]Siemens Healthineers, Erlangen, Germany

Introduction

MRI has become an increasingly important tool in the diagnosis and assessment of diseases of the female pelvic organs in recent years. In current guidelines, contrast-enhanced MRI of the female pelvis is not only part of the workup for and staging of gynecologic cancers, that is of the uterus, cervix, and ovaries [1–5], but is also recommended for the workup of indeterminate adnexal masses [4] and the pre-therapeutic assessment of leiomyomas [6], whereas contrast-enhanced sequences are currently regarded as optional in patients with endometriosis [7].

In patients with endometrial carcinoma, dynamic contrast-enhanced (DCE) MRI demonstrated similar sensitivity to T2-weighted sequences (T2w), but was more specific for the detection of deep myometrial invasion [8]. While the depth of myometrial invasion is best depicted during the equilibrium phase, that is approximately 2 min 30 s after gadolinium injection, DCE-MRI allows us to determine the presence of uninterrupted enhancement of the subendometrial zone, which is best observed 35–40 s after contrast injection [1]. This information may be important for those patients for whom fertility-sparing treatment is being considered as it can help rule out myometrial invasion, one of the fundamental criteria to approve eligibility for conservative treatment [9]. In patients with adnexal masses, quantifying DCE-MRI heterogeneity may help to characterize adnexal masses, allowing a better distinction between malignant and benign tumors [10]. Furthermore, the quantitative evaluation of tumor angiogenesis (for example, microvascular characteristics) may become increasingly important for predicting and monitoring treatment response in tumor patients receiving anti-angiogenic treatment [11].

Due to the current trade-off between spatial and temporal resolution, conventional dynamic sequences with a temporal resolution in the range of 12–18 seconds only capture the contrast agent dynamics in the different regions of the uterus insufficiently. These sequences allow only qualitative or semi-quantitative analysis, whereas full quantitative analysis is needed for robust assessment. In our opinion, there is great potential for functional assessment of uterine diseases in addition to the purely morphological assessment of the uterus in order to be able to provide detailed clinical recommendations.

In this context, kinetic models are interesting for the assessment of contrast agent dynamics [12]. Quantitative color-coded maps can be used to evaluate vascular permeability and thus vascular quality. Analyses like this, for example, are important for the detection of the hypoxic components of squamous cell carcinoma of the uterus and could contribute to even more individualized therapy in the future, especially when antiangiogenic substances are used for tumor therapy [13]. In addition, studies have shown that quantitative perfusion analysis may provide important information for the grading of endometrial carcinomas and could help to identify patients at increased risk of local recurrence [14, 15].

In the context of fertility diagnostics, several studies have shown that there is a link between myometrial perfusion and the cycle phase [16]. In addition, differences in myometrial perfusion between pre- and postmenopausal women were noted.

Compressed Sensing VIBE

The prototypical Compressed Sensing (CS) VIBE sequence[1] supports incoherent *k*-space sampling combined with a joint spatio-temporally regularized reconstruction that is tailored to dynamic imaging. In particular, it allows selection of varying temporal resolutions over the course of the acquisition. For example, in the early phase, where perfusion processes are most evident, a high temporal resolution can be selected (<8 seconds), while in later phases where the entire uterus is already contrasted,

[1]*This work has been done using a WIP version. Compressed Sensing GRASP-VIBE is available as a product.*

a lower temporal resolution can be set (> 10 seconds). With a temporal resolution of < 8 seconds, it is possible to separate the different regions of the uterus with more accuracy than with conventional sequences and the datasets can be used to generate color-coded, quantitative perfusion maps (Fig. 1). Furthermore, the sequence acquires a navigation signal along with the imaging data and more refined reconstruction algorithms can be used for motion artifact reduction. An initial fast, so-called 'hard-gated' reconstruction is based on a fixed fraction ('gating acceptance') of phase-encoding steps for each timepoint and reconstructs the dominant motion state. Another, more elegant method is the motion-state-resolved reconstruction. Using this technique, motion states are bundled, which contributes to an even more advanced artifact reduction (Fig. 2). The number of motion states selected can be flexibly adjusted. In the application presented here, 6 motion states were set.

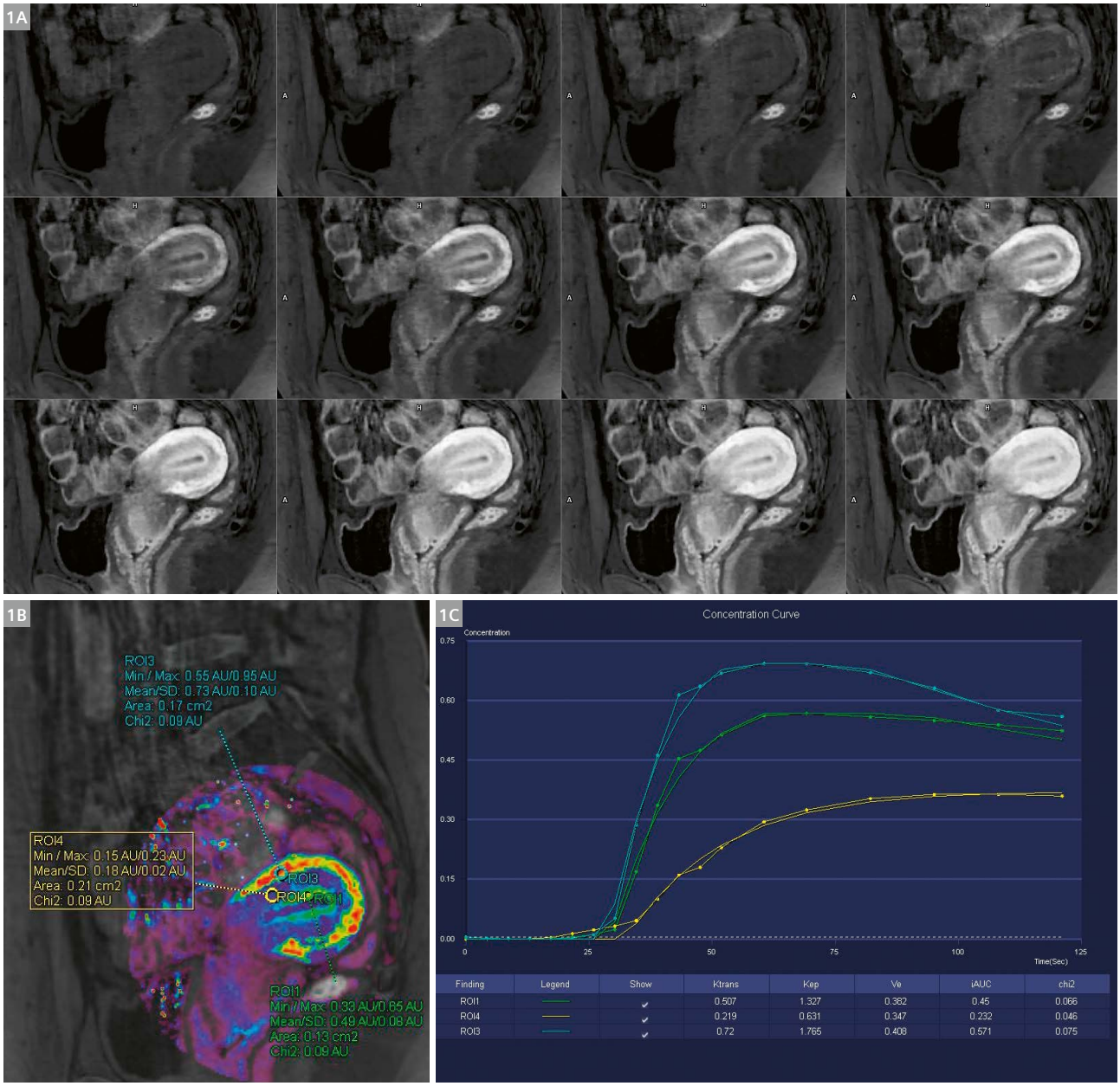

1 Images of a 28-year-old patient with a retroflected uterus. Thanks to the high temporal resolution, CS VIBE allows a detailed morphological analysis of the contrast dynamics in the different zones of the uterus **(1A)**. At the same time, color-coded perfusion maps can be generated using a two-compartment Tofts model (**1B**; here K^{trans}), and various quantitative perfusion parameters (for example, to assess the capillary leakage) and enhancement curves **(1C)** can be evaluated.

Experience in clinical routine

Compressed Sensing VIBE has proven to be superior to the conventional VIBE thanks to multiple features, which will be discussed in more detail below. In patients with malignant uterine tumors, the sequence may improve the evaluation of tumor infiltration depth thanks to its ability to clearly show the anatomical distinctness of the uterine regions (Fig. 3). In the future, this could allow more accurate T-staging with clinical implications for the therapeutic management of patients. The new sequence might also be beneficial in benign gynecological disease such as leiomyomas and teratomas (Figs. 4, 5). In teratomas, for example, the contrast agent dynamics in Rokitansky nodules was clearly recognizable (Fig. 5). In the evaluation of leiomyomas, the degree of vascularization could be better estimated and feeding arteries better depicted (Fig. 4). In addition, non-vascularized necrotic components within the lesions might be better delineated. In the diagnostic workup of patients with deep infiltrating endometriosis, the depth of infiltration and, in particular, the presence and extent of rectal wall invasion is one of the key criteria for the therapeutic approach. Based on our preliminary experience, CS VIBE might increase diagnostic confidence in this patient population (Fig. 6).

The disadvantage of CS VIBE compared to the conventional VIBE was an occasionally slightly lower lesion contrast. These differences in contrast are particularly due to the different flip angles. For the standard VIBE, a flip angle of 30° was set, while CS VIBE used a lower flip angle of 10° as is usually the case for DCE imaging owing to SNR limitations.

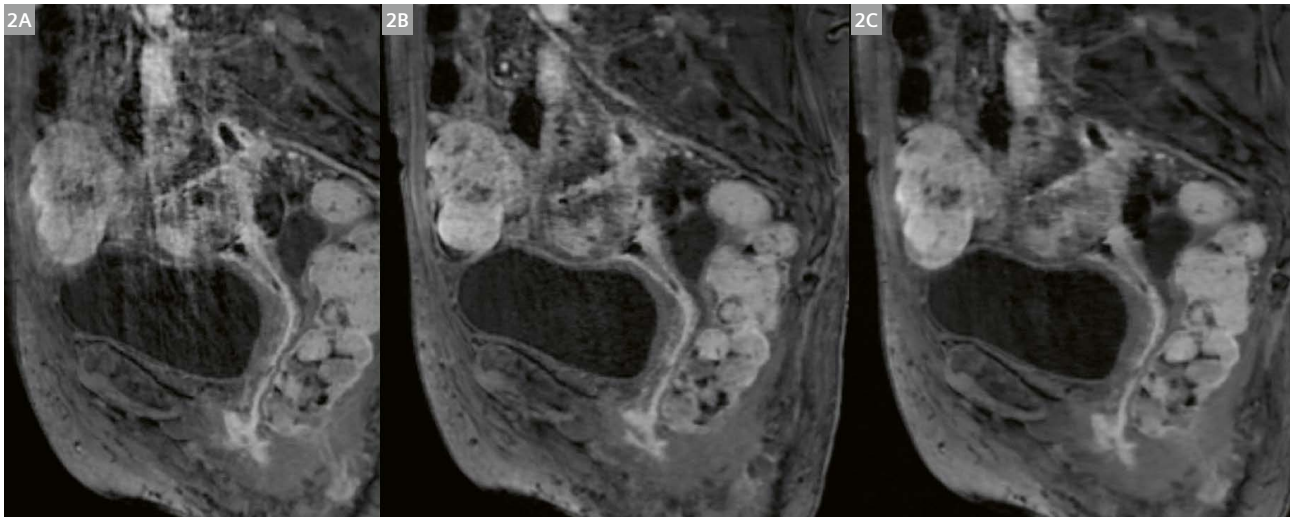

2 Images of a patient with hysterectomy. The contrast enhancement of the vaginal lining in the early arterial phase can be delineated. The hard-gated reconstruction **(2A)** shows prominent vertical motion artifacts along the abdominal wall. Two different motion states **(2B, 2C)** of the same contrast phase are seen on the right. Motion artifacts are significantly mitigated compared to the hard-gated reconstruction.

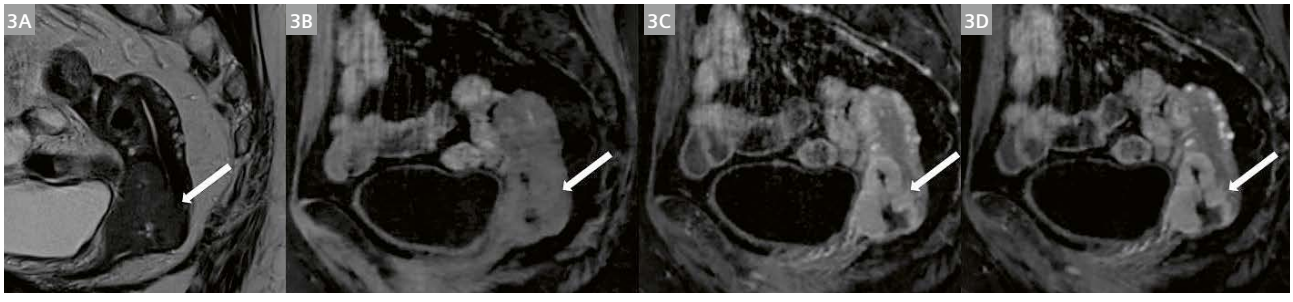

3 Images of a 51-year-old woman with bulky disease in cervical carcinoma with infiltration of the proximal vagina and parametrial involvement (FIGO IIb). The tumor can be delineated both in the sagittal T2 BLADE **(3A)** and on the native CS VIBE **(3B)**, but is best demarcated in the contrast-enhanced phases **(3C, 3D)**. Post-biopsy susceptibility artifacts are visible in the center.

In addition, we had the impression that, when compared to the hard-gated reconstruction, in some cases, the artifact reduction with the motion-state-resolved reconstruction led to sharp organ boundaries, but to a slightly diminished distinctness of the different zones of the uterus.

The additional diagnostic benefit of the quantitative color-coded perfusion maps is currently being evaluated in dedicated studies and cannot yet be conclusively assessed.

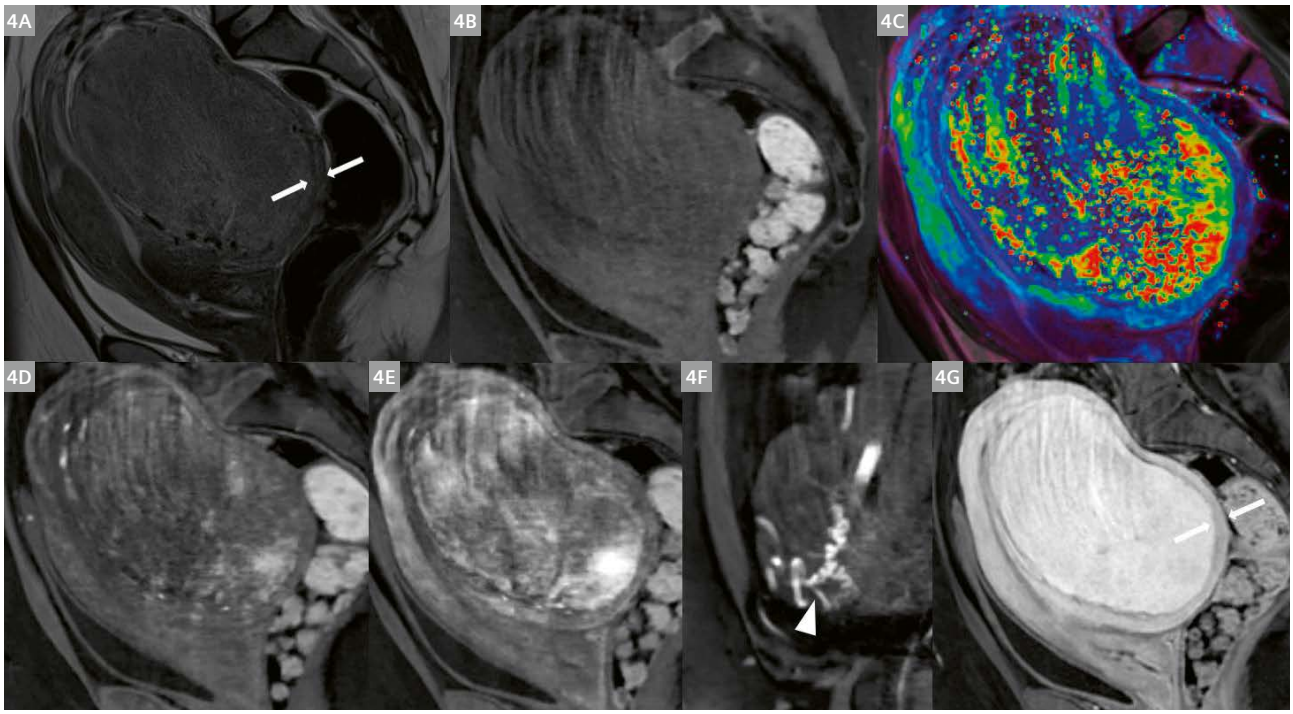

4 Images of a 30-year-old patient with a large intramural uterine leiomyoma **(4A, 4B)**. Heterogeneous enhancement is seen in early contrast-enhanced images, which is concordant with the color-coded K^{trans} map **(4C-E)**. Dilated feeding vessels are also nicely depicted in early phases **(4F)**. A myometrial stripe is best observed in the equilibrium phase, which is important for surgical planning **(4G)**. Vertical motion artifacts of the hard-gated reconstruction are depicted, but do not interfere with the interpretability of the imaging material.

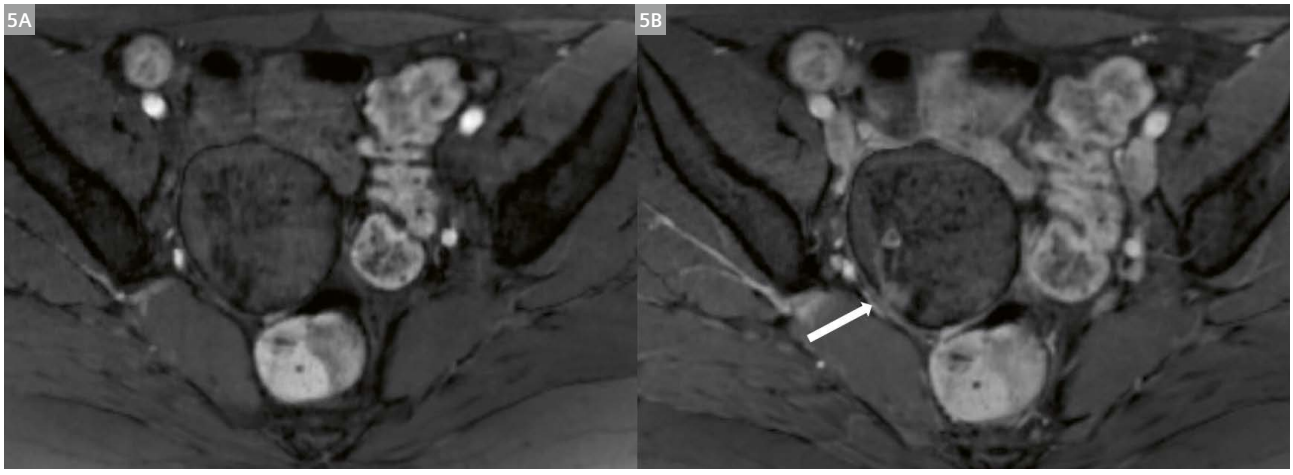

5 Images of a 26-year-old patient with a mature teratoma of the right ovary. In the early arterial phase **(5A)** of the fat-saturated CS VIBE, fatty tissue components are particularly recognizable. In a later phase, enhancement of the Rokitansky nodule can be clearly depicted.

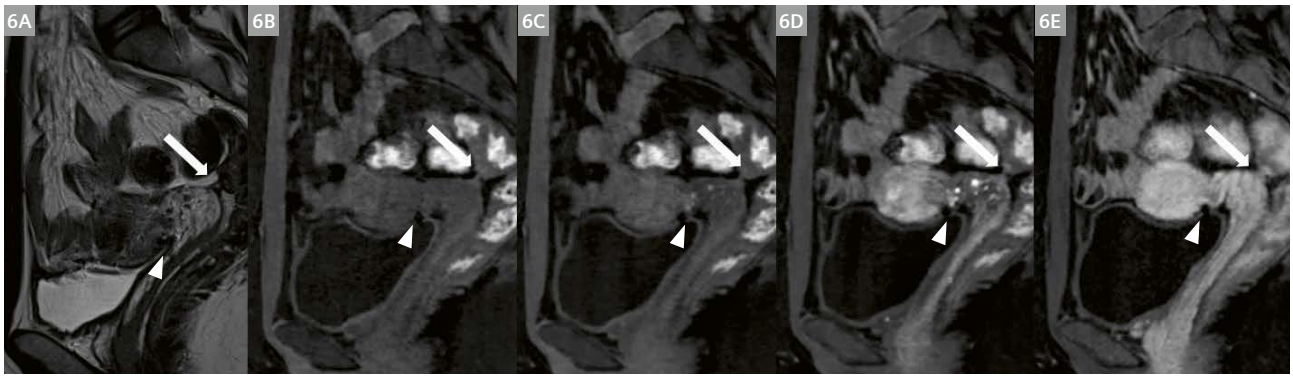

6 Images of a 30-year-old patient with endometriosis. Both in the sagittal T2w BLADE **(6A)** and in the non-contrast **(6B)**, arterial **(6C)**, venous **(6D)**, and equilibrium phase **(6E)**, infiltration of the anterior rectal wall is clearly visible (arrows). Moreover, due to a history of C-section, postoperative susceptibility artifacts in the lower anterior uterine segment are seen (arrowheads).

Conclusion

CS VIBE is a highly valuable tool for the diagnostic workup of complex uterine and adnexal pathologies and may facilitate improved staging of tumors and a more accurate evaluation of benign diseases. The additional option of a quantitative perfusion analysis could be of particular importance in the future for the response assessment of malignant tumors in order to estimate the degree of vascularization of treated tumors, and potentially also for the workup of infertility. At the same time, both the hard-gated and motion-state-resolved reconstruction lead to a noticeable reduction of motion artifacts, which in individual cases can contribute to higher diagnostic confidence of the radiologists. Both reconstructions can be performed in a clinically acceptable time using GPU-supported scanners.

References

1 Nougaret S, Horta M, Sala E, et al. Endometrial Cancer MRI staging: Updated Guidelines of the European Society of Urogenital Radiology. Eur Radiol. 2019;29(2): 792-805.
2 Sala E, Rockall A, Kubik-Huch RA. Advances in magnetic resonance imaging of endometrial cancer. Eur Radiol. 2011;21(3): 468-473.
3 Balleyguier C, Sala E, Da Cunha T, et al. Staging of uterine cervical cancer with MRI: guidelines of the European Society of Urogenital Radiology. Eur Radiol. 2011;21(5): 1102-1110.
4 Forstner R, Thomassin-Naggara I, Cunha TM, et al. ESUR recommendations for MR imaging of the sonographically indeterminate adnexal mass: an update. Eur Radiol. 2017;27(6): 2248-2257.
5 Forstner R, Sala E, Kinkel K, et al. ESUR guidelines: ovarian cancer staging and follow-up. Eur Radiol. 2010;20(12): 2773-2780.
6 Kubik-Huch RA, Weston M, Nougaret S, et al. European Society of Urogenital Radiology (ESUR) Guidelines: MR Imaging of Leiomyomas. Eur Radiol. 2018;28(8): 3125-3137.
7 Bazot M, Bharwani N, Huchon C, et al. European society of urogenital radiology (ESUR) guidelines: MR imaging of pelvic endometriosis. Eur Radiol. 2017;27(7): 2765-2775.
8 Wu LM, Xu JR, Gu HY, et al. Predictive value of T2-weighted imaging and contrast-enhanced MR imaging in assessing myometrial invasion in endometrial cancer: a pooled analysis of prospective studies. Eur Radiol. 2013;23(2): 435-449.
9 Fujii S, Kido A, Baba T, et al. Subendometrial enhancement and peritumoral enhancement for assessing endometrial cancer on dynamic contrast enhanced MR imaging. Eur J Radiol. 2015;84(4): 581-589.
10 Thomassin-Naggara I, Soualhi N, Balvay D, et al. Quantifying tumor vascular heterogeneity with DCE-MRI in complex adnexal masses: A preliminary study. J Magn Reson Imaging. 2017;46(6): 1776-1785.
11 Brandao AC, Silva AO. Diseases of the female pelvis: advances in imaging evaluation. Magn Reson Imaging Clin N Am. 2013;21(2): 447-469.
12 Tofts PS, Cutajar M, Mendichovszky IA, et al. Precise measurement of renal filtration and vascular parameters using a two-compartment model for dynamic contrast-enhanced MRI of the kidney gives realistic normal values. Eur Radiol. 2012;22(6): 1320-1330.
13 Hauge A, Wegner CS, Gaustad JV, et al. DCE-MRI of patient-derived xenograft models of uterine cervix carcinoma: associations with parameters of the tumor microenvironment. J Transl Med. 2017;15(1): 225.
14 Ippolito D, Minutolo O, Cadonici A, et al. Endometrial cancer: diagnostic value of quantitative measurements of microvascular changes with DCE-MR imaging. MAGMA. 2014;27(6): 531-538.
15 Haldorsen IS, Gruner R, Husby JA, et al. Dynamic contrast-enhanced MRI in endometrial carcinoma identifies patients at increased risk of recurrence. Eur Radiol. 2013;23(10): 2916-2925.
16 Thomassin-Naggara I, Balvay D, Cuenod CA, et al. Dynamic contrast-enhanced MR imaging to assess physiologic variations of myometrial perfusion. Eur Radiol. 2010;20(4): 984-994.

Contact

Daniel Hausmann, M.D.
Institute of Radiology
Kantonsspital Baden
Im Ergel 1
5404 Baden
Switzerland
Tel.: +41 7863 833822
Daniel.hausmann@ksb.ch


Daniel Hausmann


Rahel A. Kubik-Huch

Post Treatment MR of Prostate Cancer

Christopher R. Lunt, MB ChB, FRCR; David J. Ferguson, MB BCh BAO FFR (RCSI), FRCPC; Silvia D. Chang, MD, FRCPC, FSAR

Vancouver General Hospital and BC Cancer, Vancouver, BC, Canada

Multiparametric MRI has in recent years become the imaging method of choice in the investigation of prostate cancer, for detection, decision making regarding targeted biopsy, and to provide information for local staging. MR is also used in the follow up of patients on active surveillance and in those who have undergone treatment of their cancer in the setting of suspected recurrence.

Recurrence of prostate cancer following treatment is most often detected following a rise in serum prostate specific antigen (PSA) levels. How this biochemical recurrence (BR) is defined depends on the modality of treatment; with two consecutive serum PSA concentrations of > 0.2 ng/mL considered to represent BR in patients who have undergone radical prostatectomy (RP), and PSA > 2 ng/mL above the initial nadir value in patients treated with radiotherapy considered to represent recurrence [1].

No consensus values have been established for the newer focal therapies such as cryotherapy or high intensity focused ultrasound (HIFU).

Biochemical recurrence is reported to occur in 27–53% of men treated with curative intent. Between 16–35% of treated men will be given second line therapy, however the interval between initial BR and the need to begin treatment can often be measured in years [2].

Nonetheless local recurrence is associated with an increased risk of metastatic disease, and in patients with local recurrence who are not treated the mean time to detection of distant metastases is 3 years.

Absolute reliance on PSA in the monitoring of treated patients can be unreliable as very poorly differentiated tumors may not produce PSA and this lack of PSA production may be present in the tumor at the time of diagnosis or may occur due to novel mutation in metastatic tumor clone cells later during the period of surveillance. Therefore patients presenting with symptoms attributable to recurrence such as bone pain or symptoms of a pelvic mass or retroperitoneal nodal enlargement should be investigated even in the absence of a serum PSA rise [3].

Initial investigation of men with biochemical recurrence should attempt to establish if the tumor is localized to the residual prostate gland or within the surgical bed in which case radical salvage therapy could be considered, or if distant metastases are present in which case salvage therapy, with its significant associated comorbidity should be avoided in favor of systemic treatment, the timing and method being guided by the location and extent of disease.

Standard assessment for distant metastases in cases of biochemical recurrence in our institutions currently comprises of CT abdomen to assess for lymph node recurrence and MDP bone scan. In cases where the location of

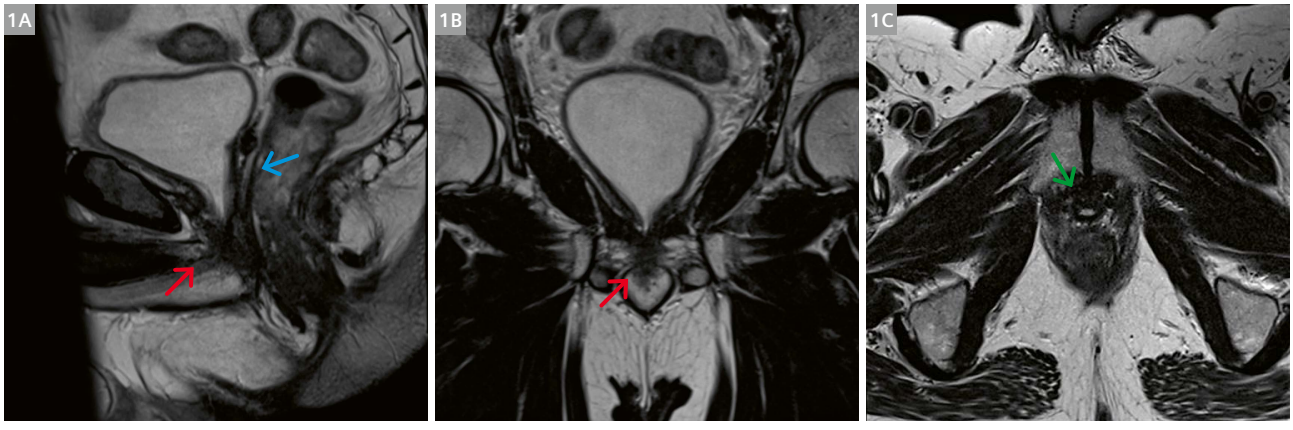

1 Orthogonal T2 sagittal **(1A)**, coronal **(1B)**, and axial **(1C)** small FOV images demonstrating normal MR appearances following radical prostatectomy. The prostate and seminal vesicles are absent and the bladder neck is pulled down to the proximal urethra (red arrows). Uniform low signal scarring is seen at the site of the seminal vesicles (blue arrow). Uniform low signal is seen at the anastomosis, similar to the bladder wall (green arrow).

recurrence is not characterized, a prostate specific membrane antigen (PSMA) PET-CT is currently being trialed.

MR of the prostate or prostate bed in post treatment patients is performed using a standard MR prostate protocol utilizing orthogonal small field of view (FOV) T2, axial diffusion-weighted imaging (DWI), axial wide FOV T1, and dynamic gadolinium enhanced sequences. The latter being crucial to accurate detection in some patients.

Assessment following radical prostatectomy

Surgical removal of the entire prostate gland necessitates the formation of a urethrovesical anastomosis and usually includes removal of the seminal vesicles [4]. Pelvic lymphadenectomy may also be performed at the surgeon's discretion depending on the stage and grade of the tumor as assessed by digital rectal examination, imaging and biopsy histology. Patients with high or intermediate risk disease will usually undergo lymph node dissection, however in low risk disease the need for lymphadenectomy is controversial.

Minimally invasive prostatectomy is now the most commonly employed surgical technique with or without robotic assistance [5]. This may include nerve sparing in suitable patients in an attempt to preserve sexual function.

Following prostatectomy the serum PSA level is expected to fall to < 0.2 ng/mL, in the event this does not occur, residual local disease or occult distant metastases should be suspected.

Normal MR appearances following RP show the bladder neck pulled down to form an inverted conical shape and the vesico-urethral anastomosis which should appear uniformly low signal on the T2 sequences due to the presence of fibrotic tissue. There should be no or minimal evidence of diffusion restriction around the anastomosis, and no early contrast enhancement, however delayed uniform enhancement of the fibrotic tissue is normal (Fig. 1).

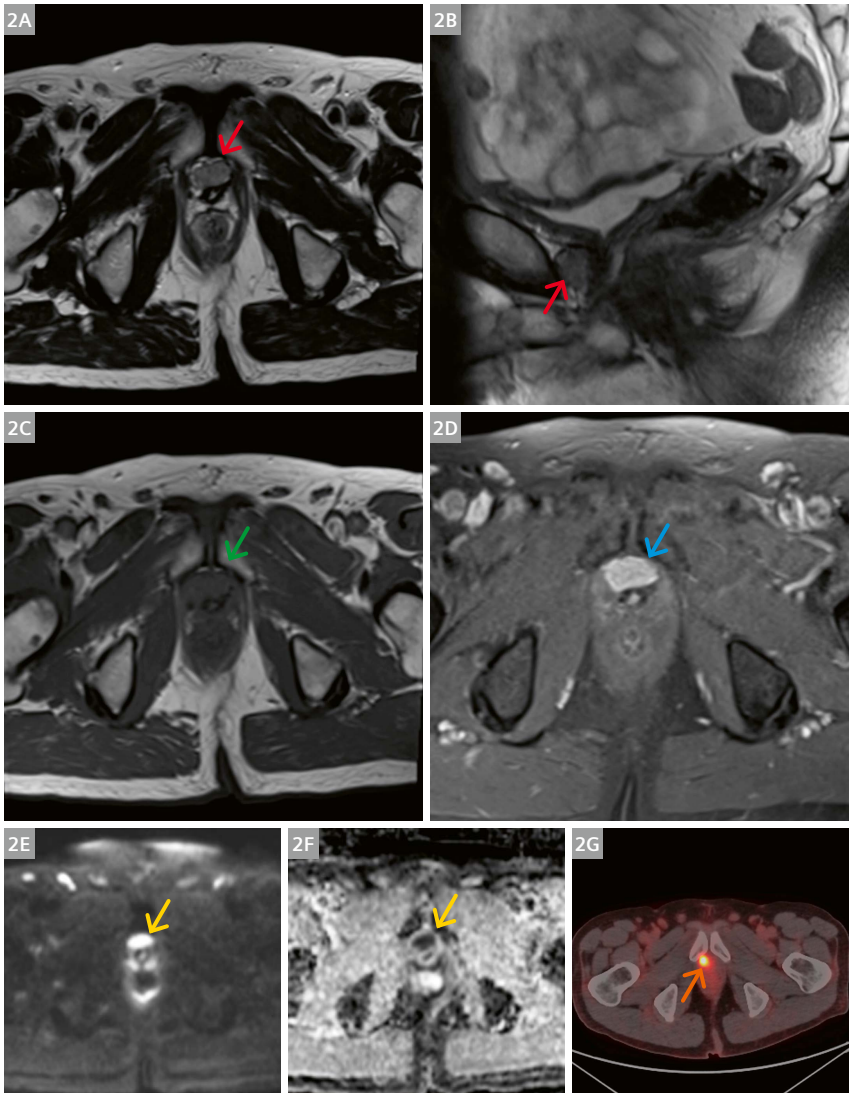

2 **(2A, B)** T2 axial and sagittal images demonstrating recurrence anterior to the anastomosis following radical prostatectomy seen as intermediate signal tumor (red arrows). **(2C)** T1 sequence, tumor is isointense to skeletal muscle (green arrow). **(2D)** Tumor shows avid enhancement following gadolinium contrast administration (blue arrow). **(2E, F)** Tumor shows restricted diffusion with low signal on ADC sequence (yellow arrows). **(2G)** PSMA PET-CT shows isotope uptake within the area of tumor seen on MR (orange arrow).

Local recurrence occurs in 23–43% of patients, most commonly at the anastomosis (75%), or in a retained portion of a seminal vesicle or vas deferens (20%). Soft tissue in the prostatectomy bed away from the anastomosis and nodal or visible skeletal metastases should also be carefully excluded in the setting of rising PSA. The typical appearance of recurrent local disease is soft tissue which is isointense to skeletal muscle on T1 sequences, slightly hyper-intense to muscle on T2 and demonstrates diffusion restriction and rapid contrast enhancement and washout (Fig. 2).

Prostate MR following external beam radiotherapy

The use of external beam radiotherapy (EBRT) for treatment of prostate cancer is primarily associated with lower risk tumors, although with the addition of androgen deprivation therapy (ADT) higher risk tumors can also be treated, often in the setting of patients with significant comorbidity precluding surgery or in patients who have declined invasive treatment [2].

Biochemical recurrence following RT is defined as a PSA rise of > 2 ng/mL above the initial PSA nadir. In this setting localization of the site of recurrence is crucial as salvage surgery carries significant morbidity and should be reserved for those patients who might still be cured. Therefore confirmation through biopsy is mandatory.

Following EBRT the prostate gland shows diffuse atrophy with reduced signal on T2 sequences which can mask areas of recurrent tumor. Normal differentiation between the peripheral and transition zones becomes indistinct and post EBRT changes in the adjacent muscle and bone marrow may be seen. Atrophy of the seminal vesicles is commonly seen [6] (Fig. 3).

Recurrence most often occurs at the site of initial tumor and may still appear lower in T2 signal than the surrounding prostate tissue. Multiparametric (mp) MRI has been shown to be superior to anatomical imaging, and diffusion restriction or tissue demonstrating early enhancement with washout should be considered suspicious. Gradual enhancement without washout is typically seen in patients treated with RT [7] (Fig. 4).

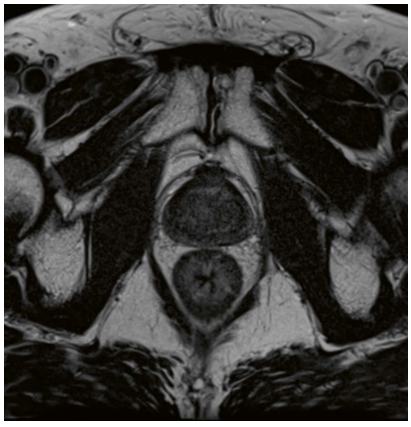

3 Expected findings following external beam radiotherapy (EBRT): Diffuse atrophy of prostate with decreased signal on T2 sequences, loss of normal distinction between peripheral and transition zones, increase T2 signal in muscle and bone marrow. Diffuse low signal thickening of bladder and rectal walls may also be seen.

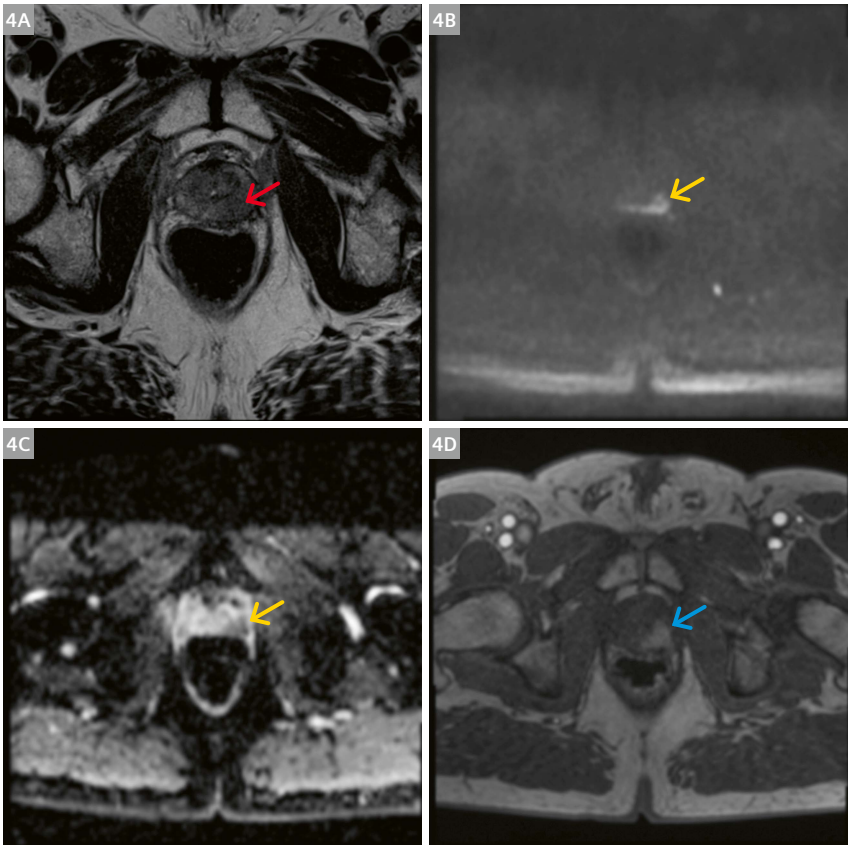

4 Recurrence of prostate cancer following EBRT. **(4A)** T2 axial image showing subtle low signal in the left midgland (red arrow), **(4B)** corresponding high signal on DWI (yellow arrow) and **(4C)** low ADC values (yellow arrow) with **(4D)** avid contrast enhancement on DCE sequence (blue arrow) in keeping with tumor.

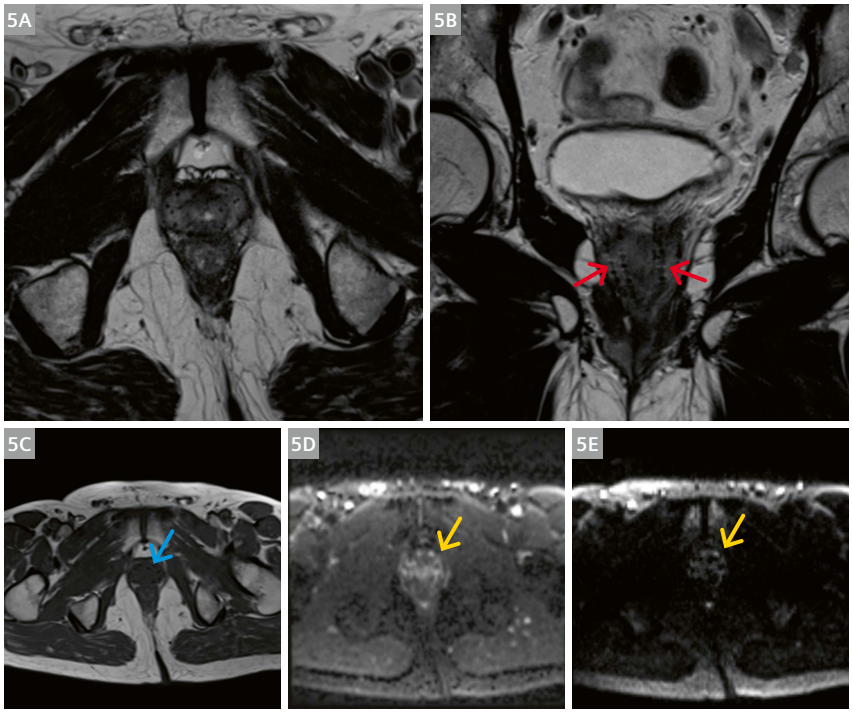

5 Normal appearances following brachytherapy: **(5A, B)** Homogeneous low T2 signal throughout the gland with reduced differentiation between peripheral and transitional zones. **(5B)** On the coronal image, seeds are seen to run in parallel (red arrows). **(5C)** T1 images show seeds with susceptibility artifact (blue arrow). **(5D, E)** DWI and ADC sequences show marked susceptibility artifact limiting use (yellow arrows).

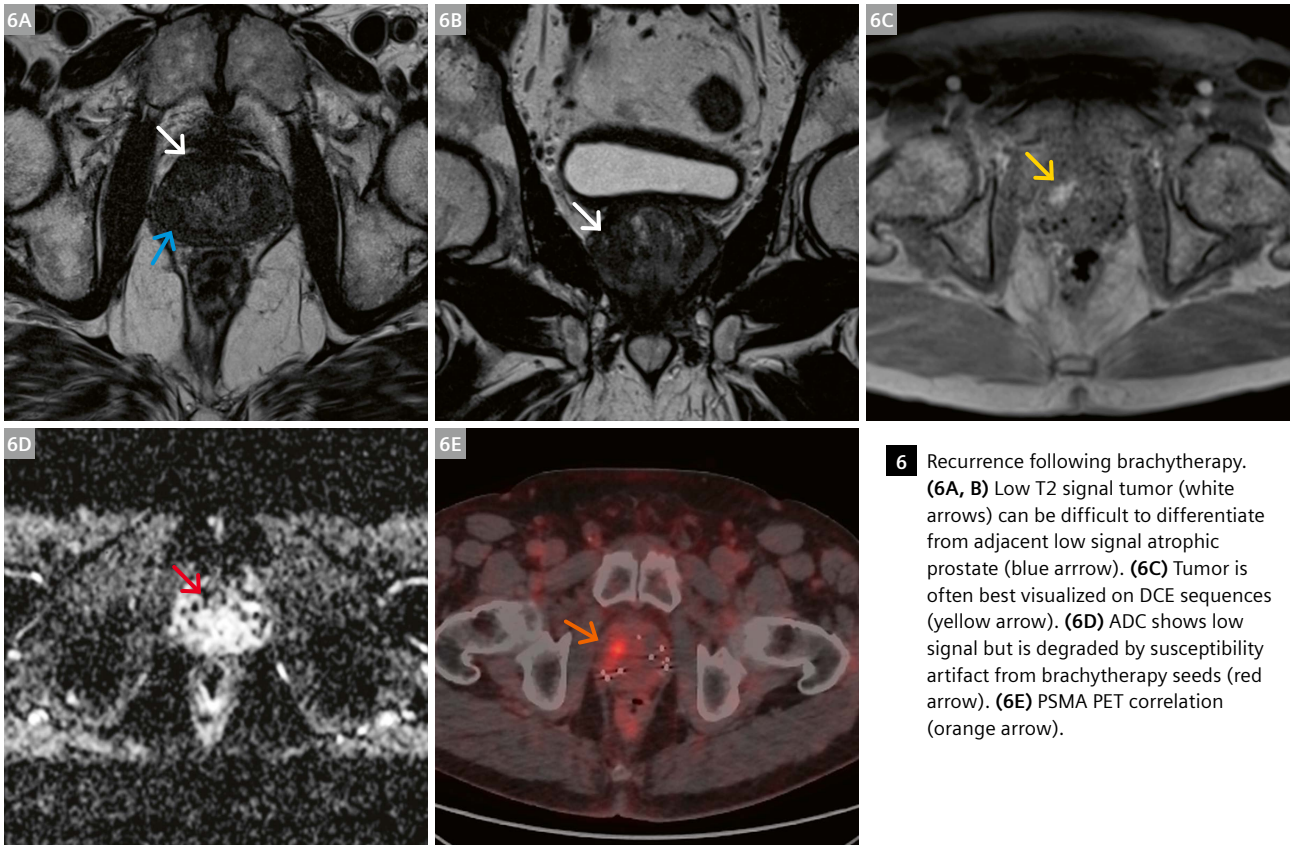

6 Recurrence following brachytherapy. **(6A, B)** Low T2 signal tumor (white arrows) can be difficult to differentiate from adjacent low signal atrophic prostate (blue arrrow). **(6C)** Tumor is often best visualized on DCE sequences (yellow arrow). **(6D)** ADC shows low signal but is degraded by susceptibility artifact from brachytherapy seeds (red arrow). **(6E)** PSMA PET correlation (orange arrow).

Trans-perineal brachytherapy

The insertion of metal seeds into the prostate to deliver highly localized doses of ionizing radiation is performed using a transrectal ultrasound probe and a template grid for guidance. Typically patients with low grade, low volume cancer are offered brachytherapy if there has been no previous prostatic surgery (TURP), the prostate volume is below 50 mL and the International Prostate Symptom Score is ≤ 12 [2].

No consensus exists regarding the definition of biochemical recurrence in patients treated with brachytherapy [1, 8]. 30–60% of patients experience a rise in PSA around one year following the insertion of the seeds which can last for around 12 months. After this period a persistently rising PSA should be viewed with suspicion.

Brachytherapy causes a similar appearance in the prostatic parenchyma to EBRT with homogeneous low T2 signal and loss of normal zonal anatomy. The low signal associated with treatment can mask low signal recurrence. In addition, multiple seeds can be visualized running in parallel on coronal images and may also be seen outside of the gland in the periprostatic fat, the bladder wall and in the base of the penis/perineum (Fig. 5). Areas of susceptibility artifact due to seeds severely limit the interpretation of DWI sequences and recurrences are often best visualized using DCE [6] (Fig. 6).

Androgen deprivation therapy (ADT)

Androgen deprivation therapy can be used in the setting of incurable disease or as an adjunct to radiotherapy. Initial treatment can often result in a significant reduction in tumor volume. Diverse morphologic and signal changes are possible following the initiation of ADT with diffuse atrophy of the gland due to apoptosis of prostate cells the most commonly seen appearance. Loss of the normal zonal definition due to decreased peripheral zone signal is often seen, and the seminal vesicles usually atrophy. Residual tumor can be identified by areas of diffusion restriction and rapid enhancement with washout [9, 10] (Figs. 7, 8).

Focal therapies

Various modalities for the focal treatments of prostate cancer have been proposed and implemented in recent years, most relying on targeted destruction of localized areas of the prostate gland where tumor is located.

Cryotherapy involves ablation tissue by extremely cold temperatures using probes inserted transperineally

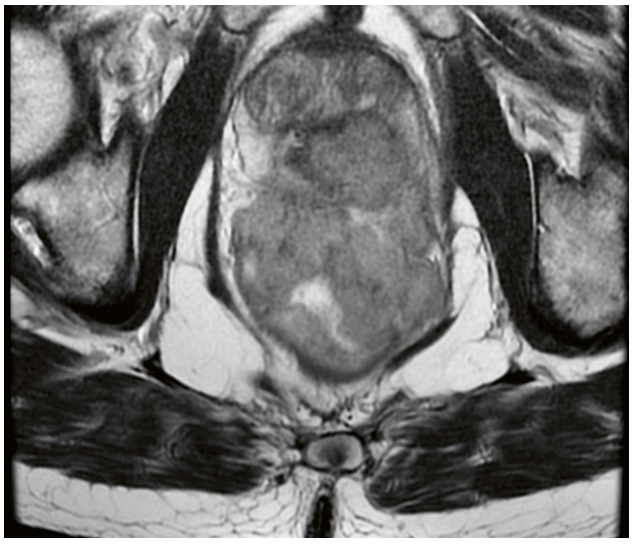

7 Pre ADT axial T2 image with extensive tumor invading the rectum and pelvic sidewall.

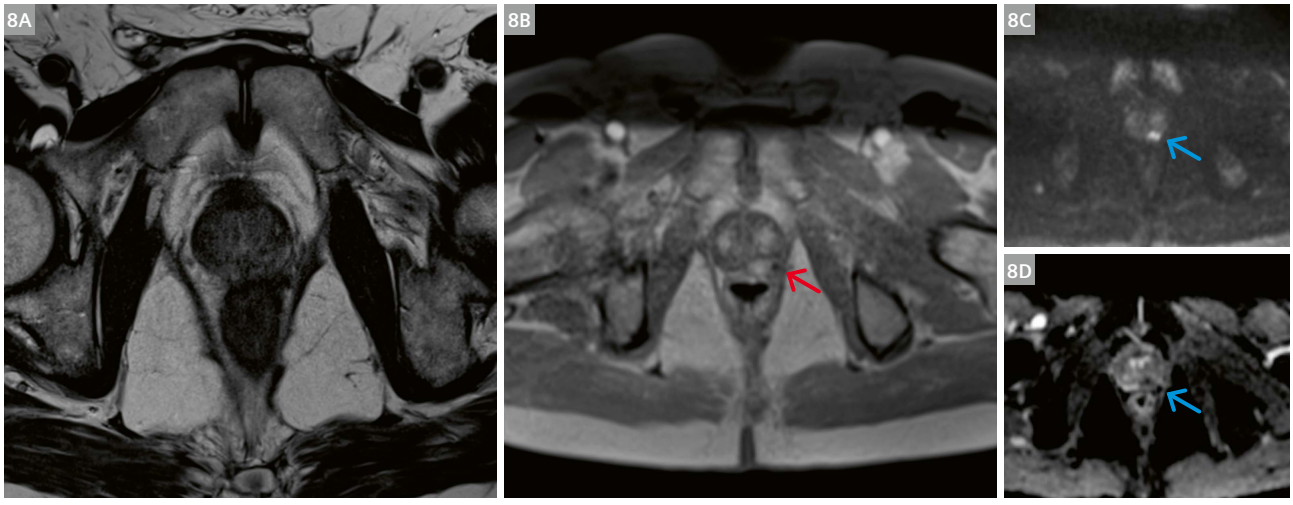

8 Same patient following 8 months of ADT treatment. **(8A)** T2 image showing marked reduction in tumor volume without clearly identifiable residual disease. **(8B)** Left mid gland peripheral zone tumor is seen on DCE (red arrow) and **(8C)** DWI, and **(8D)** ADC sequences (blue arrows).

using a template grid. Ice ball formation leads to lysis of cells within the treatment zone.

High intensity focused ultrasound causes coagulation necrosis by converting mechanical energy into heat and generating a cavitation affect.

Photodynamic therapy involves pre-treatment of the patient with a photosensitizer molecule which absorbs light of a specific frequency and transfers energy to adjacent oxygen molecules creating reactive oxygen species that trigger cell destruction.

Focal laser ablation involves thermal destruction of tissue via a fiberoptic cable placed within the tumor and is performed with MR guidance.

Irreversible electroporation uses two electrodes to increase the permeability of cell membranes leading to apoptosis and necrosis.

Post treatment appearances following focal therapy are variable; often a central zone of necrosis is demonstrated with absence of enhancement, surrounded by an enhancing rim of granulation tissue. The T2 sequences often demonstrate heterogeneous or hypointense signal in the area of treatment. High signal on T1 sequences can be seen due to hemorrhage and blood products, and therefore subtraction sequences are important to differentiate this from enhancement (Fig. 9).

Recurrence following focal therapy can appear as low signal which blends in with the adjacent low T2 signal fibrotic tissue. Low ADC values are suspicious only if combined with high signal on the DWI sequence in order to accurately distinguish recurrent tumor from areas of fibrotic tissue.

Focal enhancement with washout is also suspicious for residual viable tumor however areas of nodular enhancement at the borders of treated lesions secondary to reactive normal prostate tissue can mimic recurrence [11].

Mimics of recurrence

Retained seminal vesicle: Often first identified on CT, the seminal vesicle is retained in 20% of radical prostatectomies [12], commonly related to difficulties in surgical technique or intentionally to reduce the risk of neurovascular bundle injury. MR typically demonstrates a typical convoluted appearance with no evidence of diffusion restriction or abnormal enhancement (Fig. 11).

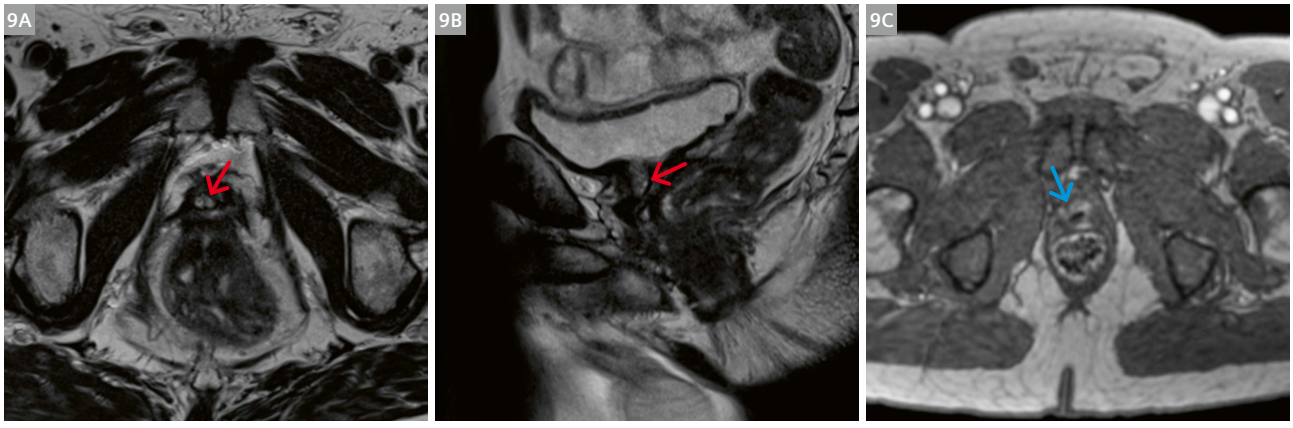

9 **(9A, B)** Axial and sagittal images showing post HIFU ablation zone with central areal of high signal necrosis (red arrows). **(9C)** Axial DCE image showing peripheral rim enhancement around the site of ablation in a different patient (blue arrow).

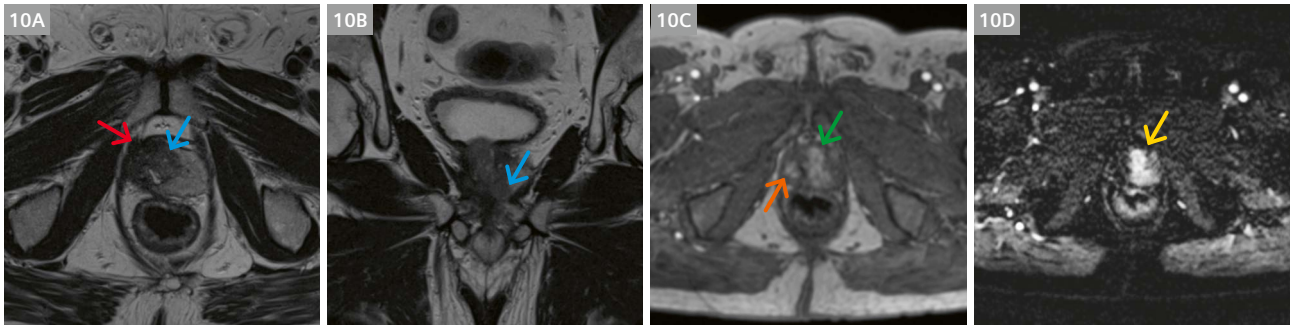

10 Recurrence following phototherapy. **(10A, B)** T2 sequence showing low signal fibrosis at treatment site (red arrow) with adjacent intermediate signal recurrence (blue arrows). **(10C, D)** DCE images show enhancement corresponding to the area of abnormality (green arrow). Subtraction images are mandatory to distinguish blood product within the treatment zone (orange arrow) from enhancing tumor (yellow arrow).

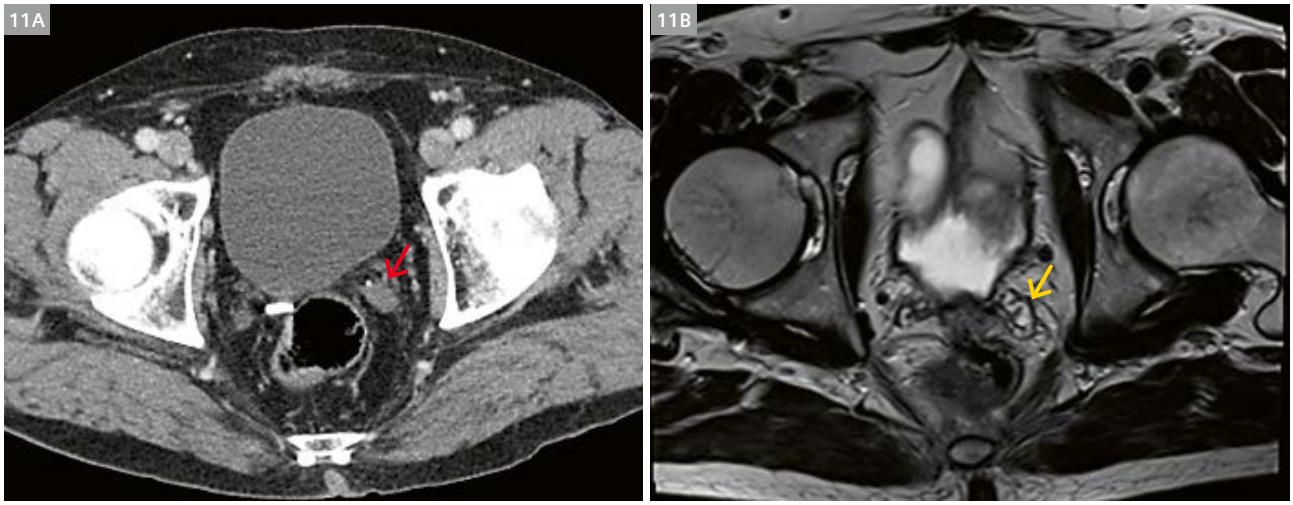

11 **(11A)** Retained seminal vesicle can be mistaken for recurrence especially on CT (red arrow). **(11B)** Characteristic convoluted appearance on T2-weighted MR confirms diagnosis (yellow arrow).

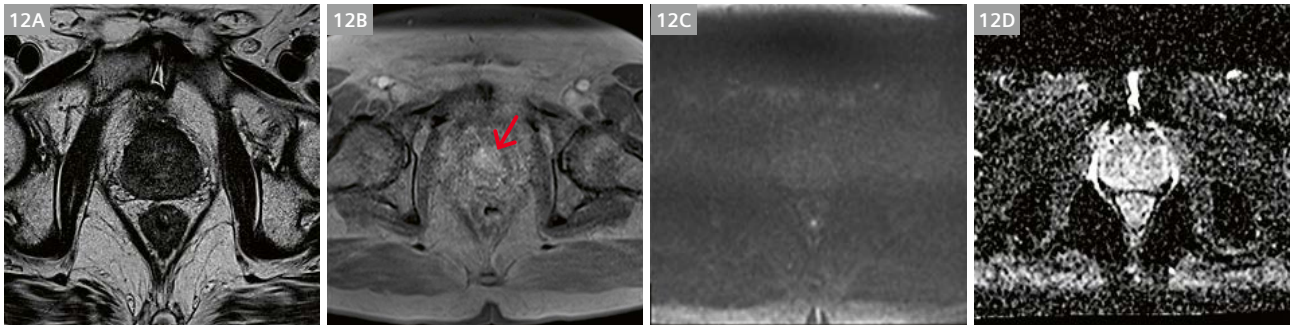

12 Fibrosis or scar tissue following radiotherapy can be difficult to distinguish from tumor. **(12A)** Scar is diffusely low signal on T2, **(12B)** 3 minute delayed post gadolinium sequence demonstrates late enhancement (red arrow). **(12C, D)** Absence of diffusion restriction.

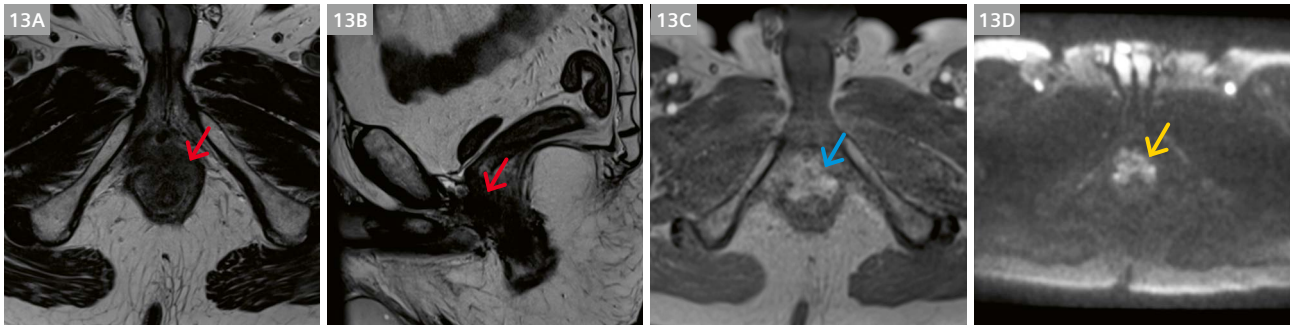

13 Low signal tumor involving prostate resection bed in a patient treated with radiotherapy and salvage cystoprostatectomy following recurrence, biopsy showed invasive rectal adenocarcinoma. **(13A, B)** Low signal in resection bed involving rectum (red arrows). **(13C)** Enhancing tumor (blue arrow), **(13D)** diffusion restriction (yellow arrow).

Focal fibrosis or scarring is commonly seen following EBRT and tissue appears low signal on T2 with no diffusion restriction and diffuse high values on the ADC map. Enhancement should be absent or show delayed gradual uptake without rapid washout (Fig. 12).

Granulation tissue tends to show high signal on T2 sequences with no evidence of diffusion restriction or early enhancement.

The occurrence of secondary cancers due to prior pelvic radiotherapy is somewhat controversial however abnormal findings within the prostatic bed following radiotherapy or prostatectomy can also be related to tumors arising in adjacent structures and careful examination of the other pelvic organs is mandatory. Unusual tumor behaviour such as failure to respond to ADT in a blockade naïve patient should prompt consideration of biopsy (Fig. 13).

Conclusion

Early detection and localization of recurrent prostate cancer is important for treatment planning and prognosis. Detection in post treatment cases can be challenging however advances in mp-MRI help to differentiate recurrence from mimics with DCE sequences being key in post treatment cases. Radiologist familiarity with imaging appearances of recurrence and mimics helps to make a correct and timely diagnosis.

Contact

Associate Professor Silvia Chang, M.D., FRCPC
Department of Radiology
Vancouver General Hospital
899 West 12th Avenue
Vancouver, BC V5Z 1M9
Canada
Tel.: +1 (604) 875-4340
Silvia.Chang@vch.ca

References

1 Cookson MS, Aus G, Burnett AL, et al. Variation in the definition of biochemical recurrence in patients treated for localized prostate cancer: the American Urological Association Prostate Guidelines for Localized Prostate Cancer Update Panel report and recommendations for a standard in the reporting of surgical outcomes. J Urol. 2007;177(2):540-545.
2 Mottet N, Bellmunt J, Bolla M, et al. EAU-ESTRO-SIOG Guidelines on Prostate Cancer. Part 1: Screening, Diagnosis, and Local Treatment with Curative Intent. Eur Urol. 2017;71(4):618-629.
3 Cornford P, Bellmunt J, Bolla M, et al. EAU-ESTRO-SIOG Guidelines on Prostate Cancer. Part II: Treatment of Relapsing, Metastatic, and Castration-Resistant Prostate Cancer. Eur Urol. 2017;71(4):630-642.
4 Allen SD, Thompson A, Sohaib SA. The normal post-surgical anatomy of the male pelvis following radical prostatectomy as assessed by magnetic resonance imaging. Eur Radiol. 2008;18(6):1281-1291.
5 Tyson MD, II, Andrews PE, Ferrigni RF, Humphreys MR, Parker AS, Castle EP. Radical Prostatectomy Trends in the United States: 1998 to 2011. Mayo Clinic Proceedings. 2016;91(1):10–16.
6 Rouvière O, Vitry T, Lyonnet D. Imaging of prostate cancer local recurrences: why and how? Eur Radiol. 2010;20(5):1254-1266.
7 Roy C, Foudi F, Charton J, et al. Comparative sensitivities of functional MRI sequences in detection of local recurrence of prostate carcinoma after radical prostatectomy or external-beam radiotherapy. AJR Am J Roentgenol. 2013;200(4):W361-368.
8 Roach M, Hanks G, Thames H, et al. Defining biochemical failure following radiotherapy with or without hormonal therapy in men with clinically localized prostate cancer: recommendations of the RTOG-ASTRO Phoenix Consensus Conference. Int J Radiat Oncol Biol Phys. 2006;65(4):965-974.
9 Kim AY, Kim CK, Park SY, Park BK. Diffusion-weighted imaging to evaluate for changes from androgen deprivation therapy in prostate cancer. AJR Am J Roentgenol. 2014;203(6):W645-650.
10 Hötker AM, Mazaheri Y, Zheng J, et al. Prostate Cancer: assessing the effects of androgen-deprivation therapy using quantitative diffusion-weighted and dynamic contrast-enhanced MRI. Eur Radiol. 2015;25(9):2665-2672.
11 De Visschere PJ, De Meerleer GO, Fütterer JJ, Villeirs GM. Role of MRI in follow-up after focal therapy for prostate carcinoma. AJR Am J Roentgenol. 2010;194(6):1427-1433.
12 Sella T, Schwartz LH, Hricak H. Retained seminal vesicles after radical prostatectomy: frequency, MRI characteristics, and clinical relevance. AJR Am J Roentgenol. 2006;186(2):539-546.

First Impressions of MAGNETOM Vida Fit in Lucerne, Switzerland

Justus E. Roos, Thomas Treumann, Markus Wyss, Alexander von Hessling

Cantonal Hospital Lucerne, Switzerland

Introduction

The Lucerne Cantonal Hospital (LUKS) is one of the largest hospitals in Switzerland, with 867 patient beds and approximately 700 000 ambulatory and 430 000 stationary visits per year [1]. It serves as a central hub for five affiliated hospitals, bringing together experts in all clinical specialties and many services including teleradiology. As a pioneer of digital transformation in the Swiss healthcare market, it has its own stringent digitization strategy, and is implementing an all-encompassing new hospital information system (EPIC®).

LUKS is an academic teaching hospital, so our physicians keep their knowledge up to date, constantly translating new research findings into clinical practice and conducting their own research projects. This requires the latest medical equipment, especially in the radiology and nuclear medicine department.

In Lucerne, we have currently three MRI scanners, one 1.5T (MAGNETOM Aera, Siemens Healthcare, Erlangen, Germany) and two 3T systems (MAGNETOM Skyra, Siemens Healthcare, and Achieva, Philips Medical Systems, Eindhoven, The Netherlands). With the 3T MAGNETOM Skyra we have a strong focus on neuroradiology examinations, accounting for approximately 52% of all patients scanned, followed by examinations of the pelvis with 10% and the heart with 8.0% (Fig. 1). Our latest research work in neuroradiology focuses on morphological and metabolic assessement of dementia and Parkinson's disease, as well as the evaluation of quantitative imaging methods [2, 3].

The opportunity of upgrading our existing MAGNETOM Skyra 3T system to a MAGNEOM Vida Fit with BioMatrix Technology was very attractive, as it would enable us to keep up with the latest technological advances in MRI and support our research work at a very effective cost-benefit ratio compared with installing an entirely new system. We decided to purchase the upgrade to improve diagnostic image quality and accelerate data acquisition, which can increase the number of patients scanned per day and also provide better patient comfort.

In August 2019, we received the world's first MAGNETOM Vida Fit upgrade here in Lucerne, and in this article we share our first impressions.

Installation

The Vida Fit upgrade (Fig. 2) included new RF components, new electrical cabinets, new covers with one-touch positioning displays, a new patient table including a new 32-channel spine coil with respiratory sensors, and a new MRI workplace with a large screen monitor. Additionally, we received a new tiltable 20-channel head/neck coil with coil shimming technology, a new 18-channel transmit/receive knee coil and an 18-channel high-density flex coil.

A first installation can be unpredictable, but the upgrade went very smoothly and surprisingly fast with a total of 13 days' down time. On the very first day going live the scanner produced high quality brain images. Initial instability and specific absorption rate (SAR) problems, as well as a defective coil heat sensor, were corrected within the first week. During the second week, the system was very stable and MR imaging of all subspecialties (neuro, MSK, body, heart) was performed without any problem.

To bridge the time required for the system upgrade we operated a mobile MR unit in addition to our fixed installations. In retrospect this decision was very wise and helped prevent our waiting list from increasing (Fig. 3).

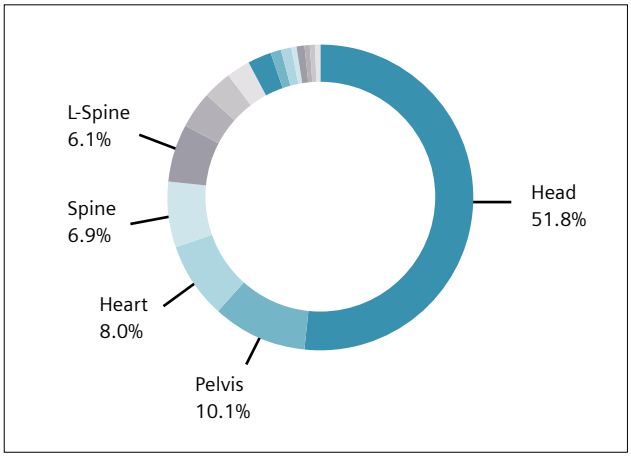

1 Case mix on MAGNETOM Skyra (Jan – Jul 2019).

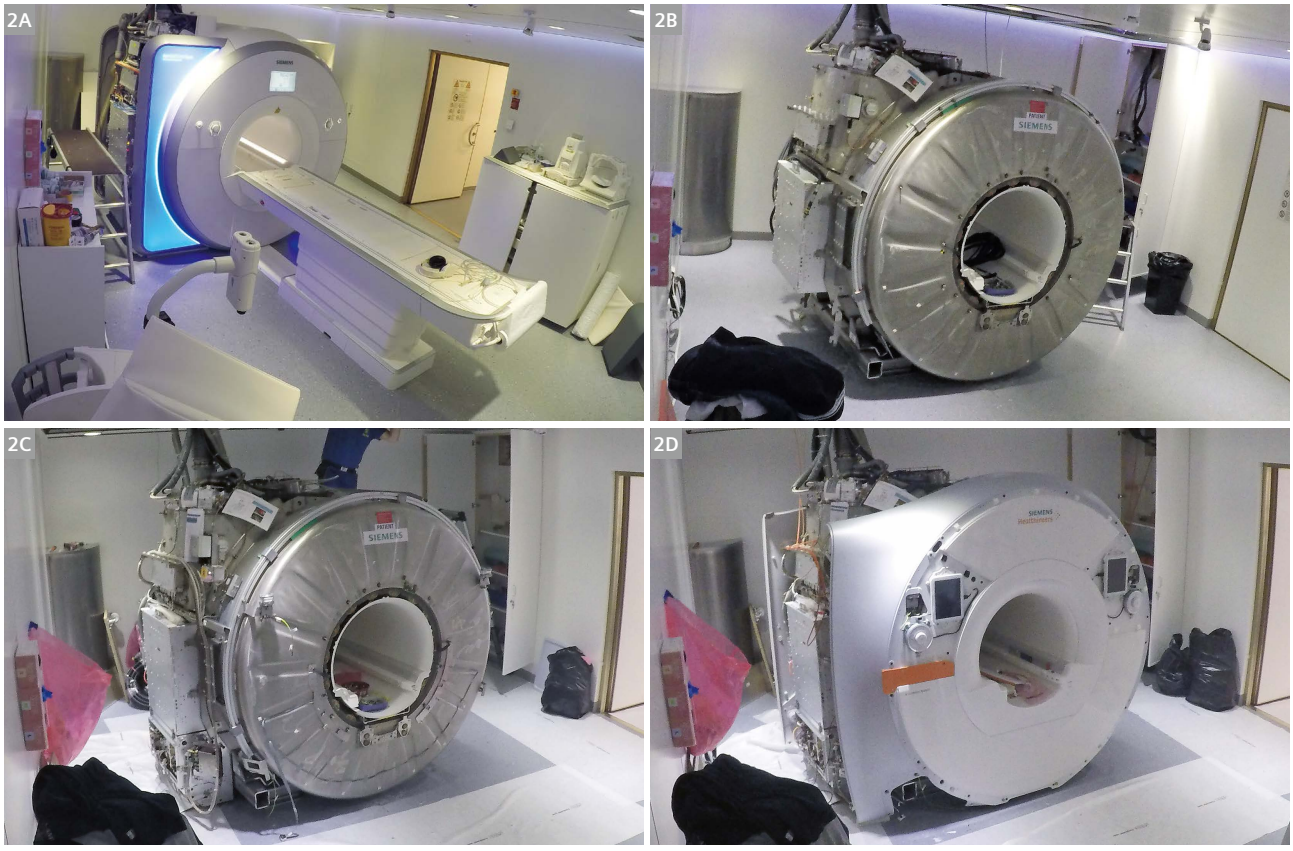

2 **(2A)** Dismantling the old MAGNETOM Skyra scanner. **(2B)** The stripped magnet. **(2C)** New RF components being installed. **(2D)** Installing new covers. **(2E)** New table being installed.

3 The mobile MR unit used during the MAGNETOM Vida Fit upgrade.

New work environment

Besides the many hardware changes, the system upgrade comes with a brand-new user interface and work environment for our technicians (new XA20 software). In particular, it combines planning, viewing and post-processing features into one platform that differs considerably from *syngo* MR E11C, the platform we have been using so far.

New to our technicians was the possibility to train themselves using a simulator, enabling them to get to know the user interface and to play around with planning and viewing the exams. This meant that our technicians were already familiar with the basic features of the new user interface before they scanned their first live case.

Adding to this upfront training with the simulator, local support by an application specialist was very constructive and helped our staff to quickly learn the specifics of the new user interface. The training included our main applications: neurological imaging, musculoskeletal imaging, body imaging, MR angiography and cardiac imaging. Now at the end of training, our MR-technicians feel comfortable enough to use the upgraded system for routine work.

First clinical impressions

Our standard brain examination consists of a transversal diffusion, T1 MPRAGE, transversal T2 spin-echo sequence, time-of-flight (TOF), postcontrast 3D FLAIR, and, finally, a second T1 MPRAGE. After the upgrade, we can carry out this standard protocol more quickly, by applying compressed sensing accleration for TOF and 3D FLAIR.

At the same time images can be acquired with thinner slices and higher resolution, especially for diffusion (DWI) by using simultaneous multi-slice. With a 1-mm isovoxel DWI from the whole brain it is now unnecessary in most cases to acquire additional planes, for example of the brainstem (Fig. 4).

We were also able to acquire high resolution susceptibility-weighted images (SWI), helping us to detect the "swallow tail sign" of Parkinson's disease. This is revealed through nigrosomes, dopaminergic cells that return high signal in SWI sequences. The presence of nigrosome within the posterior substatia nigra is often difficult to detect, but with the high resolution SWI on our MAGNETOM Vida Fit, we're now able to find this sign with higher confidence (Fig. 5).

With the Compressed Sensing GRASP–VIBE 4D sequence, we were able for the first time to acquire motion-insensitive time-resolved images from the neck to better delineate tumor tissue from adjacent mucosa and muscles of the tongue (Fig. 6A). Measuring enhancement characteristics of different tissues is possible and helps us to better delineate tissues. This can be very helpful in tumors of the neck for example, where enhancement curves differ between tumor tissue and mucosa and musculature (Fig. 6B).

A common referring question from our head and neck department is to rule out endolymphatic hydrops in patients with dizziness. With a 3D real IR sequence acquired four hours after applying a double dose of standard intravenous contrast, the anatomy of the inner ear can be visualized with excellent image quality (Fig. 7). So far, no patient with proven endolymphatic hydrops has been scanned.

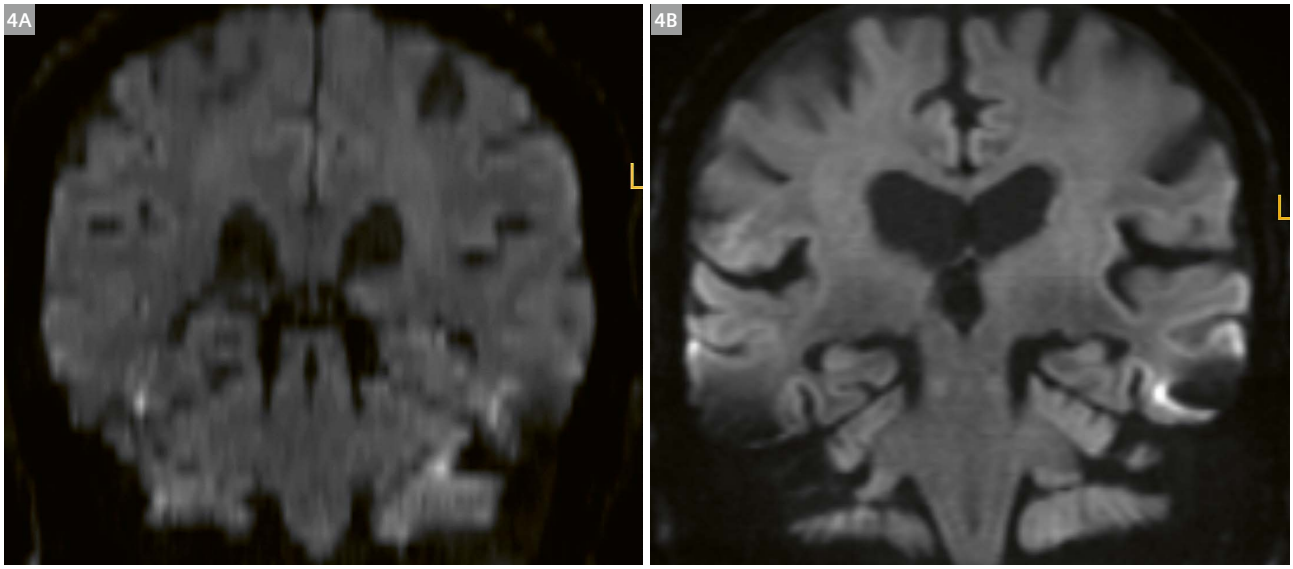

4 **(4A)** Coronal reconstruction of conventional DWI acquisition on MAGNETOM Skyra.
(4B) Coronal reconstruction from isovoxel DWI on MAGNETOM Vida Fit.

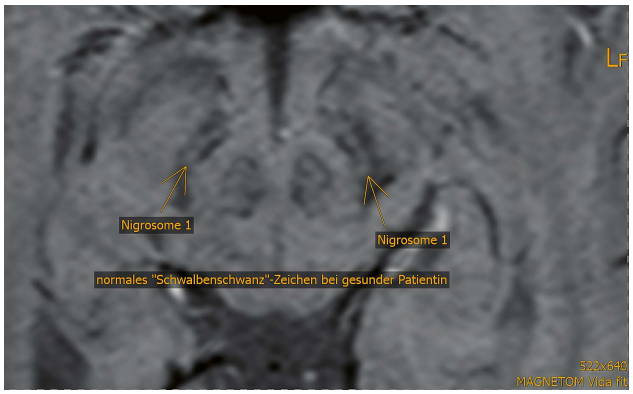

5 Normal swallow tail sign in a healthy patient. The fine white line caused by the presence of dopaminergic cells (nigrosome 1) can be seen on both sides.

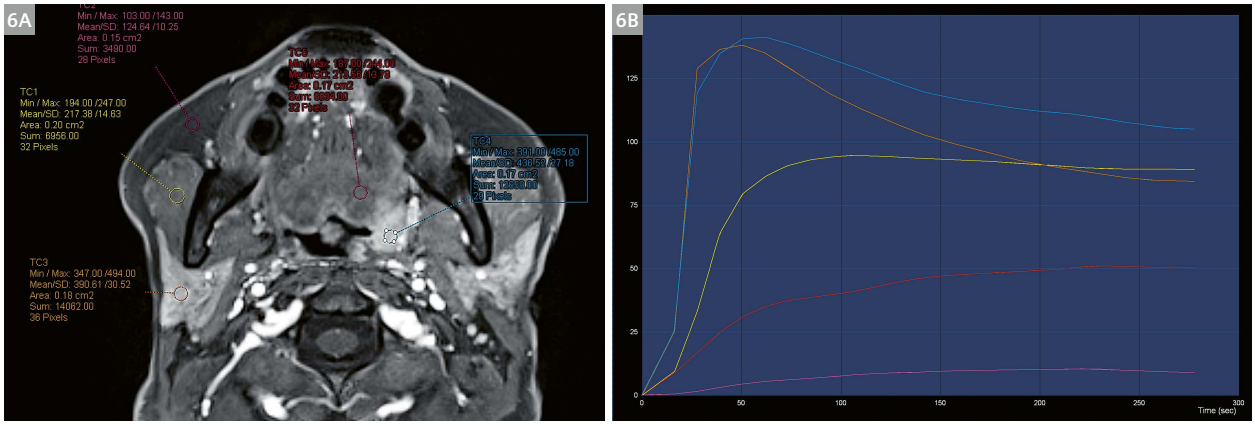

6 **(6A)** Late arterial image from a dynamic GRASP sequence (only one late arterial image shown here). On *syngo*.via, regions of interest (ROI) can be drawn in tissues of interest and specific enhancement curves, helping to distinguish tumor from normal tissue.
To access the time-resolved images/video please visit www.siemens-healthineers.com/vidafit
(6B) Enhancement curves from figure 6A, nicely visualizing the different enhancement characteristics of the color coded ROIs.

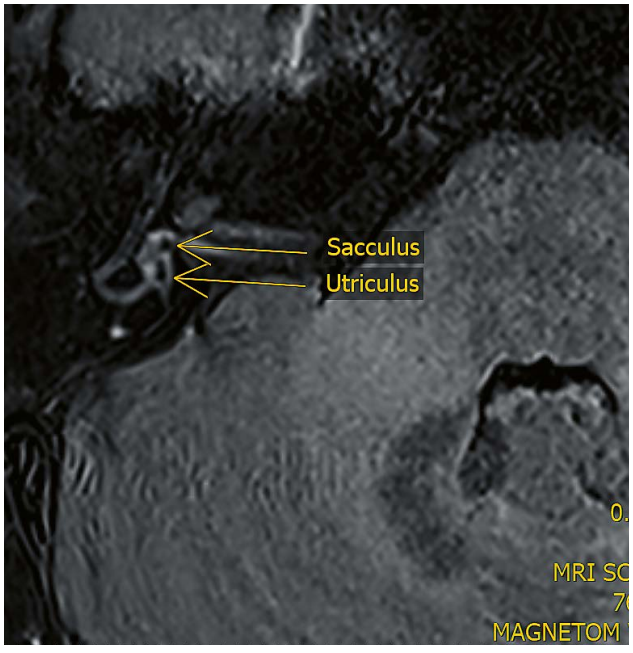

7 Anatomic example of vestibulum with sacculus and utriculus.

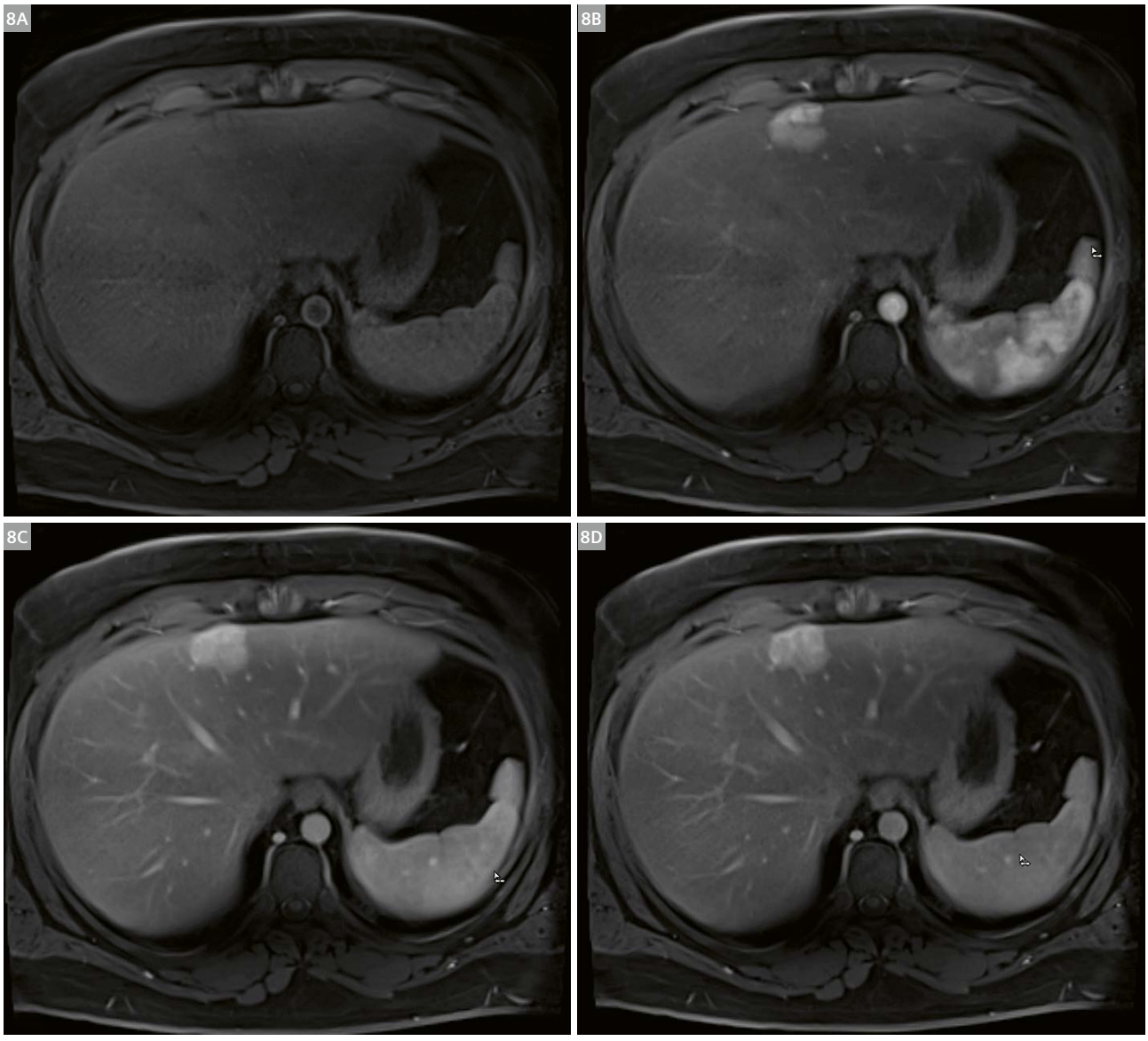

8 Dynamic GRASP-VIBE 4D sequence demonstrates the perfusion of a focal liver lesion (**8A** non-contrast, **8B** arterial phase, **8C** porto-venous phase, **8D** venous late phase). Despite patient's free breathing and short acquisition time of 5 minutes, the image is free of motion artifacts and demonstrates a very homogenous image quality.
To access the time-resolved images/video please visit www.siemens-healthineers.com/vidafit

The initial promising results in abdominal imaging give us hope of making these exams more robust and easy to acquire. As the BioMatrix respiratory sensors constantly show the respiratory cycle of the patient throughout the whole examination, sequence strategies can be planned upfront without any hustle. Figure 8 demonstrates excellent image quality of dynamic liver imaging using a 4D GRASP-VIBE sequence. The image quality is outstanding even though the sequence was acquired with the patient free-breathing, and with an image acquisition time of only 5 minutes.

The improvement in cardiac imaging was apparent from the very first patient we scanned. Accelerated image acquisition due to new compressed sensing capabilities allowed us to cover more short-axis (SAX) cine images within a single breath-hold (Fig. 9A). Furthermore, the scanning of delayed enhancement (DE) images – normally a very delicate task given the patients fatigue toward the end of a cardiac study – was very impressive, as images can be acquired with free breathing, with an image quality comparable to traditional breath-hold DE image acquisitions (Fig. 9B).

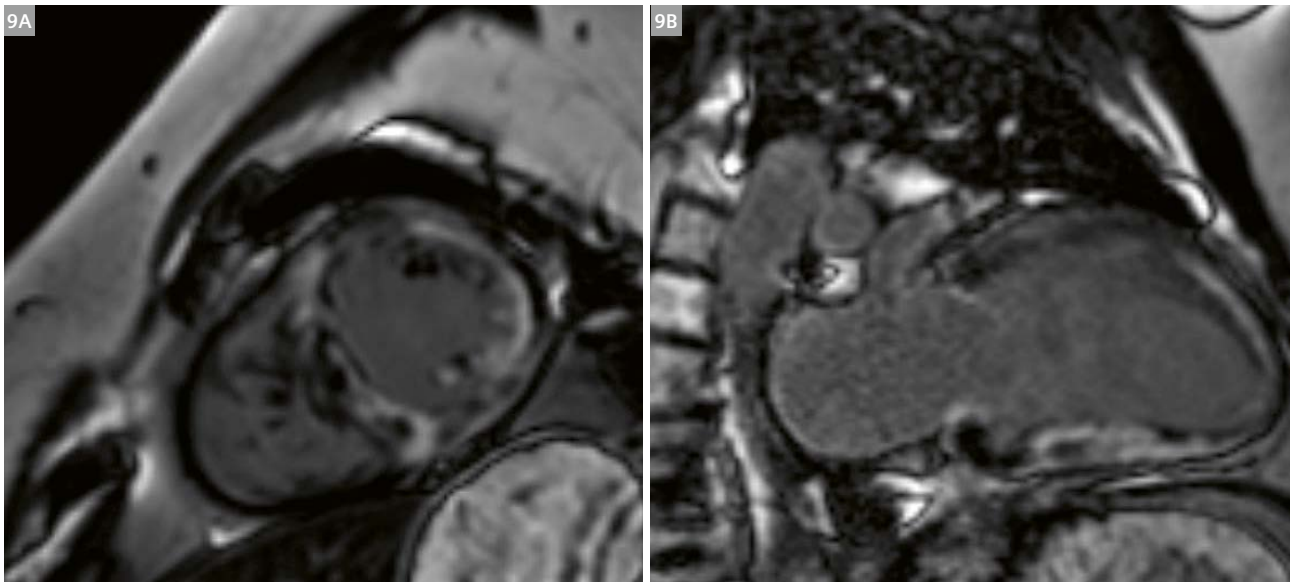

9 Short-axis **(9A)** and 2-chamber long axis **(9B)** delayed-enhancement (DE) images in a patient with familial cardiomyopathy, acquired with free breathing. Image quality and the amount of motion artifacts are comparable with traditional breath-hold images.

Conclusion

After using the MAGNETOM Vida Fit for two weeks, early results give us confidence that we will be able to achieve our goals to shorten many examinations while maintaining high image quality – or even improving it in some areas, such as abdominal and neurological scans. With this upgrade we can take advantage of the latest innovations from Siemens Healthineers while keeping investment costs down. The overall cost-benefit ratio of an upgrade to MAGNETOM Vida Fit was the decisive factor for us, and the upgraded system effectively brings the same benefits as a new system.

We are looking forward to the full benefits of our investment, once we have implemented all the new features available with the scanner, and integrated it into our clinical routine as we gather more experience.

References

1 Luzernen Kantonspital Jahres- und Finanzbericht 2018. Luzerner Kantonsspital Luzern; 2019 March 22 [cited on 2019 Sep 6]. Available from: https://www.luks.ch/sites/default/files/2019-04/luks_jahres_und_finanzbericht_2018.pdf
2 Keller D, von Hessling A, Nyffeler T, Reichert M, Strobel K. Morphologische und metabolische Bildgebung zur Demenzabklärung. Der Luzerner Arzt. 2016;5/107.
3 Keller D, Grünig H, Bohlhalter S, von Hessling A, Strobel K. Morphologische und metabolische Bildgebung bei Parkinsonismus. Der Luzerner Arzt. 2017, 110, 44-50.

Contact

PD Dr. Justus Roos
Head of the Department of
Radiology and Nuclear Medicine
Luzerner Kantonsspital
Lucerne, Switzerland
Tel: +41 41 205 4651
Fax: +41 41 205 4689
justus.roos@luks.ch
www.luks.ch

Justus Roos | Thomas Treutmann | Alexander von Hessling | Markus Wyss

GOKnee2D and GOKnee2D^{SMS} Protocols Available for Download

Redesign your clinical routine

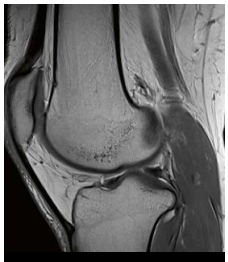

Pd tse sag p2
0.5 x 0.5 x 3 mm
TA 2:13 min

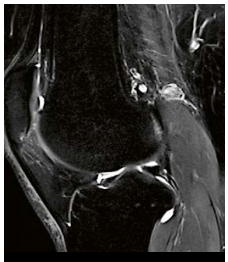

T2 tse fs sag p2
0.6 x 0.6 x 3 mm
TA 2:10 min

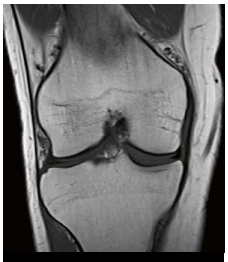

T1 cor p2
0.8 x 0.8 x 3,5 mm
TA 0:35 min

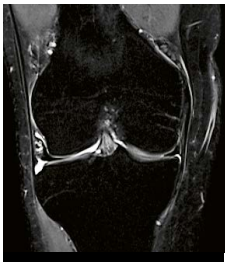

Pd tse fs cor p2
0.6 x 0.6 x 3 mm
TA 2:26 min

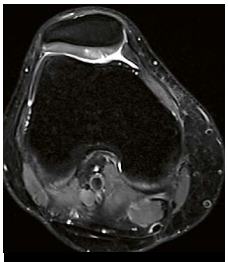

Pd tse fs tra p2
0.6 x 0.6 x 3 mm
TA 1:40 min

GOKnee2D in 9:17 minutes

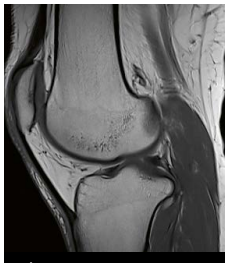

Pd tse sag p2 SMS 2
0.5 x 0.5 x 3 mm
TA 1:10 min

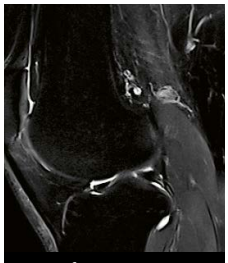

T2 tse fs sag p2 SMS 2
0.6 x 0.6 x 3 mm
TA 1:09 min

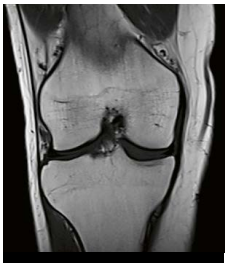

T1 cor p2 SMS 2
0.8 x 0.8 x 3,5 mm
TA 00:20 min

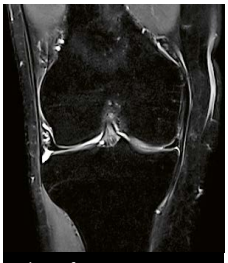

Pd tse fs cor p2 SMS 2
0.6 x 0.6 x 3 mm
TA 1:15 min

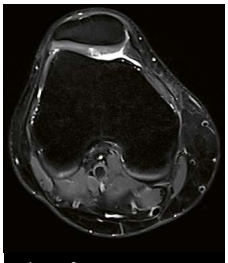

Pd tse fs tra p2 SMS 2
0.6 x 0.6 x 3 mm
TA 00:53 min

GOKnee2D^{SMS} in 5:00 minutes

GOKnee2D and GOKnee2D^{SMS} are fast and push-button 2D MRI protocols of the knee which acquire all relevant clinical information in approximately 10 or 5 minutes scan time, respectively. GOKnee2D is based on standard TSE pulse sequences with standard parallel imaging acceleration and provides 5 different, routinely used contrasts for diagnostic assessment. GOKnee2D^{SMS} provides the same datasets and contrasts and is additionally accelerated with Simultaneous Multi-Slice. Both GOKnee2D and GOKnee2D^{SMS} have been clinically validated for a broad range of clinical conditions such as cartilage defects or meniscal tears by Prof Jan Fritz and colleagues (Johns Hopkins University School of Medicine, Baltimore, MD, USA).

Machine intelligence assists in efficiently planning and performing the scans with automatic positioning and adaption of scan parameters.

GOKnee2D / GOKnee2D^{SMS} protocols are available for 1.5 and 3T at **www.siemens.com/magnetom-world > Clinical Corner > Protocols**

Achieved on MAGNETOM Vida with Tx/Rx Knee 15. Total examination times will vary with system field strength with up to 5:20 minutes on MAGNETOM Sola, Altea or Sola Fit. Study ID: 3aaaa1245 and 3aaaa1244

SIEMENS Healthineers

How a Bell Pepper Convinced the Siemens Med Board

Arnulf Oppelt, Ph.D.; Wilfried Loeffler, Ph.D.

Siemens Healthineers, Erlangen, Germany

"The best way to predict the future is to invent it."

Theodore Edward Hook, 1825

In 1983, the first Siemens MRI system bearing the MAGNETOM name was installed at the Mallinckrodt Institute of Radiology, in St. Louis, Missouri, USA. Ever since those early days, the name MAGNETOM has been associated with technological innovation and advances, such as the first wide bore 70-cm MRI system, new coil concepts like Tim and Tim4G ("from local to total") and, most recently, with the innovations of the BioMatrix platform. This allows the operator to adapt scanning to patient individuality via special sensors and interfaces and, thanks to the most modern acceleration techniques, also makes MRI faster and more patient friendly, for example with free breathing examinations.

This is the first part in a series of articles that take a retrospective view to see how we got to MRI of today.

Without doubt, Magnetic Resonance Imaging, or MRI for short, is the most flexible of all imaging methods and the diagnostic modality of choice for many clinical indications. Siemens Healthineers is the global leader in this technology. However, in the beginning MRI at Siemens was not mainly driven by market analysis or scientific progress.

In 1973, the British recording company EMI presented a completely new X-ray device at the RSNA Annual Meeting: the first computer tomograph. For established X-ray manufacturers like Siemens Medical and most of its competitors, there did not seem to be much future in such a development. Spatial resolution was of outmost importance, while few realized the benefit of significantly improved soft tissue contrast. Therefore, a tiny focal spot and a high-resolution image amplifier seemed to be what the market craved for.

When in 1976 the London Evening Standard published the headline "EMI on brink of a super scanner" in its June 11 edition, readers learned that the company was working on another revolutionary scanner, this time based on high-frequency radio waves, alarm bells started ringing: This time Siemens was not going to miss this trend.

Siemens, in fact, had its very own dedicated researcher, Dr. Alexander Ganssen, who had been investigating the possibilities of electromagnetic waves below the X-ray frequency spectrum for some time. Yet, there was little interest in Dr. Ganssens's proposals (Fig. 1) for the medical application of NMR (nuclear magnetic resonance) to determine blood flow, cystic fibrosis, and blood viscosity.

However, the article in the Evening Standard provided reason enough to visit Paul Lauterbur, a later recipient of the Nobel Prize, in the U.S. and Dr. Mansfield in England, on a fact-finding mission about advances in this field.

As a result, it was proposed that Siemens start its own work. In the fall of 1977, high-level preliminary discussions took place between Dr. Schittenhelm, Dr. Ganssen,

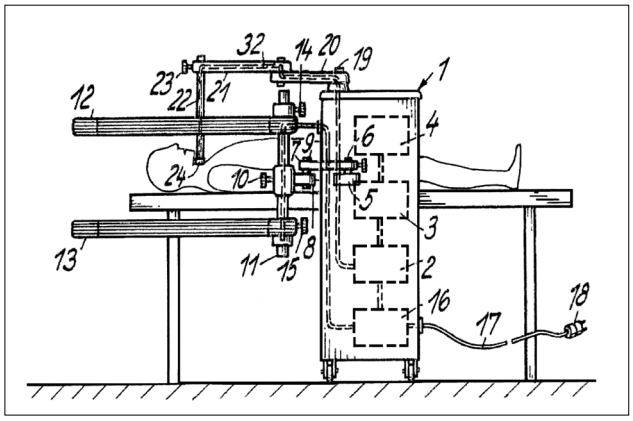

1 Dr. Ganssen's diagnostic equipment for determining the distribution of substances using nuclear magnetic resonance.

Mr. Kuckuck, Mr. Schmidt (Siemens), Dr. Mansfield (University of Nottingham, UK), Dr. Maudsley (Zürich University, Switzerland), and Dr. Oppelt (Technical University Darmstadt, Germany). This marked the beginning of the Siemens project.

The managing board now also approved the proposal. Dr. Mansfield was hired as a consultant, and Andrew Maudsley, who as part of his dissertation under Mansfield had been the first person to scan a human finger in vivo using NMR, and Arnulf Oppelt, one of the authors of this article, joined Siemens on February 1, 1978.

Development costs of some two million German Mark (DM) were approved, the head of the X-ray development department, Professor Gudden, was able assert himself amid strong protests from the X-ray CT sales department who would have liked to see that money used to further CT development. However, an image of a head presented by EMI at the RSNA in 1978 (Fig. 2) was too powerful an argument.

Specifications were drawn up for a trial scanner and an air-core whole-body magnet was ordered from Oxford Instruments (OI) in England. The gradient coils and power supply were developed at the Siemens research laboratories, RF and control electronics as well as the software were tasked to Siemens Med. A number of components were already available from Dr. Ganssen's preliminary work, such as a Magnion iron core experimental magnet, a frequency synthesizer, a 10 W RF power amplifier. A state-of-the-art PDP 11 minicomputer was available from the CT group. These components were combined to form a small imaging test set-up to develop and test the software for the planned large scanner. In particular, an experimental device for "spectroscopic imaging" was developed in order to allow fast measurements of the magnetic field homogeneity. This was published in 1979 in the Siemens Research and Development Reports [1]. At the end of 1978, the resistive whole-body magnet with a field strength of 0.1 Tesla was delivered (Fig. 3) and installed in the research system on the grounds of the Siemens research center housed in a purpose-built wooden hut, which contained no ferromagnetic parts, not even iron nails (Figs. 4 and 5).

By this time, Andrew Maudsley had again left Siemens to head an even more ambitious MRI project in the U.S. using superconducting magnets. He was succeeded by Dr. Wilfried Loeffler from CT development, the other author of this article. 1979 was spent eliminating faults in the software and hardware. It took rather a long time before we realized that the radio-frequency interference that caused us such a headache was entering via the magnet

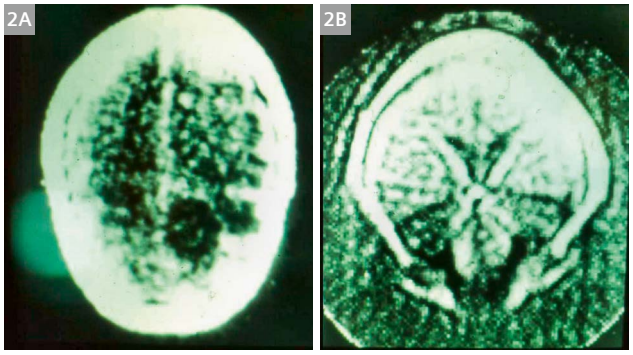

2 Comparison of an early CT image and an image of the head made with a new "radio wave scanner" at the EMI booth at RSNA 1978.

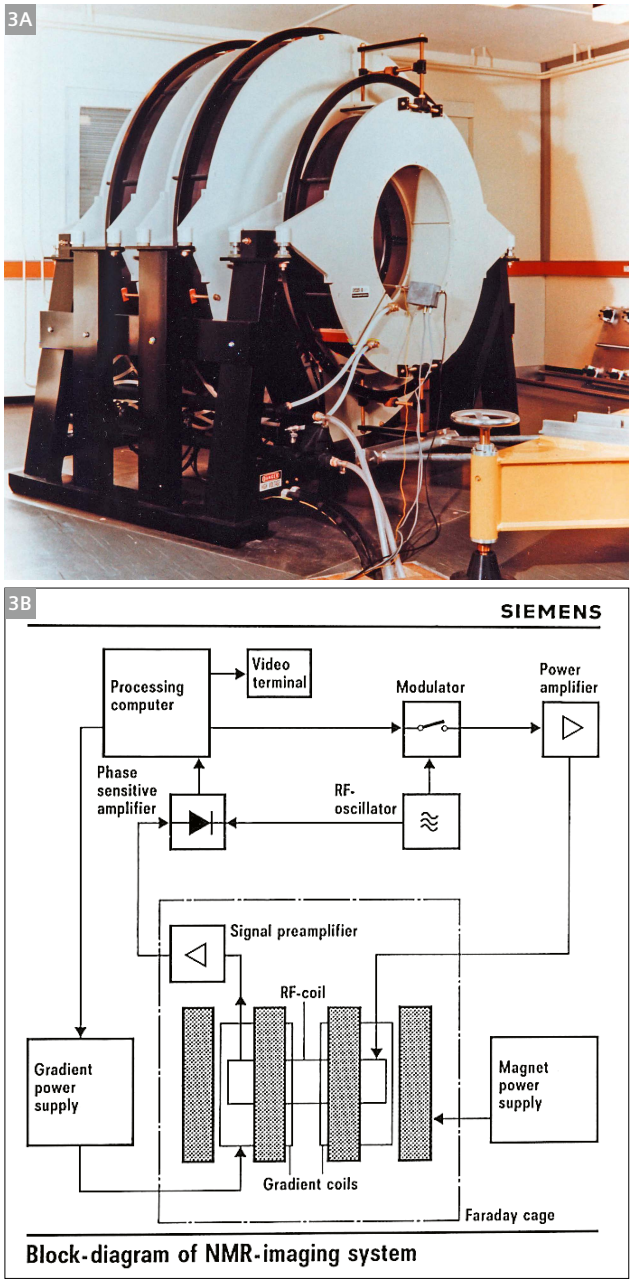

3 (3A) 0.1T whole-body magnet manufactured by Oxford Instruments for Siemens in 1978. (3B) Block diagram of an NMR imaging system.

4 First MRI measuring system at Siemens 1978.

5 RF Faraday cage built around the 0.1T magnet.

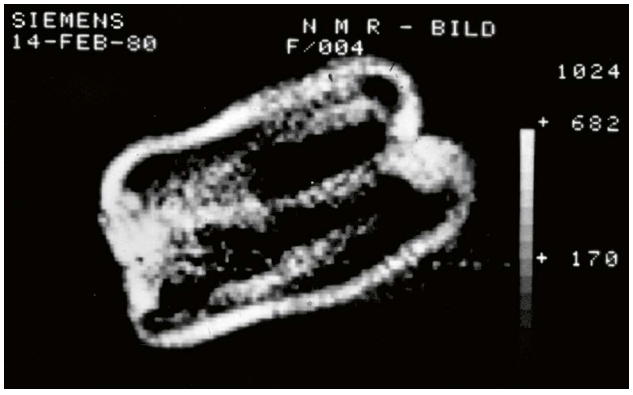

6 First Siemens MRI image of a bell pepper, 1979.

power supply cables. Although an RF filter for a current of 80 A was a product available from Siemens, the delivery time was three months. Time was running out. The business and budget negotiations for the coming year were about to begin and we were told in no uncertain terms that immediate proof of the functioning of the system in the form an image was the precondition for continuing the project. Luckily, this hard ultimatum did not shock us into forgetting all our basic physics and we remembered that random signal disturbances can be averaged out by repeated measurement. We would need an hour of measurement time to resolve this problem but the result proved worth waiting for.

We chose a green bell pepper as our measurement object, suitable because it would certainly keep still, contained water, was large enough to represent a human organ, and could be cut open to demonstrate the similarity between image and true anatomy of the object.

Since scanning took such a long time, we were not able to present the results to the managing board until the next day (Fig. 6).

Everyone involved was extremely happy with the image produced by the measurement. Little image noise, only one artifact. It took a few weeks before the cause of the artifact in image reconstruction was found. That is why the date of reconstruction that appears on the image is February 14, 1980, even though the object was scanned in November 1979.

A bell pepper had been instrumental in convincing the Siemens Med board of the potential of MRI. The decision to approve continuation of the project was a wise one, as history has shown.

Development moved fast, the first head images were presented at the annual meeting of the German Society of Neuroradiology in 1980 in Munich and at the German Röntgen congress in 1981 in Munich. Device developments were reported on in 1981 [2]. A year later, the business unit MR Tomography was established and product development started.

References

1 A.A. Maudsley, A. Oppelt, A. Ganssen Rapid Measurement of Magnetic Field Distributions Using Nuclear Magnetic Resonance Siemens Forsch. u. Entwickl. Ber. Vol. 8 (1979), No. 6, pp. 325–331.
2 A. Ganssen, W. Loeffler, A. Oppelt, F. Schmidt Kernspin-Tomographie Computertomographie 1, pp. 10–18 (1981).

Contact

Dr. Arnulf Oppelt
oppelt_arnulf@t-online.de

Dr. Wilfried Loeffler
G.W.Loeffler@t-online.de

Dr. Oppelt

Dr. Loeffler

Meet Siemens Healthineers

Siemens Healthineers: Our brand name embodies the pioneering spirit and engineering expertise that is unique in the healthcare industry. The people working for Siemens Healthineers are totally committed to the company they work for, and are passionate about their technology. In this section we introduce you to colleagues from all over the world – people who put their hearts into what they do.

Dagmar Hering

Dagmar Hering holds a degree in electrical engineering from the Nuremberg Institute of Technology in Germany. She joined Siemens Healthineers in 1995. After initially working in software development for a lithotripsy system, she moved to MR in 2004, and has been part of that family ever since. Dagmar spent her first MR years working in Quality Management for MAGNETOM Espree and postprocessing with Leonardo before moving to Product Definition and taking on responsibility for the 3T premium segment and pediatric imaging. While working, she also earned an MBA in healthcare management from the University of Bayreuth. Dagmar became MR System Test Lead in 2011, and Head of Solution Verification and Validation covering system testing in 2018.

Erlangen, Germany

How did you first come into contact with MRI?
I started my career at Siemens Healthineers in the X-ray systems department, as part of the lithotripter project. We received regular training in radiation protection. Then my grandmother was diagnosed with cancer, and that was my first contact with MRI from a patient's perspective. The exam was very exhausting for my gran. It took over an hour and was very noisy. Also, the bore was very long and narrow. I was fascinated by the results, though: images with soft tissue characterization and no radiation exposure. This opened my eyes to a new world of clinical imaging, and I decided to move into MR development.

What do you find most fascinating about MRI?
The spirit of MRI. It drives developers, researchers, and users around the world to continuously work on improvements and explore new possibilities. For me, the technological leap from MAGNETOM Impact, which was used to examine my gran, to MAGNTOM Espree and the first 70 cm bore was amazing. The development project posed many challenges, but everyone on the team was committed to solving them so that we could launch the first short and open MRI system. Of course, the progress is still ongoing; every day, we learn from each other, generate new ideas, and seek to better understand the needs of operators and patients.

What role do you play in MRI development?
My team and I are responsible for system validation. This is the last step of the product development process. It provides the design validation reports for regulatory submissions to the FDA and for CE marking, for instance. System validation involves using the MRI system and/or the new features both as defined in the product specifications and as the customer will use them. The validation process consists of three phases: preparation, execution, and reporting. The preparation phase starts approximately six months before the execution phase, with the development of the validation plan. The planning stage establishes the required MRI systems, test content, and number of testers. The testers are selected according to the project content and their skills. In general, the tester team consists of internal technologists, customer technologists, and application specialists from Siemens Healthineers. The application specialists support multiple customers in their countries, which might be as far away as Canada or Japan. Arranging for these testers to be at our MR headquarters in Erlangen in the necessary time-frame is very time consuming. On the other hand, it is very beneficial for our evaluation process because of their global experience. The test execution phase happens at the MR headquarters of Siemens Healthineers in Erlangen, where we have over 30 MRI systems available for development, testing, and training. The testers perform predefined test cases as well as "freestyle" tests. The free hands-on tests allow the tester to perform different customer work-

flows. In the final phase, the test manager collects and evaluates all the results and feedback. A summary report of the validation phase is then provided to the project manager and the department for regulatory affairs.

What do you find most motivating about your job?
That I'm learning all the time. I love being in contact with the testers who represent MAGNETOM users, and listening to what they have to say about the new MRI system or features, their own clinical experience and challenges, and their wishes. Everybody in our company has the power to move MRI forward. We cannot make every wish come true, but when I look back at where we came from and where we are today, it makes me proud. I'm certain that MRI has an exciting future in store.

If you could do anything you wanted for a month, what would it be?
The system validation phase is a busy time, so I'd like to be able to visit our MAGNETOM users more often. It's so important and helpful that we understand our customers' business needs, and that our customers understand our business. Both worlds are always changing, and it's important that we stay in touch.

When I'm not working, I prefer being outside and traveling. My husband and I are in love with Australia. We have friends there, in Bargo. We also enjoy heading into the outback, along the Gibb River Road, and eating grilled barramundi around the campfire. It's great to switch off by hiking the trail to Mitchell Falls and going stock-horse riding on the plateau.

Visit MAGNETOM World

Find more portraits of our colleagues around the world!

www.siemens-healthineers.com/magnetic-resonance-imaging/magnetom-world/meet-siemens-healthineers

The entire editorial staff at Michigan State University and Spectrum Health, and at Siemens Healthineers extends their appreciation to all the radiologists, technologists, physicists, experts, and scholars who donate their time and energy – without payment – in order to share their expertise with the readers of MAGNETOM Flash.

MAGNETOM Flash – Imprint

Publisher:
Siemens Healthcare GmbH
Magnetic Resonance,
Karl-Schall-Str. 6, D-91052 Erlangen, Germany

Editor-in-chief:
Antje Hellwich
(antje.hellwich@siemens-healthineers.com)

Guest editor:
Mark C. DeLano, MD, FACR
Director, Division of Radiology and Biomedical Imaging
College of Human Medicine
Michigan State University
Medical Director, Adult Radiology, Spectrum Health
Advanced Radiology Services, PC

Editorial Board:
Rebecca Ramb, Ph.D.; Sunil Kumar S. L., M.D.;
Wellesley Were; Gary R. McNeal, MS (BME);
Nadine Leclair, M.D.

Review Board:
Katja Böhm; André Fischer, Ph.D.;
Daniel Fischer; Christian Geppert, Ph.D.;
Berthold Kiefer, Ph.D.; Heiko Meyer, Ph.D.;
Efrén Ojeda; Gregor Thörmer, Ph.D.

Copy Editing:
Sheila Regan, Jen Metcalf, UNIWORKS,
www.uni-works.org
(with special thanks to Kylie Martin)

Layout:
Agentur Baumgärtner,
Friedrichstr. 4, D-90762 Fürth, Germany

Production:
Norbert Moser,
Siemens Healthcare GmbH

Printer:
G. Peschke Druckerei GmbH,
Taxetstr. 4, D-85599 Parsdorf b. Munich, Germany

Note in accordance with § 33 Para.1 of the German Federal Data Protection Law: Despatch is made using an address file which is maintained with the aid of an automated data processing system.

MAGNETOM Flash is sent free of charge to Siemens Healthineers MR customers, qualified physicians, technologists, physicists and radiology departments throughout the world. It includes reports in the English language on magnetic resonance: diagnostic and therapeutic methods and their application as well as results and experience gained with corresponding systems and solutions. It introduces from case to case new principles and procedures and discusses their clinical potential. The statements and views of the authors in the individual contributions do not necessarily reflect the opinion of the publisher.

The information presented in these articles and case reports is for illustration only and is not intended to be relied upon by the reader for instruction as to the practice of medicine. Any health care practitioner reading this information is reminded that they must use their own learning, training and expertise in dealing with their individual patients. This material does not substitute for that duty and is not intended by Siemens Healthcare to be used for any purpose in that regard. The drugs and doses mentioned herein are consistent with the approval labeling for uses and/or indications of the drug. The treating physician bears the sole responsibility for the diagnosis and treatment of patients, including drugs and doses prescribed in connection with such use. The Operating Instructions must always be strictly followed when operating the MR system. The sources for the technical data are the corresponding data sheets. Results may vary.

Partial reproduction in printed form of individual contributions is permitted, provided the customary bibliographical data such as author's name and title of the contribution as well as year, issue number and pages of MAGNETOM Flash are named, but the editors request that two copies be sent to them. The written consent of the authors and publisher is required for the complete reprinting of an article.

We welcome your questions and comments about the editorial content of MAGNETOM Flash. Please contact us at
magnetomworld.team@siemens-healthineers.com

Manuscripts as well as suggestions, proposals and information are always welcome; they are carefully examined and submitted to the editorial board for attention. MAGNETOM Flash is not responsible for loss, damage, or any other injury to unsolicited manuscripts or other materials. We reserve the right to edit for clarity, accuracy, and space. Include your name, address, and phone number and send to the editors, address above.

MAGNETOM Flash is also available online:

www.siemens.com/magnetom-world

Not for distribution in the US

On account of certain regional limitations of sales rights and service availability, we cannot guarantee that all products included in this brochure are available through the Siemens sales organization worldwide. Availability and packaging may vary by country and is subject to change without prior notice. Some/All of the features and products described herein may not be available in the United States.

The information in this document contains general technical descriptions of specifications and options as well as standard and optional features which do not always have to be present in individual cases, and which may not be commercially available in all countries.

Due to regulatory reasons their future availability cannot be guaranteed. Please contact your local Siemens organization for further details.

Siemens reserves the right to modify the design, packaging, specifications, and options described herein without prior notice. Please contact your local Siemens sales representative for the most current information.

Note: Any technical data contained in this document may vary within defined tolerances. Original images always lose a certain amount of detail when reproduced.

Siemens Healthineers Headquarters
Siemens Healthcare GmbH
Henkestr. 127
91052 Erlangen, Germany
Phone: +49 9131 84-0
siemens-healthineers.com

Published by Siemens Healthcare GmbH · Order No. A91MR-1000-142C-7600 · Printed in Germany · 7763 1119 ·